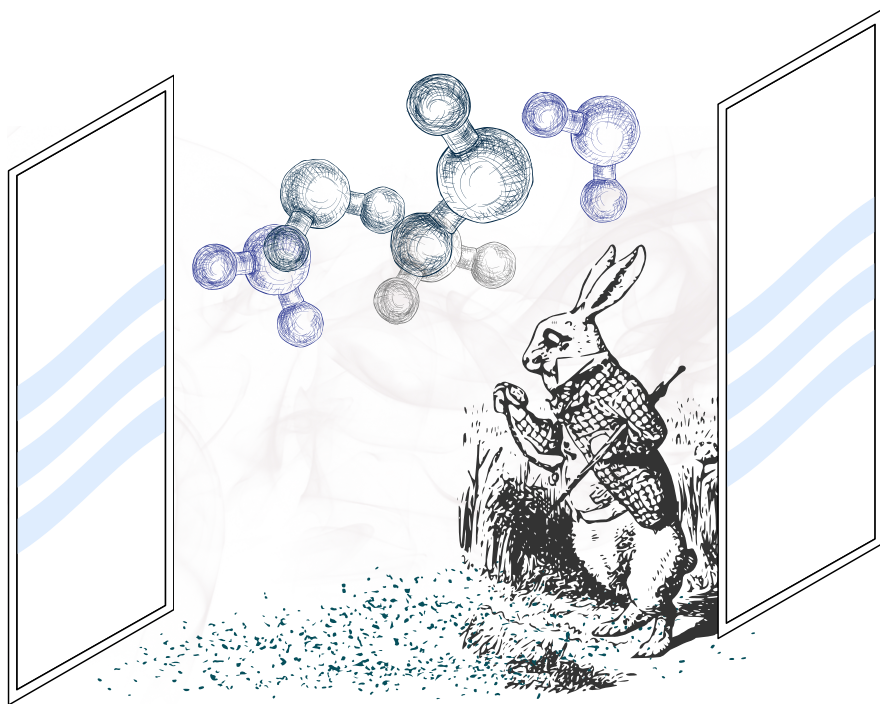
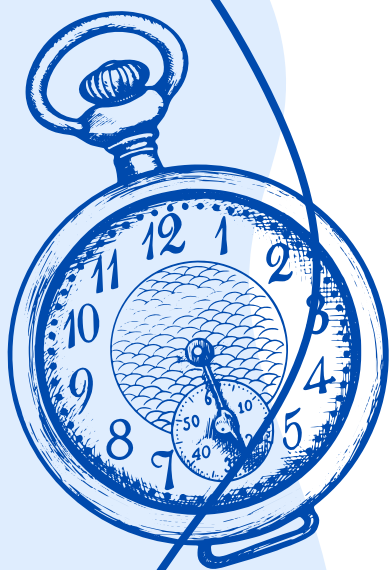


Analysis of the structure and dynamics of polaritons through multidimensional spectroscopy

Daniela Gallego Valencia



UAM

Universidad Autónoma
de Madrid

PhD Thesis



**Universidad Autónoma
de Madrid**

Analysis of the structure and dynamics of polaritons through multidimensional spectroscopy

Daniela Gallego Valencia

Universidad de Antioquia
Facultad de Ciencias Exactas y Naturales, Instituto de Física
Medellín, Colombia

and

Universidad Autónoma de Madrid
Facultad de Ciencias, Departamento de Física Teórica de la materia condensada
Madrid, España

2024

Analysis of the structure and dynamics of polaritons through multidimensional spectroscopy

Ph.D work presented as a requirement to obtain the title of:
(Trabajo de grado presentado como requisito parcial para optar al título de):

DOCTORA EN FÍSICA
and
**DOCTORA EN FÍSICA DE LA MATERIA CONDENSADA,
NANOCIENCIA Y BIOFÍSICA**

Advisor (Director):
Ph.D. José Luis Sanz-Vicario
Universidad de Antioquia

Coadvisor (Codirector):
Ph.D. Johannes Feist
Universidad Autónoma de Madrid

Area of research (Línea de Investigación):
Polariton Chemistry, Quantum Optics, Non linear multidimensional spectroscopy
(Química polaritónica, óptica cuántica. Espectroscopía non lineal multidimensional)

Grupo de Investigación:
Grupo de Física Atómica y Molecular (UdeA)
Grupo de Nanofotónica (UAM)

Tribunal members

Francesca María Marchetti

Associate Professor
Departamento de Física Teórica de la Materia Condensada
Universidad Autónoma de Madrid
Madrid, España

Juan Nicolás Quesada Mejía

Professeur Adjoint
École Polytechnique de Montréal
Montréal, Canada

Alejandra Catalina Valencia González

Associate Professor
Departamento de Física
Universidad de los Andes
Bogotá, Colombia

Publications and participation in events

Scientific article

Title: Coherent multidimensional spectroscopy in polariton systems

Daniela Gallego-Valencia, Lars Mewes, Johannes Feist, and José Luis Sanz-Vicario

Physical Review A, **109**, 063704

Published 11 June 2024

Popular science article

Title: Estroboscopia en el mundo cuántico de átomos, moléculas y fotones

Daniela Gallego-Valencia, and José Luis Sanz-Vicario

Revista Experimenta, **17**, 18

Published 28 July 2023

Poster

Title: Espectroscopía bidimensional de polaritones moleculares

XXIX Congreso Nacional de Física

Universidad del Quindío Armenia, Colombia

September 21-23, 2022

Poster

Title: Two-dimensional spectroscopy of molecular polaritons

Workshop Molecular Polaritonics 2022: Theoretical and Numerical Approaches

Straubing, Germany

September 12-14, 2022

“What we observe is not nature itself, but nature exposed to our method of questioning.”

Werner Heisenberg, *Physics and Philosophy: The Revolution in Modern Science*

To my parents...

Acknowledgments

I am deeply grateful to my thesis advisors, Prof. José Luis Sanz Vicario (UdeA) and Prof. Johannes Feist (UAM), for their unwavering commitment and dedication throughout the completion of this PhD work. Their wealth of experience and knowledge was immensely enlightening and instrumental in guiding me through this process.

I also extend my gratitude to Dr. Lars Mewes for sharing his experimental expertise and deep insight in the field of 2D spectroscopy when applied to molecular polaritons. We thank him for the many useful discussions during the completion of this work and for allowing us to use his experimental data in order to test our theoretical developments.

Furthermore, I am thankful to my colleagues and friends inside and outside the Instituto de Física at Universidad de Antioquia. Thank you to Jennyfer Morales (Jenny) and Carlos Gaviria (Carlitos) for sharing coffee breaks, for their friendship, and for the support they provided me during the most challenging moments of this process. Thank you, Jenny, and to the Optics group for allowing me to use the Barlai laboratory. Thanks to Andrés Estrada (Calambre) and Sebastián Martínez for the coffee and discussions. Thanks to Natalia Caro (Naty) for her friendship and unwavering support. I am immensely grateful to Katherine Nanclares (Kathe) for being there for me throughout my journey and for her words of encouragement that helped me overcome emotional obstacles. Thank you to Camilo López (Cami) for your companionship during difficult times, and for everything else.

Thank you to the people in Johannes Feist's group at Universidad Autónoma de Madrid. Thank you Clàudia Climent, Diego Fernández, Maksim Lednev, Jacopo Fregoni, Petros Pantazopoulos, Mónica Sánchez, Ruth Tichauer, Anael Ben-Asher and Jacob Busche. Thank you for their kind attention, help and support during this journey.

I want to express my gratitude to my parents Atanasio and Luz Marina and to my brother Hámilton, for all their support and understanding. Thank you to all my close relatives who contributed, directly or indirectly, to finish this personal endeavor, for which their support has been invaluable.

Finally, I acknowledge the funding support provided by Vicerrectoría de Investigación at Universidad de Antioquia under project CODI Programática 2022-53576, by the Spanish Ministry for Science and Innovation-Agencia Estatal de Investigación (AEI) through Grants PID2021-125894NB-I00, CEX2018-000805-M (through the María de Maeztu program for Units of Excellence in R&D), and by the European Research Council through Grant No. ERC-2016-StG-714870. Their financial assistance made this research possible.

Resumen

En este trabajo de tesis doctoral se investiga teóricamente la estructura y fotodinámica rápida de los polaritones moleculares utilizando para ello una secuencia de pulsos láser según los protocolos de la espectroscopía no lineal bidimensional. El sistema físico en estudio es un colectivo de emisores moleculares en interacción fuerte con un modo de la radiación cuantizada en una cavidad y sujeto a procesos disipativos debidos al ambiente que lo rodea.

En el límite semi-impulsivo y con la aproximación de onda rotante para los pulsos láser, se han obtenido fórmulas conceptualmente simples y computacionalmente eficientes para el cálculo de espectros bidimensionales dentro de un enfoque perturbativo. Estas expresiones son útiles para cualquier sistema cuántico abierto caracterizado con un Liouvilliano. Excepto por la diagonalización de la matriz del Liouvilliano, nuestro método es completamente general y analítico.

Se ha llevado a cabo un estudio detallado de espectros lineales y no lineales para un número finito de moléculas emisoras confinadas en una cavidad. Cada molécula se trata como un sistema de dos niveles electrónicos, sujeta a procesos de relajación vibracional y la cavidad sufre pérdidas fotónicas. Estos procesos disipativos se adicionan a la dinámica del Hamiltoniano, modelando un sistema cuántico abierto cuya dinámica se ha resuelto a través de una ecuación maestra para el operador densidad. En escenarios de un colectivo de moléculas, la dinámica de la relajación de los estados polaritónicos brillantes hacia los estados oscuros emerge como un factor crucial para explicar la asimetría observada en las señales espectrales experimentales. Esta asimetría se pone de manifiesto tanto en los picos de los espectros lineales de absorción y emisión como en los picos diagonales y cruzados de los espectros no lineales bidimensionales. La descripción teórica desarrollada en esta tesis resulta consistente con resultados experimentales recientes realizados sobre J-agregados moleculares inmersos en cavidades.

Palabras clave:

Química polaritónica. Óptica cuántica, Espectroscopías no lineales multidimensionales

Abstract

In this doctoral thesis, the theoretical structure and fast photodynamics of molecular polaritons are investigated by using a sequence of laser pulses according to protocols of two-dimensional nonlinear spectroscopy. The physical system under study is an ensemble of molecular emitters in strong interaction with a mode of quantized radiation in a cavity and subject to dissipative processes due to the surrounding environment.

In the semi-impulsive limit and within the rotating wave approximation for laser pulses, conceptually simple and computationally efficient formulas have been obtained for calculating two-dimensional spectra within a perturbative approach. These expressions are useful for any open quantum system characterized by a Liouvillian. Except for the diagonalization of the Liouvillian matrix, our method is entirely general and analytical.

A detailed study of linear and nonlinear spectra has been conducted for a finite number of emitter molecules confined in a cavity. Each molecule is treated as a two-level electronic system, subject to vibrational relaxation processes, and the cavity undergoes photon losses. These dissipative processes are added to the dynamics of the Hamiltonian, modeling an open quantum system whose dynamics is solved through a master equation for the density operator. For an ensemble of molecules, the relaxation dynamics of bright polariton states to dark states emerges as a crucial factor in explaining the asymmetry observed in experimental spectral signals. This asymmetry is evident in both the peaks of linear absorption and emission spectra and in the diagonal and cross peaks of two-dimensional nonlinear spectra. The theoretical description developed in this thesis is consistent with recent experimental results conducted on molecular J-aggregates immersed in cavities.

Keywords:

Polariton Chemistry, Quantum Optics, Nonlinear multidimensional spectroscopy.

Contents

Acknowledgments	VII
Resumen	VIII
Abstract	IX
List of acronyms	XIII
I. Introduction	1
II. Theoretical framework	10
1. Radiation-Matter Interaction	11
1.1. General Radiation-Matter interaction and confinement in cavities	11
1.1.1. Transverse and longitudinal electric fields	12
1.1.2. Obtaining a general radiation-matter Hamiltonian	13
1.1.3. Confinement in cavities and single-mode approximation	15
1.2. Description of molecular emitters	17
1.3. Modeling Radiation-Matter interaction in cavities	20
1.3.1. Tavis-Cummings model	21
1.3.2. Polariton states	22
2. Open Quantum Systems	25
2.1. Quantum dynamics in Hilbert and Liouville space	25
2.1.1. The density operator	25
2.1.2. Time evolution in Hilbert space	26
2.1.3. Representations in Hilbert space and the Liouvillian superoperator	27
2.1.4. Quantum objects in Liouville space	28
2.1.5. Time evolution in Liouville space	30
2.1.6. Eigenvalues and eigenvectors of the Liouvillian	31
2.1.7. Beyond Hamiltonian dynamics	32
2.2. Master equations for incoherent dynamics	32
2.2.1. Born-Markov master equation	33
2.2.2. Bloch-Redfield master equation	35
2.2.3. Lindblad master equation	37

2.3.	Incoherent processes for polariton systems	39
2.3.1.	Molecular relaxation due to vibrational bath	39
2.3.2.	Cavity photon losses	40
2.3.3.	Additional incoherent processes	41
3.	Coherent Multidimensional Spectroscopy	42
3.1.	General Optical Spectroscopy protocols	42
3.1.1.	Parametric semiclassical interaction	42
3.1.2.	Weak field approach	44
3.1.3.	Multiwave mixing	45
3.2.	Perturbative computation of nonlinear polarization	46
3.2.1.	Perturbative expansion of the density operator	46
3.2.2.	n-th order polarization and response function	48
3.3.	Using time correlation functions	49
3.3.1.	Linear response function	50
3.3.2.	Third-order response function	51
3.4.	Additional approximations	51
3.4.1.	Semi-impulsive limit	51
3.4.2.	Rotating wave approximation	52
3.5.	Linear spectra	53
3.5.1.	Linear absorption	54
3.5.2.	Linear emission	54
3.5.3.	Double-sided Feynman diagrams	56
3.6.	2D coherent spectroscopy	57
3.6.1.	Experimental 2D spectroscopy protocol	57
3.6.2.	Feynman diagrams contributing to non rephasing and rephasing	58
3.6.3.	Physical processes: GSB, SE, ESA	61
3.6.4.	2D nonlinear spectra	62
3.7.	Analytical computation of the third-order nonlinear response	64
3.7.1.	Representations in Liouvillian eigenbasis	65
3.7.2.	Excitation process	66
3.7.3.	Detection process	67
3.7.4.	Frequency domain spectra	68
III.	Results and discussion	70
4.	Multidimensional spectroscopy in the dissipative Jaynes-Cummings model	71
4.1.	Liouvillian eigenvalues and eigenstates	71
4.2.	Linear spectra	77
4.3.	Two-dimensional non-linear spectra (2DS)	80

4.4.	Contributing pathways	82
4.4.1.	GSB (Ground State Bleaching) and GSR (Ground State Recovery)	85
4.4.2.	SE (Stimulated Emission)	88
4.4.3.	ESA (Excited State Absorption)	90
4.4.4.	ESA' (Excited State Absorption Prime)	91
4.5.	Excitation and Detection Masks	91
4.6.	2DS building history	94
4.6.1.	Excitation	95
4.6.2.	Evolution T	97
4.6.3.	Pulse 3	97
4.6.4.	Detection	97
5.	Multidimensional spectroscopy in the dissipative Tavis-Cummings model	98
5.1.	Hamiltonian, Liouvillian and linear response	98
5.2.	Two-dimensional non-linear spectra (2DS)	102
5.3.	Population pathways	104
5.3.1.	GSR (Ground State Recovery) and dark states	104
5.3.2.	ESA (Excited State Absorption)	106
5.4.	Temperature effects on polariton states	108
5.4.1.	GSB and GSR: Population pumping L to D	110
5.4.2.	SE: Slight population pumping L to U	111
5.4.3.	ESA: Population transfer L-U-D and U-L-D	112
5.5.	Comparison with experiments	114
6.	Interacting Molecules and Energy Transport	117
6.1.	Adding molecule-molecule interaction to the TC model	117
6.1.1.	Energy structure, linear response and dynamics	117
6.1.2.	Effects of molecule-molecule interaction on 2DS	122
6.2.	Energy transport between two groups of molecules and cavity	130
6.2.1.	Properties of the model and energy distribution of the states	130
6.2.2.	Energy transfer pathways	133
6.2.3.	2D Spectroscopy applied to the energy transport process	136
IV.	Conclusions	140
	References	148

List of acronyms

Acronym	Description
cQED	cavity Quantum Electrodynamics
EM	electromagnetic
2DS	two-dimensional spectrum (or spectra)
JC	Jaynes-Cummings
TC	Tavis-Cummings
GSB	Ground State Bleaching
GSR	Ground State Recovery
SE	Stimulated Emission
ESA	Excited State Absorption
ESA'	Excited State Absorption Prime
R	Rephasing
NR	Non rephasing
PM	Phase Matching
<i>L</i>	Lower (polariton)
<i>U</i>	Upper (polariton)
<i>D</i>	Dark (polariton)
LS	Liouville Space
HS	Hilbert Space
RWA	Rotating Wave Approximation
PZW	Power - Zineaw - Woolley
IM	Interacting molecules
DA	Donor - Acceptor
HOMO	Highest occupied molecular orbital
LUMO	Least unoccupied molecular orbital
DBRs	Distributed Bragg reflectors.

Part I.

Introduction

Introduction

This PhD work intends to shed light on the fast dynamics of radiative and nonradiative processes of molecules immersed in optical cavities, subject to strong coupling with the cavity quantized radiation, by using nonlinear multidimensional spectroscopy techniques. The theoretical understanding of the many peaked signals (their intensity, position and broadening) that appear in the nonlinear spectra of this kind of entangled quantum systems help in the elucidation of the inner mechanisms of excitation, emission and dissipative relaxation of molecular polaritons. These field dressed states emerge from the interaction between light and matter in the strong coupling regime inside cavities [1, 2]. In this regime the molecular emitters coherently interact with the cavity and they emit and reabsorb cavity photons to undergo Rabi oscillations between excited states and the ground state, with an associated process of photon-matter hybridization.

Polaritons have proven to be effective in many photodynamics applications, for instance, they have been used for modifying molecular chemical reactions [3, 4, 5, 6, 7, 8], even suppressing some reaction pathways [9]. They have also been exploited to significantly enhance energy transport processes [10, 11, 12, 13, 14, 15]. Other applications can be found in [16, 17]. The potential uses of polaritons to modify chemical properties has given rise to the field of polaritonic chemistry [18, 19, 20, 21, 22, 23, 24], which bridges two major fields of research: i) cavity quantum electrodynamics (cQED), which describes the quantum nature of electromagnetic (EM) fields confined in cavities, necessary for obtaining polariton states, and ii) chemistry, which describes the material emitters (usually atoms or molecules), the second ingredient necessary to forming polaritons. The confinement of EM fields in cavities is what enables, in principle, achieving a strong coupling regime between matter and radiation, although polaritons can also be formed without cavities (see e.g. the paper [25] for a discussion).

Each polaritonic component (radiation and matter) undergoes relaxation or decay processes [26, 27, 28, 29]. The EM field modes exhibit significant photon losses due to the imperfections of the cavities, while the material emitters, in our case for electronic excitations, interact with vibrational baths and undergo spontaneous emission and vibrational relaxation, among other phenomena. Achieving a complete ab initio theoretical model of these systems would be impractical due to the computational cost and complexity. To address these loss mechanisms, techniques from the formalism of open quantum systems are extensively used [30].

The polariton states involving simultaneous excitation of the matter (excitons) and the EM field (pho-

tons) are stable enough to be monitored through spectroscopy techniques before their decay due to the decoherence induced by the environment. Linear and nonlinear spectroscopy protocols make use of short laser pulses in the weak field regime (where the pulses are represented by classical light, and they excite the photons present inside the cavity in the form of polaritons). This weak field limit for the laser pulses allows for a perturbative approach from the theoretical point of view. This is the main goal of our study here, to understand in detail the structure and fast dynamics of molecular polaritons upon linear and, more extensively, nonlinear response of these systems upon a number of perturbative interactions in multidimensional spectroscopy.

In the near-infrared and infrared ranges, multidimensional spectroscopy has enabled the observation of multi-polariton coherences in quantum wells coupled to semiconductor microcavities [31, 32] and the examination and control of optical nonlinearities in vibrational polaritons [33, 34]. In the visible spectrum, multidimensional spectroscopy has been employed to investigate broadening and relaxation mechanisms in strongly coupled exciton-plasmon (plexitonic) systems and to provide a detailed understanding of the interaction between polaritons and the bath in a molecule-microcavity system [35, 36, 37].

A recent experiment has employed two-dimensional electronic spectroscopy to probe the ultrafast dynamics of a polaritonic system involving molecular J-aggregates within optical cavities [38]. Motivated by the asymmetric signals observed in the experimental spectra, we conduct a theoretical study of coherent multidimensional spectroscopy of organic molecular polaritons. To provide a comprehensive and clear framework, we initially examine the prototypical Jaynes-Cummings model for a single emitter, and subsequently expand our analysis to the Tavis-Cummings model with multiple molecules. We investigate the theoretical spectroscopic signals originating from open quantum systems governed by these Hamiltonian models, subject to relaxation processes due to both molecular vibrational modes and photonic losses of the cavity (see Fig. 0.1). Our simple models are intended for systems such as dye molecules with weak exciton-phonon interactions, allowing a perturbative treatment of coupling to molecular vibrations. Specifically, molecular J-aggregates used in [38] create delocalized collective electronic states that exhibit weak coupling to vibrational modes. In this regard, our theoretical results capture some of the features observed in the experimental spectra from [38] and provide a deeper understanding of the dynamics and asymmetries of the diagonal and cross spectral peaks, explained by the critical role of dark states.

The polariton photodynamics of the Tavis-Cummings model has also been explored recently in the context of pump-probe spectroscopies [39]. Additionally, recent research on two-dimensional electronic spectroscopy beyond the Markovian approximation use quantum stochastic Liouville equations or the Heisenberg-Langevin model to identify signatures of the polariton-polaron interaction and to characterize the dynamics of population transfer [40, 41, 42].

In our attempt to simulate two-dimensional polaritonic spectra, we develop an efficient pseudo-analytic procedure for computing the spectra within a perturbative framework, where the three pulses of the spectroscopic protocol do not overlap (semi-impulsive limit). Our method, which involves solving the

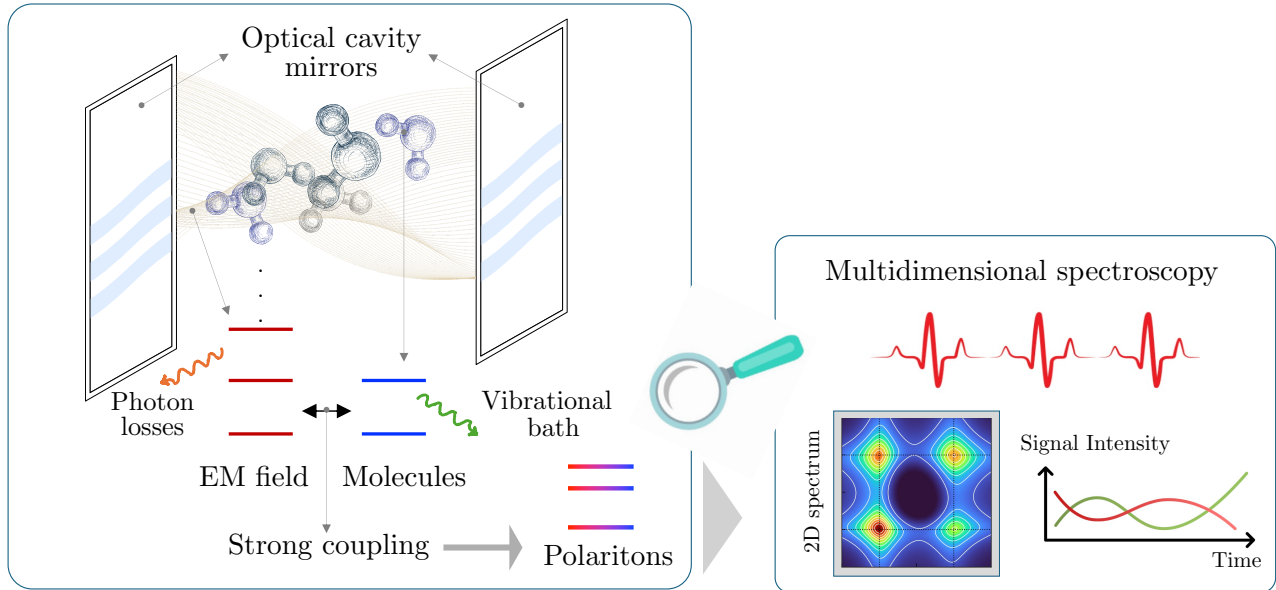


Fig. 0.1.: Schematic representation of our study problem: an open system of molecules embedded in an optical cavity under strong interaction with the electromagnetic field. The single-mode field is depicted as a harmonic oscillator with the cavity frequency, subject to photon losses. Each molecule is represented as a two-electronic-level system coupled to a vibrational bath. The strong interaction between the molecules and the quantum field generates polaritonic states, which are hybridized states between radiation and matter. This polaritonic system is subject to multidimensional nonlinear spectroscopy techniques. Specifically, in the case of 2D spectroscopy, the system interacts with three classical ultrashort laser pulses. Temporal analysis of the signals collected in the 2D spectra allows us to probe the dynamics of the formed polaritonic states, including their decay channels, population transfer, energy transport, among others.

system dynamics analytically in the Liouville space, not only results in low computational time costs but also enables an interpretation of the two-dimensional spectra by analyzing their formation at any spectroscopic experimental stage: excitation, evolution, probing, and detection.

We extend our study to a Hamiltonian where molecules interact directly with each other, not just through the cavity, as assumed in the Tavis-Cummings model. This approach allows us to observe novel signals in the two-dimensional spectra, indicating the formation of new polaritonic states and alternative decay pathways. Additionally, we analyze a simple donor-acceptor polariton model to explore many energy transport mechanisms. Other parallel research in this area has demonstrated that energy cascades through a series of new electronic states generated by intermolecular coupling and the distinct bandgaps of the donor and acceptor [43].

The development of the present research requires a series of concepts and methods, which are the key ingredients in molecular polaritonics, namely i) the quantum nature of radiation: in contrast to

the typical radiation-matter interaction based on a semiclassical approach where light is treated classically, this scenario changes when matter is confined in optical cavities. ii) quantum emitters: let them be atoms or molecules with a given internal structure. In the case of molecules, their electronic and vibrational structure is mostly relevant in our study when they are confined in optical cavities with modes resonant with electronic transitions. iii) Strong light-matter coupling: quantum radiation and molecular emitters are strongly coupled to form new hybridized states (matter + light) called polaritons, which display energy splittings proportional to the coupling strength, with respect to the uncoupled state energies. These molecular polaritons are the main physical system under study in this thesis. iv) Multidimensional spectroscopy: the appropriate tool to follow and understand the structure and fast inner photodynamics of molecular polaritons is their interaction with short laser pulses using pump-probe protocols under a weak-field regime. In our case, multidimensional spectroscopy is a well-developed technique that involves a series of sequential pulses separated by controlled time intervals within a time window of femtoseconds, the natural time for excitation and decay of polaritons.

We briefly describe each separate ingredient in the following.

The EM field confined in cavities

For the generation of molecular polaritons, most experiments can be classified according to the use of two types of cavities: optical Fabry-Perot and plasmonic nanocavities. A Fabry-Perot cavity consists of two highly reflecting mirrors separated by a short distance. Between the mirrors, the standing waves compatible with the cavity length can be tuned to a cavity mode frequency ω_c . Any cavity possess its characteristic lifetime $\tau_c = Q/\omega_c$ that indicates the average lifetime of a photon excitation, which increases for high quality factors Q .

It is worth noting that the light-matter interaction strength for a single molecule (here $\hbar g$) depends inversely on the active volume of the cavity, i.e., $g \propto 1/\sqrt{V}$, which means that single molecules are unable to reach the strong coupling regime in optical cavities. In fact, a large ensemble of N molecules is required due to the enhancement scaling factor $g\sqrt{N}$ [44]. This situation is overcome in plasmonic nanocavities produced when the light irradiates metallic nanostructures. The light induces electron collective oscillations (plasmons) with a set of plasmonic modes. These kind of plasmonic cavities may reach a strong-coupling regime even with a single molecule, although their drawback is to have large dissipative losses, thus a poor quality factor Q .

The matter emitters: molecules

The other ingredient in the formation of polaritons are the quantum emitters. We describe the molecular emitters by using parametric models in which only two electronic states are considered. The introduction of a two-level approximation for the structure of emitters can be justified by i) the theory of frontier orbitals in molecular photo reactions, ii) the fact that these two states are coupled through the largest transition dipole moment, and iii) the photon blockade effect once the molecular polaritons are formed, which avoids higher matter excitations due to the strong anharmonicity of the polariton

energy spectrum along the series of excitation manifolds.

The molecules inside the cavities exhibit both radiative (r) and non radiative (nr) decay processes, from spontaneous (r) emission to (nr) intramolecular vibrational relaxation due to energy exchange with other molecules through collision processes.

The strong light-matter coupling

Our multidimensional spectroscopy study over molecular polaritons is always carried out in the strong-coupling regime, characterized by i) the rapid exchange of energy between photons and excitons, that induce Rabi oscillations with a frequency $\Omega_R = 2g$. ii) the energy splitting $\hbar\Omega_R$ between the lower L and the upper L polaritons, large enough to be detected experimentally but smaller than the energies related to the natural frequency of the molecule ω_0 and the cavity mode frequency ω_c . iii) decay rates κ for photon losses and vibrational relaxation rates γ smaller or at the most comparable to the coupling strength g .

Multidimensional spectroscopy

Multidimensional spectroscopy [45, 46, 47, 48, 49], a set of techniques widely utilized in the study of molecular systems, offers insights into their structure and dynamics with high temporal and spectral resolution. This tool, applied both at optical and at infrared frequencies and with femtosecond time resolution, has been instrumental in investigating various physical and chemical processes such as in charge transfer in donor-acceptor models [50], vibrational and electronic energy transfer, photoisomerization, and chemical reactions [51]. Specifically, two-dimensional spectra (2DS) provide valuable information about vibrational and electronic motions, interactions, and relaxation channels. Recent advancements have extended multidimensional spectroscopy to molecular-cavity (polaritonic) systems [42, 41, 52, 37, 53, 40], enabling the study of vibrational [54, 55, 56, 57] and electronic [38] polariton states dynamics. In a typical 2D spectroscopy experiment, the system interacts with three delayed ultrashort classic pulses, and the resulting signal reflects the third-order nonlinear polarization. By adjusting the delay times between pulses, it is possible to construct 2D maps at different times, facilitating the observation of fast processes involved in the system dynamics.

The experimental work [58] that launched the present study was performed using organic dye molecules TDBC, which have a complex vibrational structure in addition to their electronic one. For these organic molecules the absorption and fluorescence emission spectra lie in the visible and UV window of frequencies, and the spectral lines show the fingerprint of electronic transitions with linewidths broadened by the inner vibrational processes (vibronic bands). The mentioned experiment claim that their dye polar molecules TDBC are in the form of J-aggregates, which are ensembles of molecules clustered due to intermolecular forces, and their collective optical properties may differ from those of the isolated molecules. J-aggregates show indeed rather small Stokes shifts (the difference in frequency between the main absorption and emission bands) which reflects weak effects due to intramolecular vibrational relaxation. This property may help in our model, since it means that the electronic and

vibrational degrees of freedom are weakly coupled in J-aggregates and, consequently, molecular relaxation can be treated within a perturbative approach without an explicit introduction of the complex vibrational structure.

Structure of the thesis

This work is divided in four parts:

- I. Introduction.
- II. Theoretical framework.
- III. Results and discussion, and
- IV. Conclusions.

In this introduction we provide a general flavor of the research topic with its basic concepts, nomenclature and general considerations that serve to delimit the scope of the work.

Chapter 1: In part II, Theoretical framework, we provide in [Chap. 1](#) a comprehensive description of the radiation-matter interaction, starting from the minimal coupling Hamiltonian, then providing the field quantization, and the Power-Zienau-Wooley transformation, that introduces the transversal part of the polarization for the matter and the dipole length form $\hat{\boldsymbol{\mu}} \cdot \hat{\boldsymbol{E}}$ for the field-matter interaction. Since the matter in our study is represented by molecules, we make a short account of the approximations that lead to our model that represents the system of molecular J-aggregates. We also introduce the well-known collective Tavis-Cummings model in quantum optics, the concepts of excitation manifolds, bright and dark states and the general structure of polariton states up to the second excitation manifold.

Chapter 2: This chapter introduces the concepts and methods of open quantum systems. It is important to distinguish the representations in Hilbert and Liouville spaces of the density and other operators. We arrive to the Liouville-von Neumann equation in terms of the Liouville superoperator. We clarify the nature of quantum objects (states and operators) as represented in Hilbert space or Liouville space. In fact, the master equation can be expressed in both spaces. We make a revision of the theory of open quantum systems by introducing the master equations for the reduced density operator of the quantum system surrounded by a coupled bath, the Born and Markov approximations, the Bloch-Redfield master equation and its reduction to the Lindblad master equation after additional approximations. In our work we have used the Bloch-Redfield formalism for the vibrational relaxation but a Lindblad form for the photon loss.

Chapter 3: This chapter presents the core for the principles of coherent multidimensional spectroscopy, assuming that the four lasers involved in the protocol represent a weak field interaction, which justifies a perturbative approach. 2DS implies a four-wave mixing process with a chosen phase-matching condition for the wave vectors and their corresponding frequencies. A n -dimensional spectroscopy requires the computation of the n th-order component of the density operator using n th-order perturbation

theory. The observed signal is proportional to the n th order polarization, built from the n th-order density operator, which can be expressed in terms of the n th order response function convoluted by the n laser field amplitudes. We focus on the third order response function, as required for 2D spectroscopy, which can be expressed in terms of three-time correlation functions. An important approximation in our work is to assume an impulsive limit for the external electric fields, i.e., they are instantaneous sudden perturbations with a temporal shape provided by delta functions. This well-justified approximation is crucial to find analytical expressions of the 2D spectra and to shorten the computations by orders of magnitude.

Previous to non-linear spectra we also study the theory of linear (absorption and emission) spectra, with expressions related to two-time correlation functions. For 2D spectra it is mandatory to describe the doubly sided Feynman diagrams with the different paths that contribute to the third order non-linear response function, which represent the well-known processes GSB (ground state bleaching), SE (stimulated emission) and ESA (excited state absorption). The experimental protocol of a non-linear third-order (four-wave mixing, with heterodyne detection) optical spectroscopy is also described, with the fundamental steps: 1) excitation process, with pulse 1 and pulse 2, separated by an excitation time interval τ . 2) Waiting step with a time T 3) detection process after the pulse 3; the system eventually emits radiation at any time t after the third pulse, a temporal interval named detection time. Among the many choices for the phase matching conditions, we focus on the rephasing and non-rephasing cases, since they correspond to the experimentally relevant case.

One of the major developments in this work is the derivation of an analytical expression for the third-order nonlinear response in the time domain and, ultimately, after its Fourier transform a simple formula for the construction of the 2D spectra in the frequency domain.

Part III deals with our computational results and discussions.

Chapter 4: We start with the comprehensive description of 2D spectroscopy applied to the polariton structure of a dissipative Jaynes-Cummings model. It turns out that the Liouvillian matrix $\mathcal{L}_{\alpha\beta,\gamma\delta}$ is block diagonal in the basis of Hamiltonian eigenstates and these blocks (containing population and coherence contributions) do not mix upon time evolution. The structure of this Liouvillian matrix serves to roughly understand the irreversibility of the dissipative decay processes and its set of complex eigenvalues allows for a produce a hierarchy of states according to its decay width, with the ground state being the only stationary state. It shows a larger decay width for the upper U polariton than for the lower L polariton, from which an $L - U$ asymmetry in the peak strengths in linear spectra is expected. We also explain how other asymmetries in the diagonal L/L and U/U and cross peaks L/U and U/L develop during the waiting time T (the main time window for decay). [Chap. 4](#) includes a very detailed analysis of the temporal buildup of the 2D spectrum for the prototype dissipative Jaynes-Cummings model. We separate the contributions from the populations and the coherences in the spectra, indicating that the coherence contribution carries most of the Rabi oscillations during the waiting time T . The Jaynes-Cummings model has no dark states at all, but asymmetries in 2D spectra develop for waiting times $T > 0$, largely contributed by the SE, ESA and ESA' components

of the spectrum, ultimately due to the different decay rates of lower and upper polaritons.

Chapter 5: We expand our study to an ensemble of molecules through the collective Tavis-Cummings model with N emitters, subject to the same dissipative processes. Now $N - 1$ dark states are present in the Hamiltonian eigenspectrum, and the polariton U has new decay channels in contrast to the lower polariton L . We give a detailed separate analysis for each contributing Feynman path, stressing the differences with the Jaynes-Cummings model and the role played by dark states. The study of an ensemble of emitters allows us to see the variation in the robustness of signals in 2D spectra when the number of molecules increases (and the number of dark states too). By analyzing the different pathways GSB, GSR, SE, ESA and ESA' we realize that GSB and GSR components require much longer waiting times to cancel each other (an effect caused by the presence of dark states). In this collective case we introduce temperature effects through the bath noise-power spectrum function and we discuss how the 2D spectral signals are modified. Finally, to fulfill the major goal in this work we use our method of solution to compare with a recent available experimental 2D spectrum with molecular polaritons [38].

Chapter 6: In this last chapter we extend our study for an ensemble of polar molecules inside a cavity that show an electrostatic dipole-dipole interaction among the emitters, thus representing a simple model for the case of molecular J-aggregates. The ratio $\gamma = G/g$ between the dipole-dipole interaction strength G and the emitter-cavity coupling strength g now dramatically determines the shape and peak intensities of linear and non-linear spectra. In fact, the energy eigenspectrum of the Hamiltonian displays a series of anticrossings (with the interchange of polariton characters) against the variation of the ratio γ . Finally we deal with energy transport phenomena in polaritons by separating the total ensemble between molecular donors D and acceptors A, molecules with different natural frequencies ω_D and ω_A in strong coupling with a cavity mode of frequency ω_c . This system present new middle polaritons and more than one set of degenerated dark states. By modifying the cavity mode frequency ω_c the nature of polariton states may change as associated to the donor, the acceptor or the cavity. For instance, for a weighted cavity frequency $\omega_c = (\omega_D + \omega_A)/2$ the lower polariton L involves the acceptor group, the upper polariton U represents the donor group and the new middle polariton shows a cavity character. A detailed study of the relevant energy transport paths serves to finish the content of this PhD work.

Conclusions: We end up with a composition that includes the main conclusions derived from this research work.

Part II.

Theoretical framework

1. Radiation-Matter Interaction

The strong light-matter coupling between molecules and confined electromagnetic (EM) field modes enables novel photodynamical processes [59, 21, 20, 60]. The strong coupling regime can be achieved by confining the EM field within cavities [22]. In this regime, the eigenstates of the system are called polaritons: hybrids of quantum light and matter. Polaritons combine properties from both their constituents and they present significant alterations in the photophysics and photochemistry of the coupled system [9, 8, 61]. The two isolated systems necessary to form polaritons, namely matter (often organic dye molecules) and EM field modes (commonly confined in optical or nanocavities), exhibit considerable complexity [1]. The study of each subsystem requires an entire field: chemistry and photonics, respectively. Furthermore, the application of techniques from (cavity) quantum electrodynamics [62] (cQED) and quantum optics [63] is necessary to accurately describe the quantized nature of EM fields and their interaction with matter [64, 65, 66, 67]. Given the often high losses of EM modes in cavities, these techniques typically need to be combined with those of open quantum systems. In this chapter, we present some theoretical tools essential for addressing the radiation-matter interaction, describing molecular structure, and modeling the dissipative processes of both systems within the framework of open quantum systems [30]. Additionally, we introduce the approximations and quantum optical model Hamiltonians that will be employed in the subsequent sections of this thesis to investigate dynamic processes of polaritons through two dimensional spectroscopy [45].

1.1. General Radiation-Matter interaction and confinement in cavities

In this section, we do not provide a detailed derivation of the quantization process of the Hamiltonian associated with the radiation-matter interaction from QED. However, we qualitatively outline some of the steps, transformations, and approximations required to obtain a general interaction Hamiltonian (see [68] and [69] for details). Subsequently, we explore the confinement of EM field modes within two types of cavities: optical and plasmonic cavities. These are the two most commonly used setups in recent experiments of polaritonic physics [70, 1]. In optical cavities, that may have different sizes and geometries [71] (a common case corresponding to Fabry-Pérot cavities of parallel flat mirrors), the radiation-matter interaction is governed by transverse EM fields. On the other hand, in plasmonic cavities [72], which are formed by a metallic structure, the “radiation modes” are characterized by collective electronic excitations. Consequently, the coupling to matter is primarily mediated by longitudinal (Coulomb) EM modes [4]. To gain insight into the nature of transverse and longitudinal electric fields, we turn to the tools of classical electrodynamics in the following sections.

1.1.1. Transverse and longitudinal electric fields

From classical electrodynamics, the electric field \mathbf{E} and the magnetic field \mathbf{B} satisfy Maxwell's equations in the presence of an electric charge density ρ associated with an electric current \mathbf{J} . The electric and magnetic fields can be expressed in terms of a vector potential \mathbf{A} and a scalar potential ϕ , such that $\mathbf{E} = -\partial_t \mathbf{A} - \nabla \phi$ and $\mathbf{B} = \nabla \times \mathbf{A}$. Since Maxwell's equations are invariant under electromagnetic gauge transformations, the choice of a particular gauge does not alter the physical predictions. In a nonrelativistic context, the Coulomb gauge, where the condition $\nabla \cdot \mathbf{A} = 0$ is imposed, is useful as it simplifies the wave equations, resulting in

$$\nabla^2 \mathbf{A} - \frac{1}{c^2} \frac{\partial^2 \mathbf{A}}{\partial t^2} + \frac{1}{c^2} \frac{\partial(\nabla \phi)}{\partial t} = -\mu_0 \mathbf{J} \quad (1.1a) \quad \nabla^2 \phi = -\frac{1}{\epsilon_0} \rho, \quad (1.1b)$$

where ϵ_0 and μ_0 are the vacuum electric permittivity and magnetic permeability, respectively, and $c = 1/\sqrt{\epsilon_0 \mu_0}$ is the vacuum speed of light. According to Helmholtz's theorem [73], it is possible to decompose the electric field $\mathbf{E} = \mathbf{E}_T + \mathbf{E}_L$ and electric current $\mathbf{J} = \mathbf{J}_T + \mathbf{J}_L$ into a transverse part and a longitudinal part. For an arbitrary field \mathbf{O} , by definition, each part satisfies:

$$\text{Transverse } (\mathbf{O}_T): \nabla \cdot \mathbf{O}_T = 0 \quad \text{Longitudinal } (\mathbf{O}_L): \nabla \times \mathbf{O}_L = 0.$$

Due to the condition imposed in the Coulomb gauge, the vector potential \mathbf{A} is purely transverse. Consequently, from the expression for the electric field in terms of \mathbf{A} and ϕ , we can conclude that

$$\mathbf{E}_T = -\partial_t \mathbf{A}, \quad \mathbf{E}_L = -\nabla \phi. \quad (1.2)$$

The transverse electric field and the purely transverse magnetic field describe electromagnetic waves in free space.

Transverse electric field: electromagnetic waves

Given the identification of both components of the electric field in Eq. (1.2), we can separate Eq. (1.1a) into a transverse part and a longitudinal part. The transverse part corresponds to the equation satisfied by the vector potential \mathbf{A} (associated with the transverse electric field):

$$\nabla^2 \mathbf{A} - \frac{1}{c^2} \frac{\partial^2 \mathbf{A}}{\partial t^2} = -\mu_0 \mathbf{J}_T. \quad (1.3)$$

Eq. (1.3) indicates that the transverse electric field accounts for radiation and retarded interactions via electromagnetic waves. This equation is valid even in the absence of charges, where $\rho = \mathbf{J} = 0$. In fact, by itself, neither the transverse nor the longitudinal fields fulfill retardation. The longitudinal field is instantaneous everywhere in space since it just depends on the position of the charges. This implies that the transverse field also has an instantaneous component that cancels the longitudinal one at short times so that overall, retardation is fulfilled.

Longitudinal electric field: Coulomb interaction

The longitudinal electric field defined in Eq. (1.2) satisfies the Poisson equation Eq. (1.1b), whose solution corresponds to the instantaneous electrostatic Coulomb potential. For a system of particles, each with charge q_i and position vector \mathbf{r}_i , the scalar field corresponds to the Coulomb potential generated by the charges, i.e., $\phi(\mathbf{r}) = \sum_i q_i/4\pi\epsilon_0|\mathbf{r} - \mathbf{r}_i|$. Consequently, the longitudinal electric field arises from the Coulomb interactions among the charged particles.

1.1.2. Obtaining a general radiation-matter Hamiltonian

Minimal Coupling Hamiltonian and quantization

The interaction of a system of particles, each with charge q_i , mass m_i and momentum \mathbf{p}_i at position vector \mathbf{r}_i , with an electromagnetic field characterized by the vector potential \mathbf{A} is described by the classical minimal coupling Hamiltonian [62]

$$H_{\text{mc}} = \sum_i \frac{1}{2m_i} [\mathbf{p}_i - q_i \mathbf{A}(\mathbf{r}_i)]^2 + \frac{1}{4\pi\epsilon_0} \sum_{i<j} \frac{q_i q_j}{|\mathbf{r}_i - \mathbf{r}_j|} + \frac{1}{2} \int d^3\mathbf{r} \left[\epsilon_0 \mathbf{E}_T^2 + \frac{1}{\mu_0} \mathbf{B}^2 \right]. \quad (1.4)$$

The first term contains the kinetic energy of the charged particles and the radiation-matter interaction. The second term represents the usual instantaneous Coulomb interaction (we call it V_{Coulomb}), i.e., the energy of the longitudinal component of the electric field, and the third term describes the total energy carried by the transverse electromagnetic field (H_{EM}) [73]. It is important to highlight that in this Hamiltonian, no boundary conditions due to the confinement in a cavity have been imposed.

Below, we describe the steps to quantize the electromagnetic field H_{EM} :

- The vector potential can be written as a Fourier expansion of modes with associated wave vectors \mathbf{k} and polarizations $\lambda = \{1, 2\}$.

$$\mathbf{A}(\mathbf{r}, t) = \frac{1}{(2\pi)^{3/2}} \int d^3\mathbf{k} \sum_{\lambda} \left[\mathcal{Q}_{\lambda}(\mathbf{k}, t) e^{i\mathbf{k}\cdot\mathbf{r}} \mathbf{u}_{\lambda} + \text{c.c.} \right]. \quad (1.5)$$

Here \mathbf{u}_{λ} are unitary orthogonal vectors representing the two only possible polarization directions of the purely transverse field and $\mathcal{Q}_{\lambda}(\mathbf{k}, t)$ can be determined from Eq. (1.3).

- We introduce the canonically conjugate momentum variables corresponding to each Fourier component of \mathbf{A} , namely $\mathcal{P}_{\lambda}(\mathbf{k}, t) = \epsilon_0 \dot{\mathcal{Q}}_{\lambda}(\mathbf{k}, t)$.
- The Eq. (1.5) is substituted on the left-hand side of Eq. (1.2) and in the original definition of the vector potential, according to which $\mathbf{B} = \nabla \times \mathbf{A}$. Thus, the transverse electric field \mathbf{E}_T and the magnetic field \mathbf{B} are obtained in terms of the functions $\mathcal{Q}_{\lambda}(\mathbf{k}, t)$ and $\mathcal{P}_{\lambda}(\mathbf{k}, t)$. Substituting both expressions into the third term of Eq. (1.4) yields:

$$H_{\text{EM}} = \int d^3\mathbf{k} \sum_{\lambda} \left[\frac{\mathcal{P}_{\lambda}^2(\mathbf{k}, t)}{2\epsilon_0} + \frac{1}{2} \epsilon_0 (ck)^2 \mathcal{Q}_{\lambda}^2(\mathbf{k}, t) \right]. \quad (1.6)$$

- Since $\mathcal{Q}_\lambda(\mathbf{k}, t)$ and $\mathcal{P}_\lambda(\mathbf{k}, t)$ are canonically conjugate variables, i.e., they satisfy the canonical Poisson bracket relations $\{\mathcal{Q}_\lambda(\mathbf{k}, t), \mathcal{P}_{\lambda'}(\mathbf{k}', t)\}_{\text{Poisson}} = \delta_{\lambda\lambda'}\delta(\mathbf{k} - \mathbf{k}')$, they can be promoted to operators which satisfy the quantum commutation relations $[\hat{\mathcal{Q}}_\lambda(\mathbf{k}, t), \hat{\mathcal{P}}_{\lambda'}(\mathbf{k}', t)] = i\hbar\delta_{\lambda\lambda'}\delta(\mathbf{k} - \mathbf{k}')$. On the other hand, note that Eq. (1.6) presents the form of harmonic oscillators. It is convenient to define the ladder operator $\hat{a}_\lambda(\mathbf{k}, t)$ as

$$\hat{a}_\lambda(\mathbf{k}, t) = \frac{1}{\sqrt{2\epsilon_0\hbar\omega_k}}[\epsilon_0\omega_k\hat{\mathcal{Q}}_\lambda(\mathbf{k}, t) + i\hat{\mathcal{P}}_\lambda(\mathbf{k}, t)], \quad (1.7)$$

where the mode frequency is defined as $\omega_k = ck$. This operator and its adjoint $\hat{a}_\lambda^\dagger(\mathbf{k}, t)$ satisfy the commutation relation $[\hat{a}_\lambda(\mathbf{k}, t), \hat{a}_{\lambda'}^\dagger(\mathbf{k}', t)] = \delta_{\lambda\lambda'}\delta(\mathbf{k} - \mathbf{k}')$.

- After removing the vacuum energy term $E_0 = \frac{1}{2} \int d^3\mathbf{k} \sum_\lambda \hbar\omega_k$ to avoid the infinity in energy, we obtain the Hamiltonian operator corresponding to the transverse electromagnetic field, which in the absence of charges (in this case $\hat{a}_\lambda(\mathbf{k}, t) = \hat{a}_\lambda(\mathbf{k})e^{-i\omega_k t}$), takes the form

$$\hat{H}_{\text{EM}} = \int d^3\mathbf{k} \sum_\lambda \hbar\omega_k \hat{a}_\lambda^\dagger(\mathbf{k}) \hat{a}_\lambda(\mathbf{k}). \quad (1.8)$$

The classical variables \mathbf{p}_i and $\mathbf{A}(\mathbf{r}_i)$ from Eq. (1.4) can also be promoted to operators: $\hat{\mathbf{p}}_i$ satisfies the canonical commutation relation $[\hat{r}_{i\alpha}, \hat{p}_{j\beta}] = i\hbar\delta_{ij}\delta_{\alpha\beta}$ (α and β run over x, y, z components) and $\hat{\mathbf{A}}(\mathbf{r})$ can be obtained from Eq. (1.5), given the operator $\hat{\mathcal{Q}}_\lambda(\mathbf{k})$ ¹. Now the fully quantized minimal coupling Hamiltonian can be written as

$$\hat{H}_{\text{mc}} = \sum_i \frac{1}{2m_i} [\hat{\mathbf{p}}_i - q_i \hat{\mathbf{A}}(\mathbf{r}_i)]^2 + \hat{V}_{\text{Coulomb}} + \hat{H}_{\text{EM}}. \quad (1.9)$$

PZW transformation and the dipole approximation

In the Hamiltonian Eq. (1.9), the first term, which contains the interaction between the transverse electromagnetic field and the charges, is described in terms of the vector potential operator $\hat{\mathbf{A}}$. However, it is sometimes convenient to find an expression for the interaction in terms of the transverse electric field operator $\hat{\mathbf{E}}_T$. The unitary transformation $\hat{U} = \exp\left[\frac{1}{i\hbar} \int_V d^3\mathbf{r} \hat{\mathbf{P}}(\mathbf{r}) \cdot \hat{\mathbf{A}}(\mathbf{r})\right]$, known as the Power-Zienau-Woolley (PZW) transformation [74, 75, 76, 62], is useful for this purpose. The operator $\hat{\mathbf{P}}(\mathbf{r})$

¹The operators $\hat{\mathbf{A}}$, $\hat{\mathbf{E}}_T$ y $\hat{\mathbf{B}}$ are

$$\begin{aligned} \hat{\mathbf{A}}(\mathbf{r}) &= \frac{1}{(2\pi)^{3/2}} \int d^3\mathbf{k} \sum_\lambda \sqrt{\frac{\hbar}{2\epsilon_0\omega_k}} (\hat{a}_\lambda(\mathbf{k}) e^{i(\mathbf{k}\cdot\mathbf{r} - \omega_k t)} \mathbf{u}_\lambda + \text{h.c.}) \\ \hat{\mathbf{E}}_T &= \frac{1}{(2i\pi)^{3/2}} \int d^3\mathbf{k} \sum_\lambda \sqrt{\frac{\hbar\omega_k}{2\epsilon_0}} (\hat{a}_\lambda(\mathbf{k}) e^{i(\mathbf{k}\cdot\mathbf{r} - \omega_k t)} \mathbf{u}_\lambda - \text{h.c.}) \\ \hat{\mathbf{B}} &= \frac{a}{(2\pi)^{3/2}} \int d^3\mathbf{k} \sum_\lambda \sqrt{\frac{\hbar}{2\epsilon_0\omega_k}} (\hat{a}_\lambda(\mathbf{k}) e^{i(\mathbf{k}\cdot\mathbf{r} - \omega_k t)} [\nabla \times \mathbf{u}_\lambda] + \text{h.c.}) \end{aligned}$$

refers to the polarization field of the matter, which in the dipole approximation (or long-wavelength approximation, where the dependence of the fields with the coordinates is neglected) satisfies [77]

$$\int d^3\mathbf{r} \hat{\mathbf{P}}(\mathbf{r}) \cdot \hat{\mathbf{E}}_T(\mathbf{r}) \approx \hat{\boldsymbol{\mu}} \cdot \hat{\mathbf{E}}_T(0), \quad (1.10)$$

where $\hat{\boldsymbol{\mu}} = \sum_i q_i \hat{\mathbf{r}}_i$ is the total electric dipole moment of the charge distribution and the transverse electric field operator can be written in the Schrödinger picture as

$$\hat{\mathbf{E}}_T(\mathbf{r}) = \frac{1}{(2\pi)^{3/2}} \int d^3\mathbf{k} \sum_{\lambda} \sqrt{\frac{\hbar\omega_{\mathbf{k}}}{2\epsilon_0}} (\hat{a}_{\lambda}(\mathbf{k}) e^{i\mathbf{k}\cdot\mathbf{r}} \mathbf{u}_{\lambda} + \text{h.c.}) \quad (1.11)$$

The transformed PZW Hamiltonian is obtained through the operation $\hat{U} \hat{H}_{\text{mc}} \hat{U}^{\dagger}$. It is important to highlight that the kinetic energy and the Coulomb interaction terms are invariant under this operation. After PZW transformation and the subsequent application of the dipole approximation, we write a new radiation-matter Hamiltonian of the form [78, 69]

$$\hat{H} = \underbrace{\sum_i \frac{\hat{\mathbf{p}}_i^2}{2m_i} + \hat{V}_{\text{Coulomb}} + \frac{1}{2\epsilon_0} \int d^3\mathbf{r} \hat{\mathbf{P}}_T^2(\mathbf{r})}_{\text{Matter}} + \underbrace{\hat{H}_{\text{EM}}}_{\text{Rad}} - \underbrace{\hat{\boldsymbol{\mu}} \cdot \hat{\mathbf{E}}_T}_{\text{Interaction}}. \quad (1.12)$$

Here $\hat{\mathbf{P}}_T(\mathbf{r})$ represents the transverse part of the polarization. The first three terms of the Hamiltonian Eq. (1.12) describe operators from the material part of the system. Indeed, the third term is often neglected as it only introduces a change in the energy levels. In this thesis, we omit it. The fourth term represents the Hamiltonian of the transverse electromagnetic field (Eq. (1.8)), and the last term accounts for the dipole interaction between matter and the transverse field.

1.1.3. Confinement in cavities and single-mode approximation

Given that the formation of polaritons requires strong interaction between radiation and matter, to achieve this coupling regime requires confining the electromagnetic field in cavities. For the strong-coupling regime, different scenarios are possible according to cavity nature. In the case of optical cavities, a huge number of molecules is necessary at room temperature, where all transitions are described by broad lines [79, 80, 81] (10^6 to 10^{10} molecules per cavity mode at optical frequencies, when radiation couples with electronic excitations of matter). However, at extremely low temperatures and with extremely good cavities, single-atom strong coupling in optical cavities is possible, with a very small coupling but larger than the extremely small cavity losses. Conversely, in plasmonic nanocavities, the strong-coupling regime can be attained with just a few molecules, or even a single emitter [82, 83, 84]. Plasmonic “cavities” involve high electric fields in localized regions induced from the resonant collective oscillations of free electrons present at the bulk and surface of conducting materials or near conducting nanoparticles. Below, we describe the radiation-matter interaction in these two types of cavities: optical and plasmonic cavities.

Optical cavities

An optical cavity [71] can be made of parallel flat mirrors (the Fabry-Perot cavity is an example), can be characterized with different cavity losses, according to the material from which they are constructed. These reflectors can modify the boundary conditions of the system, forcing it to exhibit stationary electromagnetic waves. The radiation-matter interaction is governed by the transverse EM field. In this case, the wave vectors \mathbf{k} associated with the field modes, which can take continuous values in vacuum, become discrete within the cavity². In fact, in a Fabry-Pérot cavity, only the modes with a \mathbf{k} direction normal to the mirrors becomes discrete, the others inside the cavity are still continuous. On the other hand, the cavity energetics allows in practice that matter emitters only couple to a few discrete modes \mathbf{k} or even just to a single mode, since off-resonant modes do not considerably couple. Within this **single-mode approximation** and after contracting the three matter terms in Eq. (1.12) (in this case, matter refers to the molecular emitters inside the cavity) into a single term that we call \hat{H}_{em} , the radiation-matter Hamiltonian can be written as

$$\hat{H} = \hat{H}_{\text{em}} + \hbar\omega_c \hat{a}^\dagger \hat{a} + \sqrt{\frac{\hbar\omega_c}{2\epsilon_0 V}} (\hat{a} + \hat{a}^\dagger) (\hat{\boldsymbol{\mu}} \cdot \mathbf{u}_{E_T}), \quad (1.13)$$

when the periodic boundary conditions of the cavity are imposed. Here \mathbf{u}_{E_T} is an unitary vector in the direction of the transverse electric field, ω_c is the single mode cavity frequency with ladder operators a and a^\dagger and V is the effective volume of the cavity. In this expression, we have made use of the representation of \mathbf{E}_T in the Schrödinger picture, given in Eq. (1.11). The effect of including multiple cavity modes can be reviewed in [85].

Plasmonic cavities and quasistatic approximation

For small plasmon-polariton and phonon-polariton nanoantennas and nanoresonators (nanocavities) [86, 87, 88], it is possible to apply the **quasistatic approximation**, in which all distances in the system are significantly smaller than the relevant wavelengths. Under this condition, the transverse EM field is negligible [4], and the radiation-matter interaction is mediated by the longitudinal field. This field represents the Coulomb interaction of the charges in the material medium of the nanocavity. Thus, the minimal coupling Hamiltonian in Eq. (1.9) reduces to

$$\hat{H} = \sum_i \frac{\hat{\mathbf{p}}_i^2}{2m_i} + \hat{V}_{\text{Coulomb}}, \quad (1.14)$$

since the terms containing $\hat{\mathbf{A}}$ and \hat{H}_{EM} in Eq. (1.9) describe the transverse fields. In this case, the Coulomb potential \hat{V}_{Coulomb} contains not only the interaction between the charges of the molecular emitters (\hat{V}_{em}), but also between those of the material medium of the nanocavity (\hat{H}_{cav}) and between the emitters and the medium of the cavity ($\hat{H}_{\text{em-cav}}$). The material of the cavity can be treated macroscopically. This implies that it responds linearly to external fields. Consequently, it can be

²The discretization can be obtained by changing $\frac{1}{(2\pi)^{3/2}} \int d^3\mathbf{k} \implies \frac{1}{\sqrt{V}} \sum_{\mathbf{k}}$, where V is the effective volume of the cavity.

described as a collection of instantaneous plasmon modes [88], which satisfy bosonic statistics. In the single-mode approximation, after removing the zero point energy, $\hat{H}_{\text{cav}} = \hbar\omega_c a^\dagger a$, where ω_c is the frequency of the ‘‘cavity’’ plasmon mode and a^\dagger , a are its respective ladder operators. On the other hand, the emitters-cavity interaction takes the form $\hat{H}_{\text{em-cav}} = \sum_i q_i \phi(\mathbf{r}_i)$, with i running over both electrons and nuclei of all molecular emitters. The total radiation-matter Hamiltonian can be read as

$$\hat{H} = \hat{H}_{\text{em}} + \hbar\omega_c a^\dagger a + \sum_i q_i \phi(\mathbf{r}_i), \quad (1.15)$$

where $\hat{H}_{\text{em}} = \sum_i \frac{\hat{\mathbf{p}}_i^2}{2m_i} + \hat{V}_{\text{em}}$. After the application of the dipole approximation and assuming that the molecules are uncharged and sufficiently localized, it is possible approximate the Hamiltonian in Eq. (1.15) as

$$\hat{H} = \hat{H}_{\text{em}} + \hbar\omega_c \hat{a}^\dagger \hat{a} + \sqrt{\frac{\lambda}{V}} (\hat{a} + \hat{a}^\dagger) (\hat{\boldsymbol{\mu}} \cdot \mathbf{u}_{\mathbf{E}_L}). \quad (1.16)$$

Here $\sqrt{\lambda/V}$ represents a coupling constant, which is related to the (position-dependent) effective mode volume V of the quantized mode and $\mathbf{u}_{\mathbf{E}_L}$ is an unitary vector in the direction of longitudinal electric field of the cavity material.

Additional studies exploring the use of plasmonic cavities or surface lattice resonances on arrays of plasmonic nanoparticles can be found for instance in [89, 90, 61, 91].

1.2. Description of molecular emitters

The development of the present work was inspired by an experiment where molecular J-aggregates were introduced in an optical cavity and subject to a 2DS protocol [38]. A J-aggregate is a complex molecular dye that tends to aggregate under the influence of solvent, another additive or just the increase of concentration due to supramolecular self-organization. This means that we are dealing with a molecular ensemble of complex organic molecules in special arrangements. In addition, the experimental 2DS protocol made use of optical frequencies, thus inducing electronic excitations in these molecules. An accurate theoretical description of the molecular electronic spectroscopy requires a quantum method of solution to resolve the electronic, vibrational and rotational structure and dynamics of molecules. The high number of degrees of freedom in molecular dyes makes it impossible to use full ab initio methods in quantum chemistry and a number of approximations are required to have a starting point to model an ensemble of dye molecules within optical cavities.

The molecular Hamiltonian reads [92]

$$\hat{H} = \hat{T}_N + \hat{T}_e + \hat{V}_{NN} + \hat{V}_{eN} + \hat{V}_{ee} = \hat{T}_N + \hat{H}_{el} \quad (1.17)$$

that contains the kinetic energy of nuclei (vibrations and rotations) \hat{T}_N , the kinetic energy of electrons \hat{T}_e , plus the Coulomb interactions among nuclei \hat{V}_{NN} and electrons \hat{V}_{ee} and between electrons and nuclei

V_{eN} . To solve the Schrödinger equation associated to this Hamiltonian, even for simple molecules, is a formidable task. A first usual step is to separate the electronic and nuclear motions, thanks to the well-known Born-Oppenheimer approximation [92]. It amounts to solve the electronic motion (with electronic coordinates $\{q_i\}$) for each fixed nuclear geometry (with parametric coordinates $\{q_\alpha\}$) through the electronic equation

$$\left[\hat{H}_{el} - E_j(\{q_\alpha\})\right] \Psi_j(\{q_i\}; \{q_\alpha\}), \quad (1.18)$$

where the energy eigenvalues $E_j(\{q_\alpha\})$ form a set of j potential energy surfaces for the electronic ground state $j = 0$ and excited states $j > 1$. The latter electronic equation still represents a problem with high computational cost, and many approximations and methods have been proposed along the years to facilitate approximate solutions at a different stages of sophistication, from partially correlated Hartree-Fock methods to highly correlated methods based on configuration interaction methods.

For our purposes in this work, we will keep the molecular structure description reduced to a minimum and based on the Hartree-Fock solution [93] and the configuration interaction method. In the Hartree-Fock method, the electronic wave function for N electrons is built as the best variationally optimized single Slater determinant for the ground state $|\Psi_0\rangle = |\phi_1\phi_2\dots\phi_N\rangle$, built from a set of one-particle spin orbitals $\{\phi_i\}_{i=1}^N$. These spin orbitals become solutions of a single-particle Hartree-Fock equation

$$F(i)\phi_a(i) = \varepsilon_a\phi_a(i), \quad (1.19)$$

where the Fock operator reads $F(i) = h(i) + \sum_{b \neq a} J_b(i) - \sum_{b \neq a} K_b(i)$, with the one-electron uncorrelated Hamiltonian $h(i) = T_{el}(i) + V_{iN}$, the Coulomb potential J_b whose operation over each spin orbital is

$$J_b(i)\phi_a(i) = \left[\int dx_j \phi_b^*(j) \frac{1}{r_{ij}} \phi_b(j) \right] \phi_a(i), \quad (1.20)$$

and the operation of exchange operator K_b is non local

$$K_b(i)\phi_a(i) = \left[\int dx_j \phi_b^*(j) \frac{1}{r_{ij}} \phi_a(j) \right] \phi_b(i). \quad (1.21)$$

The introduction of a non-orthogonal basis set to expand the orbitals $\phi_a = \sum_{\mu} C_{\mu a} \psi_{\mu}$ leads to the Roothaan equations [93], that involve a generalized eigenvalue problem for the Fock operator $\mathbf{FC} = \mathbf{\epsilon SC}$. These Roothaan equations are solved in a recursive procedure, since the operators depend upon the orbitals to be optimized. This procedure is performed through the so called self-consistent-field. Once the density matrix or field potential is converged, the eigenvalues $\{\varepsilon_a\}$ of the Fock operator \hat{F} are the orbital energies. In the restricted Hartree-Fock case (closed-shell), the dimension M of the basis set $\{\psi_{\mu}\}_{\mu=1}^M$ is chosen to be much larger than the number $N/2$ of occupied orbitals $\{\phi_a\}_{a=1}^{N/2}$. It results in a number of occupied orbitals ε_a (the highest occupation indicates the Fermi level of the molecule) and a number of virtual unoccupied orbitals ε_r above the Fermi level.

Koopmans' theorem [93] provides a physical meaning for these occupied ε_a and virtual ε_r orbital energies: the ionization potential of removing the electron represented by the orbital ϕ_a is approximately

$-\varepsilon_a$ and the electron affinity for an electron to be captured in ϕ_r is approximately $-\varepsilon_r$. From the seminal works of Fukui and Hoffman [94], one realizes that a rather good approximation to understand photo reactivity consist of looking at the frontier orbitals HOMO and LUMO, the highest occupied molecular orbital and the lowest unoccupied molecular orbital, respectively. This simplifies the multi-electron excitation to a single active electron excitation from HOMO to LUMO at the equilibrium geometry of the molecule. The more sophisticated configuration interaction (CI) method consist of using a large expansion in terms of Slater determinants with all the possible orbital excitations (configurations) considered from the ground state determinant, within the adopted orbital basis set [93]. The diagonalization of the CI matrix provides very accurate energies and wave functions not only for the ground state but also for excited states. In this fully correlated CI method we restrict our description to the lowest two electronic states (ground and first excited). In many molecules the energy difference between these two fully correlated states is similar to the HOMO-LUMO energy difference due to an effect of compensation between electron correlation and orbital relaxation [93].

In conclusion we will adopt this CI picture of two fully correlated states to deal with the electronic structure of the dye molecules, and the adoption of a two-state model for each dye-molecule is justified by the fact that higher excited states are far in energy in all the considered molecular geometries. The justification of the adopted two-state electronic model for molecules is already explained in the introduction. We stress that when molecules interact strongly with quantum radiation in cavities, the new light-matter states exhibit a high degree of anharmonicity. This means that the higher energy states are difficult to excite with a fixed laser frequency, a phenomenon known as photon blockade. We will not produce ab initio calculations of emitters in this work, the energy difference between the ground g and first excited e state will be fully parameterized following the experiment, which eventually means that we "have" the complete CI energies. The fundamental models in quantum optics for strong field-matter interaction (Jaynes-Cummings and Tavis-Cummings models) are based in two-state atoms or molecules. Once the electronic structure is solved within the BO approximation, the molecular nuclear motion is solved for the nuclei subject to the electronic potential energy surfaces $E_{el}(\{q_\alpha\})$

$$\left[\hat{T}_N + E_{el}(\{q_\alpha\})\right] \Psi_N(\{q_\alpha\}) = E \Psi_N(\{q_\alpha\}), \quad (1.22)$$

where $\Psi_N(\{q_\alpha\})$ accounts for the vibrational and rotational motions. Molecular motions have different time scales; the motion of electrons occurs on a time scale of attoseconds, the vibrational motion happens from ten to hundred of femtoseconds, while the rotational motion is slower, on the picosecond time scale. Our study of 2D molecular spectroscopy implies ultrafast processes within a few femtoseconds time scale, so that we can disregard the rotational motion in our approach.

A first approach to consider the vibrational motion is to include the vibrational states explicitly. In the case of diatomic molecules one may assume a simple model where the potential energy curves for the two electronic states g and e are modeled with simple harmonic oscillator potentials with a bosonic Hamiltonian $\hat{H}_{vib} = \hbar(\omega_g + \omega_e)\hat{b}^\dagger\hat{b}$. A more realistic model that considers anharmonicity and dissociation is provided by Morse potentials, with approximate vibrational energy levels given by [92]

$$E_v = \hbar\omega_{g/e} \left[(v + 1/2) - \beta_{g/e}(v + 1/2)^2 \right] \quad (1.23)$$

where $\omega\beta$ is known as the anharmonicity constant.

A well known model that considers that explicit introduction of the vibrational states (phonons) with the field-matter strong coupling along with electronic-vibration coupling is known as the Holstein-Jaynes-Cummings model in the form [95, 7]

$$\hat{H} = \hbar\omega_0\hat{\sigma}^+\hat{\sigma}^- + \hbar\omega_c\hat{a}^\dagger\hat{a} + \hbar g(\hat{\sigma}^+\hat{a} + \hat{\sigma}^-\hat{a}^\dagger) + \hbar\omega_v(\hat{b}^\dagger\hat{b} + \lambda\hat{\sigma}^+\hat{\sigma}^-(\hat{b}^\dagger + \hat{b} + \lambda)) \quad (1.24)$$

where the operators \hat{a}^\dagger , $\hat{\sigma}^+$ and \hat{b}^\dagger are operators that create one cavity photon, one molecular exciton and one vibrational quantum, respectively, and their adjoint operators annihilate the corresponding excitations. Both \hat{a} and \hat{b} are bosonic operators, while the $\hat{\sigma}$'s are transition operators between electronic states ($\hat{\sigma}^+ = |e\rangle\langle g|$ and $\hat{\sigma}^- = (\hat{\sigma}^+)^\dagger$). The last Holstein exciton-phonon term implies that the electronic excitation couples to vibration, and its strength is characterized by the Huang-Rhys factor λ , which is also related to the separation between the equilibrium distances of the two harmonic potentials. This model can be extended to an ensemble of molecules, thus taking the name Holstein-Tavis-Cummings. Upon photoexcitation of molecules by a laser pulse, the the band of vibrational states reached in the electronic excited state is selected by the Franck-Condon overlap rule. However the absorption peak and fluorescence peaks are usually separated by a Stokes frequency shift, with the emission peak found at lower frequency. This Stokes shift is due to non-radiative vibrational relaxation or dissipation to the ground vibrational state in the electronic excited state, which originates from solvent or environment interaction and reorganization.

In this work, to avoid computational complexity we focus our 2DS study on vibrationless electronic excitation and we do not include vibrational states explicitly. However, we include the vibrational relaxation as a dephasing-like dissipation introduced by the environment to the system, This is modeled with the theory of open quantum systems, and the vibrational matter dissipation in the excited state will be introduced through a Bloch-Redfield term in the master equations.

1.3. Modeling Radiation-Matter interaction in cavities

In the single-mode approximation, the Hamiltonians that represent the interaction between material emitters and a cavity mode (Eq. (1.13) for optical planar cavities and Eq. (1.16) for plasmonic cavities) have a similar mathematical description. In both cases, the mode of the EM field (whether transverse or longitudinal) can be seen as a harmonic oscillator with ladder operators \hat{a} and \hat{a}^\dagger satisfying the bosonic commutation relation $[\hat{a}, \hat{a}^\dagger] = 1$. On the other hand, when the Hamiltonian of each emitter can be approximated to a two-level system, it is possible to make use of some quantum optical models to describe the emitters-cavity interaction [63]. In particular we describe below the Tavis-Cummings model. Some experimental realizations of the radiation-matter strong interaction for the formation of polaritons can be found in [96, 97, 98, 80, 82, 81, 83, 84, 99, 100].

1.3.1. Tavis-Cummings model

The Tavis-Cummings (TC) model [101, 102, 103] provides a parametric description of both emitters and a single mode of the EM field confined in a cavity. Parametric models do not explicitly consider the geometric profile of the EM field and they do not include the complexity of the potential energy surfaces of the molecular emitters, with their dependence on all possible degrees of freedom. However, these models capture many of the essential physical characteristics of the radiation-matter interaction at reasonable computational cost [1].

Cavity mode and emitters operators

The eigenstates of the single mode cavity Hamiltonian $\hat{H}_{\text{cav}} = \hbar\omega_c \hat{a}^\dagger \hat{a}$, described as a harmonic oscillator (see section 1.1.3) with frequency ω_c , represent excitations of the EM field named photons. These eigenstates form a **Fock basis**, with the n -photon states $\{|n\rangle\}$ with $n = 1, 2, 3, \dots$ (the 0-photon state $|0\rangle$ is often called the “vacuum”state). The energy of a state $|n\rangle$ is $\hbar\omega_c n$. The action of the ladder bosonic operators a and a^\dagger over Fock states is described in the table 1.1 [63].

On the other hand, we consider a collection of N identical non-interacting³ molecular emitters, each with two possible energy states: ground $|g\rangle$ and excited $|e\rangle$, with transition frequency ω_e . If the zero point energy corresponds to the energy of $|g\rangle$, the Hamiltonian for each emitter is $\hbar\omega_e |e\rangle\langle e|$. We introduce the transition molecular operators

$$\hat{\sigma} = |g\rangle\langle e|, \quad \hat{\sigma}^\dagger = |e\rangle\langle g|, \quad (1.25)$$

which annihilate and create molecular electronic excitations, respectively and they satisfy the commutation and anticommutation relations shown in Tab. 1.1. In terms of these operators, the Hamiltonian describing the collection of N emitters is $\hat{H}_{\text{em}} = \hbar\omega_e \sum_{i=1}^N \hat{\sigma}_i^\dagger \hat{\sigma}_i$, with i running over all the emitters. The total dipole operator can be written as $\hat{\boldsymbol{\mu}} = \mu \sum_{i=1}^N (\hat{\sigma}_i + \hat{\sigma}_i^\dagger) \mathbf{u}_{\mu_i}$, where we have omitted the diagonal dipole terms, and \mathbf{u}_{μ_i} is a unitary vector in the direction of the i -th emitter dipole. According to the expressions Eq. (1.13) for planar optical cavities or Eq. (1.16) for plasmonic nanocavities, this operator $\hat{\boldsymbol{\mu}}$, together with the electric field operator (which is proportional to $(\hat{a} + \hat{a}^\dagger)$) are responsible for the interaction between the emitters and the cavity mode.

Cavity-emitters interaction Hamiltonian

By replacing the expressions for \hat{H}_{em} and $\hat{\boldsymbol{\mu}}$ in any of the interaction Hamiltonians Eq. (1.13) or Eq. (1.16), and after parameterizing the cavity-emitters coupling strength with the term $\hbar g = \sqrt{\frac{\hbar\omega_c}{2\epsilon_0 V}} \mu (\mathbf{u}_\mu \cdot$

³This is possible if the emitters are sufficiently distant or if their dipole interaction is weak. They only interact collectively through the cavity mode.

Subsystem	Operator	Action	Algebra
Cavity	Annihilation: a	$\hat{a} n\rangle = \sqrt{n} n-1\rangle, \hat{a} 0\rangle = 0$	$[\hat{a}, \hat{a}^\dagger] = 1$
	Creation: \hat{a}^\dagger	$\hat{a}^\dagger n\rangle = \sqrt{n+1} n+1\rangle$	
	Number: $\hat{a}^\dagger \hat{a}$	$\hat{a}^\dagger \hat{a} n\rangle = n n\rangle$	
i th Emitter	Annihilation: $\hat{\sigma}_i$	$\hat{\sigma}_i g_i\rangle = 0, \hat{\sigma}_i e_i\rangle = g_i\rangle$	$\{\hat{\sigma}_i, \hat{\sigma}_i^\dagger\} = 1, [\hat{\sigma}_i, \hat{\sigma}_j] = [\hat{\sigma}_i^\dagger, \hat{\sigma}_j^\dagger] = 0$ $[\hat{\sigma}_i, \hat{\sigma}_j^\dagger] = 0$ (if $i \neq j$)
	Creation: $\hat{\sigma}_i^\dagger$	$\hat{\sigma}_i^\dagger g_i\rangle = e_i\rangle, \hat{\sigma}_i^\dagger e_i\rangle = 0$	

Tab. 1.1.: Description of cavity and emitter operators and their action on Fock states $\{|n\rangle\}$ and electronic states $\{|g_i\rangle, |e_i\rangle\}$ of the i th molecule, respectively. Here, the brackets $[\cdot, \cdot]$ represent commutators and the braces $\{\cdot, \cdot\}$ represent anticommutators.

\mathbf{u}_{E_T}) (for planar optical cavities), we obtain the Hamiltonian

$$\hat{H}_D = \hbar\omega_c \hat{a}^\dagger \hat{a} + \hbar\omega_e \sum_{i=1}^N \hat{\sigma}_i^\dagger \hat{\sigma}_i + \hbar g \sum_{i=1}^N (\hat{a}^\dagger + \hat{a})(\hat{\sigma}_i + \hat{\sigma}_i^\dagger), \quad (1.26)$$

where we have fixed the zero point energy in the energy of $|g\rangle$ plus the energy of the vacuum Fock state ($\hbar\omega_c/2$). This is the named **Dicke model** for an ensemble of emitters [104, 105] and for the particular case of one emitter ($N = 1$) is referred as the **Rabi model** [106]. In the interaction picture, the interaction term in the Hamiltonian contains terms that oscillate in time with the frequency $\omega_c + \omega_e$ and others that oscillate with the frequency $\Delta \equiv \omega_c - \omega_e$, which is named the **detuning**. In the strong coupling regime (not ultra-strong [107]), the non-conserving energy terms with the fast frequency are negligible and can be removed. This is known as the **rotating wave approximation** (RWA) and in this case the Hamiltonian Eq. (1.26) becomes

$$\hat{H}_{TC} = \hbar\omega_c \hat{a}^\dagger \hat{a} + \hbar\omega_e \sum_{i=1}^N \hat{\sigma}_i^\dagger \hat{\sigma}_i + \hbar g \sum_{i=1}^N (\hat{a}^\dagger \hat{\sigma}_i + \hat{\sigma}_i^\dagger \hat{a}), \quad (1.27)$$

which is known as the Tavis-Cummings (TC) Hamiltonian, which for a single emitter is known as the **Jaynes-Cummings** (JC) Hamiltonian [108].

1.3.2. Polariton states

The eigenstates of the TC model represent hybrid excitations between radiation and matter and they are known as polariton states (see Fig. 1.1). Some of them are bright and can be accessed via dipole transition with the radiation from a laser pulse from the ground state, while others are called **dark states** [109, 110, 111]. Dark states represent excitations of the material emitters while the radiation field remain unexcited. Consequently, they do not exhibit dipole radiative transitions from the ground state and they do not display visible peaks in the linear absorption spectra. We can label the bare basis (eigenstates of the non interacting Hamiltonian i.e., with $g = 0$ in Eq. (1.27)) as

$$|n, e_1, e_2, \dots, e_N\rangle,$$

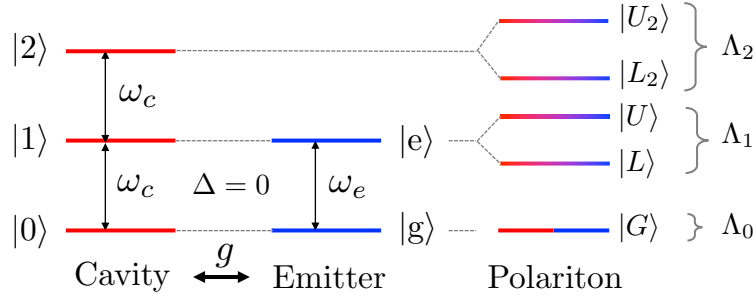


Fig. 1.1.: Scheme of energies of a polariton JC system with detuning $\Delta = \omega_c - \omega_e = 0$.

where the first label corresponds to the number of photonic excitations in the cavity, denoted by $n = 0, 1, 2, \dots$, and the label e_i , with $i = 1, \dots, N$, corresponds to excitations of the i th emitter, i.e., $e_i = 0, 1$. In this notation, $e_i = 0$ indicates the electronic state $|g\rangle$ of the i th molecule, and $e_i = 1$ indicates its respective excited state $|e\rangle$. The total number of excitations k in a state (both photon and matter excitations) is determined by the action of the operator $\hat{\Lambda} \equiv \hat{a}^\dagger \hat{a} + \sum_i \hat{\sigma}_i^\dagger \hat{\sigma}_i$, such that $\hat{\Lambda} |n, e_1, e_2, \dots, e_N\rangle = \Lambda_k |n, e_1, e_2, \dots, e_N\rangle$, with $k = n + \sum_i e_i$.

The polariton states with the same number k of excitations form the **excitation manifold** Λ_k . The operator $\hat{\Lambda}$ commutes with the polariton Hamiltonian H_{TC} . Consequently, this Hamiltonian can be diagonalized in each excitation manifold independently, and each of them represents a Hilbert subspace. The number of polariton states in each excitation manifold is then equivalent to the number of bare states in the corresponding manifold. If the N material emitters are identical, we can use a more compact notation for all states with the same number of electronic excitations in the form $|n, e\rangle$, where $e = \sum_i e_i$ represents the total purely electronic excitation. We describe below the properties and the dimension of the excitation manifolds Λ_0 , Λ_1 , and Λ_2 , which are those of our interest for the study of 2D spectroscopy applied to polariton systems in the second part of this thesis.

Λ_0 : Corresponds to states without excitations in any of the subsystems (neither in the quantum radiation nor in the material emitters). Only the polariton (which is also the bare) ground state $|G\rangle = |0, 0\rangle$ forms this manifold. The dimension \dim_0 of the excitation manifold Λ_0 is therefore $\dim_0 = 1$.

Λ_1 : Represents combinations between bare states of the form $|0, 1\rangle$ and/or $|1, 0\rangle$, where only one of the subsystems is excited. For N material emitters plus the cavity, there are a total of $N + 1$ possible states that make up the first excitation manifold, namely $\dim_1 = N + 1$. We can identify two type of polariton states in Λ_1 :

Polaritons from bright emitter states coupled to the cavity: The state of higher energy in Λ_1 is called the upper polariton $|U\rangle$ and the one of lower energy is the lower polariton $|L\rangle$. With detuning $\Delta = 0$, they are polariton states of the form (in the compact bare states notation)

$$|L\rangle = \frac{1}{\sqrt{2}}(|1, 0\rangle - |0, 1\rangle), \quad |U\rangle = \frac{1}{\sqrt{2}}(|1, 0\rangle + |0, 1\rangle). \quad (1.28)$$

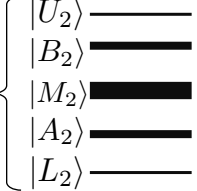
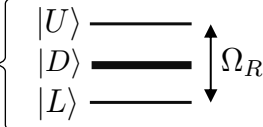

Name	Number of degenerated states	Dimension of the manifold
Λ_2 	1 $N - 1, N \geq 3$ $1 + N(N - 3)/2, N \geq 3$ $N - 1, N \geq 3$ 1	$\frac{1}{2}N(N + 1) + 1$
Λ_1 	1 $N - 1$ 1	$N + 1$
Λ_0 	1	1

Fig. 1.2.: Polariton states up to Λ_2 with detuning $\Delta = 0$.

Dark emitter states not coupled to the cavity: The remaining $N - 1$ states in Λ_1 are dark states $|D\rangle$, which represent superpositions of bare states fulfilling the compact form $|0, 1\rangle$, which do not contain photon excitations of the cavity. They are all degenerated in energy.

Λ_2 : Contains superpositions of bare states of the compact form $|2, 0\rangle$, $|0, 2\rangle$ and/or $|1, 1\rangle$. There is only one bare state of the form $|2, 0\rangle$, but due to the combinatorial arrangement among the N emitters, there are $\frac{1}{2} \frac{N!}{(N-2)!} = \frac{1}{2}N(N-1)$ states of the form $|0, 2\rangle$ and N states of the form $|1, 1\rangle$. Consequently, we can establish $\dim_{\Lambda_2} = \frac{1}{2}N(N+1) + 1$. The polariton state of highest energy in Λ_2 is denoted by $|U_2\rangle$ and the one of lowest energy by $|L_2\rangle$. Additionally, for detuning $\Delta = 0$, there is a degenerate intermediate level with $N(N-3)/2$ dark states in Λ_2 . We denote all these intermediate states by $|M_2\rangle$. Furthermore, there is a $N - 1$ degenerate energy level denoted by $|A_2\rangle$, below the $|M_2\rangle$ states, and another $N - 1$ degenerate energy level denoted by $|B_2\rangle$, above the $|M_2\rangle$ states. [Fig. 1.2](#) provides a compilation of all polariton states up to Λ_2 .

The frequency difference between the states $|U\rangle$ and $|L\rangle$ within the first excitation manifold is defined as the **Rabi frequency** Ω_R .

2. Open Quantum Systems

As discussed in the previous chapter, polaritonic systems are composed of two main subsystems: EM fields confined in cavities and material emitters. Each of these constituents undergoes relaxation or decay processes [26, 27, 28, 29]. The modes of the electromagnetic field exhibit a high-loss nature, and the material emitters, which in our case represent molecular electronic excitations [112], are subject to coupling with vibrational baths (which can induce dephasing and nonradiative decay between states) and may exhibit spontaneous emission, among others. A complete ab initio theoretical modeling of these systems is impossible without a large number of approximations to reduce the computational cost. Furthermore, even if a microscopic approach were feasible in practice, the solution to the microscopic equations would correspond to a “numerical experiment” that contains all the relevant physics, but does not necessarily give direct insight into the main processes at play. To address these loss processes, we employ techniques from the formalism of open quantum systems [30]. The theory of open quantum systems plays a crucial role in various applications of quantum physics where achieving a complete microscopic description or control of environmental degrees of freedom is either impossible or only partially achievable.

2.1. Quantum dynamics in Hilbert and Liouville space

When the dynamical evolution of a quantum system includes loss processes, the quantum state of the system cannot be characterized by a ket state vector or wave function; it must be represented by a **density operator**.

2.1.1. The density operator

The density operator $\hat{\rho}(t)$ represents a more general quantum state, which may or may not be represented by a ket vector from the Hilbert space. When it is possible to assign a ket vector $|\psi(t)\rangle$, the quantum state is named **pure**, and its corresponding density operator is defined as

$$\hat{\rho}(t) \equiv |\psi(t)\rangle \langle \psi(t)|. \quad (2.1)$$

On the other hand, when it is not possible to assign a unique ket vector, the state is said to be **mixed** (as is the case for systems subject to losses). A mixed state can be understood as a statistical mixture or superposition of a set of N pure density operator states or projectors $\{|\psi_k(t)\rangle \langle \psi_k(t)|\}$, each with probability $P_k \geq 0$. The density operator for a mixed state can be written as

$$\hat{\rho}(t) = \sum_{k=1}^N P_k |\psi_k(t)\rangle \langle \psi_k(t)|, \quad (2.2)$$

where $\sum_{k=1}^N P_k = 1$. If the system is in a pure state, all $P_k = 0$, except for one. The density operator satisfies the following properties for both pure and mixed states:

- It is an hermitian operator: $\hat{\rho} = \hat{\rho}^\dagger$.
- It has unit trace: $\text{Tr}(\hat{\rho}) = 1$.
- Its eigenvalues are non negative: $\lambda_k \geq 0$.
- The purity of a state is determined by the trace of the squared operator $\hat{\rho}^2$, with the value $\text{Tr}(\hat{\rho}^2) = 1$ for a pure state and $\text{Tr}(\hat{\rho}^2) < 1$ for a mixed state.

Expectation value: For an arbitrary operator \hat{A} , its expected value in the state described by the density operator $\hat{\rho}(t)$ is obtained as

$$\langle \hat{A} \rangle = \text{Tr}[\hat{A}\hat{\rho}(t)] = \sum_k P_k \langle \psi_k | \hat{A} | \psi_k \rangle. \quad (2.3)$$

2.1.2. Time evolution in Hilbert space

The time evolution of a pure state $|\psi(t)\rangle$ is governed by the time dependent Schrödinger equation

$$\frac{d}{dt} |\psi(t)\rangle = -\frac{i}{\hbar} \hat{H} |\psi(t)\rangle, \quad (2.4)$$

where \hat{H} is the Hamiltonian operator of the system. Taking the adjoint of the Schrödinger equation and using the definition of the general density operator in Eq. (2.2), we obtain the Liouville-von Neumann equation

$$\frac{d\hat{\rho}(t)}{dt} = -\frac{i}{\hbar} [\hat{H}, \hat{\rho}(t)]. \quad (2.5)$$

The formal integral solution to the differential equation Eq. (2.5) is

$$\hat{\rho}(t) = \hat{U}(t, t_0) \hat{\rho}(t_0) \hat{U}^\dagger(t, t_0), \quad (2.6)$$

where $\hat{U}(t, t_0)$ represents the time evolution operator (propagator) from an initial time t_0 to a posterior time t .

Time independent Hamiltonian: If the system Hamiltonian does not explicitly depend on time,

$$\hat{U}(t, t_0) = \exp \left[-\frac{i}{\hbar} \hat{H}(t - t_0) \right]. \quad (2.7)$$

Time dependent Hamiltonian: In optical spectroscopy, it is common to find Hamiltonian operators composed of two parts: the Hamiltonian \hat{H}_0 of the system under study and the Hamiltonian $\hat{H}'(t)$ associated with the interaction between the system and EM fields. In these cases, \hat{H}_0 does not explicitly depend on time, while the interaction $\hat{H}'(t)$ does. When the coupling between the system and the fields

is weak, it is possible to perform a perturbative expansion of the propagator $\hat{U}(t, t_0)$ in powers of \hat{H}' as follows [113]:

$$\hat{U}(t, t_0) = \hat{U}_0(t, t_0) + \sum_{n=1}^{\infty} \left(-\frac{i}{\hbar}\right)^n \int_{t_0}^t d\tau_n \int_{t_0}^{\tau_n} d\tau_{n-1} \cdots \int_{t_0}^{\tau_2} d\tau_1 \quad (2.8)$$

$$\hat{U}_0(t, \tau_n) \hat{H}'(\tau_n) \hat{U}_0(\tau_n, \tau_{n-1}) \hat{H}'(\tau_{n-1}) \cdots \hat{U}_0(\tau_2, \tau_1) \hat{H}'(\tau_1) \hat{U}_0(\tau_1, t_0),$$

which can be written in a compact form as:

$$\hat{U}(t, t_0) = \hat{U}_0(t, t_0) \exp_+ \left[-\frac{i}{\hbar} \int_{t_0}^t d\tau \hat{U}_0^\dagger(\tau, t_0) \hat{H}'(\tau) \hat{U}_0(\tau, t_0) \right]. \quad (2.9)$$

The subscript + denotes positive time ordering exponential operator, ensuring that the operators are ordered according to their chronological times. Here $\hat{U}_0(t, t_0)$ is the propagator associated to the time independent Hamiltonian \hat{H}_0 .

2.1.3. Representations in Hilbert space and the Liouvillian superoperator

Density operator: Note that in the Hilbert space (HS), the density operator, although representing the state of the system, does not have a vector character (like ket states). It has a matrix character because it is an operator. For example, if the ket state $|\psi(t)\rangle$ is expanded in a basis $\{|\alpha\rangle\}$ of the HS,

$$|\psi(t)\rangle = \sum_{\alpha} c_{\alpha}(t) |\alpha\rangle, \quad (2.10)$$

with $c_{\alpha}(t) = \langle\alpha|\psi(t)\rangle$, then its corresponding density operator is a matrix of the form

$$\hat{\rho}(t) = \sum_{\alpha\beta} \rho_{\alpha\beta}(t) |\alpha\rangle \langle\beta|, \quad (2.11)$$

with matrix elements $\rho_{\alpha\beta}(t) = c_{\alpha}^*(t)c_{\beta}(t)$.

Dynamic equation and the Liouville superoperator: On the other hand, the representation of the Liouville-von Neumann equation Eq. (2.5) in a basis of the HS takes the form

$$\begin{aligned} \left\langle \alpha \left| \frac{d\hat{\rho}}{dt} \right| \beta \right\rangle &= -\frac{i}{\hbar} (\langle\alpha|\hat{H}\hat{\rho}|\beta\rangle - \langle\alpha|\hat{\rho}\hat{H}|\beta\rangle) \\ \frac{d\rho_{\alpha\beta}}{dt} &= -\frac{i}{\hbar} \sum_{\theta\phi} (\langle\alpha|\hat{H}|\theta\rangle \langle\theta|\hat{\rho}|\phi\rangle \langle\phi|\beta\rangle - \langle\alpha|\theta\rangle \langle\theta|\hat{\rho}|\phi\rangle \langle\phi|\hat{H}|\beta\rangle) \\ &= -\frac{i}{\hbar} \sum_{\theta\phi} (H_{\alpha\theta} \delta_{\beta\phi} - \delta_{\alpha\theta} H_{\beta\phi}^*) \rho_{\theta\phi}. \end{aligned} \quad (2.12)$$

We have used the completeness and orthonormality relations of the HS basis ($\delta_{\alpha\beta}$ is the Kronecker delta). At this point, it is convenient to write compactly

$$\frac{d\rho_{\alpha\beta}}{dt} = -\frac{i}{\hbar} \sum_{\theta\phi} \mathcal{L}_{\alpha\beta, \theta\phi} \rho_{\theta\phi}, \quad (2.13)$$

where $\mathfrak{L}_{\alpha\beta,\theta\phi} = H_{\alpha\theta}\delta_{\beta\phi} - \delta_{\alpha\theta}H_{\beta\phi}^*$ represents the tetradric “matrix” element of a superoperator $\check{\mathfrak{L}}$ (it is an object that acts on the operators of HS, in particular on the density operator). It is known in the literature as the **Liouvillian superoperator** [77, 30]. To simplify the notation in this thesis, a procedure which is also common in the literature, we introduce the factor $-\frac{i}{\hbar}$ in the expression of the Liouvillian such that

$$\mathfrak{L}_{\alpha\beta,\theta\phi} = -\frac{i}{\hbar}(H_{\alpha\theta}\delta_{\beta\phi} - \delta_{\alpha\theta}H_{\beta\phi}^*), \quad (2.14)$$

$$\frac{d\rho_{\alpha\beta}}{dt} = \sum_{\theta\phi} \mathfrak{L}_{\alpha\beta,\theta\phi} \rho_{\theta\phi}. \quad (2.15)$$

In operator and superoperator form, the Liouville-von Neumann equation can finally be written as

$$\frac{d\hat{\rho}(t)}{dt} = \check{\mathfrak{L}}[\hat{\rho}(t)]. \quad (2.16)$$

The action of $\check{\mathfrak{L}}$ on the operator $\hat{\rho}$ should be understood as a functional in the form

$$\check{\mathfrak{L}}[\hat{\rho}] \equiv -\frac{i}{\hbar}[\hat{H}, \hat{\rho}]. \quad (2.17)$$

Eq. (2.16) is formally identical to the Schrödinger equation Eq. (2.4), but the objects involved have different mathematical nature. In the Schrödinger equation, the states $|\psi(t)\rangle$ are vectors, while in the Liouville equation, the states $\hat{\rho}(t)$ are matrix operators. In the Schrödinger equation, the Hamiltonian \hat{H} is an operator (it has a two-index matrix representation), while in the Liouville equation, the Liouvillian $\check{\mathfrak{L}}$ is a superoperator (it has a four-index representation). Since the states of open quantum systems must necessarily be characterized by density operators, it is convenient to define a new space in which these operators can be treated as vectors and the superoperators (for example the Liouvillian) can be treated as matrix operators. This space is called Liouville space (LS) [77].

2.1.4. Quantum objects in Liouville space

Since the density operator $\hat{\rho}$ and any arbitrary operator \hat{A} acting on the HS are vectors in the LS, we could represent them as kets in the form $|\hat{\rho}\rangle$ and $|\hat{A}\rangle$, respectively. However, to distinguish them from kets in the HS, we use the notation of double ket

$$\hat{\rho} \leftrightarrow |\rho\rangle\rangle. \quad (2.18)$$

The left-hand side in this equation represents the object in the HS, and the right-hand side, its equivalent in the LS. Of course, this correspondence is valid for any arbitrary operator $\hat{A} \leftrightarrow |\hat{A}\rangle\rangle$.

Basis of LS

In HS, the density operator can be represented in a basis $\{|\alpha\rangle\}$ as expressed in Eq. (2.11). Each object $|\alpha\rangle\langle\beta|$ that appears in this representation is an operator in HS, which we represent in LS as a vector

$$|\alpha\rangle\langle\beta| \leftrightarrow |\alpha\beta\rangle\rangle \equiv |m\rangle\rangle. \quad (2.19)$$

Here we introduce the single-index notation (with Latin letters instead of Greek letters), which is more useful for representing vectors in the LS. The matrix representation in HS and the vector representation in LS of the object in Eq. (2.19) are related with the following index correspondence (for a matrix M with dimension $N \times N$ we have a vector V with dimension N^2):

$$M_{ij} \rightarrow V_{(i-1)N+j}, \quad (2.20)$$

where $i, j = 1, 2, \dots, N$. Now, the vectors $|\alpha\beta\rangle\rangle$ or $|m\rangle\rangle$ form the basis of the LS. Note that each index α and β runs over the dimension of the HS basis \dim_H , while the single index m runs over \dim_H^2 . This means that the dimension of the LS is

$$\dim_L = \dim_H^2. \quad (2.21)$$

The completeness relation in the LS is established as

$$\hat{1} = \sum_{\alpha\beta} |\alpha\beta\rangle\rangle \langle\langle \alpha\beta| = \sum_m |m\rangle\rangle \langle\langle m|, \quad (2.22)$$

where the double-bra represents a state in the dual space

$$(|\alpha\rangle \langle\beta|)^\dagger \leftrightarrow |\alpha\beta\rangle\rangle^\dagger = \langle\langle \alpha\beta|, \quad (2.23)$$

and the orthogonality relation can be written as

$$\langle\langle \alpha\beta|\theta\phi\rangle\rangle = \delta_{\alpha\theta}\delta_{\beta\phi} \quad \text{or} \quad \langle\langle m|n\rangle\rangle = \delta_{mn}. \quad (2.24)$$

Inner product

Note that the counterpart of $\langle\langle \alpha\beta|\theta\phi\rangle\rangle$ in Eq. (2.24) is in the HS $(|\alpha\rangle \langle\beta|)^\dagger \cdot (|\theta\rangle \langle\phi|)$, where the product \cdot should represent a type of inner product between operators, such that the result is the scalar $\delta_{\alpha\theta}\delta_{\beta\phi}$. This product in HS is defined as

$$(|\alpha\rangle \langle\beta|)^\dagger \cdot (|\theta\rangle \langle\phi|) \equiv \text{Tr} \left[(|\alpha\rangle \langle\beta|)^\dagger (|\theta\rangle \langle\phi|) \right] = \delta_{\alpha\theta}\delta_{\beta\phi}. \quad (2.25)$$

In general, for two operators \hat{A} and \hat{B} acting on the HS, we define their inner product and its counterpart in the LS as follows

$$\hat{A}^\dagger \cdot \hat{B} \equiv \text{Tr} \left[\hat{A}^\dagger \hat{B} \right] \leftrightarrow \langle\langle A|B\rangle\rangle. \quad (2.26)$$

Since the result is a scalar, we can simply write

$$\langle\langle A|B\rangle\rangle \equiv \text{Tr} \left[\hat{A}^\dagger \hat{B} \right]. \quad (2.27)$$

Expectation value: Note that the expectation value of an operator \hat{A} can be understood in LS as an inner product

$$\langle\langle \hat{A} \rangle\rangle = \text{Tr} \left[\hat{A} \hat{\rho} \right] \leftrightarrow \langle\langle A^\dagger|\rho\rangle\rangle = \langle\langle \rho|A\rangle\rangle. \quad (2.28)$$

Representations in Liouville space

As previously stated, for any matrix operator \hat{A} in HS there is a corresponding vector $|A\rangle\rangle$ in LS, and it can be represented as an expansion in both spaces as

$$\hat{A} = \sum_{\alpha\beta} A_{\alpha\beta} |\alpha\rangle \langle\beta| \leftrightarrow |A\rangle\rangle = \sum_{\alpha\beta} A_{\alpha\beta} |\alpha\beta\rangle\rangle, \quad (2.29)$$

with

$$A_{\alpha\beta} = \langle\alpha| \hat{A} |\beta\rangle \leftrightarrow \langle\langle\alpha\beta|A\rangle\rangle = \text{Tr} \left[|\beta\rangle \langle\alpha| \hat{A} \right]. \quad (2.30)$$

In particular, the state vector $|\rho\rangle\rangle$ in LS can be expanded as

$$|\rho\rangle\rangle = \sum_{\alpha\beta} \rho_{\alpha\beta} |\alpha\beta\rangle\rangle, \quad (2.31)$$

with $\rho_{\alpha\beta} = \langle\langle\alpha\beta|\rho\rangle\rangle$. On the other hand, a superoperator $\check{\mathcal{A}}$ acting on operators in the HS, which can be understood as a matrix operator $\hat{\mathcal{A}}$ in LS (we use calligraphic letters to distinguish from operators in the HS), expands as

$$\hat{\mathcal{A}} = \sum_{\alpha\beta, \theta\phi} \mathcal{A}_{\alpha\beta, \theta\phi} |\alpha\beta\rangle\rangle \langle\langle\theta\phi|, \quad (2.32)$$

with $\mathcal{A}_{\alpha\beta, \theta\phi} = \langle\langle\alpha\beta|\hat{\mathcal{A}}|\theta\phi\rangle\rangle$. In particular, for the Liouvillian superoperator with matrix elements defined in Eq. (2.14),

$$\hat{\mathfrak{L}} = \sum_{\alpha\beta, \theta\phi} \mathfrak{L}_{\alpha\beta, \theta\phi} |\alpha\beta\rangle\rangle \langle\langle\theta\phi|. \quad (2.33)$$

To avoid confusion, Tab. 2.1 clarifies the notation we use in each vector space. The special Liouvillian superoperator is denoted with another calligraphic font.

Hilbert Space (HS)	Liouville space (LS)
Operator \hat{A} (double-index matrix)	Vector $ A\rangle\rangle$ (single-index vector)
Superoperator $\check{\mathcal{A}}$ (tetra-index matrix)	Operator $\hat{\mathcal{A}}$ (double-index matrix)

Tab. 2.1.: Notation for quantum objects in Hilbert and Liouville spaces.

2.1.5. Time evolution in Liouville space

The Liouville-von Neumann equation Eq. (2.16), written in LS, takes the form

$$\frac{d|\rho(t)\rangle\rangle}{dt} = \hat{\mathfrak{L}}|\rho(t)\rangle\rangle, \quad (2.34)$$

with formal solution

$$|\rho(t)\rangle\rangle \equiv \hat{\mathcal{U}}(t, t_0) |\rho(t_0)\rangle\rangle. \quad (2.35)$$

Here we introduce the LS propagator between times t_0 and t , $\hat{\mathcal{U}}(t_0, t)$. The counterpart of this equation in the HS is Eq. (2.6).

Time independent Liouvillian: If the system Liouvillian does not explicitly depend on time, the time propagator reads

$$\hat{U}(t, t_0) = \exp \left[\hat{\mathcal{L}}(t - t_0) \right]. \quad (2.36)$$

Time dependent Liouvillian: As discussed in [Subsec. 2.1.2](#), in optical spectroscopy applications, it is common to find Liouvillian operators of the form

$$\hat{\mathcal{L}}(t) = \hat{\mathcal{L}}_0 + \hat{\mathcal{L}}'(t), \quad (2.37)$$

with a time independent part $\hat{\mathcal{L}}_0$ and a time dependent interaction $\hat{\mathcal{L}}'(t)$. In analogy to [Eq. \(2.8\)](#), the time propagator in the LS can be expanded perturbatively in powers of the interaction as

$$\begin{aligned} \hat{U}(t, t_0) &= \hat{U}_0(t, t_0) + \sum_{n=1}^{\infty} \int_{t_0}^t d\tau_n \int_{t_0}^{\tau_n} d\tau_{n-1} \cdots \int_{t_0}^{\tau_2} d\tau_1 \\ &\hat{U}_0(t, \tau_n) \hat{\mathcal{L}}'(\tau_n) \hat{U}_0(\tau_n, \tau_{n-1}) \hat{\mathcal{L}}'(\tau_{n-1}) \cdots \hat{U}_0(\tau_2, \tau_1) \hat{\mathcal{L}}'(\tau_1) \hat{U}_0(\tau_1, t_0), \end{aligned} \quad (2.38)$$

where $\hat{U}_0(t, t_0)$ is the LS propagator for the time independent Liouvillian part $\hat{\mathcal{L}}_0$.

2.1.6. Eigenvalues and eigenvectors of the Liouvillian

Let us consider a general Hamiltonian \hat{H} , with corresponding Liouvillian superoperator $\check{\mathcal{L}}$ in the form of [Eq. \(2.17\)](#), that can be generalized to the action over any operator \hat{O} as

$$\check{\mathcal{L}}[\hat{O}] = -\frac{i}{\hbar} [\hat{H}, \hat{O}]. \quad (2.39)$$

If $\{|\alpha\rangle\}$ is the eigenbasis of this Hamiltonian, such that

$$\hat{H} |\alpha\rangle = \hbar\omega_\alpha |\alpha\rangle, \quad (2.40)$$

then, the set of states in LS with the form $\{|\alpha\beta\rangle\}$ correspond to the eigenbasis of $\hat{\mathcal{L}}$, with an eigenvalue equation that reads

$$\hat{\mathcal{L}} |\alpha\beta\rangle = -i\omega_{\alpha\beta} |\alpha\beta\rangle, \quad (2.41)$$

with $\omega_{\alpha\beta} \equiv \omega_\alpha - \omega_\beta$. This can be shown using [Eq. \(2.14\)](#) with $H_{\alpha\beta} = H_{\alpha\beta}^* = \hbar\omega_\alpha \delta_{\alpha\beta}$

$$\begin{aligned} \mathcal{L}_{\alpha\beta, \theta\phi} &= -\frac{i}{\hbar} \left(H_{\alpha\theta} \delta_{\beta\phi} - \delta_{\alpha\theta} H_{\beta\phi}^* \right) \\ &= -i (\omega_\alpha \delta_{\alpha\theta} \delta_{\beta\phi} - \omega_\beta \delta_{\alpha\theta} \delta_{\beta\phi}) \\ &= -i (\omega_\alpha - \omega_\beta) \delta_{\alpha\theta} \delta_{\beta\phi}. \end{aligned} \quad (2.42)$$

Then, the operator $\hat{\mathcal{L}}$ in LS admits a spectral representation (see [Eq. \(2.33\)](#)) in the form

$$\begin{aligned} \hat{\mathcal{L}} &= \sum_{\alpha\beta, \theta\phi} -i\omega_{\alpha\beta} \delta_{\alpha\theta} \delta_{\beta\phi} |\alpha\beta\rangle \langle\langle \theta\phi | \\ &= \sum_{\alpha\beta} -i\omega_{\alpha\beta} |\alpha\beta\rangle \langle\langle \alpha\beta |, \end{aligned} \quad (2.43)$$

which is diagonal in the Hamiltonian eigenbasis. Now, [Eq. \(2.41\)](#) can be easily evaluated and verified.

Time propagator

For a time independent Liouvillian, the time propagator in Eq. (2.36) can be easily represented in the Liouvillian (and Hamiltonian) eigenbasis as

$$\hat{U}(t, t_0) = \exp \left[\hat{\mathcal{L}}(t - t_0) \right] = \sum_{\alpha\beta} \exp[-i\omega_{\alpha\beta}(t - t_0)] |\alpha\beta\rangle \langle\langle\alpha\beta|. \quad (2.44)$$

2.1.7. Beyond Hamiltonian dynamics

The Liouvillian we have constructed in the form of Eq. (2.39) is associated with a Hamiltonian. The dynamical evolution subject to that Liouvillian (or its respective Hamiltonian) is named **coherent**. However, when a quantum system is considered open, its Liouvillian does not necessarily have an associated Hamiltonian. A more general form of the Liouvillian in the context of optical spectroscopy for an open quantum system can be written as

$$\hat{\mathcal{L}} = \hat{\mathcal{L}}_{H_0} + \hat{\mathcal{L}}_D + \hat{\mathcal{L}}_{H_{\text{int}}}(t), \quad (2.45)$$

where $\hat{\mathcal{L}}_{H_0}$ (with the form in Eq. (2.39)) is the part of the Liouvillian associated to the system Hamiltonian \hat{H}_0 ; $\hat{\mathcal{L}}_D$ represents decay or loss processes, resulting from the coupling of the open quantum system to a bath. These processes usually do not have a counterpart Hamiltonian and they lead to **incoherent dynamics** of the system [30, 114]. These two parts of the Liouvillian are usually time independent. Finally, $\hat{\mathcal{L}}_{H_{\text{int}}}(t)$ represents the interaction of the system with time dependent EM fields, widely used in spectroscopic methods [77], as discussed later in Chap. 3. This last part has an associated Hamiltonian \hat{H}_{int} . Unlike $\hat{\mathcal{L}}_D$, the other two parts of the Liouvillian are responsible for coherent dynamics of the system.

The equations we have developed in Subsec. 2.1.4 and Subsec. 2.1.5 are entirely general for any form of the Liouvillian and they are not restricted to the form in Eq. (2.39) that gives rise to the matrix elements Eq. (2.14) and to the equations from Subsec. 2.1.6.

At this point, we can appreciate the importance of introducing the Liouvillian superoperator, the density operator, and their representations in the LS. In the Liouvillian formalism, it is possible to account for these incoherent processes that generally cannot be represented by a Hamiltonian. Only in some cases is it possible to find a non-Hermitian effective Hamiltonian to account for the incoherent dynamics. Similarly, the states of an open system, subject to incoherent dynamics, are mixed states and cannot be represented as vectors in the HS, requiring their representation as density operators or vectors in the LS. In the following section, we discuss two forms that the part $\hat{\mathcal{L}}_D$ can take, depending on the incoherent processes that must be taken into account in the dynamic evolution of the open quantum system.

2.2. Master equations for incoherent dynamics

Let us consider a quantum system (characterized by states in the Hilbert space \mathcal{H}_S) coupled to a bath, reservoir, or environment (represented in the Hilbert space \mathcal{H}_B). The Hilbert space of the composite

system (system S + bath B) is obtained from the direct or tensor product $\mathcal{H} = \mathcal{H}_S \otimes \mathcal{H}_B$. If this composite system is treated from a coherent (closed) dynamics approach, we must consider the total Hamiltonian

$$\hat{H} = \hat{H}_S + \hat{H}_B + \hat{H}_{\text{int}}, \quad (2.46)$$

where \hat{H}_S and \hat{H}_B are the system and bath Hamiltonian respectively and \hat{H}_{int} is an interaction Hamiltonian between both parts. The operators associated with a subsystem (S or B) in Eq. (2.46) should be understood as a direct product between the respective operator and the identity operator of the other subsystem: $\hat{H}_S \equiv \hat{H}_S \otimes \hat{1}_B$ and $\hat{H}_B = \hat{H}_B \otimes \hat{1}_S$. In this coherent approach the dynamics of the density operator of the composite system $\hat{\rho}(t)$ is governed by the Liouvillian Eq. (2.17). However, the bath is often a complex quantum system with numerous degrees of freedom, and considering it explicitly in the Hamiltonian turns out to be a difficult or in some cases impossible task due to the huge computational cost. Since S is often the subsystem of interest and not the composite S+B system, it is convenient to focus only on the **reduced density operator** of the system, which is obtained as

$$\hat{\rho}_S(t) = \text{Tr}_B [\hat{\rho}(t)], \quad (2.47)$$

where Tr_B denotes the partial trace over the degrees of freedom of the bath. This represents a map from the LS associated to \mathcal{H} (where $\hat{\rho}(t)$ lies) to the LS associated to \mathcal{H}_S (where $\hat{\rho}_S(t)$ lies). The state $\hat{\rho}_S$ is now a mixed state, and its dynamics is governed by a Liouvillian of the form in Eq. (2.45). Without the external interaction with time dependent EM fields (this interaction is included in Chap. 3 for multidimensional spectroscopy), it reads in the LS of the system as¹

$$\hat{\mathcal{L}} = \hat{\mathcal{L}}_{H_S} + \hat{\mathcal{L}}_D. \quad (2.48)$$

This is an incoherent dynamics approach, where S is treated as an open quantum system (with coherent dynamics governed by $\hat{\mathcal{L}}_{H_S}$), coupled to a phenomenological bath represented by $\hat{\mathcal{L}}_D$ that leads to incoherent dynamics.

2.2.1. Born-Markov master equation

To determine the form of the incoherent part of the Liouvillian $\hat{\mathcal{L}}_D$ (which is a superoperator in the Hilbert space \mathcal{H}_S), we start from the Liouville-von Neumann equation Eq. (2.5) satisfied by the density operator of the composite system $\hat{\rho}(t)$ in the Hilbert space \mathcal{H} . In the interaction picture, this equation takes the form² (the left-hand side of the arrows in the following expressions represents objects in the composite HS, while the right-hand side represents their respective representation in the composite LS)

$$\frac{d\hat{\rho}(t)}{dt} = -\frac{i}{\hbar} [\hat{H}_{\text{int}}(t), \hat{\rho}(t)] \leftrightarrow \frac{d|\tilde{\rho}(t)\rangle\rangle}{dt} = \hat{\mathcal{L}}_{\text{int}}(t) |\tilde{\rho}(t)\rangle\rangle. \quad (2.49)$$

For any operator \hat{A} in HS, the interaction picture transformation is

$$\hat{\hat{O}}(t) = \hat{U}_0^\dagger(t, t_0) \hat{O} \hat{U}_0(t, t_0) = e^{i(\hat{H}_S + \hat{H}_B)t/\hbar} \hat{O} e^{-i(\hat{H}_S + \hat{H}_B)t/\hbar} \quad (2.50)$$

¹In the previous section we denote $\hat{\mathcal{L}}_{H_S}$ as $\hat{\mathcal{L}}_{H_0}$. We assume this a time independent Hamiltonian.

²To facilitate the notation, in this section we use a tilde instead of the subscript I to indicate that the operators are represented in the interaction picture.

Here $\hat{U}_0(t, t_0)$ is the time propagator associated to the free interaction Hamiltonian $\hat{H}_S + \hat{H}_B$. When substituting the integral form of Eq. (2.49) into itself, we obtain for the reduced density operator of the system (after taking the partial trace over the degrees of freedom of the bath) and assuming that at time zero there are no correlations between S and B,

$$\begin{aligned} \frac{d\hat{\rho}_S(t)}{dt} &= -\frac{1}{\hbar^2} \int_0^t d\tau \text{Tr}_B \left\{ [\hat{H}_{\text{int}}(t), [\hat{H}_{\text{int}}(\tau), \hat{\rho}(\tau)]] \right\} \\ &\leftrightarrow \frac{d|\tilde{\rho}_S(t)\rangle\rangle}{dt} = \int_0^t d\tau \sum_b \langle\langle bb | \hat{\mathfrak{L}}_{\text{int}}(t) \hat{\mathfrak{L}}_{\text{int}}(\tau) | \tilde{\rho}(\tau) \rangle\rangle, \end{aligned} \quad (2.51)$$

where $\langle\langle bb |$ in the LS representation is equivalent to $|b\rangle\langle b|$ in the HS of the bath \mathcal{H}_B and $\{|b\rangle\}$ is a basis set of \mathcal{H}_B . The operation $\sum_b \langle\langle bb |$ is a projection onto the ‘‘diagonal elements’’ of the bath LS basis, which is equivalent to the partial trace over the degrees of freedom of B. In this equation, the left-hand side of the arrow is now an object represented in \mathcal{H}_S , and the right-hand side is its respective representation in the associated LS. Below, we outline two approximations that we use to derive the master equations employed throughout this thesis.

Born approximation

We assume that the coupling between S and B is weak and that the correlations between them are not significant, such that at any time instant, the global state is separable ($\hat{\rho}(t) = \hat{\rho}_S(t) \otimes \hat{\rho}_B(t)$). Additionally, we consider the bath to be much larger than the system, and consequently, the influence of the system on the bath is negligible. Thus, the state of the bath remains unaltered, in some reference state $\hat{\rho}_B$, during the timescale over which the system dynamics unfold. It means

$$\hat{\rho}(t) = \hat{\rho}_S(t) \otimes \hat{\rho}_B. \quad (2.52)$$

Markov approximation

We assume that the timescales over which the bath correlation functions decay are much shorter than the timescales of system evolution. Consequently, we can neglect memory effects in the dynamics of the reduced system. Note that in Eq. (2.51), there is a dependence of $\hat{\rho}(\tau)$ for all times $\tau \in [0, t]$. Under the Markov approximation, by eliminating these memory effects for times prior to the current time t , we can replace $\hat{\rho}(\tau)$ with $\hat{\rho}(t)$. With this substitution, we obtain a time-local equation (Redfield equation), which still depends on the choice for the preparation of the initial state at $t = 0$. To eliminate this dependence and obtain a Markovian equation, we must change τ in the integral to $t - \tau$ and extend the upper limit of the integral to infinity.

Under Born and Markov approximations we obtain the Born-Markov master equation [30, 68]

$$\begin{aligned} \frac{d\hat{\rho}_S(t)}{dt} &= -\frac{1}{\hbar^2} \int_0^\infty d\tau \text{Tr}_B \left\{ [\hat{H}_{\text{int}}(t), [\hat{H}_{\text{int}}(t - \tau), \hat{\rho}_S(t) \otimes \hat{\rho}_B]] \right\} \\ &\leftrightarrow \frac{d|\tilde{\rho}_S(t)\rangle\rangle}{dt} = \int_0^\infty d\tau \sum_b \langle\langle bb | \hat{\mathfrak{L}}_{\text{int}}(t) \hat{\mathfrak{L}}_{\text{int}}(t - \tau) (|\tilde{\rho}_S(t)\rangle\rangle \otimes |\rho_B\rangle\rangle). \end{aligned} \quad (2.53)$$

2.2.2. Bloch-Redfield master equation

The Bloch–Redfield formalism [115, 116] provides a framework to account for dissipation of the reduced density operator of the system, where the bath is modeled as a continuum of oscillators in the thermal equilibrium state. In the Born-Markov master equation, we assume that the interaction Hamiltonian between the system and the bath can be written in the composite HS as

$$\hat{H}_{\text{int}} = \sum_k \hat{Q}_k \otimes \hat{R}_k, \quad (2.54)$$

where \hat{Q}_k are operators acting on \mathcal{H}_S and \hat{R}_k on \mathcal{H}_B . In the interaction picture this reads as

$$\hat{H}_{\text{int}}(t) = \sum_k \hat{Q}_k(t) \otimes \hat{R}_k(t). \quad (2.55)$$

Now, by inserting the Eq. (2.55) in the Born-Markov master equation Eq. (2.53) in the representation of HS, we obtain

$$\frac{d\hat{\rho}_S(t)}{dt} = -\frac{1}{\hbar^2} \sum_{jk} \int_0^\infty d\tau \left\{ \left[\hat{Q}_j(t), \hat{Q}_k(t-\tau) \hat{\rho}_S(t) \right] S_{jk}(-\tau) + \text{h.c.} \right\}, \quad (2.56)$$

where we have assumed that the system operators $\hat{Q}_k(t)$ are Hermitian.

Bath correlation functions

In the previous equation we have introduced the correlation functions S_{jk} for bath operators. These are defined in \mathcal{H}_B as follows

$$S_{jk}(-\tau) \equiv \langle \hat{R}_j(t) \hat{R}_k(t-\tau) \rangle_{\rho_B} = \langle \hat{R}_j(0) \hat{R}_k(-\tau) \rangle_{\rho_B} = \text{Tr}_B \left\{ \hat{R}_j(t) \hat{R}_k(t-\tau) \hat{\rho}_B \right\}, \quad (2.57)$$

and

$$S_{jk}^*(-\tau) = \langle \hat{R}_k(t-\tau) \hat{R}_j(t) \rangle_{\rho_B} = \langle \hat{R}_k(-\tau) \hat{R}_j(0) \rangle_{\rho_B}. \quad (2.58)$$

In the frequency domain, we define

$$S_{jk}(\omega) \equiv \int_0^\infty d\tau S_{jk}(\tau) e^{i\omega\tau}. \quad (2.59)$$

The complex-valued correlation functions can also be written as

$$S_{jk}(\omega) = \gamma_{jk}(\omega) + i\chi_{jk}(\omega), \quad (2.60)$$

with

$$\gamma_{jk}(\omega) \equiv \frac{1}{2} [S_{jk}(\omega) + S_{kj}^*(\omega)] = \frac{1}{2} \int_{-\infty}^\infty d\tau S_{jk}(\tau) e^{i\omega\tau}, \quad \gamma_{jk}^*(\omega) = \gamma_{kj}(\omega). \quad (2.61)$$

$$\chi_{jk}(\omega) \equiv \frac{1}{2i} [S_{jk}(\omega) - S_{kj}^*(\omega)]. \quad (2.62)$$

The coefficients $\chi_{jk}(\omega)$ form a Hermitian matrix that leads to coherent dynamics. They represent a shift in the energy levels of the system due to its coupling with the bath, known as the **Lamb shift** [30]. On the other hand, the coefficients $\gamma_{jk}(\omega)$ form a positive-definite matrix and, consequently, the matrix γ formed by them can always be diagonalized.

Returning to the Schrödinger picture

In the Schrödinger picture, Eq. (2.56) transforms into

$$\frac{d\hat{\rho}_S(t)}{dt} = -\frac{i}{\hbar}[\hat{H}_S, \hat{\rho}_S(t)] - \frac{1}{\hbar^2} \sum_{jk} \int_0^\infty d\tau \left[\hat{Q}_j, e^{-i\hat{H}_S\tau/\hbar} \hat{Q}_k e^{i\hat{H}_S\tau/\hbar} \hat{\rho}_S(t) \right] S_{jk}(-\tau) + \text{h.c.}, \quad (2.63)$$

where $e^{-i\hat{H}_S\tau/\hbar} = \hat{U}_S(\tau)$ is the time propagator in \mathcal{H}_S .

We can now identify that the first term in the right-hand side of Eq. (2.63) accounts for the coherent dynamics of the system. This is equivalent to $\check{\mathfrak{L}}_{H_S}[\hat{\rho}_S(t)]$. On the other hand, the second term (which actually includes four terms upon expanding the commutator and the respective Hermitian conjugate) represents the incoherent dynamics (if we neglect the Lamb shift that arises when we develop the integrals in τ) and can be interpreted as the HS dissipative superoperator $\check{\mathfrak{L}}_D$ in Eq. (2.47). Then, we can write

$$\check{\mathfrak{L}}_D[\hat{\rho}_S(t)] \equiv -\frac{1}{\hbar^2} \sum_{jk} \int_0^\infty d\tau \left[\hat{Q}_j, e^{-i\hat{H}_S\tau/\hbar} \hat{Q}_k e^{i\hat{H}_S\tau/\hbar} \hat{\rho}_S(t) \right] S_{jk}(-\tau) + \text{h.c.} \quad (2.64)$$

Representation in the system Hamiltonian eigenbasis

If we consider the LS basis $\{|\alpha\beta\rangle\}$, constructed from the eigenstates $\{|\alpha\rangle\}$ of \hat{H}_S in HS, such that $\hat{H}_S|\alpha\rangle = \hbar\omega_\alpha|\alpha\rangle$, it can be shown from Eq. (2.64) that the LS matrix elements of $\hat{\mathfrak{L}}_D$ are [68]

$$\begin{aligned} \mathfrak{L}_{D_{\alpha\beta,\theta\phi}} &= \langle\langle\alpha\beta|\hat{\mathfrak{L}}_D|\theta\phi\rangle\rangle \\ &= -\frac{1}{\hbar^2} \sum_{jk} \int_0^\infty d\tau \left\{ \left(\delta_{\beta\phi} \sum_{\xi} Q_{\alpha\xi}^j Q_{\xi\theta}^k e^{-i\omega_{\xi\theta}\tau} - Q_{\alpha\theta}^k Q_{\phi\beta}^j e^{-i\omega_{\alpha\theta}\tau} \right) S_{jk}(-\tau) \right. \\ &\quad \left. + \left(\delta_{\alpha\theta} \sum_{\xi} Q_{\phi\xi}^k Q_{\xi\beta}^j e^{-i\omega_{\phi\xi}\tau} - Q_{\alpha\theta}^j Q_{\phi\beta}^k e^{-i\omega_{\phi\beta}\tau} \right) S_{jk}^*(-\tau) \right\}, \end{aligned} \quad (2.65)$$

which, unlike the Liouvillian associated with coherent dynamics (see Eq. (2.42)), is not diagonal in the Hamiltonian basis. Note that when expanding the integrals over τ , expressions of the form in Eq. (2.59) arise, which we can express in terms of the bath correlation functions in the frequency domain. At this point we take $S_{jk}(\omega) = \gamma_{jk}(\omega)$. This means that we disregard the Lamb shift resulting from including $\chi_{jk}(\omega)$ in Eq. (2.60). Then, we obtain the **Bloch-Redfield superoperator** $\check{\mathfrak{L}}_D = \check{\mathfrak{B}}$ (operator $\hat{\mathfrak{B}}$ in LS), whose matrix elements in the eigenbasis of \hat{H}_S are of the form

$$\begin{aligned} \mathcal{B}_{\alpha\beta,\theta\phi} &= \langle\langle\alpha\beta|\hat{\mathfrak{B}}|\theta\phi\rangle\rangle \\ &= -\frac{1}{\hbar^2} \sum_{jk} \left\{ \delta_{\beta\phi} \sum_{\xi} Q_{\alpha\xi}^j Q_{\xi\theta}^k \gamma_{jk}(\omega_{\xi\theta}) - Q_{\alpha\theta}^k Q_{\phi\beta}^j \gamma_{jk}(\omega_{\alpha\theta}) \right. \\ &\quad \left. + \delta_{\alpha\theta} \sum_{\xi} Q_{\phi\xi}^k Q_{\xi\beta}^j \gamma_{jk}^*(\omega_{\phi\xi}) - Q_{\alpha\theta}^j Q_{\phi\beta}^k \gamma_{jk}^*(\omega_{\phi\beta}) \right\}. \end{aligned} \quad (2.66)$$

The Bloch-Redfield superoperator in HS can be finally reorganized as

$$\check{\mathfrak{B}}[\hat{\rho}(t)] = -\frac{1}{\hbar^2} \sum_{jk} \sum_{\alpha\beta} Q_{\alpha\beta}^k \left[\hat{Q}_j, |\alpha\rangle\langle\beta| \hat{\rho}(t) \right] \gamma_{jk}(\omega_{\alpha\beta}) + \text{h.c.}, \quad (2.67)$$

if the operators \hat{Q}_k are Hermitian. We have omitted the subscript S for the reduced density operator of the system. Note that it is necessary to define the system Hermitian operators \hat{Q}_k involved in the coupling to the bath and the bath correlation functions $S_{jk}(\omega)$ to fully evaluate the Bloch-Redfield superoperator. If the bath coupling operators \hat{R}_k are uncorrelated, meaning that the functions $\gamma_{jk}(\omega)$ are zero when $j \neq k$ and they are $\gamma(\omega)$ for $j = k$, for each system operator \hat{Q} , we can write

$$\check{\mathcal{B}}(\hat{Q})[\hat{\rho}(t)] = -\frac{1}{\hbar^2} \sum_{\alpha\beta} Q_{\alpha\beta} \left[\hat{Q}, |\alpha\rangle \langle\beta| \hat{\rho}(t) \right] \gamma(\omega_{\alpha\beta}) + \text{h.c.} \quad (2.68)$$

With this functional for the bath interaction, the Bloch-Redfield master equation is then defined in HS as

$$\frac{d\hat{\rho}(t)}{dt} = \check{\mathcal{L}}_{HS}[\hat{\rho}(t)] + \sum_k \check{\mathcal{B}}(\hat{Q}_k)[\hat{\rho}(t)]. \quad (2.69)$$

2.2.3. Lindblad master equation

The Bloch-Redfield equation, although it allows for the consistent inclusion of the bath through its correlation function, does not guarantee complete positivity from its mathematical form. When additional considerations are assumed (described below), a new dissipative superoperator $\check{\mathcal{L}}_D = \check{\mathcal{L}}$ is obtained, named the **Lindblad superoperator**. This is the Markovian most general form of a completely positive and trace-preserving map from the composite L+B Liouville space to S Liouville space [117, 118].

Secular approximation

If the time scales of the intrinsic evolution of the closed system S (these scales are of the order of $|\omega - \omega'|^{-1}$, where $\omega \neq \omega'$ are transition frequencies between eigenstates of \hat{H}_S) are much larger than the relaxation scales of S (when considered open), then the non-secular terms, i.e., those in which $\omega \neq \omega'$, can be neglected as they oscillate very rapidly during the relaxation times of the open system. This approximation is another type of RWA. To apply the secular approximation, we use the basis $\{|\alpha\rangle\}$ of \hat{H}_S and define the operators

$$\hat{A}_k(\omega_{\alpha\beta}) \equiv Q_{\alpha\beta}^k |\alpha\rangle \langle\beta|, \quad \hat{A}_k^\dagger(\omega_{\alpha\beta}) = Q_{\beta\alpha}^k |\beta\rangle \langle\alpha| = \hat{A}_k(-\omega_{\alpha\beta}), \quad (2.70)$$

where we assume that \hat{Q}_k are Hermitian operators. Note that in the LS, the states $|A_k(\omega_{\alpha\beta})\rangle\rangle$ are eigenstates of $\hat{\mathcal{L}}_{HS}$ with eigenvalues $-i\omega_{\alpha\beta}$ and they form a basis set. In the interaction picture,

$$\hat{A}_k(\omega_{\alpha\beta}) = e^{i\omega_{\alpha\beta}t} \hat{A}_k(\omega_{\alpha\beta}), \quad \hat{A}_k^\dagger(\omega_{\alpha\beta}) = e^{-i\omega_{\alpha\beta}t} \hat{A}_k^\dagger(\omega_{\alpha\beta}), \quad (2.71)$$

With these basis operators we can expand $\hat{Q}_k(t)$ as

$$\hat{Q}_k(t) = \sum_{\alpha\beta} e^{i\omega_{\alpha\beta}t} \hat{A}_k(\omega_{\alpha\beta}) = \sum_{\alpha\beta} e^{-i\omega_{\alpha\beta}t} \hat{A}_k^\dagger(\omega_{\alpha\beta}). \quad (2.72)$$

By using these expansions in Eq. (2.56), which is still written in the interaction picture, we obtain

$$\frac{d\hat{\rho}_S(t)}{dt} = -\frac{1}{\hbar^2} \sum_{jk} \sum_{\alpha\beta\theta\phi} e^{i(\omega_{\theta\phi} - \omega_{\alpha\beta})t} \left[\hat{A}_j^\dagger(\omega_{\alpha\beta}), \hat{A}_k(\omega_{\theta\phi}) \hat{\rho}_S(t) \right] \int_0^\infty d\tau e^{-i\omega_{\theta\phi}\tau} S_{jk}(-\tau) + \text{h.c.} \quad (2.73)$$

In the secular approximation, we omit the oscillating terms that arise when $\omega_{\alpha\beta} \neq \omega_{\theta\phi}$, thus, the previous expression reduces to

$$\frac{d\hat{\rho}_S(t)}{dt} = -\frac{1}{\hbar^2} \sum_{jk} \sum_{\alpha\beta} \left[\hat{A}_j^\dagger(\omega_{\alpha\beta}), \hat{A}_k(\omega_{\alpha\beta}) \hat{\rho}_S(t) \right] \gamma_{jk}(\omega_{\alpha\beta}) + \text{h.c.}, \quad (2.74)$$

where we have used the bath correlation functions in the frequency domain, neglecting the Lamb shift. Returning to the Schrödinger picture, we obtain an additional term associated with the coherent evolution of the system and we can identify that the dissipative Liouvillian part, in the secular approximation, takes the form

$$\begin{aligned} \check{\mathfrak{L}}_D[\hat{\rho}(t)] &= -\frac{1}{\hbar^2} \sum_{jk} \sum_{\alpha\beta} \left[\hat{A}_j^\dagger(\omega_{\alpha\beta}), \hat{A}_k(\omega_{\alpha\beta}) \hat{\rho}(t) \right] \gamma_{jk}(\omega_{\alpha\beta}) + \text{h.c.} \\ &= -\frac{1}{\hbar^2} \sum_{jk} \sum_{\alpha\beta} Q_{\alpha\beta}^k Q_{\alpha\beta}^j [|\alpha\rangle \langle\beta|, |\alpha\rangle \langle\beta| \hat{\rho}(t)] \gamma_{jk}(\omega_{\alpha\beta}) + \text{h.c.}, \end{aligned} \quad (2.75)$$

which is similar to the non-secular Bloch-Redfield superoperator in Eq. (2.67), but in the expansion of \hat{Q}_j we only consider the transition operators $|\alpha\rangle \langle\beta|$ in the secular approximation. Expanding the commutator in the upper expression of Eq. (2.75) and exchanging the subscripts j and k in the h.c. part, considering that $\gamma_{jk}^*(\omega) = \gamma_{kj}(\omega)$ (see Eq. (2.61)), we obtain

$$\check{\mathfrak{L}}_D[\hat{\rho}(t)] = \frac{1}{\hbar^2} \sum_{jk} \sum_{\alpha\beta} \gamma_{jk}(\omega_{\alpha\beta}) \left(2\hat{A}_k(\omega_{\alpha\beta}) \hat{\rho}(t) \hat{A}_j^\dagger(\omega_{\alpha\beta}) - \left\{ \hat{A}_j^\dagger(\omega_{\alpha\beta}) \hat{A}_k(\omega_{\alpha\beta}), \hat{\rho}(t) \right\} \right), \quad (2.76)$$

where $\{\hat{A}, \hat{B}\} \equiv \hat{A}\hat{B} + \hat{B}\hat{A}$ represents the anticommutator.

Diagonal form

Since the coefficients $\gamma_{jk}(\omega)$ define a positive-semidefinite (PSD) matrix, we can find a unitary transformation \hat{W} such that $\hat{W}\hat{\gamma}(\omega)\hat{W}^\dagger$ (we denote these objects with a hat since they are matrices in HS) is a diagonal matrix with elements λ_i on its diagonal. We define $\gamma_i \equiv 2\lambda_i$ to obtain

$$\check{\mathfrak{L}}_D[\hat{\rho}(t)] = \frac{1}{\hbar^2} \sum_i \sum_{\alpha\beta} \gamma_i(\omega_{\alpha\beta}) \left(\hat{L}_i(\omega_{\alpha\beta}) \hat{\rho}(t) \hat{L}_i^\dagger(\omega_{\alpha\beta}) - \frac{1}{2} \left\{ \hat{L}_i^\dagger(\omega_{\alpha\beta}) \hat{L}_i(\omega_{\alpha\beta}), \hat{\rho}(t) \right\} \right), \quad (2.77)$$

where

$$\hat{L}_i(\omega_{\alpha\beta}) = \sum_k W_{ki} \hat{A}_i(\omega_{\alpha\beta}). \quad (2.78)$$

In general, the Eq. (2.76) can be written in the diagonal form Eq. (2.77) if and only if there exists the invertible matrix \hat{W} such that $\hat{W}\hat{\gamma}(\omega)\hat{W}^\dagger$ is diagonal with nonnegative eigenvalues [119]. The Eq. (2.77) is named the Lindblad-Gorini-Kossakowski-Sudarshan superoperator [30]. In the case where only one frequency is relevant, it is obtained for each operator \hat{L} the named **Lindblad term**

$$\check{\mathfrak{L}}(\hat{L})[\hat{\rho}(t)] \equiv \hat{L}\hat{\rho}(t)\hat{L}^\dagger - \frac{1}{2} \left\{ \hat{L}^\dagger \hat{L}, \hat{\rho}(t) \right\}, \quad (2.79)$$

and the Lindblad master equation [120] can be written as³

$$\frac{d\hat{\rho}(t)}{dt} = \check{\mathcal{L}}_{H_S}[\hat{\rho}(t)] + \frac{1}{\hbar^2} \sum_i \gamma_i \check{\mathcal{L}}(\hat{L}_i)[\hat{\rho}(t)]. \quad (2.80)$$

The Lindblad master equation can be also derived if it is assumed that the bath correlation functions decay rapidly, so that

$$S_{jk}(\tau) = \gamma_{jk} \delta(\tau). \quad (2.81)$$

Using this approximation in Eq. (2.64) leads also to Eq. (2.80) [68].

The advantage of the Lindblad master equation over the Bloch-Redfield equation is that it preserves the positivity and trace of the density matrix, but the bath must be phenomenologically considered through the decay rates γ_i .

Matrix elements

Using the LS basis $\{|\alpha\beta\rangle\}$, constructed from the eigenstates $\{|\alpha\rangle\}$ of \hat{H}_S it can be shown that the Lindblad term in LS has the matrix elements

$$\mathcal{L}_{\alpha\beta,\theta\phi} = \langle\langle\alpha\beta|\hat{\mathcal{L}}|\theta\phi\rangle\rangle = L_{\alpha\theta}L_{\beta\phi}^* - (L^\dagger L)_{\alpha\theta}\delta_{\beta\phi} - (L^\dagger L)_{\phi\beta}\delta_{\theta\alpha}. \quad (2.82)$$

2.3. Incoherent processes for polariton systems

In the specific case of polariton systems described by parametric models such as the TC (see Sec. 1.3), incoherent processes can be considered through the Bloch-Redfield or Lindblad superoperators [121, 122, 26, 123]. Other techniques are studied in [124, 114, 125]. In the second part of this thesis we consider the processes described below.

2.3.1. Molecular relaxation due to vibrational bath

When a single molecule is described by a parametric Hamiltonian $\hbar\omega_e\sigma^\dagger\sigma$ (considering only two electronic levels), the coupling between the electronic transition and a set of k vibrational modes can be described by the interaction Hamiltonian

$$\hat{H}_{\text{int}} = \sigma^\dagger\sigma \otimes \sum_k \hbar\lambda_k(\hat{b}_k + \hat{b}_k^\dagger), \quad (2.83)$$

where \hat{b}_k (\hat{b}_k^\dagger) are the bosonic annihilation (creation) operators associated with each k vibrational mode. We want to treat these vibrational modes as a bath for the electronic transition within the framework of open quantum systems. By comparing with Eq. (2.54), we observe that there is only one system and one bath operator involved in the coupling, and they are of the form

$$\hat{Q} = \sigma^\dagger\sigma, \quad \hat{R} = \sum_k \hbar\lambda_k(\hat{b}_k + \hat{b}_k^\dagger). \quad (2.84)$$

³In the literature, it is common to define the correlation function of bath operators $S_{jk}(\omega)$ as $S_{jk}(\omega) = \frac{1}{\hbar^2} \int_0^\infty d\tau S_{jk}(\tau)e^{i\omega\tau}$, such that the factor $\frac{1}{\hbar^2}$ does not appear in the Lindblad master equation.

For this bath operator, the correlation function in the frequency domain (Eq. (2.59)) takes the form [68]

$$S(\omega) = \sum_k \hbar^2 \lambda^2 (n(\omega_k) \delta(\omega + \omega_k) + [1 + n(\omega_k)] \delta(\omega - \omega_k)), \quad (2.85)$$

where $n(\omega)$ is the Bose-Einstein distribution function at certain temperature T :

$$n(\omega) = \left[e^{\hbar\omega/k_B T} - 1 \right]^{-1}. \quad (2.86)$$

This result is obtained by considering the time correlation function $S(t)$ as the average over all vibrational modes in thermal equilibrium with an environment at temperature T . To include broadening for the vibrational modes, we generalize the bath noise-power spectrum function $S(\omega)$ in the form [95]

$$S(\omega) = \begin{cases} [1 + n(\omega)] J(\omega) & \omega \geq 0 \\ n(-\omega) J(-\omega) & \omega < 0, \end{cases} \quad (2.87)$$

with $J(\omega)$ being a broadening spectral density function. In fact, $J(\omega)$ is a compact way to write the discrete distribution $\sum_k \hbar^2 \lambda^2 \delta(\omega - \omega_k)$, but it can be approximated as being a continuous function if there is enough density of modes (and they are broadened by their interaction with the solvent or environment). Examples of $J(\omega)$ functions are plotted in Chap. 4. The vibrational bath for a single molecule can then be included as a Bloch-Redfield superoperator of the form (see Eq. (2.68))

$$\check{\mathcal{B}}(\hat{\sigma}^\dagger \hat{\sigma})[\hat{\rho}(t)] = -\frac{1}{\hbar^2} \sum_{\alpha\beta} (\hat{\sigma}^\dagger \hat{\sigma})_{\alpha\beta} \left[\hat{\sigma}^\dagger \hat{\sigma}, |\alpha\rangle \langle \beta| \hat{\rho}(t) \right] S(\omega_{\alpha\beta}) + \text{h.c.} \quad (2.88)$$

Remember that the indices α and β run over the eigenstates of the molecular electronic Hamiltonian. The matter dephasing operator $\hat{\sigma}^\dagger \hat{\sigma}$ is in this work introduced using the Bloch-Redfield, which is not equivalent to a Lindblad term with the same operator. The reasons for this are discussed in Sec. 4.2.

2.3.2. Cavity photon losses

Cavities, whether optical or plasmonic, exhibit photon excitations losses. They are characterized by the **cavity quality factor** \mathcal{Q} , defined as the ratio between the cavity mode frequency ω_c and its decay rate κ . Cavity lifetimes are typically on the order of 10 fs for Fabry-Perot cavities constructed with thin metallic mirrors. Distributed Bragg reflectors (DBRs) [126, 127], which consist of alternating layers of dielectric materials with different refractive indices, can be fabricated with relatively high reflectivity and low losses, resulting in quality factors on the order of $\mathcal{Q} = 1000$ and cavity mode lifetimes on the picosecond scale [1]. On the other hand, plasmonic nanocavity modes have shorter lifetimes, typically below 10 fs, due to the intrinsic losses present in metals [128].

Cavity losses can be included in the Liouvillian of the polaritonic system as a Lindblad term for the photon annihilation operator \hat{a} , with a decay rate κ (see Eq. (2.80)):

$$\kappa \check{\mathcal{L}}(\hat{a})[\hat{\rho}(t)] = \kappa \hat{a} \hat{\rho}(t) \hat{a}^\dagger - \frac{1}{2} \left\{ \hat{a}^\dagger \hat{a}, \hat{\rho}(t) \right\}. \quad (2.89)$$

2.3.3. Additional incoherent processes

Within the Lindblad formalism, other incoherent polaritonic processes could be included that we do not discuss in the second part of this thesis. Some examples are described below.

- The decay of electronic excitations, characterized by a Lindblad term for the operator $\hat{\sigma}$. This would account for other processes such as spontaneous emission, which occur on timescales much longer than the cavity (and hence the polaritons) lifetimes. For this reason, we do not include them in our calculations in the second part of this thesis.
- Incoherent pumping or electronic excitations, characterized by a Lindblad term for the operator $\hat{\sigma}^\dagger$. This could be the return of an excitation from the bath to the system as a result of its finite temperature, and is not included because it is negligible at room temperature (where $k_B T = 26$ meV) for typical electronic excitation energies of a few eV.
- Simultaneous processes of the cavity and the molecular emitters, characterized by Lindblad terms associated with operators like $\hat{a}\hat{\sigma}$, $\hat{a}\hat{\sigma}^\dagger$, $\hat{a}^\dagger\hat{\sigma}$, that represent processes not present in our systems.

3. Coherent Multidimensional Spectroscopy

Multidimensional spectroscopy [46, 49] is a widely used tool for the study of structure and dynamics of molecular systems in optical or infrared frequencies and femtosecond time resolution [129, 130, 131]. It is useful to understand physical-chemical processes such as charge transfer in donor-acceptor models [50], vibrational and electronic energy transfer, photoisomerization, and chemical reactions [51]. In particular, two-dimensional spectra (2DS) provide information about vibrational and electronic motions, interactions, and relaxation channels [132, 133, 134, 135]. Recently, multidimensional spectroscopy has been implemented in molecular-cavity systems to track the dynamics of vibrational and electronic polariton states [38, 41, 32, 136, 56, 33, 137, 54]. In a 2D spectroscopy experiment [47, 138, 77, 48], the system under study interacts with three delayed ultrashort classic pulses. The system response signal is proportional to the third-order nonlinear polarization. By varying the delay times between the three pulses, it is possible to construct 2D maps at different times, allowing the tracking of the fast processes involved in the dynamics of the system. Below, we describe the theoretical concepts necessary to explain in detail the construction and interpretation of 2DS.

3.1. General Optical Spectroscopy protocols

In a semiclassical approach, a general protocol in optical spectroscopy can be represented as the interaction of a quantum system (the system under study) with a classical transverse electric field [77]. This electric field could be generated from a pulsed or continuous laser or even a sequence of pulses. The signal emitted after the interaction allows for extracting information about the structure and dynamics of the system.

3.1.1. Parametric semiclassical interaction

Usually, the system under study is a material (atoms, dimmers, polyatomic molecules, clusters, etc.). However, in this work, our quantum system of interest is composed of matter emitters embedded in a cavity (either optical or plasmonic), meaning the system under study is (matter + cavity). When the system is only material, the property that couples to EM external classical field is the polarization [77, 48]. This can be seen for example in Eq. (1.10), where the polarization \hat{P} is related to the matter transition dipole $\hat{\mu}$ in the dipole approximation. Fig. 3.1 qualitatively illustrates this point. In this case, having a comprehensive understanding of the optical polarization is crucial for interpreting spectroscopic measurements in both the time and frequency domains. Electronic and nuclear motions, as well as relaxation processes, manifest in optical measurements through their impact on the polarization [77, 139, 140, 138]. On the other hand, if the system is composed by matter emitters + cavity, in recent spectroscopy experiments with such polariton systems, the external classical field only directly

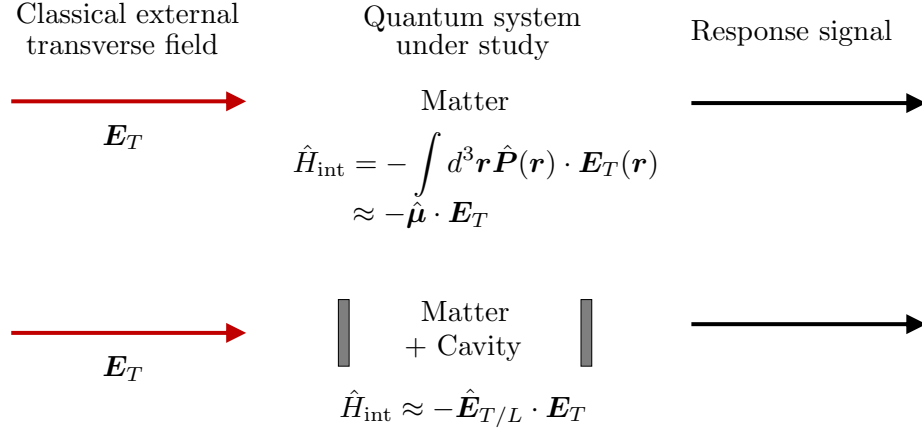


Fig. 3.1.: Schematic representation of an optical spectroscopy protocol, where an external transverse EM field (treated classically) interacts with a system under study (treated quantum mechanically) and a response signal is emitted. When the system under study is material (top panel), the property that couples to the external field is the material polarization $\hat{\mathbf{P}}$. In the dipole approximation, the interaction is mediated by the material transition dipole $\hat{\boldsymbol{\mu}}$. When the system under study is material + cavity (bottom panel), the classical external field $\hat{\mathbf{E}}_T$ couples with the quantum field confined in the cavity $\hat{\mathbf{E}}_T$ (for optical cavities) or $\hat{\mathbf{E}}_L$ (for plasmonic cavities).

interacts with the cavity [141]. In that case, the coupling can be understood as $\hat{H}_{\text{int}} \approx \hat{\mathbf{E}}_{T/L} \cdot \mathbf{E}_T$, where $\hat{\mathbf{E}}_T$ is the quantum operator of the transverse field (used if the cavity is optical) and $\hat{\mathbf{E}}_L$ is the operator of the longitudinal field (used if the cavity is plasmonic). Fig. 3.1 shows the differentiation between both matter and (matter + cavity) systems.

In Sec. 1.3 we discussed that the dipole operator $\hat{\boldsymbol{\mu}}$ can be expressed as proportional to the sum of the operators $\hat{\sigma} + \hat{\sigma}^\dagger$ (ladder fermionic operators) when the material system can be described as a two-level system. Similarly, it was discussed that in the single mode approximation, the electric field operator, whether transverse or longitudinal, can be written as proportional to the sum of the operators $\hat{a} + \hat{a}^\dagger$ (ladder bosonic operators). Then, parametrically, we can define a generalized transition “dipole” operator $\hat{\mathbf{V}}$ as

$$\hat{\mathbf{V}} = v(\hat{\mathbf{V}}^- + \hat{\mathbf{V}}^+)\mathbf{u}_V = v\hat{\mathbf{V}}\mathbf{u}_V, \quad (3.1)$$

with v a parametric constant representing the magnitude of transition dipole, $\hat{\mathbf{V}} = \hat{\mathbf{V}}^- + \hat{\mathbf{V}}^+$ (a dimensionless transition dipole operator) and \mathbf{u}_V an unitary vector in the direction of $\hat{\mathbf{V}}$. Of course, $\hat{\mathbf{V}}^-(\hat{\mathbf{V}}^+) = \hat{\sigma}(\hat{\sigma}^\dagger)$ for a matter system or $\hat{\mathbf{V}}^-(\hat{\mathbf{V}}^+) = \hat{a}(\hat{a}^\dagger)$ for matter + cavity system. In general, $\hat{\mathbf{V}}^-(\hat{\mathbf{V}}^+)$ produces deexcitations (excitations) in the respective system, either matter (of electronic nature) or matter + cavity (of photonic nature). In terms of this operator $\hat{\mathbf{V}}$ we can introduce a generalized “polarization” $\mathbf{P}(t)$ in the dipole approximation as

$$\mathbf{P}(t) \equiv \langle \hat{\mathbf{V}} \rangle = \text{Tr}[\hat{\mathbf{V}}\hat{\rho}(t)] = \langle \langle \mathbf{V} | \rho(t) \rangle \rangle. \quad (3.2)$$

Here we have used Eq. (2.28), with $\hat{\mathbf{V}}$ hermitian, to calculate the expected value as an inner product

in LS. The interaction between the system under study and the external EM field of the spectroscopic protocol is now, in the dipole approximation

$$\hat{H}_{\text{int}}(t) = -\hat{\mathbf{V}} \cdot \mathbf{E}(\mathbf{r}, t) = -v\hat{V}E(\mathbf{r}, t)(\mathbf{u}_V \cdot \mathbf{u}_E), \quad (3.3)$$

where \mathbf{u}_E is an unitary vector in the direction of the external electric field. In the case of a matter + cavity system, although the external electric field only directly couples with the cavity mode (acting as a pump), due to the coupling between the material emitters and the cavity, the spectroscopic protocol accounts for both systems (emitters and cavity) and their interaction. More specifically, the spectroscopy of the matter + cavity system (in the emitters-cavity strong coupling regime) allows to probe the polariton states formation and to track their dynamical processes including the relaxation mechanisms.

3.1.2. Weak field approach

Since the interaction of the system under study with the classical external field of the spectroscopic protocol is mediated by the generalized polarization¹, we can classify spectroscopic measurements in terms of this polarization. We begin by introducing the weak field approach, according to which we assume that the classical external fields are weak enough to allow for a perturbative expansion, order by order, of the response functions in terms of the fields. Such expansion is appropriate for experiments involving radiation fields that are not too strong, so that the expansion can be truncated at some low power of the field. This approximation is valid even for fields from powerful lasers since their intensities are often much weaker than the internal electric fields of the system under study.

In this perturbative approach the response of the system to the interaction with the classical external electric fields can be classified according to the power-law dependence on the field. Each component or n th order polarization (which in the optical response accompanies the n th power of the field) is denoted as $P^{(n)}$ and we can expand the total polarization to contributions from different orders

$$P = P^{(1)} + P^{(2)} + P^{(3)} + \dots \quad (3.4)$$

The components at each order of polarization can be directly computed using perturbation theory when the weak field limit is valid. This is the method we will describe in the following sections and the one we employ throughout this thesis. However, these components can also be computed using a more general method [142, 50], where each of them is extracted from the total polarization obtained from the full non-perturbative solution of the quantum dynamic equations. Both methods yield the same result in the weak-field limit, but the perturbative method proves to be much more efficient than the non-perturbative one.

Linear and nonlinear polarization

The linear optical response, which is present in processes such as absorption, emission, among others, dominates when the coupling to classical radiation is very weak. This linear response is described

¹From now on, we use the terms “polarization” and “generalized polarization” to refer to the generalized polarization.

by the first order polarization $P^{(1)}$. Any nonlinear process is governed by the nonlinear polarization $P_{\text{NL}} = P^{(2)} + P^{(3)} + \dots$

3.1.3. Multiwave mixing

The most common techniques involving nonlinear polarization are those related to multiwave mixing [77, 140, 143, 142]. An $(n + 1)$ -wave mixing process consists of the interaction of the system under study with n laser pulses with wave vectors $\mathbf{k}_1, \mathbf{k}_2, \dots, \mathbf{k}_n$ and frequencies $\omega_1, \omega_2, \dots, \omega_n$, respectively. A **coherent signal** can be detected if the mixed incoming wave vector satisfies one of the following relationships:

$$\mathbf{k} = \pm \mathbf{k}_1 \pm \mathbf{k}_2 \dots \pm \mathbf{k}_n, \quad (3.5)$$

with the corresponding frequency

$$\omega = \mp \omega_1 \mp \omega_2 \dots \mp \omega_n. \quad (3.6)$$

Phase matching condition

Each combination of signs in Eq. (3.5) and Eq. (3.6) represents a phase matching condition. The resulting wave vectors are the regions where coherent signals with appreciable intensity are observed. In the most general configuration, the system response signal \mathbf{k} does not necessarily coincide with any of the incident wave vectors. As a result, this signal does not present a significant background. This is an advantage of wave mixing techniques compared to other spectroscopy techniques.

Heterodyne detection

Despite the advantage of having low background in a wave mixing process, the nonlinear polarization and response signals are often weak. To increase sensitivity and the ratio between signal and noise, heterodyne detection is commonly used [144, 138]. In this configuration a new field denoted the local oscillator LO is added. This field E_{LO} has the same wave vector as the response signal E_{NL} and it is located in the receiver of the signal. After the nonlinear process is over, the superposition of the local oscillator field and the signal field is detected, i.e., $E_D = E_{LO} + E_{NL}$, such that $|E_D|^2 = |E_{LO}|^2 + 2\text{Re}(E_{LO}E_{NL}) + |E_{NL}|^2$. Usually the response signal is much weaker than the applied local oscillator field ($2\text{Re}(E_{LO}E_{NL}) \gg |E_{NL}|^2$ if $|E_{LO}| \gg |E_{NL}|$), and under this approximation the resulting heterodyne signal contains the information of the response, amplified by the intensity of the local oscillator (in fact it corresponds to an interference between both). Heterodyne signals are much stronger and easier to detect than pure response signals.

When the signal field is generated along the direction of one of the incoming beams, we have an intrinsic heterodyne detection. Examples are pump-probe, linear absorption, stimulated Raman, and the accumulated photon echo. Furthermore, the signal has the same frequency of the carrier wave and the local oscillator field is one of the incoming fields.

3.2. Perturbative computation of nonlinear polarization

To determine each order of polarization in the weak field approach, we must compute its perturbative expansion. We start with the interaction Hamiltonian between the classical EM field used in the spectroscopic protocol and the system under study. Under the dipolar approximation, and using a parametric model of the quantum system, this Hamiltonian is of the form in Eq. (3.3). In a standard nonlinear optical measurement, the electric field $E(\mathbf{r}, t)$ can be expressed as a combination of multiple incoming modes, whether they are pulsed or continuous. The different nonlinear optical spectroscopies vary based on the timing, detuning, and direction of these modes. Currently, we maintain a general description of the radiation field.

In general, both the electric field $\mathbf{E}(\mathbf{r}, t)$ and the dipole operator \hat{V} are vectors, and Eq. (3.3) involves their scalar product. Consequently, the optical response functions to be introduced below are high rank tensors. The vector nature becomes particularly significant for the optical response of anisotropic media, such as crystals or multilayers, or in polarization spectroscopy. For the sake of clarity, we avoid specifying the components of these vector quantities. With this consideration, the (time dependent) interaction Liouvillian between the system and the external electric field can be written using the Eq. (2.39) for the interaction Hamiltonian Eq. (3.3) as (in HS notation)

$$\check{\mathcal{L}}_{\text{int}}(t)[\hat{O}] = -\frac{i}{\hbar}[\hat{H}_{\text{int}}, \hat{O}] = -vE(\mathbf{r}, t)\check{\mathcal{V}}, \quad (3.7)$$

where we have introduced the generalized (dimensionless) dipole superoperator

$$\check{\mathcal{V}}[\hat{O}] \equiv -\frac{i}{\hbar}[\hat{V}, \hat{O}]. \quad (3.8)$$

To compute the optical generalized polarization, we begin at time $t = t_0$ and assume that the system is in the steady state with respect to its Liouvillian. As discussed in Subsec. 2.1.7, the (time independent) Liouvillian of the system can be written as

$$\hat{\mathcal{L}}_s = \hat{\mathcal{L}}_{H_0} + \hat{\mathcal{L}}_D, \quad (3.9)$$

where $\hat{\mathcal{L}}_{H_0}$ and $\hat{\mathcal{L}}_D$ stand for coherent and incoherent dynamics respectively. Typically, the steady state

$$|\rho(t_0)\rangle\rangle = |\rho(-\infty)\rangle\rangle \quad (3.10)$$

corresponds to the ground state of the system, due to the decay processes included in the term $\hat{\mathcal{L}}_D$.

3.2.1. Perturbative expansion of the density operator

Since the total Liouvillian of the spectroscopic protocol has the form (in LS)

$$\hat{\mathcal{L}}(t) = \hat{\mathcal{L}}_s + \hat{\mathcal{L}}_{\text{int}}(t), \quad (3.11)$$

which is completely analogous to Eq. (2.37), in the weak field approach we can make use of the perturbative expansion Eq. (2.38) for the temporal propagator in the LS. Using this expansion in

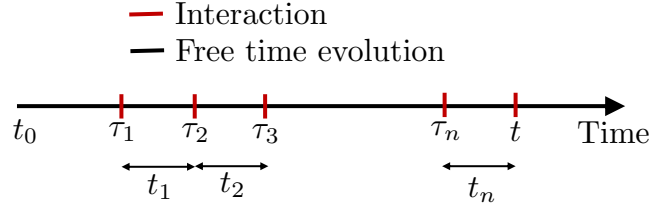


Fig. 3.2.: Schematic representation of times in the perturbative expansion of the density operator.

Eq. (2.35), we obtain

$$|\rho(t)\rangle\rangle = \sum_{n=0}^{\infty} \hat{\mathcal{U}}^{(n)}(t, t_0) |\rho(t_0)\rangle\rangle = \sum_{n=0}^{\infty} |\rho^{(n)}(t)\rangle\rangle, \quad (3.12)$$

with $\hat{\mathcal{U}}^{(0)}(t, t_0) = \hat{\mathcal{U}}_s(t, t_0)$ the propagator associated to the Liouvillian $\hat{\mathcal{L}}_s$ of the (time-independent) system under study, which is computed from Eq. (2.36). We can identify that $|\rho^{(n)}(t)\rangle\rangle \equiv \hat{\mathcal{U}}^{(n)}(t, t_0) |\rho(t_0)\rangle\rangle$ for $n > 0$ has the following form

$$|\rho^{(n)}(t)\rangle\rangle = \int_{t_0}^t d\tau_n \int_{t_0}^{\tau_n} d\tau_{n-1} \cdots \int_{t_0}^{\tau_2} d\tau_1 \quad (3.13)$$

$$\hat{\mathcal{U}}_s(t, \tau_n) \hat{\mathcal{L}}_{\text{int}}(\tau_n) \hat{\mathcal{U}}_s(\tau_n, \tau_{n-1}) \hat{\mathcal{L}}_{\text{int}}(\tau_{n-1}) \cdots \hat{\mathcal{U}}_s(\tau_2, \tau_1) \hat{\mathcal{L}}_{\text{int}}(\tau_1) \hat{\mathcal{U}}_s(\tau_1, t_0) |\rho(t_0)\rangle\rangle,$$

where τ_j , which satisfy the chronological ordering, $t \geq \tau_n \cdots \geq \tau_1 \geq t_0$, represent the actual times of the interactions.

Physical interpretation

The expansion in Eq. (3.13) can be interpreted as follows: At n th order the system interacts n times with the external electric field, at time τ_1, \dots, τ_n . The system first propagates freely from time t_0 to τ_1 , then interacts with the external field at time τ_1 , then propagates from time τ_1 to τ_2 , then interacts with the field at time τ_2 , and so forth, until the last interaction at τ_n , followed by a free propagation (see Fig. 3.2). The time arguments are chronologically ordered, but apart from this constraint, they can assume any value. The n fold integration runs over all possible intermediate times. Note that as we assume $|\rho(t_0)\rangle\rangle$ is the steady state of the system,

$$\hat{\mathcal{U}}_s(\tau_1, t_0) |\rho(t_0)\rangle\rangle = |\rho(\tau_1)\rangle\rangle = |\rho(t_0)\rangle\rangle. \quad (3.14)$$

By inserting Eq. (3.7) and Eq. (3.14) in Eq. (3.13), we obtain

$$|\rho^{(n)}(t)\rangle\rangle = (-v)^n \int_{t_0}^t d\tau_n \int_{t_0}^{\tau_n} d\tau_{n-1} \cdots \int_{t_0}^{\tau_2} d\tau_1 E(\mathbf{r}, \tau_n) E(\mathbf{r}, \tau_{n-1}) \cdots E(\mathbf{r}, \tau_1) \quad (3.15)$$

$$\hat{\mathcal{U}}_s(t, \tau_n) \hat{\mathcal{V}} \hat{\mathcal{U}}_s(\tau_n, \tau_{n-1}) \hat{\mathcal{V}} \cdots \hat{\mathcal{U}}_s(\tau_2, \tau_1) \hat{\mathcal{V}} |\rho(t_0)\rangle\rangle,$$

which is an expression in terms of the commutators $\hat{\mathcal{V}}$ for the interactions.

Green's function

To account for the temporal ordering, we introduce the Green's function of the system (in the absence of interaction) as

$$\hat{\mathcal{G}}_s(t - t_0) \equiv \Theta(t - t_0)\hat{\mathcal{U}}(t, t_0), \quad (3.16)$$

where $\Theta(t - t_0)$ is the Heaviside function ($\Theta(t - t_0) = 0$ if $t < t_0$ and $\Theta(t - t_0) = 1$ if $t > t_0$). The Green's function has a more physical meaning as it depends on the time evolution interval $t - t_0$ rather than specific times t and t_0 .

Now we change the time variables in expression Eq. (3.15) from absolute times $\tau_1, \tau_2, \dots, \tau_n$ to time intervals

$$t_1 \equiv \tau_2 - \tau_1, \quad t_2 \equiv \tau_3 - \tau_2, \quad \dots, \quad t_n \equiv t - \tau_n,$$

as shown in Fig. 3.2. In terms of the Green's function, using the time interval variables and by setting $t_0 \rightarrow -\infty$ we arrive at

$$\begin{aligned} |\rho^{(n)}(t)\rangle\rangle &= (-v)^n \int_0^\infty dt_n \int_0^\infty dt_{n-1} \cdots \int_0^\infty dt_1 \hat{\mathcal{G}}_s(t_n) \hat{\mathcal{V}} \hat{\mathcal{G}}_s(t_{n-1}) \hat{\mathcal{V}} \cdots \hat{\mathcal{G}}_s(t_1) \hat{\mathcal{V}} |\rho(t_0)\rangle\rangle \\ &\times E(\mathbf{r}, t - t_n) E(\mathbf{r}, t - t_n - t_{n-1}) E(\mathbf{r}, t - t_n - t_{n-1} \cdots - t_1). \end{aligned} \quad (3.17)$$

3.2.2. n-th order polarization and response function

The polarization in Eq. (3.2) can now be expanded (omitting its vector character) as

$$P(t) = \sum_n P^{(n)}(t) = v \sum_n \langle\langle V | \rho^{(n)}(t) \rangle\rangle, \quad (3.18)$$

with $P^{(n)}(t) = v \langle\langle V | \rho^{(n)}(t) \rangle\rangle$. From Eq. (3.17) we can identify, with its explicit position and time dependence, the n th order polarization ($n > 0$) due to the external field $E(\mathbf{r}, t)$ applied at different times

$$\begin{aligned} P^{(n)}(\mathbf{r}, t) &= (-1)^n v^{n+1} \int_0^\infty dt_n \int_0^\infty dt_{n-1} \cdots \int_0^\infty dt_1 \langle\langle V | \hat{\mathcal{G}}_s(t_n) \hat{\mathcal{V}} \hat{\mathcal{G}}_s(t_{n-1}) \hat{\mathcal{V}} \cdots \hat{\mathcal{G}}_s(t_1) \hat{\mathcal{V}} | \rho(t_0) \rangle\rangle \\ &\times E(\mathbf{r}, t - t_n) E(\mathbf{r}, t - t_n - t_{n-1}) E(\mathbf{r}, t - t_n - t_{n-1} \cdots - t_1). \end{aligned} \quad (3.19)$$

We assume that the polarization vanishes at thermal equilibrium or steady state, so that $P^{(0)} = 0$. Note that $P^{(n)}$ contains products of $n + 1$ dipole operator factors. As discussed in Subsec. 3.1.2, each order in this expansion represents a different class of optical measurements. The linear polarization $P^{(1)}$ is responsible for linear optics, $P^{(2)}$ represents second order nonlinear processes such as sum frequency generation, and $P^{(3)}$ is the third order polarization that enters in a broad variety of techniques including four wave mixing, pump-probe spectroscopy and the specific two-dimensional spectroscopy [49, 47] that we use in this work. In general, a response function contribution P^{2n} with even order [145], disappears in an isotropic medium due to symmetry.

Response function in the Schrödinger picture

The n th order polarization can be written in terms of the system n th order response function $S^{(n)}$, defined as follows [77, 135, 48]

$$S^{(n)}(t_n, t_{n-1}, \dots, t_1) \equiv (-1)^n v^{n+1} \langle \langle V | \hat{\mathcal{G}}_s(t_n) \hat{\mathcal{V}} \hat{\mathcal{G}}_s(t_{n-1}) \hat{\mathcal{V}} \cdots \hat{\mathcal{G}}_s(t_1) \hat{\mathcal{V}} | \rho(t_0) \rangle \rangle, \quad (3.20)$$

such that

$$P^{(n)}(\mathbf{r}, t) = \int_0^\infty dt_n \int_0^\infty dt_{n-1} \cdots \int_0^\infty dt_1 S^{(n)}(t_n, t_{n-1}, \dots, t_1) \times E(\mathbf{r}, t - t_n) E(\mathbf{r}, t - t_n - t_{n-1}) E(\mathbf{r}, t - t_n - t_{n-1} \cdots - t_1). \quad (3.21)$$

Note that the response function only depends on properties of the system, whereas in the polarization, the form of the external electric field at different times of interaction is already taken into account. In fact, the n th order response function needs to be convolved with the electric field at the respective times, to find the n th order polarization. Such convolution is different for each spectroscopy technique. The n th order response function carries the complete microscopic information necessary for the calculation of optical measurements. Note also that this function vanishes if any of its time arguments t_i become negative (by the Heaviside function incorporated in the Green's propagator). This reflects the principle of causality. Consequently, the lower time limit of integrals in Eq. (3.21) could be changed to $-\infty$.

Response function in the Interaction picture

We can introduce the representation in the interaction picture of the dipole operator both in the LS and in the HS, as follows

$$\hat{\mathcal{V}}_I(t) \equiv \hat{\mathcal{U}}_s^\dagger(t) \hat{\mathcal{V}} \hat{\mathcal{U}}_s(t), \quad \hat{V}_I(t) \equiv \hat{U}_s^\dagger(t) \hat{V} \hat{U}_s(t) \quad (3.22)$$

with $\hat{\mathcal{U}}_s(t) \equiv \hat{\mathcal{U}}_s(t, 0)$ and $\hat{U}_s(t) \equiv \hat{U}_s(t, 0)$ being the respective time propagator of the system in each Liouville and Hilbert spaces. We note that in HS

$$\check{\mathcal{V}}_I[\hat{O}] = -\frac{i}{\hbar} [\hat{V}_I(t), \hat{O}], \quad (3.23)$$

whereas in the LS representation

$$\hat{\mathcal{U}}_s^\dagger(t) |V\rangle = |V_I(t)\rangle. \quad (3.24)$$

With these definitions we can write the n th order response function in the interaction picture within the LS representation as follows

$$S^{(n)}(t_n, t_{n-1}, \dots, t_1) = (-1)^n v^{n+1} \Theta(t_n) \Theta(t_{n-1}) \cdots \Theta(t_1) \times \langle \langle V_I(t_n + \cdots + t_1) | \hat{\mathcal{V}}_I(t_{n-1} + \cdots + t_1) \cdots \hat{\mathcal{V}}_I(t_1) \hat{\mathcal{V}}_I(0) | \rho(t_0) \rangle \rangle. \quad (3.25)$$

3.3. Using time correlation functions

The nonlinear response function $S^{(n)}$ contains the Liouville space dipole operator to n th order. Since each represents a commutator in Hilbert space (see Eq. (3.8)), which can act either from the left or

from the right, $S^{(n)}$ contains 2^n terms once these commutators are evaluated. In practice only half of the 2^n terms are independent, and need to be considered. The contribution of the other half is simply the complex conjugate of the former. The overall sign of each term is determined by simply counting the number of times it acts from the right, since there is a (-) factor associated with each “right”. The resulting 2^n terms, are named in literature as Liouville space pathways.

3.3.1. Linear response function

For the specific case of the linear response function, in LS Schrödinger picture we have from Eq. (3.20),

$$S^{(1)}(t_1) = -v^2 \langle \langle V | \hat{\mathcal{G}}_s(t_1) \hat{\mathcal{V}} | \rho(t_0) \rangle \rangle, \quad (3.26)$$

and in the LS interaction picture, from Eq. (3.25),

$$S^{(1)}(t_1) = -v^2 \Theta(t_1) \langle \langle V_I(t_1) | \hat{\mathcal{V}}_I(0) | \rho(t_0) \rangle \rangle. \quad (3.27)$$

In HS, the last equation reads as (see Subsec. 2.1.4)

$$S^{(1)}(t_1) = -v^2 \Theta(t_1) \left(-\frac{i}{\hbar} \right) \text{Tr} \left[\hat{\mathcal{V}}_I(t_1) [\hat{\mathcal{V}}_I(0), \hat{\rho}(t_0)] \right],$$

where we have used the relations Eq. (2.27) and Eq. (3.23). Expanding the commutator and applying the cyclic permutation invariance of the trace, we can obtain

$$S^{(1)}(t_1) = \frac{i}{\hbar} v^2 \Theta(t_1) \text{Tr} \left[[\hat{\mathcal{V}}_I(t_1), \hat{\mathcal{V}}_I(0)] \hat{\rho}(t_0) \right],$$

and from Eq. (2.3) we can conclude that

$$S^{(1)}(t_1) = \frac{i}{\hbar} v^2 \Theta(t_1) \langle \langle \hat{\mathcal{V}}_I(t_1), \hat{\mathcal{V}}_I(0) \rangle \rangle, \quad (3.28)$$

taking into account that the expected value must be calculated in the steady state $\hat{\rho}(t_0)$, which usually is the ground state.

One-time correlation function

Finally we introduce the one-time correlation function $J_1(t_1)$ (in the time domain) for the interaction HS dipole operator as

$$J_1(t_1) \equiv \langle \hat{\mathcal{V}}_I(t_1) \hat{\mathcal{V}}_I(0) \rangle, \quad J_1^*(t_1) = \langle \hat{\mathcal{V}}_I(0) \hat{\mathcal{V}}_I(t_1) \rangle. \quad (3.29)$$

If we use Eq. (2.28), this correlation function can be computed in LS as

$$J_1(t_1) = \langle \langle V_I(t_1) V_I(0) | \rho_0 \rangle \rangle \quad (3.30)$$

The linear response function then reads

$$S^{(1)}(t_1) = \frac{i}{\hbar} v^2 \Theta(t_1) [J_1(t_1) - J_1^*(t_1)]. \quad (3.31)$$

The two terms appearing in Eq. (3.31) are the named Liouvillian space pathways.

3.3.2. Third-order response function

Of particular interest to us is the third-order response function [146, 147, 148, 149], which controls the 2D spectroscopy process we study in the second part of this thesis. Analogously to the procedure carried out for the linear response function, we can obtain the following two expressions for the third order $S^{(3)}$. In the Schrödinger picture within the LS representation

$$S^{(3)}(t_3, t_2, t_1) = -v^4 \langle \langle V | \hat{\mathcal{G}}_s(t_3) \hat{V} \hat{\mathcal{G}}_s(t_2) \hat{V} \hat{\mathcal{G}}_s(t_1) \hat{V} | \rho(t_0) \rangle \rangle. \quad (3.32)$$

Three-time correlation functions

On the other hand, in terms of three-time correlation functions $R_k(t_3, t_2, t_1)$,

$$S^{(3)}(t_3, t_2, t_1) = \left(\frac{i}{\hbar}\right)^3 v^4 \Theta(t_3) \Theta(t_2) \Theta(t_1) \sum_{k=1}^4 [R_k(t_3, t_2, t_1) - R_k^*(t_3, t_2, t_1)], \quad (3.33)$$

with (in the HS interaction picture)

$$\begin{aligned} R_1(t_3, t_2, t_1) &\equiv \langle \hat{V}_1(t_1 + t_2 + t_3) \hat{V}_1(t_1 + t_2) \hat{V}_1(t_1) \hat{V}_1(0) \rangle \\ R_2(t_3, t_2, t_1) &\equiv \langle \hat{V}_1(t_1) \hat{V}_1(t_1 + t_2) \hat{V}_1(t_1 + t_2 + t_3) \hat{V}_1(0) \rangle \\ R_3(t_3, t_2, t_1) &\equiv \langle \hat{V}_1(0) \hat{V}_1(t_1 + t_2) \hat{V}_1(t_1 + t_2 + t_3) \hat{V}_1(t_1) \rangle \\ R_4(t_3, t_2, t_1) &\equiv \langle \hat{V}_1(0) \hat{V}_1(t_1) \hat{V}_1(t_1 + t_2 + t_3) \hat{V}_1(t_1 + t_2) \rangle. \end{aligned} \quad (3.34)$$

Correlation functions provide a natural link between theory and experiment and they can be formally defined without alluding to a particular spectroscopy technique.

3.4. Additional approximations

Now that we have detailed the linear and third-order nonlinear response functions, we can specifically compute the polarization at these two orders. Remember from Eq. (3.21) that each n th order polarization is obtained from the convolution of the respective n th order response function with the external field.

3.4.1. Semi-impulsive limit

In a general experimental setup to measure the n th order polarization, the external electric field $E(\mathbf{r}, t)$ is usually generated with a different laser pulse E_j in each interaction time τ_j , i.e.,

$$E(\mathbf{r}, t - t_n - t_{n-1} \cdots - t_j) = E(\mathbf{r}, \tau_j) = E_j(\mathbf{r}, \tau_j). \quad (3.35)$$

In an ideal time-domain optical process, all the incident laser pulses are short compared to any time-scale of the system, but long compared to the oscillation period of the light field. In this case, we say that we are in the semi-impulsive limit, in which the envelopes of the pulses are approximated by Dirac δ functions

$$E_j(\mathbf{r}, t) = E_j \delta(t - \tau_j) \exp[\mp i \omega_j t \pm i \mathbf{k}_j \cdot \mathbf{r}], \quad (3.36)$$

with E_j , ω_j and \mathbf{k}_j are the field amplitude, frequency and wave vector respectively of pulse j th and the signs \pm depend on the phase matching condition chosen to detect the system response signal $\mathbf{k}_s = \pm \mathbf{k}_1 \pm \mathbf{k}_2 \cdots \pm \mathbf{k}_n$. Using the form of the field under this semi-impulsive limit in Eq. (3.21), we obtain

$$P^{(n)}(\mathbf{r}, t) = S^{(n)}(t_n, t_{n-1}, \dots, t_1) E_n E_{n-1} \cdots E_1 \times e^{\mp i\omega_n(t-t_n) \pm i\mathbf{k}_n \cdot \mathbf{r}} e^{\mp i\omega_{n-1}(t-t_n-t_{n-1}) \pm i\mathbf{k}_{n-1} \cdot \mathbf{r}} \dots e^{\mp i\omega_1(t-t_n \cdots -t_1) \pm i\mathbf{k}_1 \cdot \mathbf{r}}, \quad (3.37)$$

where $t_j \equiv \tau_{j+1} - \tau_j$, $j = 1, \dots, n-1$, and $t_n \equiv t - \tau_n$. The nonlinear polarization is in this case directly proportional to the nonlinear response function, with the time arguments being the delays between successive pulses. In the semi-impulsive limit, the $n+1$ -wave mixing signal is proportional to [77]

$$I_s \sim \left| S^{(n)}(t_n, t_{n-1}, \dots, t_1) \right|^2. \quad (3.38)$$

Heterodyne detection

When heterodyne detection is used, if the additional pulse (local oscillator) also satisfies the semi-impulse limit, the detected signal is proportional to [77, 140]

$$I_s \sim S^{(n)}(t_n, t_{n-1}, \dots, t_1). \quad (3.39)$$

Thus, under this approximation, we are directly measuring the n -order response of the system. Times t_1, \dots, t_n are the delay times between the $n+1$ laser pulses (the last one is the local oscillator) that are directly controlled by the experiment. In addition, the phase of the emitted polarization is also measured.

3.4.2. Rotating wave approximation

By inserting Eq. (3.20) into Eq. (3.37), we arrive at the expression

$$P^{(n)}(\mathbf{r}, t) = (-1)^n v^{n+1} \langle \langle V | \hat{\mathcal{G}}_s(t_n) \hat{\mathcal{V}} \hat{\mathcal{G}}_s(t_{n-1}) \hat{\mathcal{V}} \cdots \hat{\mathcal{G}}_s(t_1) \hat{\mathcal{V}} | \rho(t_0) \rangle \rangle E_n E_{n-1} \cdots E_1 \times e^{\mp i\omega_n(t-t_n) \pm i\mathbf{k}_n \cdot \mathbf{r}} e^{\mp i\omega_{n-1}(t-t_n-t_{n-1}) \pm i\mathbf{k}_{n-1} \cdot \mathbf{r}} \dots e^{\mp i\omega_1(t-t_n \cdots -t_1) \pm i\mathbf{k}_1 \cdot \mathbf{r}}.$$

Note that at each time τ_j where the j th pulse interacts with the system, the LS dipole operator $\hat{\mathcal{V}}$ appearing in $S^{(n)}$ must be multiplied by the respective field factor $E_j e^{\mp i\omega_j(t-t_n \cdots -t_j) \pm i\mathbf{k}_j \cdot \mathbf{r}}$ in the expression for $P^{(n)}$. Remember from our definition of the dimensionless dipole operator in Eq. (3.1) implies that $\hat{\mathcal{V}} = \hat{\mathcal{V}}^- + \hat{\mathcal{V}}^+$ can be written in terms of deexcitation ($\hat{\mathcal{V}}^-$) and excitation ($\hat{\mathcal{V}}^+$) operators. Consequently, the j th field-system interaction can be written as

$$\begin{aligned} (\hat{\mathcal{V}}^- + \hat{\mathcal{V}}^+) &\times E_j e^{\mp i\omega_j(t-t_n \cdots -t_j) \pm i\mathbf{k}_j \cdot \mathbf{r}} \\ &\approx \hat{\mathcal{V}}^\pm \times E_j e^{\mp i\omega_j(t-t_n \cdots -t_j) \pm i\mathbf{k}_j \cdot \mathbf{r}}. \end{aligned} \quad (3.40)$$

The last line in the above equation corresponds to the rotating wave approximation (RWA). We select only resonant terms in $S^{(n)}$ where the optical frequency is essentially cancelled by a system frequency of opposite sign, and neglect terms that oscillate at faster optical frequencies. Depending on the choice of

k_s , and the particular spectroscopic technique, we should therefore use in Eq. (3.33) only the few terms in $S^{(n)}$ that survive under the RWA. This, of course, simplifies the calculation and the interpretation of time domain measurements since they require fewer contributions. Within the RWA, reorganizing the exponential factors we obtain for the n th order polarization

$$P^{(n)}(\mathbf{r}, t) = (-1)^n v^{n+1} \langle \langle V^+ | \hat{\mathcal{G}}_s(t_n) \hat{V}^\pm \hat{\mathcal{G}}_s(t_{n-1}) \hat{V}^\pm \dots \hat{\mathcal{G}}_s(t_1) \hat{V}^\pm | \rho(t_0) \rangle \rangle E_n E_{n-1} \dots E_1 \\ \times \exp[i(\mp \omega_1 \mp \omega_2 \dots \mp \omega_n)t] \dots \exp[i(\mp \omega_1 \mp \omega_2)t_2] \exp[i(\mp \omega_1)t_1] \exp[i\mathbf{k}_s \cdot \mathbf{r}].$$

Note that now the inner product is performed with $\langle \langle V^+ |$ instead of $\langle \langle V |$. This corresponds to the expectation value of \hat{V}^- . With this restriction we ensure that interaction of the emitted signal with the local oscillator detection pulse must be one of deexcitation. It is useful for the computation of absorption spectra, where we require that both signals interfere destructively on the detector. As a result, the amount of light that the detector collects is less than without the system, which is consistent with the light being absorbed by the system. On the other hand, for emission spectra we need to calculate the expectation value of \hat{V}^+ as we do it in Subsec. 3.5.2.

If the polarization is measured at $\mathbf{r} = \mathbf{k}_s$, for a given phase matching condition (PM), we finally obtain

$$P_{[\text{PM}]}^{(n)}(t) = S_{[\text{PM}]}^{(n)}(t_n, t_{n-1} \dots t_1) E_n E_{n-1} \dots E_1 \exp[i\omega_s t] \\ \times \exp[i(\mp \omega_1 \mp \omega_2 \dots \mp \omega_{n-1})t_{n-1}] \dots \exp[i(\mp \omega_1 \mp \omega_2)t_2] \exp[i(\mp \omega_1)t_1], \quad (3.41)$$

where the nonlinear response function is defined as

$$S_{[\text{PM}]}^{(n)}(t_n, t_{n-1} \dots t_1) \equiv (-1)^n v^{n+1} \langle \langle V^+ | \hat{\mathcal{G}}_s(t_n) \hat{V}^\pm \hat{\mathcal{G}}_s(t_{n-1}) \hat{V}^\pm \dots \hat{\mathcal{G}}_s(t_1) \hat{V}^\pm | \rho(t_0) \rangle \rangle, \quad (3.42)$$

inherits the respective \pm signs of the pulse wave vectors for the selected PM, and they oppose the respective signs of ω_j ; and ω_s is the frequency of the response signal as in Eq. (3.6).

3.5. Linear spectra

A linear optical spectroscopy process can be understood as a 2-wave mixing process, where the system interacts with a laser pulse of wave vector \mathbf{k}_1 . To satisfy a PM condition, the wave vector of the system response signal \mathbf{k}_s is taken as $\mathbf{k}_s = \mathbf{k}_1$. In this case, for absorption, the direction of the emitted signal coincides with the wave vector of the input pulse, thus leading to intrinsic heterodyne detection (or homodyne detection), where the incident pulse itself acts as the local oscillator (see Fig. 3.3).

Within the semi-impulsive limit, the detected signal is proportional to $S^{(1)}(t)$ as Eq. (3.39) shows (here we change the notation used in last section and we set $t \equiv t_1$). Under the RWA, Eq. (3.28) now takes the form

$$S_{[+]}^{(1)}(t) = \frac{i}{\hbar} v^2 \Theta(t) \langle [\hat{V}_I^-(t), \hat{V}_I^+(0)] \rangle, \\ = \frac{i}{\hbar} v^2 \Theta(t) \left(\langle \hat{V}_I^-(t) \hat{V}_I^+(0) \rangle - \langle \hat{V}_I^+(0) \hat{V}_I^-(t) \rangle \right) \\ = \frac{i}{\hbar} v^2 \Theta(t) \langle \hat{V}_I^-(t) \hat{V}_I^+(0) \rangle. \quad (3.43)$$

The subscript $[+]$ is the PM condition. Note that $\langle \hat{V}_I^+(0) \hat{V}_I^-(t) \rangle = 0$ for the expected value calculated at the equilibrium state of the system, particularly when this state corresponds to the ground state $|g\rangle$, since $\hat{V}^- |g\rangle = 0$.

3.5.1. Linear absorption

The respective linear response function can be calculated in the frequency domain by performing a Fourier transform as follows [150]

$$S_{[+]}^{(1)}(\omega) = \frac{i}{\hbar} v^2 \int_0^\infty dt \langle \hat{V}_I^-(t) \hat{V}_I^+(0) \rangle e^{i\omega t} \quad (3.44)$$

When the signal emitted by the system and the incident field are collected (see Fig. 3.3), the detector records an intensity that contains an interference term between them. This term accounts for the absorption spectrum of the system and it is proportional to the linear response. The linear absorption spectrum can be calculated as

$$\begin{aligned} S_A^{(1)}(\omega) &= 2\mathcal{R} \left\{ -i S_{[+]}^{(1)}(\omega) \right\} \\ &= \frac{v^2}{\hbar} 2\mathcal{R} \left\{ \int_0^\infty dt \langle \hat{V}_I^-(t) \hat{V}_I^+(0) \rangle e^{i\omega t} \right\}. \end{aligned} \quad (3.45)$$

We use this expression to compute the linear absorption spectrum of polariton systems in the second part of this thesis, with $\hat{V}^- = \hat{a}$ and $\hat{V}^+ = \hat{a}^\dagger$, the ladder operators of the quantum radiation field confined in a cavity. As an example, the linear absorption spectrum for an anharmonic oscillator is presented later in Fig. 3.4.

3.5.2. Linear emission

The measure of the linear emission spectrum [150] of the system involves keeping the system interacting with a continuous-wave laser of frequency ω_L . Under the RWA and the dipole approximation, the new system + pumping laser Hamiltonian is given by

$$\hat{H}(t) = \hat{H}_0 + \hbar\Omega_0 v (\hat{V}^- e^{i\omega_L t} + V^+ e^{-i\omega_L t}), \quad (3.46)$$

with Ω_0 a parametric coupling constant. In this context, the continuous-wave pumping laser is not treated within the perturbation theory; its interaction is directly included in the Hamiltonian and this composed system is the new “system under study”.

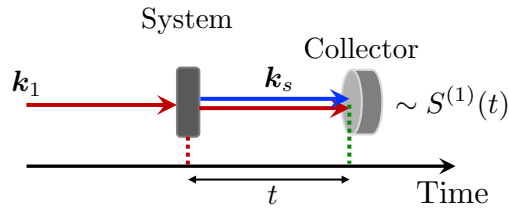


Fig. 3.3.: Schematic representation of a linear optical spectroscopy protocol for absorption. Under the semi-impulsive limit the signal collected in the detector is proportional to the linear response function.

Rotating frame

To obtain a time independent Hamiltonian, we can perform a transformation to a rotating frame by using the unitary operator

$$\hat{U}(t) = \exp\left[-\frac{i}{\hbar}\hat{O}t\right], \quad (3.47)$$

where \hat{O} is an arbitrary time independent operator. The density operator transforms as $\hat{\rho}(t) = \hat{U}^\dagger(t)\hat{\rho}(t)\hat{U}(t)$. We define the rotating frame Hamiltonian \hat{H}_{RF} such that the Liouville-von Neumann equation

$$\frac{d\hat{\rho}(t)}{dt} = -\frac{i}{\hbar}[\hat{H}_{RF}, \hat{\rho}(t)] \quad (3.48)$$

is satisfied. It can be shown [68] that

$$\hat{H}_{RF} = \hat{U}^\dagger(t)\hat{H}(t)\hat{U}(t) - \hat{O}. \quad (3.49)$$

For an appropriate choice of the operator \hat{O} , it is possible to obtain a rotating frame Hamiltonian independent of time. For example, in the case of a polariton system composed of a two-level molecule interacting with a cavity, where $\hat{H}_0 = \hat{H}_{JC}$ (see Chap. 1) and $\hat{V}^- (\hat{V}^+) = a(a^\dagger)$, the operator

$$\hat{O} = \hbar\omega_L(\hat{a}^\dagger\hat{a} + \hat{\sigma}^\dagger\hat{\sigma}) \quad (3.50)$$

makes \hat{H}_{RF} time independent. Now it takes the form

$$\hat{H}_{RF} = \hat{H}_{JC} - \hat{O} + \hbar\omega_0(\hat{a} + \hat{a}^\dagger). \quad (3.51)$$

This transformation is used in the second part of this thesis to compute the linear emission of the open JC model. In the rotating frame, we can calculate the steady state of the new system, which is no longer the ground state as is usual in experimental protocols for absorption spectrum, but rather some excited state resonant with the frequency ω_L of the pumping laser.

Linear emission spectrum

For emission processes, the expected value taken at the final time of the computation of $S^{(n)}$ is not that of \hat{V}^- (as in the case of absorption spectra) but that of \hat{V}^+ . Now, the relevant PM condition in the calculation corresponds to $\mathbf{k}_s = -\mathbf{k}_1$. Under the RWA, Eq. (3.28) becomes

$$\begin{aligned} S_{[-]}^{(1)}(t) &= \frac{i}{\hbar}v^2\Theta(t)\langle[\hat{V}_I^+(t), \hat{V}_I^-(0)]\rangle, \\ &= \frac{i}{\hbar}v^2\Theta(t)\left(\langle\hat{V}_I^+(t)\hat{V}_I^-(0)\rangle - \langle\hat{V}_I^-(0)\hat{V}_I^+(t)\rangle\right) \\ &= \frac{i}{\hbar}v^2\Theta(t)\langle\hat{V}_I^+(t)\hat{V}_I^-(0)\rangle. \end{aligned} \quad (3.52)$$

Note that $\langle\hat{V}_I^-(0)\hat{V}_I^+(t)\rangle$ corresponds to a second order process for the expectation value calculated in an excited state $|e\rangle$ of the system, since $\hat{V}^+|e\rangle$ leads to a two-excitation state. Now in the frequency domain

$$S_{[-]}^{(1)}(\omega) = \frac{i}{\hbar}v^2 \int_0^\infty dt \left[\langle\hat{V}_I^+(t)\hat{V}_I^-(0)\rangle - \lim_{t\rightarrow\infty} \langle\hat{V}_I^+(t)\hat{V}_I^-(0)\rangle \right] e^{-i\omega t}, \quad (3.53)$$

where we have extracted the constant asymptotic value of the correlation function at infinite time. This corresponds to Rayleigh scattering, i.e., coherent oscillation at the frequency of the driving laser. The sign of the exponential in the Fourier transform inherits the sign of the PM condition to ensure that the spectrum can be observed at positive frequencies. We can finally define the linear emission spectrum as

$$\begin{aligned} S_E^{(1)}(\omega; \omega_L) &= 2\mathcal{R} \left\{ -iS_{[-]}^{(1)}(\omega) \right\} \\ &= \frac{v^2}{\hbar} 2\mathcal{R} \left\{ \int_0^\infty dt \left[\langle \hat{V}_I^+(t) \hat{V}_I^-(0) \rangle - \lim_{t \rightarrow \infty} \langle \hat{V}_I^+(t) \hat{V}_I^-(0) \rangle \right] e^{-i\omega t} \right\}. \end{aligned} \quad (3.54)$$

3.5.3. Double-sided Feynman diagrams

The time correlation functions appearing in the linear and nonlinear response functions of the system can be represented as double-sided Feynman diagrams [77, 140, 138, 55]. These diagrams are introduced by the following rules:

- The density operator is represented by two vertical lines. The line on the left represents the ket and the line on the right represents the bra.
- Time is running from the bottom to the top.
- An interaction with the radiation field is represented by a red solid arrow. An arrow pointing to the right represents a contribution of $E_j \exp[-i\omega_j \tau_j + i\mathbf{k}_j \cdot \mathbf{r}]$ to the polarization. In the RWA this means an interaction with \hat{V}^+ . An arrow pointing to the left represents a contribution of $E_j \exp[i\omega_j \tau_j - i\mathbf{k}_j \cdot \mathbf{r}]$ or an interaction with \hat{V}^- .
- In the RWA, an arrow pointing into the diagram indicates an excitation on the respective side it acts upon. An arrow pointing out of the diagram indicates a deexcitation of the respective side it acts upon. For absorption processes, the last (black dashed) arrow, representing the interaction with the local oscillator pulse, must act from the left and induce a deexcitation. For the diagram to have a non-zero contribution, the final state must be of population ($|\alpha\rangle\langle\alpha|$).
- Each diagram has an overall sign of $(-1)^n$, where n is the number of interactions from the right (bra). This is because each time an interaction \hat{V}^\pm acts from the right in a commutator, it carries a minus sign.

As an example, let us consider the case of an anharmonic oscillator whose energy² scheme is depicted in the left panel of Fig. 3.4. Under RWA, for absorption process, only one time correlation function $\langle \hat{V}_I^-(t) \hat{V}_I^+(0) \rangle$ appears in the linear response in Eq. (3.43). This correlation function is represented in the Feynman diagram of Fig. 3.4 and the respective normalized linear absorption spectrum, calculated with Eq. (3.45) is shown in the right panel of the figure. In this case, we have taken the system ground state as the initial state for the spectroscopic absorption process. We use $\hat{V}^- = |0\rangle\langle 1| + \sqrt{2}|1\rangle\langle 2|$ and $\hat{V}^+ = (\hat{V}^-)^\dagger$. A dissipative Lindblad term $\check{\mathcal{L}}_D = \kappa \check{\mathcal{L}}(\hat{V}^-)$ is included in the system Liouvillian.

²Throughout this thesis, especially in some figures, we may refer to energies or frequencies interchangeably. When this happens, we should understand that the energy associated with a frequency ω is $\hbar\omega$.

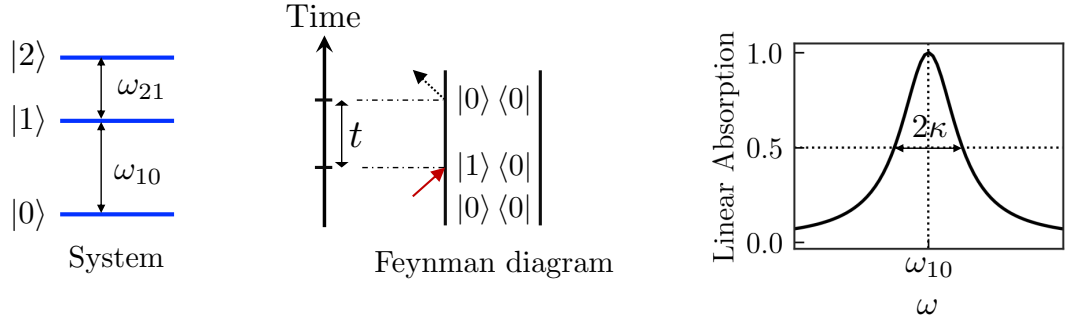


Fig. 3.4.: Left panel: Energy scheme of a system represented as an anharmonic oscillator. Middle panel: Double-sided Feynman diagram associated to the linear response function of the system. Right panel: Normalized linear absorption spectrum of the system, calculated with Eq. (3.45) with $\hat{V}^- = |0\rangle\langle 1| + \sqrt{2}|1\rangle\langle 2|$ and $\hat{V}^+ = (\hat{V}^-)^\dagger$. A dissipative Lindblad term for the operator \hat{V}^- is included in the Liouvillian, with decay rate κ , which has its fingerprint in the spectral width.

Clearly, from the ground state, we can only probe one-excitation states using linear spectroscopy. The absorption spectrum in our example is maximum at the transition frequency $\omega_{10} \equiv \omega_1 - \omega_0$ between the oscillator ground state $|0\rangle$ and the first excited state $|1\rangle$. The full width at half maximum of the spectrum accounts for the decay rate $|1\rangle \xrightarrow{t} |0\rangle$ occurring during the system temporal evolution at time t . In our example, it corresponds to a rate of 2κ .

3.6. 2D coherent spectroscopy

The 2D spectroscopy process implemented for the study of polariton systems in the second part of this thesis (see also [42, 52]), requires the computation of third-order nonlinear response function under the RWA and semi-impulsive limit. In this section, we outline the experimental protocol for measuring this response function and discuss the physical processes that can be studied using this 2D spectroscopic technique.

3.6.1. Experimental 2D spectroscopy protocol

As discussed in previous sections, the experimental protocol for measuring the third-order nonlinear response function requires the interaction of the system with three delayed laser pulses and an additional local oscillator pulse for heterodyne detection, leading to a four-wave mixing process. This protocol is illustrated in Fig. 3.5. We change the notation used in last sections and set $\tau \equiv t_1$ (excitation time), $T \equiv t_2$ (waiting time) and $t \equiv t_3$ (detection time). These names for the temporal delay between successive pulses are discussed in Subsec. 3.6.2. Under the semi-impulsive limit, the heterodyned signal is proportional to the third-order non linear response of the system $S^{(3)}(\tau, T, t)$. We are particularly interested in two PM conditions that are named [140]

$$\begin{aligned} \text{Non Rephasing (NR)} \quad \mathbf{k}_s &= +\mathbf{k}_1 - \mathbf{k}_2 + \mathbf{k}_3, \quad \text{and} \\ \text{Rephasing (R)} \quad \mathbf{k}_s &= -\mathbf{k}_1 + \mathbf{k}_2 + \mathbf{k}_3. \end{aligned} \tag{3.55}$$

For the computation of $S^{(3)}(\tau, T, t)$ in both PM conditions under RWA, we prefer Eq. (3.42), which is written in the Liouville space (LS), from which we obtain (note that the PM signs for NR and R are carried by the interaction operator \hat{V}^\pm)

$$S_{[\text{NR(R)}]}^{(3)}(\tau, T, t) = -v^4 \langle \langle V^+ | \hat{\mathcal{G}}_s(t) \hat{V}^+ \hat{\mathcal{G}}_s(T) \hat{V}^\mp \hat{\mathcal{G}}_s(\tau) \hat{V}^\pm | \rho(t_0) \rangle \rangle. \quad (3.56)$$

3.6.2. Feynman diagrams contributing to non rephasing and rephasing

It is convenient to write the expression resulting in the interaction picture in Hilbert space (HS) to analyze the double-sided Feynman diagrams that contribute to both NR and R PM conditions. In Eq. (3.34), we find the total three-time correlation functions R_k that contribute to $S^{(3)}(\tau, T, t)$ (their complex conjugate are also relevant as shown in Eq. (3.33)). Within the semi-impulsive limit, each interaction \hat{V} comes from a single pulse used in the spectroscopic protocol. Thus, to simplify the notation, we denote

$$\begin{aligned} \hat{V}_1(0) &\equiv \hat{V}_1 \\ \hat{V}_1(t_1) &\equiv \hat{V}_1(\tau) \equiv \hat{V}_2 \\ \hat{V}_1(t_1 + t_2) &\equiv \hat{V}_1(\tau + T) \equiv \hat{V}_3 \\ \hat{V}_1(t_1 + t_2 + t_3) &\equiv \hat{V}_1(\tau + T + t) \equiv \hat{V}_{\text{LO}}, \end{aligned} \quad (3.57)$$

where each number label represents the respective pulse (ordered by their respective time interaction) and the last \hat{V}_{LO} represents the interaction with the local oscillator pulse for heterodyne detection (see Fig. 3.5). Before constructing the Feynman diagrams associated with each correlation function R_k , we

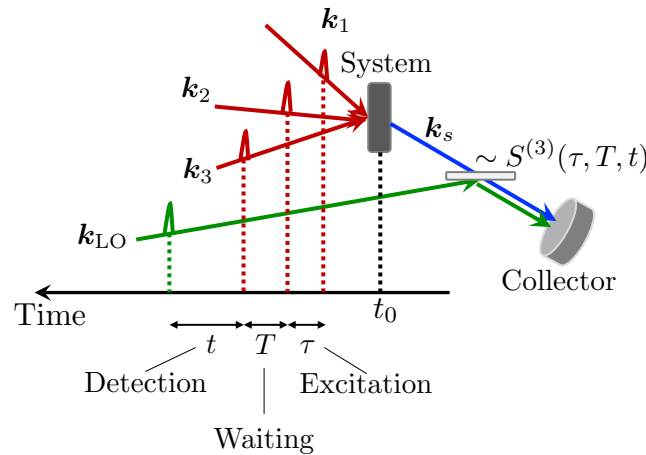


Fig. 3.5.: Schematic representation of a nonlinear third-order (four-wave mixing) optical spectroscopy protocol with heterodyne detection. Under the semi-impulsive limit, the combined emitted and local oscillator signals collected in the detector is proportional to the third-order nonlinear response of the system.

can rewrite these functions as follows

$$\begin{aligned}
R_1 &= \langle \hat{V}_{\text{LO}} \hat{V}_3 \hat{V}_2 \hat{V}_1 \rangle = \text{Tr} \left[\hat{V}_{\text{LO}} \hat{V}_3 \hat{V}_2 \hat{V}_1 \hat{\rho}(0) \right], & R_1^* &= \langle \hat{V}_1 \hat{V}_2 \hat{V}_3 \hat{V}_{\text{LO}} \rangle = \text{Tr} \left[\hat{V}_{\text{LO}} \hat{\rho}(0) \hat{V}_1 \hat{V}_2 \hat{V}_3 \right] \\
R_2 &= \langle \hat{V}_2 \hat{V}_3 \hat{V}_{\text{LO}} \hat{V}_1 \rangle = \text{Tr} \left[\hat{V}_{\text{LO}} \hat{V}_1 \hat{\rho}(0) \hat{V}_2 \hat{V}_3 \right], & R_2^* &= \langle \hat{V}_1 \hat{V}_{\text{LO}} \hat{V}_3 \hat{V}_2 \rangle = \text{Tr} \left[\hat{V}_{\text{LO}} \hat{V}_3 \hat{V}_2 \hat{\rho}(0) \hat{V}_1 \right] \\
R_3 &= \langle \hat{V}_1 \hat{V}_3 \hat{V}_{\text{LO}} \hat{V}_2 \rangle = \text{Tr} \left[\hat{V}_{\text{LO}} \hat{V}_2 \hat{\rho}(0) \hat{V}_1 \hat{V}_3 \right], & R_3^* &= \langle \hat{V}_2 \hat{V}_{\text{LO}} \hat{V}_3 \hat{V}_1 \rangle = \text{Tr} \left[\hat{V}_{\text{LO}} \hat{V}_3 \hat{V}_1 \hat{\rho}(0) \hat{V}_2 \right] \\
R_4 &= \langle \hat{V}_1 \hat{V}_2 \hat{V}_{\text{LO}} \hat{V}_3 \rangle = \text{Tr} \left[\hat{V}_{\text{LO}} \hat{V}_3 \hat{\rho}(0) \hat{V}_1 \hat{V}_2 \right], & R_4^* &= \langle \hat{V}_3 \hat{V}_{\text{LO}} \hat{V}_2 \hat{V}_1 \rangle = \text{Tr} \left[\hat{V}_{\text{LO}} \hat{V}_2 \hat{V}_1 \hat{\rho}(0) \hat{V}_3 \right]
\end{aligned} \tag{3.58}$$

Now it is easy to identify whether each interaction acts on the right side or the left side of the density operator in each respective correlation function. For the NR PM condition, where we choose the positive wave vector $+\mathbf{k}_1$ for the first pulse, within the RWA we know that this corresponds to an interaction with \hat{V}_1^+ . Note that if $\rho(0)$ corresponds to the ground state of the system, $\hat{V}_1^+ \rho(0)$ produces an excitation on the left side (ket) of the density operator (as discussed in the rules for constructing double-sided Feynman diagrams in [Subsec. 3.5.3](#)). However, $\hat{\rho}(0) \hat{V}_1^+ = 0$ since the interaction acts from the right side of the density operator, then \hat{V}_1^+ produces a deexcitation on the right side (bra), which cancels out when applied to the ground state. For this reason, the contributions R_k or R_k^* that contain $\rho(0) \hat{V}_1^+$ (with the first interaction acting from the right) are null in the NR PM. The same reasoning applies for the R PM condition, where the contributions that cancel out in this case are those containing $\hat{V}_1 \rho(0)$ (the first interaction acting from the left), since for the R PM, the first pulse goes with the negative wave vector, $-\mathbf{k}_1$, corresponding to an interaction with \hat{V}_1^- . On the other hand, for the NR PM condition, the contribution $R_{4[\text{NR}]}$ vanishes because after the interaction with the first two pulses (acting from the left), the third pulse, representing an interaction with \hat{V}^+ , acts from the right (bra) of the ground state, i.e., $\langle g | \hat{V}^+$, resulting in zero, as we have already mentioned. Similarly, for the R PM condition, the contribution $R_{1[\text{R}]}$ vanishes because it represents the excitation of the ground state bra (with the first pulse), followed by the deexcitation (with the second pulse), bringing it back to $\langle g |$, and followed by the action of the third pulse on the right $\langle g | \hat{V}^+ = 0$. The explicit nonzero contributions to each NR and R PM conditions are shown below within the RWA

$$\begin{aligned}
R_{1[\text{NR}]} &= \text{Tr} \left[\hat{V}_{\text{LO}}^- \hat{V}_3^+ \hat{V}_2^- \hat{V}_1^+ \hat{\rho}(0) \right] & R_{4[\text{R}]} &= \text{Tr} \left[\hat{V}_{\text{LO}}^- \hat{V}_3^+ \hat{\rho}(0) \hat{V}_1^- \hat{V}_2^+ \right] \\
R_{2[\text{NR}]} &= \text{Tr} \left[\hat{V}_{\text{LO}}^- \hat{V}_1^+ \hat{\rho}(0) \hat{V}_2^- \hat{V}_3^+ \right] & R_{3[\text{R}]} &= \text{Tr} \left[\hat{V}_{\text{LO}}^- \hat{V}_2^+ \hat{\rho}(0) \hat{V}_1^- \hat{V}_3^+ \right] \\
R_{3[\text{NR}]}^* &= \text{Tr} \left[\hat{V}_{\text{LO}}^- \hat{V}_3^+ \hat{V}_1^+ \hat{\rho}(0) \hat{V}_2^- \right] & R_{2[\text{R}]}^* &= \text{Tr} \left[\hat{V}_{\text{LO}}^- \hat{V}_3^+ \hat{V}_2^+ \hat{\rho}(0) \hat{V}_1^- \right]
\end{aligned} \tag{3.59}$$

Here we recall that each interaction \hat{V}_j appearing in the correlation functions in [Eq. \(3.59\)](#) actually represents the generalized dipole operator in the interaction picture in HS, and they are propagated at different time intervals, as indicated by [Eq. \(3.57\)](#). These temporal propagations are reflected in the respective double-sided Feynman diagrams shown in [Fig. 3.6](#) for both NR and R PM conditions using the anharmonic oscillator of [Fig. 3.4](#) and with the ground state as initial state at $t_0 = 0$.

Depending on the incoherent processes involved in the dynamic evolution of the system, it is possible that new states emerge in these Feynman diagrams during the τ , T , and t temporal evolution. This leads to new Feynman diagrams. In the second part of this thesis, we study polariton systems in

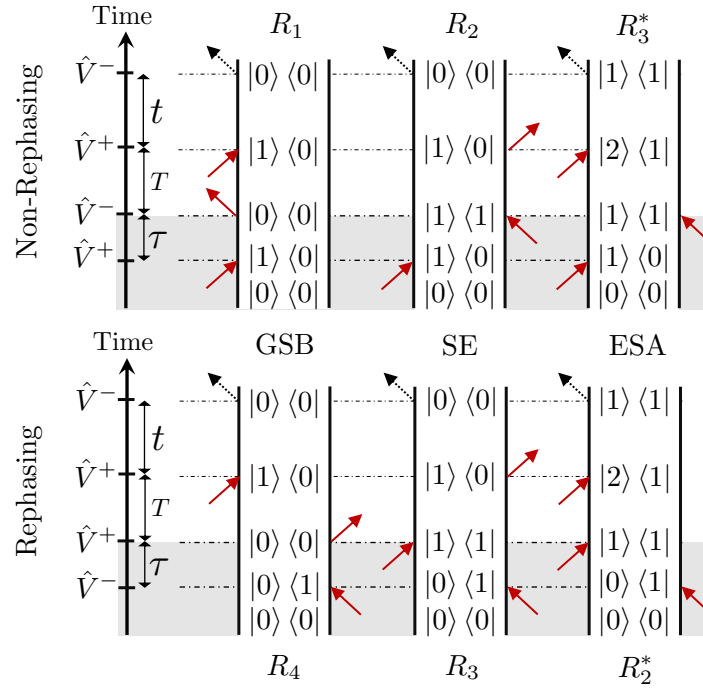


Fig. 3.6.: Nonzero double-sided Feynman diagrams contributing to the third-order nonlinear response function $S^{(3)}(\tau, T, t)$ for the NR and R PM conditions under semi-impulsive limit and RWA.

which two new diagrams arise due to the presence of dissipation during the temporal intervals T and t .

Some systems, like polaritons, exhibit varieties of multi-state excitations (see, for example, the TC model studied in [Chap. 1](#)). In those cases, the ket states $|1\rangle$ or bra states $\langle 1|$ appearing in the Feynman diagrams represent any of the single-excitation states (connected by dipolar interaction with the ground state), and the ket $|2\rangle$ represents any of the two-excitation states (connected by dipolar interaction with the single-excitation states).

The visualization of the Feynman diagrams in [Fig. 3.6](#) allows us to understand the physical processes that occur simultaneously during the spectroscopic protocol for each PM condition. In both NR and R signals, the action of the first pulse takes the ground state $|0\rangle \langle 0|$ to a **coherence** state $|1\rangle \langle 0|$ (for NR) and $|0\rangle \langle 1|$ (for R). Subsequently, this state evolves with the system propagator during the time interval τ . Then, the interaction with the second pulse generates a population state that can be $|0\rangle \langle 0|$ or $|1\rangle \langle 1|$. As the interaction with the first two pulses is required to generate a population state, it is named

Excitation process: Interaction with pulse 1 + τ evolution + Interaction with pulse 2.

Now it is understood that the time interval τ is referred to as the excitation time. The excitation process is highlighted in the shaded gray area in the Feynman diagrams plotted in [Fig. 3.6](#). It is during this stage where the R and NR PM conditions differ. From this point onward, the Feynman pathways

are the same for both PM conditions. The population state obtained during the excitation process evolves with the system propagator during the interval T . This time is called the waiting time:

Waiting: T evolution.

This waiting time is used as a parameter to analyze the fast dynamics of the excited system from the temporal changes in the 2D spectra, as discussed later in [Subsec. 3.6.4](#). The evolved state during the waiting time then interacts with the third pulse, which brings it back to a coherent state, which in our example of the anharmonic oscillator can be $|1\rangle\langle 0|$ or $|2\rangle\langle 1|$. This state propagates during the time interval t in which the system emits a signal, that eventually may combine with the local oscillator detection pulse. This signal is produced with a deexcitation on the left (ket) side of the density operator leading to a population state. The combined process is called

Detection process: Interaction with pulse 3 + t evolution

Of course the time t is called the detection time. With the detection process, it is possible to probe the states that were formed during the excitation process and during their respective dynamic evolution in the waiting time T .

3.6.3. Physical processes: GSB, SE, ESA

The three Feynman diagrams contributing to each NR and R PM conditions also reveal three different physical processes, which we explain below.

Ground State Bleaching (GSB)

The contributions $R_{1[\text{NR}]}$ and $R_{4[\text{R}]}$ are labeled in [Fig. 3.6](#) as GSB because they represent the named ground state bleaching physical process. This means that after the excitation process the system returns to the ground state, from which the second and third steps of the spectroscopic protocol follow. Note that in fact, in these two Feynman pathways $R_{1[\text{NR}]}$ and $R_{4[\text{R}]}$ the state $|0\rangle\langle 0|$ is obtained after the excitation process. If we compare the GSB diagrams in [Fig. 3.6](#) with the linear absorption Feynman diagram in [Fig. 3.4](#), we observe that a GSB diagram represents a double linear absorption process. Except for some normalization factor, any cut of the 2D GSB spectrum (shown later in [Subsec. 3.6.4](#)) matches the linear absorption spectrum shown in the right panel of [Fig. 3.4](#). In this sense, GSB spectra allow for the test of single-excitation states and the extraction of their respective decay rates towards the ground state of the system. The GSB spectra do not vary with the waiting time T , as expected, since during this time interval T , the state remains in the ground state.

Stimulated Emission (SE)

The contributions $R_{2[\text{NR}]}$ and $R_{3[\text{R}]}$ are labeled in [Fig. 3.6](#) as SE because they represent the named stimulated emission physical process. This means that after the excitation process, a population is obtained in single-excitation states $|1\rangle\langle 1|$ of the system (those connected by dipolar interaction with

the ground state). However, this population undergoes stimulated emission after the interaction with the third pulse at a given detection time t , ultimately returning to the ground state $|0\rangle\langle 0|$. The SE spectra allow for tracking the dynamic evolution during the waiting time T of the population in states from single-excitation manifold. Additionally, it is possible to analyze their decays, not only towards the ground state but also towards other non-degenerate single-excitation states, in the case of multi-state excitation manifolds.

Excited State Absorption (ESA)

Excited state absorption (ESA) represents cases where, after the excitation process, population is already reached in the form of single-excitation states $|1\rangle\langle 1|$ (those connected by dipolar interaction with the ground state). After the evolution of these states during the waiting time T , the third pulse of the spectroscopic protocol achieves coherence $|2\rangle\langle 1|$ involving two-excitation states (those connected by dipolar interaction with the single-excitation states). Once the system in a coherence $|2\rangle\langle 1|$ emits a photon after a time interval t , field which is detected, some population remains in the single-excitation manifold $|1\rangle\langle 1|$. The diagrams $R_{3[\text{NR}]}^*$ and $R_{2[\text{R}]}^*$ in Fig. 3.6 represent ESA contributions to the third-order nonlinear response in their respective PM conditions. With ESA spectra, it is possible to test states that may not have a dipolar connection with the ground state, but instead they do have connections with two-excitation states. This represents a great advantage of the 2D spectroscopic technique compared to linear methods.

3.6.4. 2D nonlinear spectra

In the frequency domain, we can define a 2D spectrum analogously to the linear spectrum in Eq. (3.45). For our study, we are interested in considering the sum of both NR and R PM conditions, so we define

$$S_{(\text{NR}+\text{R})}^{(3)}(\omega_\tau, T, \omega_t) \equiv i \int_0^\infty d\tau dt \left[S_{[\text{NR}]}^{(3)}(\tau, T, t) e^{i\omega_t t} e^{i\omega_\tau \tau} + S_{[\text{R}]}^{(3)}(\tau, T, t) e^{i\omega_t t} e^{-i\omega_\tau \tau} \right]. \quad (3.60)$$

Note that we have applied the Fourier transform only for the excitation time τ (with respective excitation frequency ω_τ) and the detection time t (with respective detection frequency ω_t). The dependence on the waiting time T is kept explicitly in the time domain. Now we can define the following 2D spectra

$$\begin{aligned} \text{Absorptive spectrum} &\equiv \mathcal{R}\{S_{(\text{NR}+\text{R})}^{(3)}(\omega_\tau, T, \omega_t)\} \\ \text{Absolute value spectrum} &\equiv |S_{(\text{NR}+\text{R})}^{(3)}(\omega_\tau, T, \omega_t)|. \end{aligned} \quad (3.61)$$

The 2D spectra are constructed by defining the excitation frequency ω_τ on the ordinate axis and the detection frequency ω_t on the abscissa axis, while the waiting time T is taken as a parameter. This allows for the study of the temporal evolution in T of the 2D spectra. Each 2D map is a “snapshot” of the spectrum at a specific time T . We can also define the spectra corresponding to each physical process, we name **path**: GSB, SE and ESA as follows

$$\begin{aligned} S_{(\text{NR}+\text{R}) \text{ path}}^{(3)}(\omega_\tau, T, \omega_t) &\equiv i \int_0^\infty d\tau dt \left[S_{[\text{NR}] \text{ path}}^{(3)}(\tau, T, t) e^{i\omega_t t} e^{i\omega_\tau \tau} \right. \\ &\quad \left. + S_{[\text{R}] \text{ path}}^{(3)}(\tau, T, t) e^{i\omega_t t} e^{-i\omega_\tau \tau} \right], \end{aligned} \quad (3.62)$$

where

$$S_{[\text{NR/R}] \text{ path}}^{(3)}(\tau, T, t) = \left(\frac{i}{\hbar}\right)^3 v^4 \Theta(\tau) \Theta(T) \Theta(t) \left[R_{[\text{NR/R}] \text{ path}} \right] \quad (3.63)$$

is obtained from Eq. (3.59) in the RWA, and $R_{[\text{NR/R}] \text{ path}}$ is the respective contribution to each path process according to Fig. 3.6. It has a negative sign if it corresponds to a conjugate term R_k^* . For example, $R_{[\text{NR}] \text{ GSB}} = R_{1[\text{NR}]}$, and $R_{[\text{R}] \text{ ESA}} = -R_{2[\text{NR}]}$. Now we define the GSB, SE, or ESA spectrum as the real part of $S_{(\text{NR+R}) \text{ path}}^{(3)}(\omega_\tau, T, \omega_t)$, so that the total absorptive spectrum can be constructed as the sum [148]

$$\text{Absorptive spectrum} = \text{GSB spectrum} + \text{SE spectrum} + \text{ESA spectrum},$$

if these are the only pathways contributing to the NR+R third-order nonlinear response function. If new pathways emerge when incoherent process are included in the system Liouvillian, it is necessary to add the new contributing components to the full spectrum.

As an example, let us consider the anharmonic oscillator shown in the Fig. 3.4. Once again, we include a Lindblad term of the form $\check{\mathcal{L}}_D = \kappa \check{\mathcal{L}}(\hat{V}^-)$, but this time, we set to zero the elements $\mathfrak{L}_{01,12}$ and $\mathfrak{L}_{10,21}$ of the Liouvillian to prevent the formation of a new pathway during the detection time. This new pathway is studied in the second part of this thesis, and we refer to it as ESA'. For now, we do not consider it.

For the waiting time $T = 0$, we obtain the spectra shown in the Fig. 3.7. Note that there are only signals at the excitation frequency $\omega_\tau = \omega_{10}$ since during the excitation process only transitions between the states $|0\rangle$ and $|1\rangle$ are involved, as shown by the orange arrows in Fig. 3.7. A direct transition from the ground state to state $|2\rangle$ is avoided by the selection rules of the dipole operator. Along the excitation frequency, the signals then exhibit the same width at half maximum as the linear absorption spectrum, which in this case is 2κ . During the detection process, both GSB and SE contributions also account for transitions between the states $|0\rangle$ and $|1\rangle$, as indicated by the green arrows for these two signals in the Fig. 3.7. Therefore, both signals are expected to be observed at the detection frequency $\omega_t = \omega_{10}$, and the width along this frequency is also expected to be 2κ . This is why the GSB and SE signals appear quite symmetric along both frequencies. On the other hand, the ESA contribution, which involves transitions between the states $|1\rangle$ and $|2\rangle$ during detection, is observed consequently at the detection frequency $\omega_t = \omega_{21}$ and has a wider width along this frequency, indicating that the decay rate of the state $|2\rangle$ is higher.

The sum of the three contributions results in the absorptive spectrum shown in Fig. 3.7. The GSB and SE contributions are positive, while the ESA contribution is negative. Remember that the ESA signal comes from the sum of $R_{3[\text{NR}]}^*$ and $R_{2[\text{R}]}^*$, which are conjugate terms and they contribute to the nonlinear response function with a negative sign, indicating that the dipole operator \hat{V} is applied an odd number of times on the right side of the density operator. Thus, the GSB and SE processes interfere constructively while the ESA process interferes destructively with the other two. The GSB and SE contributions are proportional to $(vV_{10})^4$, while the ESA is proportional to $(vV_{10})^2(vV_{21})^2$.

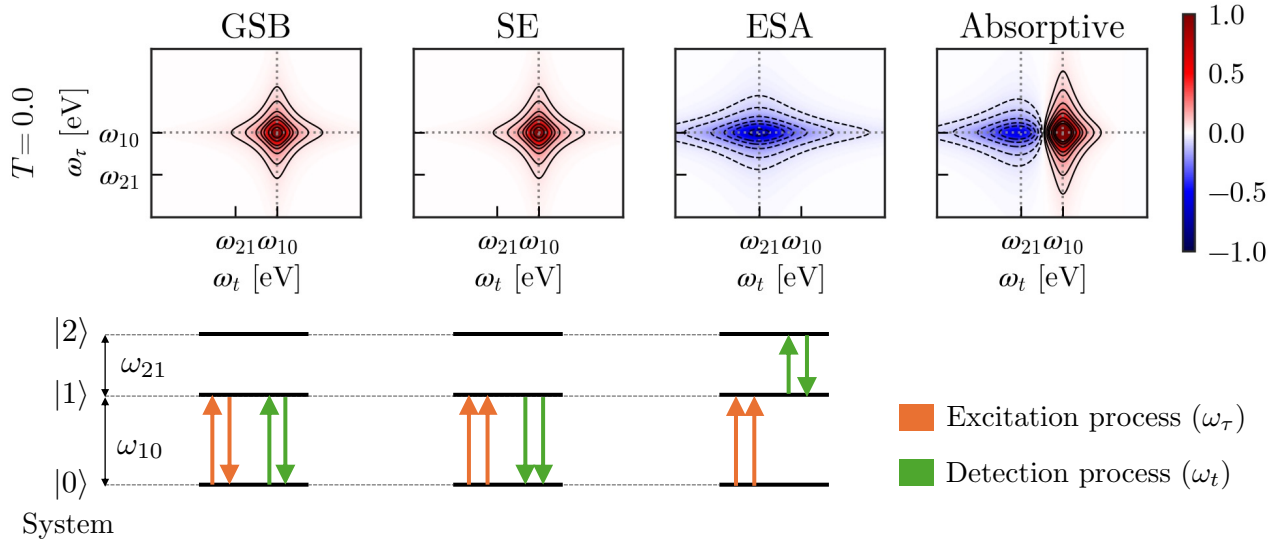


Fig. 3.7.: Upper panel: GSB, SE, ESA and total absorptive normalized spectra at the waiting time $T = 0$ for the anharmonic oscillator in Fig. 3.4. The elements $\mathcal{L}_{01,12}$ and $\mathcal{L}_{10,21}$ of the Liouvillian have been nullified to prevent the formation of new pathways. Lower panel: Schematic representation of the physical processes occurring in each contribution to third-order non linear response. Orange arrows represent the two pulses of the excitation process, and the green arrows represent the pulses of the detection process.

For dipole transition operators in oscillators, it is usually the case that $(vV_{21}) = \sqrt{2}(vV_{10})$, thus the ESA signal has twice the magnitude of the SE and GSB signals. If the decay rates are the same for all states, the ESA signal would have the same shape as any of the GSB or SE signals. In this sense, if $\omega_{01} = \omega_{12}$ (harmonic oscillator), the sum of the GSB+SE+ESA contributions would cancel out under these conditions. Therefore, the 2D spectrum is useful then to account for the anharmonicity of the system.

3.7. Analytical computation of the third-order nonlinear response

To compute the third-order nonlinear response function, which is directly measured with the 2D spectroscopy protocol in Fig. 3.5 under the semi-impulsive limit and RWA, we employ Eq. (3.56) written in the Liouville space (LS), before applying the RWA:

$$S^{(3)}(\tau, T, t) = -v^4 \langle \langle V | \hat{\mathcal{G}}_s(t) \hat{V} \hat{\mathcal{G}}_s(T) \hat{V} \hat{\mathcal{G}}_s(\tau) \hat{V} | \rho(t_0) \rangle \rangle.$$

Our aim in this section is to rewrite this equation in the basis of the Liouvillian eigenstates. The resulting expression can be easily calculated with a computational code and it is quite efficient because, aside from diagonalizing the Liouvillian matrix, the calculation is entirely analytical. Other algorithms and methods (including non-perturbative ones) for computation can be found in [142, 42, 151, 152].

3.7.1. Representations in Liouvillian eigenbasis

To construct the new expression, we need to use the tools introduced in [Chap. 2](#) for the mathematical formulation of states, operators, and superoperators in the LS. In particular, we return to the following considerations obtained in that chapter:

- In [Subsec. 2.1.6](#), we studied the eigenstates of the Liouvillian when it has a Hamiltonian counterpart. We found that in this case, such eigenstates $\{|\alpha\beta\rangle\}$ can be written from the Hamiltonian eigenstates $\{|\alpha\rangle\}$. The eigenvalues of the Liouvillian are of the form $\lambda_{\alpha\beta} = -i\omega_{\alpha\beta}$ (see [Eq. \(2.41\)](#)). On the other hand, in [Subsec. 2.1.7](#) we discussed the general case, when processes leading to incoherent dynamics are included in the Liouvillian, and it is not possible to find a Hamiltonian representation. In this case, the Liouvillian eigenstates cannot be constructed from those of the Hamiltonian. They are more general eigenstates, which, in the single-index notation, can be written as $\{|v_i\rangle\rangle\}$, such that

$$\hat{\mathcal{L}}_s |v_i\rangle\rangle = \lambda_i |v_i\rangle\rangle, \quad (3.64)$$

with respective eigenvalues $\{\lambda_i\}$. The subscript s indicates that it is the Liouvillian of the system under study in the 2D spectroscopy, free from interaction with the classical fields. This is the basis we use below to write $S^{(3)}(\tau, T, t)$. Remember that $|v_i\rangle\rangle$ represents an operator \hat{v}_i in Hilbert space (HS). Once the set of eigenvalues and eigenvectors of $\hat{\mathcal{L}}_s$ is obtained (typically it is a numerical process), the subsequent calculations are entirely analytical.

- Any LS state $|\rho\rangle\rangle$ can be expanded in the $\{|v_i\rangle\rangle\}$ basis following the [Eq. \(2.31\)](#) as

$$|\rho\rangle\rangle = \sum_i c_i |v_i\rangle\rangle, \quad \text{with } c_i = \langle\langle v_i | \rho \rangle\rangle. \quad (3.65)$$

The LS expansion coefficient c_i can be computed in the HS by using the definition of the LS inner product [Eq. \(2.27\)](#) as

$$c_i = \langle\langle v_i | \rho \rangle\rangle = \text{Tr} [\hat{v}_i^\dagger \hat{\rho}] = \langle\hat{v}_i^\dagger\rangle_{\hat{\rho}}. \quad (3.66)$$

- The dipole LS operator $\hat{\mathcal{V}}$ can be expanded in the $\{|v_i\rangle\rangle\}$ basis according to [Eq. \(2.32\)](#) as follows

$$\hat{\mathcal{V}} = \sum_{ij} \mathcal{V}_{ij} |v_i\rangle\rangle \langle\langle v_j|, \quad \text{with } \mathcal{V}_{ij} = \langle\langle v_i | \hat{\mathcal{V}} | v_j \rangle\rangle. \quad (3.67)$$

The LS matrix element \mathcal{V}_{ij} can be computed in the HS using the definition of the dipole HS superoperator in [Eq. \(3.8\)](#) and the definition of the LS inner product [Eq. \(2.27\)](#), as follows

$$\mathcal{V}_{ij} = \langle\langle v_i | \hat{\mathcal{V}} | v_j \rangle\rangle = -\frac{i}{\hbar} \text{Tr} [\hat{v}_i^\dagger [\hat{\mathcal{V}}, \hat{v}_j]] = -\frac{i}{\hbar} \text{Tr} [\hat{v}_j \hat{v}_i^\dagger \hat{\mathcal{V}} - \hat{v}_i^\dagger \hat{v}_j \hat{\mathcal{V}}] = -\frac{i}{\hbar} \text{Tr} [[\hat{v}_j, \hat{v}_i^\dagger] \hat{\mathcal{V}}], \quad (3.68)$$

which can be interpreted as the “expected value”

$$\mathcal{V}_{ij} = -\frac{i}{\hbar} \langle\langle [\hat{v}_j, \hat{v}_i^\dagger] \rangle\rangle_{\hat{\mathcal{V}}}. \quad (3.69)$$

Now, the LS dipole operator acting on an arbitrary state $|\rho\rangle\rangle$ can be computed using [Eq. \(3.65\)](#) and [Eq. \(3.67\)](#) as

$$\hat{\mathcal{V}} |\rho\rangle\rangle = \sum_{ijk} \mathcal{V}_{ij} c_k |v_i\rangle\rangle \langle\langle v_j | v_k \rangle\rangle = \sum_{ik} \mathcal{V}_{ik} c_k |v_i\rangle\rangle, \quad (3.70)$$

where we have used the orthogonality relation of the Liouvillian eigenbasis $\langle\langle v_j | v_k \rangle\rangle = \delta_{jk}$. Particularly, when acting on a Liouvillian eigenstate $|v_k\rangle\rangle$, we obtain

$$\hat{\mathcal{V}} |v_k\rangle\rangle = \sum_{ij} \mathcal{V}_{ij} |v_i\rangle\rangle \langle\langle v_j | v_k \rangle\rangle = \sum_i \mathcal{V}_{ik} |v_i\rangle\rangle. \quad (3.71)$$

- The field-free Liouvillian of the system $\hat{\mathcal{L}}_s$ is time independent. Consequently, its LS time propagator $\hat{\mathcal{U}}_s(t)$ is that of Eq. (2.36) and the respective Green's function is, from the definition in Eq. (3.16),

$$\hat{\mathcal{G}}_s(t) = \Theta(t) e^{\hat{\mathcal{L}}_s t}. \quad (3.72)$$

The great advantage of using the Liouvillian basis is that the temporal evolution of an arbitrary state $|\rho\rangle\rangle$ is quite straightforward, as shown below

$$\hat{\mathcal{G}}_s(t) |\rho\rangle\rangle = \Theta(t) \sum_i c_i e^{\hat{\mathcal{L}}_s t} |v_i\rangle\rangle = \Theta(t) \sum_i c_i e^{\lambda_i t} |v_i\rangle\rangle, \quad (3.73)$$

where we have used the expansion in Eq. (3.65) and we have taken into account that if the eigenvalue Eq. (3.64) is satisfied, then a function f of the Liouvillian satisfies $f(\hat{\mathcal{L}}_s) |v_i\rangle\rangle = f(\lambda_i) |v_i\rangle\rangle$. Particularly, when acting on an eigenstate $|v_k\rangle\rangle$, we obtain

$$\hat{\mathcal{G}}_s(t) |v_k\rangle\rangle = \Theta(t) e^{\hat{\mathcal{L}}_s t} |v_k\rangle\rangle = \Theta(t) e^{\lambda_k t} |v_k\rangle\rangle. \quad (3.74)$$

Now it is straightforward to compute the expression for the third-order nonlinear response function as indicated in the next subsections.

3.7.2. Excitation process

The initial state $|\rho(t_0)\rangle\rangle$ is expanded in the Liouvillian eigenbasis by using Eq. (3.65)

$$|\rho(t_0)\rangle\rangle = \sum_l c_l |v_l\rangle\rangle. \quad (3.75)$$

If $|\rho(t_0)\rangle\rangle$ is the ground state $|gg\rangle\rangle$ and since the ground state is also a Liouvillian eigenvector, only the term $c_0 |v_0\rangle\rangle \equiv |gg\rangle\rangle$ is different from zero. The interaction $\hat{\mathcal{V}}$ with the first pulse of the 2D spectroscopy protocol is computed as

$$\hat{\mathcal{V}} |\rho(t_0)\rangle\rangle = \sum_l c_l \hat{\mathcal{V}} |v_l\rangle\rangle = \sum_{il} \mathcal{V}_{il} c_l |v_i\rangle\rangle, \quad (3.76)$$

by using Eq. (3.71). The subsequent temporal evolution during the excitation time τ , resulting when applying $\hat{\mathcal{G}}_s(\tau)$, is obtained as

$$\hat{\mathcal{G}}_s(\tau) \hat{\mathcal{V}} |\rho(t_0)\rangle\rangle = \sum_{il} \mathcal{V}_{il} c_l \hat{\mathcal{G}}_s(\tau) |v_i\rangle\rangle = \Theta(\tau) \sum_{il} e^{\lambda_i \tau} \mathcal{V}_{il} c_l |v_i\rangle\rangle, \quad (3.77)$$

where we have used the relation in Eq. (3.74). The interaction $\hat{\mathcal{V}}$ with the second pulse is again computed by using Eq. (3.71). At this point, the excitation process finishes, and yields the excitation state

$$|\rho(\tau)\rangle\rangle \equiv \hat{\mathcal{V}} \hat{\mathcal{G}}_s(\tau) \hat{\mathcal{V}} |\rho(t_0)\rangle\rangle = \Theta(\tau) \sum_{jil} \mathcal{V}_{ji} e^{\lambda_i \tau} \mathcal{V}_{il} c_l |v_j\rangle\rangle. \quad (3.78)$$

Excitation function

We can define an excitation function $E_j(\tau)$ as

$$E_j(\tau) \equiv \Theta(\tau) \sum_{il} \mathcal{V}_{ji} e^{\lambda_i \tau} \mathcal{V}_{il} c_l, \quad (3.79)$$

such that the excitation state is

$$|\rho(\tau)\rangle\rangle = \sum_j E_j(\tau) |v_j\rangle\rangle. \quad (3.80)$$

Only those j th Liouvillian eigenvectors for which the excitation function $E_j(\tau)$ is nonzero contribute to the excited state and consequently to the third-order response function.

3.7.3. Detection process

In a completely analogous manner, we keep on calculating the temporal evolution during the waiting time T , the subsequent interaction with the third pulse of the 2D spectroscopic protocol, and the evolution during the detection time t to obtain the final state $|\rho(\tau + T + t)\rangle\rangle$ as follows

$$\begin{aligned} |\rho(\tau + T + t)\rangle\rangle &\equiv \hat{\mathcal{G}}_s(t) \hat{\mathcal{V}} \hat{\mathcal{G}}_s(T) \hat{\mathcal{V}} \hat{\mathcal{G}}_s(\tau) \hat{\mathcal{V}} |\rho(t_0)\rangle\rangle \\ &= \Theta(t) \Theta(T) \Theta(\tau) \sum_{kjil} e^{\lambda_k t} \mathcal{V}_{kj} e^{\lambda_j T} \mathcal{V}_{ji} e^{\lambda_i \tau} \mathcal{V}_{il} c_l |v_k\rangle\rangle \\ &= \Theta(t) \Theta(T) \sum_{kj} e^{\lambda_k t} \mathcal{V}_{kj} e^{\lambda_j T} E_j(\tau) |v_k\rangle\rangle. \end{aligned} \quad (3.81)$$

The final step to compute $S^{(3)}(\tau, T, t)$ is the inner product between the LS state bra $\langle\langle V |$ and the state $|\rho(\tau + T + t)\rangle\rangle$, where the detection process ends.

$$\begin{aligned} S^{(3)}(\tau, T, t) &= -v^4 \langle\langle V | \rho(\tau + T + t)\rangle\rangle \\ &= -v^4 \Theta(t) \Theta(T) \Theta(\tau) \sum_{kjil} e^{\lambda_k t} \mathcal{V}_{kj} e^{\lambda_j T} \mathcal{V}_{ji} e^{\lambda_i \tau} \mathcal{V}_{il} c_l \langle\langle V | v_k\rangle\rangle \\ &= -v^4 \Theta(t) \Theta(T) \Theta(\tau) \sum_{kjil} V_k e^{\lambda_k t} \mathcal{V}_{kj} e^{\lambda_j T} \mathcal{V}_{ji} e^{\lambda_i \tau} \mathcal{V}_{il} c_l \\ &= -v^4 \Theta(t) \Theta(T) \sum_{kj} V_k e^{\lambda_k t} \mathcal{V}_{kj} e^{\lambda_j T} E_j(\tau), \end{aligned} \quad (3.82)$$

with

$$V_k = \langle\langle V | v_k\rangle\rangle = \text{Tr} \left[\hat{V}^\dagger \hat{v}_k \right] = \langle \hat{V}^\dagger \rangle_{\hat{v}_k}. \quad (3.83)$$

Detection function

We also define the detection function $D_j(t)$ in the form

$$D_j(t) \equiv \Theta(t) \sum_k V_k e^{\lambda_k t} \mathcal{V}_{kj}. \quad (3.84)$$

In terms of these excitation and detection functions we can write a compact expression for the third-order response function, which accounts for the three experimental processes in its measurement, namely excitation, waiting (evolution during time T), and detection, as

$$S^{(3)}(\tau, T, t) = -v^4 \Theta(T) \sum_j D_j(t) e^{\lambda_j T} E_j(\tau). \quad (3.85)$$

Only those j th Liouvillian eigenvectors for which both the excitation and detection functions are nonzero contribute to the third-order response function. In this sense, these functions act as masks or filters that select the relevant eigenvectors and eigenvalues for the calculation.

Non Rephasing and Rephasing PM conditions

Under the RWA, the third expression in Eq. (3.82) can be rewritten for the NR and R PM conditions as

$$S_{[\text{NR(R)}]}^{(3)}(\tau, T, t) = -v^4 \Theta(t) \Theta(T) \Theta(\tau) \sum_{kjil} V_k^- e^{\lambda_k t} \mathcal{V}_{kj}^+ e^{\lambda_j T} \mathcal{V}_{ji}^\mp e^{\lambda_i \tau} \mathcal{V}_{il}^\pm c_l. \quad (3.86)$$

The excitation and detection functions for both PM conditions are now of the form

$$E_{j[\text{NR(R)}]}(\tau) = \Theta(\tau) \sum_{il} \mathcal{V}_{ji}^\mp e^{\lambda_i \tau} \mathcal{V}_{il}^\pm c_l, \quad D_{j[\text{NR(R)}]}(t) = \Theta(t) \sum_k V_k^- e^{\lambda_k t} \mathcal{V}_{kj}^+. \quad (3.87)$$

The detection function is the same for both PM conditions since \mathbf{k}_3 has a positive sign in both. In terms of these functions

$$S_{[\text{NR(R)}]}^{(3)}(\tau, T, t) = -v^4 \Theta(T) \sum_j D_{j[\text{R}]}(t) e^{\lambda_j T} E_{j[\text{NR(R)}]}(\tau). \quad (3.88)$$

3.7.4. Frequency domain spectra

The frequency domain expression for the third-order nonlinear response resulting from the sum of the NR and R PM contributions is obtained by inserting Eq. (3.86) (or Eq. (3.88)) into Eq. (3.60)

$$\begin{aligned} S_{(\text{NR+R})}^{(3)}(\omega_\tau, T, \omega_t) &= -iv^4 \sum_{kjil} V_k^- \left(\int_0^\infty dt e^{\lambda_k t} e^{i\omega_t t} \right) \mathcal{V}_{kj}^+ e^{\lambda_j T} \\ &\times \left[\mathcal{V}_{ji}^- \left(\int_0^\infty d\tau e^{\lambda_i \tau} e^{i\omega_\tau \tau} \right) \mathcal{V}_{il}^+ c_l + \mathcal{V}_{ji}^+ \left(\int_0^\infty d\tau e^{\lambda_i \tau} e^{-i\omega_\tau \tau} \right) \mathcal{V}_{il}^- c_l \right]. \end{aligned} \quad (3.89)$$

Note that this method allows for the analytical development of the integrals resulting from the 2D Fourier transform, further enhancing the computational efficiency of the calculation. It is important to clarify that the eigenvalues of the Liouvillian, as discussed later in the second part of this thesis, are generally of the form $\lambda_i = -\Gamma_i + i\omega_i$, where Γ_i and ω_i are real numbers. This prevents the integrals in the above equation from diverging when evaluated at $+\infty$. Finally, we obtain

$$S_{(\text{NR+R})}^{(3)}(\omega_\tau, T, \omega_t) = -iv^4 \sum_{kjil} \frac{V_k^- \mathcal{V}_{kj}^+}{\lambda_k + i\omega_t} e^{\lambda_j T} \left[\frac{\mathcal{V}_{ji}^- \mathcal{V}_{il}^+}{\lambda_i + i\omega_\tau} + \frac{\mathcal{V}_{ji}^+ \mathcal{V}_{il}^-}{\lambda_i - i\omega_\tau} \right] c_l, \quad (3.90)$$

or in the compact form

$$\mathcal{S}_{(\text{NR}+\text{R})}^{(3)}(\omega_\tau, T, \omega_t) = -iv^4 \sum_j D_{j[\text{R}]}(\omega_t) e^{\lambda_j T} \left[E_{j[\text{NR}]}(\omega_\tau) + E_{j[\text{R}]}(\omega_\tau) \right], \quad (3.91)$$

with

$$E_{j[\text{NR}(\text{R})]}(\omega_\tau) = \sum_{il} \frac{\mathcal{V}_{ji}^\mp \mathcal{V}_{il}^\pm}{\lambda_i \pm i\omega_\tau} c_l, \quad D_{j[\text{R}]}(\omega_t) = \sum_k \frac{V_k^- \mathcal{V}_{kj}^+}{\lambda_k + i\omega_t}, \quad (3.92)$$

being the respective Fourier transforms of excitation and detection functions in Eq. (3.87). The expression Eq. (3.90) can be computed very efficiently as simple matrix and vector products. Note, for example, that one can construct the matrices \mathbb{V}^\pm such that their elements $\{i, j\}$ are \mathcal{V}_{ij}^\pm (values obtained from Eq. (3.68)).

Part III.

Results and discussion

4. Multidimensional spectroscopy in the dissipative Jaynes-Cummings model

The simplest polaritonic model used to describe the strong interaction between molecules and radiation is the Jaynes-Cummings (JC) model, which represents a single two-state emitter (atom, molecule, etc.) interacting with one mode of the quantized electromagnetic field confined in a cavity¹. The Hamiltonian associated to the JC model reads

$$H_{JC} = \hbar\omega_c a^\dagger a + \hbar\omega_e \sigma^\dagger \sigma + \hbar g(a^\dagger \sigma + \sigma^\dagger a), \quad (4.1)$$

where ω_c , ω_e are the cavity and molecule frequencies respectively; a , σ are the cavity annihilation and molecule de-excitation operators respectively (a^\dagger , σ^\dagger are their adjoints) and g is the radiation-matter coupling constant. The left panel of Fig. 4.1 shows the energy scheme of this model up to the second excitation manifold Λ_2 and the possible radiative dipole transitions between the states. The dimension of the Hilbert space is $\dim_H = 5$ [i.e., Λ_0 (1), Λ_1 (2), Λ_2 (2)]. Except Λ_0 , composed only by the ground state $|G\rangle$, in each excitation manifold Λ_i there are two polariton states: the lower (L) and the upper (U). The splitting between polaritons of Λ_1 is the Rabi frequency $\Omega_R = \sqrt{4g^2 + \Delta^2}/2$. If the system is resonant then the detuning is zero $\Delta \equiv \omega_c - \omega_e = 0$ and the Rabi frequency is $\Omega_R = 2g$. We introduce cavity photon losses as a Lindblad term for the operator a , with a cavity decay rate $\kappa = 1/t_\kappa$, where t_κ is the cavity lifetime (related with the cavity quality factor \mathcal{Q}). The molecular vibrational relaxation is taken into account within the Bloch-Redfield formalism for the dephasing-type operator $\sigma^\dagger \sigma$ with a vibrational bath spectral function $J(\omega) = \gamma$ for $\omega \geq 0$ and $J(\omega) = 0$ for $\omega < 0$. The molecular exciton lifetime then corresponds to $t_\gamma = 1/\gamma$. The Liouvillian superoperator \mathcal{L} for this open system reads as

$$\mathcal{L}[\rho] = -\frac{i}{\hbar}[H_{JC}, \rho] + \kappa\mathcal{L}(a)[\rho] + \mathcal{B}(\sigma^\dagger \sigma)[\rho]. \quad (4.2)$$

4.1. Liouvillian eigenvalues and eigenstates

The Liouvillian is a superoperator with a related eigenvalue equation, $(\mathcal{L} - \lambda_i)|v_i\rangle = 0$. For our example with 5 Hamiltonian states the dimension of the Liouvillian matrix is $\dim_H^2 \times \dim_H^2 = 25 \times 25$ complex. The right panel of Fig. 4.1 shows the position of these 25 Liouvillian eigenvalues in the complex plane for a given set of parameters. The real part of each eigenvalue accounts for a decay Γ , while the imaginary part is approximately the frequency difference $\omega_{\alpha\beta} = \omega_\alpha - \omega_\beta$ between any two respective eigenstates $|\alpha\rangle$ and $|\beta\rangle$ of the JC Hamiltonian. We have decided to identify each Liouvillian

¹Experimentally, achieving strong coupling between radiation and a single or few molecules is only possible by using nanoplasmonic cavities [1]

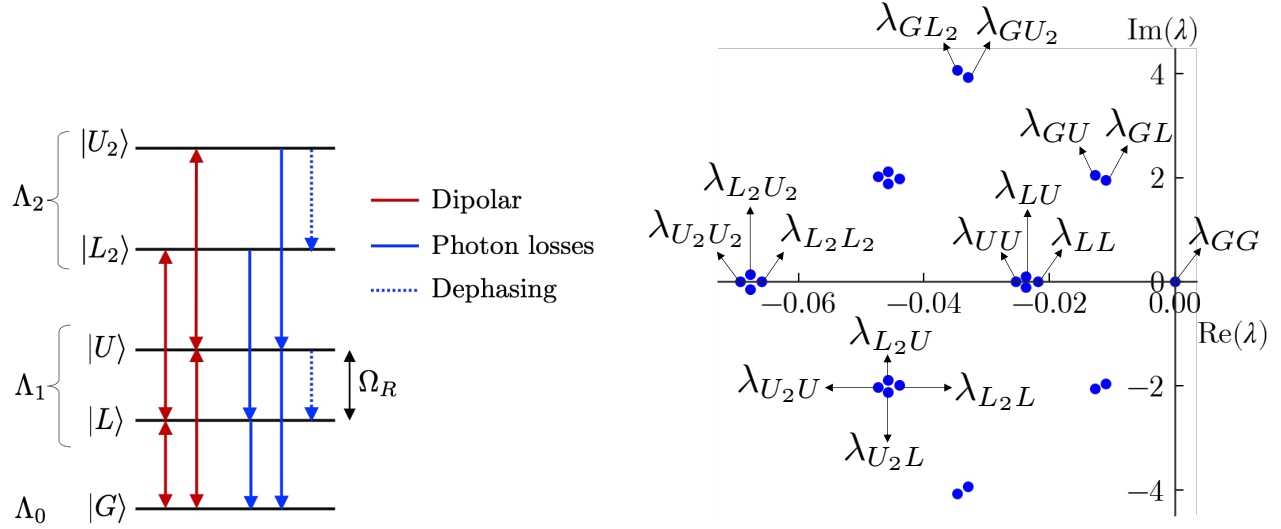


Fig. 4.1.: Left panel: energy scheme of the Jaynes-Cummings (JC) model eigenstates for the excitation manifolds Λ_0 , Λ_1 and Λ_2 (not to scale). Each manifold, except $\Lambda_0 = |G\rangle$, is characterized by a lower polariton L and an upper polariton U . The splitting between polaritons of Λ_1 is called the Rabi frequency Ω_R . Red arrows indicate the allowed radiative dipole transitions. Blue arrows indicate transitions due to cavity photons losses (solid lines) and molecular dephasing-type vibrational relaxation (dotted lines). Right panel: blue points represent Liouvillian eigenvalues for the open Jaynes-Cummings (JC) model up to the second excitation manifold. We have chosen $\hbar\omega_c = \hbar\omega_e = 2$ eV and $\hbar\Omega_R = 0.1$ eV. Cavity lifetime is 15 fs ($\kappa = 44$ meV/ \hbar) and molecular exciton lifetime is 50 fs ($\gamma = 13$ meV/ \hbar). The real parts of the eigenvalues are related to decays and their imaginary parts are close to energy differences between any two JC Hamiltonian eigenstates.

eigenvalue by using the two labels α and β of the Hamiltonian states whose energy difference closely approximates its corresponding imaginary part²:

$$\lambda_{\alpha\beta} = -\Gamma_{\alpha\beta} - i(\omega_{\alpha\beta} + \delta_{\alpha\beta}), \quad (4.3)$$

where $\delta_{\alpha\beta}$ is a small frequency shift. For the cases $\alpha = \beta$, both $\omega_{\alpha\beta}$ and $\delta_{\alpha\beta}$ are zero and these Liouvillian eigenvalues (λ_{GG} , λ_{LL} , λ_{UU} , $\lambda_{L_2L_2}$ and $\lambda_{U_2U_2}$) are real. We may classify these eigenvalues by ordering their decays in such a way that³ $\Gamma_{GG} = 0$ and $\Gamma_{LL} < \Gamma_{UU} < \Gamma_{L_2L_2} < \Gamma_{U_2U_2}$. The eigenvalues with an imaginary part (λ_{GL} , λ_{GU} , etc.) in the positive imaginary plane are accompanied by their respective complex conjugate (λ_{LG} , λ_{UG} , etc.) in the negative imaginary plane. Except $\lambda_{GG} = 0$, the real part ($-\Gamma_{\alpha\beta}$) of all eigenvalues is negative, producing losses to the initial density matrix and decay transitions as shown by the blue arrows in the left panel of Fig. 4.1. In general, any eigenvalue with

²Note that although we label the Liouvillian eigenvalues with the Hamiltonian states, this does not mean that the corresponding Liouvillian eigenvector $|v_{\alpha\beta}\rangle$ corresponds to the operator $|\alpha\rangle\langle\beta| = |\alpha\beta\rangle$.

³Experimentally it is known that U polaritons decay faster than L polaritons and the states of Λ_2 decay faster than those of Λ_1 .

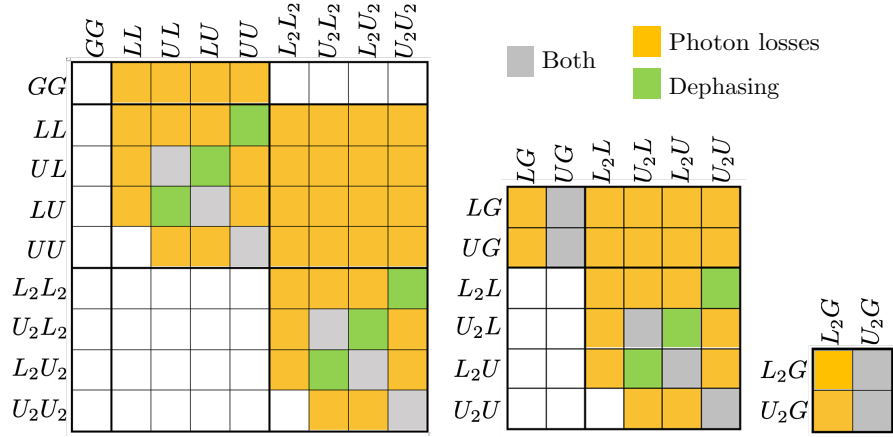


Fig. 4.2.: Schematic representation of non-zero Liouvillian elements in the Hamiltonian eigenbasis for three independent blocks. Orange color represents contributions due to cavity photon losses, green color are due to molecular dephasing-type vibrational relaxation, while gray color represent contributions of both molecular relaxation and cavity losses. Additionally, diagonal elements have the energy contribution of Hamiltonian.

$\Gamma_{\alpha\beta} = 0$ corresponds to a steady state of the system. In this dissipative TC model, only the ground state is stationary.

In the Liouville space (LS) representation of density operator (see [Subsec. 2.1.4](#)) the Liouvillian in [Eq. \(4.2\)](#) can be visualized as a matrix in the Hamiltonian eigenbasis $\{|\alpha\beta\rangle\}$, exhibiting the existence of five independent diagonal blocks. Three of these blocks are shown in the [Fig. 4.2](#). The double-label notation in this figure (and henceforth) refers to the Liouvillian space labels $\alpha\beta = |\alpha\beta\rangle = |\alpha\rangle\langle\beta|$, so that the Liouvillian element $\mathfrak{L}_{\alpha\beta,\alpha'\beta'}$ accounts for transitions in the density matrix formalism of the form $|\alpha'\rangle\langle\beta'| \rightarrow |\alpha\rangle\langle\beta|$.

The first block at the left side in the [Fig. 4.2](#) is composed by states of the form⁴ $\Lambda_i\Lambda_i$, with $i = 0, 1, 2$. The colors in each element of the figure identify whether the respective transition is due to cavity decay (orange), molecular dephasing-type vibrational relaxation (green) or a combination of both processes (gray). Additionally, there is a diagonal Hamiltonian contribution (not colored). For example, we can observe transitions of the form $\Lambda_2\Lambda_2 \rightarrow \Lambda_1\Lambda_1$ mediated entirely by photon losses, while the transitions $\Lambda_1\Lambda_1 \rightarrow \Lambda_2\Lambda_2$ (which represent pumping) are forbidden. Molecular relaxation only causes transitions between some populations (or coherences) of the same form ($\Lambda_i\Lambda_j \rightarrow \Lambda_i\Lambda_j$). The transitions between populations are also represented by blue arrows in the left panel of [Fig. 4.1](#). The second independent block is composed by coherences of type $\Lambda_i\Lambda_{i-1}$, with $i = 1, 2$, and the third block by coherences of the form $\Lambda_2\Lambda_0$. The two missing blocks (not shown in the figure) are the adjoint matrices of the second and third ones and are composed by coherences $\Lambda_{i-1}\Lambda_i$ ($i = 1, 2$) and $\Lambda_0\Lambda_2$, respectively. Each diagonal block in the Liouvillian evolves in time independently and the transitions

⁴The notation $\Lambda_i\Lambda_j = |\Lambda_i\rangle\langle\Lambda_j|$ refers to all possible ket states in Λ_i and all possible bra states in Λ_j .

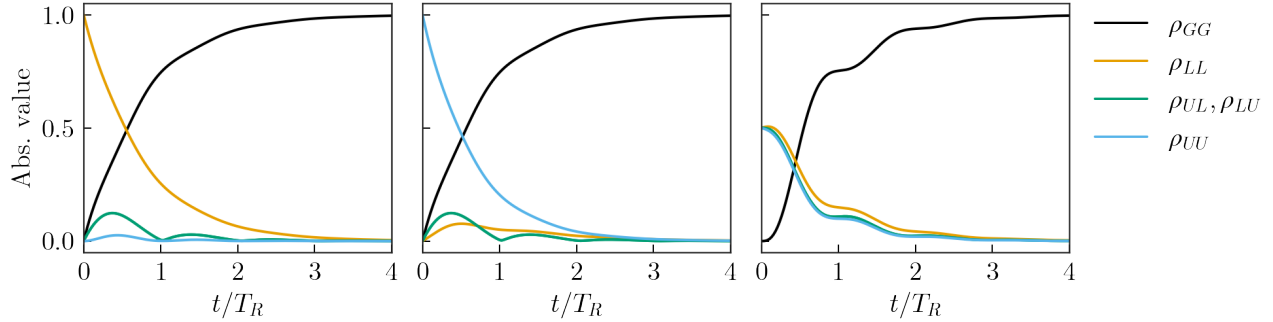


Fig. 4.3.: Absolute value of the non-zero elements $\rho_{GG}(t)$, $\rho_{LL}(t)$, $\rho_{UL}(t)$, $\rho_{LU}(t)$, $\rho_{UU}(t)$ of the density matrix $\rho(t) = e^{\mathfrak{L}t}\rho(0)$ for the initial conditions $\rho(0) = |L\rangle\langle L|$ (left panel), $\rho(0) = |U\rangle\langle U|$ (middle panel) and $\rho(0) = \frac{1}{2}(|L\rangle\langle L| + |U\rangle\langle U| + |L\rangle\langle U| + |U\rangle\langle L|)$ (right panel). The same parameters as in Fig. 4.1 have been used. In the left panel, $\rho_{LL}(t)$ exhibits a behavior of the form $e^{-(\kappa/2)t}$ and in the middle panel, $\rho_{UU}(t)$ decreases according to $e^{-(\kappa/2+\gamma/4)t}$. In the right panel, it is possible to observe oscillations with the Rabi frequency Ω_R . Here κ and γ are the cavity photon losses rate and molecular relaxation rate respectively. The evolution time t is in units of the Rabi period of the system $T_R = 2\pi/\Omega_R = 41.47$ fs.

shown in the Fig. 4.2 will help us to understand the behavior of 2D spectra later on.

As an example of the dynamics governed by the Liouvillian, the Fig. 4.3 shows the absolute value of the time-dependent density matrix elements $\rho_{\alpha,\beta}$ involving the ground state and the first excitation manifold $\{G, L, U\}$, for three different initial conditions. When the initial condition is $|LL\rangle$ or $|UU\rangle$ (left and middle panels in Fig. 4.3, respectively), we can observe that those polaritonic states exhibit a roughly exponential decay with a rate equivalent to $\kappa/2$ for $\rho_{LL}(t)$ and $\kappa/2 + \gamma/4$ for $\rho_{UU}(t)$, where κ and γ are cavity photon losses and molecular relaxation rates respectively. Rabi oscillations are also present, especially when coherences $|UL\rangle$ and $|LU\rangle$ are initially populated (right panel in Fig. 4.3). It is because the only complex eigenvalues of the Liouvillian involved in this dynamics are just λ_{UL} and λ_{LU} , which contribute with the temporal phases $\pm i(\omega_{UL} + \delta_{UL})t = \pm i\Omega_R t$ (shifted Rabi frequency). When the upper polariton is the initial condition (middle panel of figure), there is a small population that migrates to the lower polariton. This transition is solely due to the molecular relaxation (as indicated by the element $\mathfrak{L}_{LL,UU}$ in the first block of Fig. 4.2). On the other hand, when the lower polariton is initially populated (left panel in Fig. 4.3), there is a much smaller population that migrates towards the upper polariton. This migration must occur through the coherences (mediated only by cavity decay) because the direct transition $LL \rightarrow UU$ is forbidden⁵.

All dynamical cases studied in the Fig. 4.3 have an analytical solution if the populations and coherences associated to $\Lambda_2\Lambda_2$ in the first block of the Fig. 4.2 are not taken into account. In this case, the Liouvillian sub-block matrix $\mathfrak{L}_{\Lambda_1\Lambda_1}$ corresponding to this minimal basis in the Liouvillian space takes

⁵This transition would be possible if temperature effects are included in the Liouvillian, as will be studied later. For now, we are considering zero temperature.

the form

$$\mathfrak{L}_{\Lambda_1\Lambda_1} = \begin{matrix} & GG & LL & UL & LU & UU \\ \begin{matrix} GG \\ LL \\ UL \\ LU \\ UU \end{matrix} & \left(\begin{array}{ccccc} 0 & \kappa/2 & \kappa/2 & \kappa/2 & \kappa/2 \\ 0 & -\kappa/2 & -\kappa/4 & -\kappa/4 & \gamma/4 \\ 0 & -\kappa/4 & -\kappa/2 - \gamma/8 - i\tilde{\Omega}_R & \gamma/8 & -\kappa/4 \\ 0 & -\kappa/4 & \gamma/8 & -\kappa/2 - \gamma/8 + i\tilde{\Omega}_R & -\kappa/4 \\ 0 & 0 & -\kappa/4 & -\kappa/4 & -\kappa/2 - \gamma/4 \end{array} \right) \end{matrix}. \quad (4.4)$$

This reduced Liouvillian has analytic eigenvalues $\lambda_{GG} = 0$, $\lambda_{UU} = -\kappa/2 - \gamma/4$ and the eigenvalues λ_{LL} , λ_{LU} , λ_{UL} correspond respectively to the three analytical roots of the polynomial⁶ $256\kappa\Omega_R^2 + (16\gamma\kappa + 32\kappa^2 + 64\omega_R^2)\lambda + (2\gamma + 12\kappa)\lambda^2 + \lambda^3 = 0$. Although these solutions are analytical, they are complex functions of κ and γ , which can be approximated by simpler forms as follows: $\lambda_{LL} \approx -\kappa/2$, $\lambda_{LU} \approx -\kappa/2 - \gamma/8 + i\tilde{\Omega}_R$ and $\lambda_{UL} \approx -\kappa/2 - \gamma/8 - i\tilde{\Omega}_R$. We have labeled those eigenvalues according to previously established rules. For any initial condition that is a linear combination of states of the form $\Lambda_1\Lambda_1$, the exact analytic solutions to $\rho_{\alpha\beta}(t)$ takes the form

$$\begin{aligned} \rho_{\alpha\beta}(t) &= \sum_{\alpha'\beta'} C_{\alpha'\beta'}^{\alpha\beta} e^{\lambda_{\alpha'\beta'} t} \\ &= C_{LL}^{\alpha\beta} e^{-\Gamma_{LL} t} + C_{UU}^{\alpha\beta} e^{-\Gamma_{UU} t} + e^{-\Gamma_{UL} t} \left[(C_{LU}^{\alpha\beta} + C_{UL}^{\alpha\beta}) \cos(\tilde{\Omega}_R t) + i(C_{LU}^{\alpha\beta} - C_{UL}^{\alpha\beta}) \sin(\tilde{\Omega}_R t) \right] \end{aligned} \quad (4.5)$$

where $C_{\alpha'\beta'}^{\alpha\beta} = \langle\langle v_{\alpha'\beta'} | \rho(0) \rangle\rangle \langle\langle \alpha\beta | v_{\alpha'\beta'} \rangle\rangle$.

In general, the $\Gamma_{\alpha\beta}$ decay values in Eq. (4.3) for all JC Liouvillian eigenvalues exhibit a linear behavior as a function of the cavity and molecular decay rates. Some examples are plotted in the Fig. 4.4. The dependence on κ (cavity loss rate) can be observed in the left panel of the figure. Those eigenvalues of the form $\Gamma_{\Lambda_1\Lambda_1}$ increase linearly with slope $\kappa/2$, while those of the form $\Gamma_{\Lambda_2\Lambda_2}$ follow a line with slope $3\kappa/2$. All JC Liouvillian eigenvalues, except Γ_{GG} , are affected by the decay due to photon loss. In the right panel of the Fig. 4.4 the linear dependence with the cavity photon loss rate γ is also shown. Lower polaritons, both of first and second excitation manifolds, do not decay by molecular relaxation. In fact, in the absence of photon loss, the associated eigenvalues for $\lambda_{L_n L_n}$ ($n \geq 1$) would be zero, meaning that $|L_n\rangle$ states would be stationary. All the other eigenvalues are affected by molecular relaxation. The Γ decay values of both upper polaritons increase linearly with κ with a slope $\gamma/4$, while the coherences increase linearly with a slope $\gamma/8$.

These linear dependencies for the widths Γ in Fig. 4.4 were obtained for the full 25×25 Liouvillian matrix. They match perfectly with the analytical results obtained with the reduced model of Eq. (4.4). In conclusion, we can say that $\Gamma_{LL} \approx \kappa/2$, $\Gamma_{UU} \approx \kappa/2 + \gamma/4$, $\Gamma_{UL} = \Gamma_{LU} \approx \kappa/2 + \gamma/8$, $\Gamma_{L_2 L_2} \approx 3\kappa/2$, $\Gamma_{U_2 U_2} \approx 3\kappa/2 + \gamma/4$, $\Gamma_{U_2 L_2} = \Gamma_{L_2 U_2} \approx 3\kappa/2 + \gamma/8$.

⁶Solutions calculated in Mathematica, Wolfram Research, Inc.

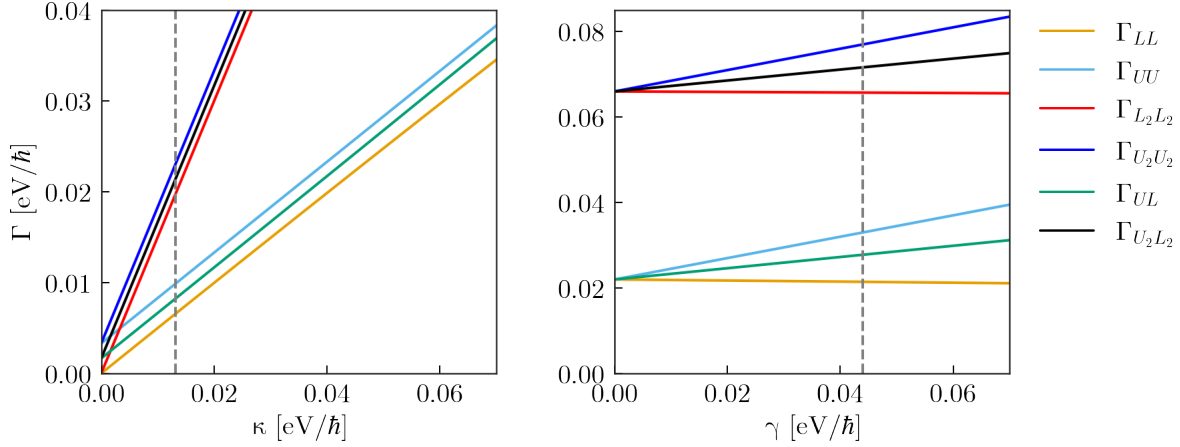


Fig. 4.4.: Negative real part (Γ in Eq. (4.3)) of some Liouvillian eigenvalues (those in the first block in the Fig. 4.2) in function of cavity photon losses rate κ (left panel) and in function of molecular relaxation rate γ (right panel). Gray dashed lines represent the fixed chosen values of $\gamma = 13$ meV/ \hbar and $\kappa = 44$ meV/ \hbar in each respective case. Hamiltonian JC parameters of Fig. 4.1 have been used.

Regarding the Liouvillian eigenstates, we describe below those that belong to the sub-block⁷ $\mathcal{L}_{\Lambda_1\Lambda_1}$. For the same parameters as in Fig. 4.1, we obtain⁸

$$\begin{aligned}
|v_{GG}\rangle &= |GG\rangle \\
|v_{LL}\rangle &= 0.7112 |GG\rangle - 0.6940 |LL\rangle - 0.0172 |UU\rangle \\
&\quad + (-0.0027 + 0.0782i) |UL\rangle + (-0.0027 - 0.0782i) |LU\rangle \\
|v_{UU}\rangle &= -0.7071 |LL\rangle + 0.7071 |UU\rangle \\
|v_{UL}\rangle &= (0.0056 - 0.2148i) |GG\rangle + (-0.0064 + 0.1074i) |LL\rangle + (0.0008 + 0.1074i) |UU\rangle \\
&\quad + 0.9646 |UL\rangle + (-0.0120 + 0.0077i) |LU\rangle \\
|v_{LU}\rangle &= |v_{UL}\rangle^\dagger
\end{aligned} \tag{4.6}$$

⁷The eigenstates obtained by diagonalizing the reduced sub-block $\mathcal{L}_{\Lambda_1\Lambda_1}$ remain unchanged when including the other states ($\Lambda_2\Lambda_2$) from the full 9×9 block of the Fig. 4.2 in the calculation. This is because the states in the reduced block do not evolve in time towards the $\Lambda_2\Lambda_2$ states.

⁸Double kets in terms of capital letters $|\alpha\beta\rangle$ (i.e. GG , LL , LU , etc.) refer to Hamiltonian eigenstates. Double kets denoted $|v_{\alpha\beta}\rangle$ refer to Liouvillian eigenstates, with subscripts according to the respective eigenvalue $\lambda_{\alpha\beta}$. For the sake of clarity, in the Liouvillian space $|\alpha\beta\rangle = |\alpha\rangle\langle\beta|$ and $|\beta\alpha\rangle = |\beta\rangle\langle\alpha| = |\alpha\beta\rangle^\dagger$.

We can also write the Hamiltonian basis of eigenstates in terms of the Liouvillian eigenstates:

$$\begin{aligned}
|GG\rangle &= |v_{GG}\rangle \\
|LL\rangle &= |v_{GG}\rangle - 1.4775 |v_{LL}\rangle \\
&\quad + (-0.0032 + 0.1183i) |v_{UL}\rangle + (-0.0032 - 0.1183i) |v_{LU}\rangle \\
|UU\rangle &= |v_{GG}\rangle - 1.4775 |v_{LL}\rangle + 1.4142 |v_{UU}\rangle \\
&\quad + (-0.0032 + 0.1183i) |v_{UL}\rangle + (-0.0032 - 0.1183i) |v_{LU}\rangle \\
|UL\rangle &= (-0.0113 + 0.3250i) |v_{LL}\rangle - 0.1556i |v_{UU}\rangle \\
&\quad + (1.0629 + 0.0016i) |v_{UL}\rangle + (-0.0132 - 0.0085i) |v_{LU}\rangle \\
|LU\rangle &= |UL\rangle^\dagger
\end{aligned} \tag{4.7}$$

With the knowledge of the eigenvalues and left/right eigenvectors of the Liouvillian, the time evolution of the density matrix is readily computed using the spectral decomposition of the time propagator as applied to the initially chosen state $|\rho(0)\rangle$, i.e., $|\rho(t)\rangle = \sum_{\alpha\beta} C_{\alpha\beta} e^{\lambda_{\alpha\beta} t} |v_{\alpha\beta}\rangle$, with $C_{\alpha\beta} = \langle\langle v_{\alpha\beta} | \rho(0) \rangle\rangle$.

4.2. Linear spectra

In order to study the linear response of the JC model subject to the radiation of a laser pulse, we calculate the linear absorption spectrum defined in Eq. (3.45) as

$$S_A^{(1)}(\omega) = 2\mathcal{R} \left\{ \int_0^\infty \langle a(t) a^\dagger(0) \rangle e^{i\omega t} \right\}, \tag{4.8}$$

and the linear emission spectrum for different laser frequencies ω_L (see Eq. (3.54))

$$S_E^{(1)}(\omega; \omega_L) = 2\mathcal{R} \left\{ \int_0^\infty \left[\langle a^\dagger(t) a(0) \rangle_{ss} - \lim_{t \rightarrow \infty} \langle a^\dagger(t) a(0) \rangle_{ss} \right] e^{-i\omega t} \right\}, \tag{4.9}$$

where we assume that only the cavity interacts with the laser pulse⁹. The subscript ss in the emission spectrum indicates that the expected value is calculated in the steady state of the system, by using the rotating frame transformation (see Subsec. 3.5.2). So far, in all the calculations we have presented, we have used the Bloch-Redfield formalism to simulate the molecular relaxation through a vibrational bath with spectral density function for broadening of the form

$$J_{\text{Step}}(\omega) = \eta \Theta(\omega), \tag{4.10}$$

with $\Theta(\omega)$ the Heaviside step function. Note that in this case η is identical to γ introduced previously for the molecular relaxation rate. Unless otherwise stated, we take the temperature to be $T = 0$, so that the bath noise-power spectrum defined in Eq. (2.87) is equivalent to the spectral function, i.e., $S(\omega) = J(\omega)$. At this point, we can evaluate the possibility of using other spectral density functions

⁹For closed cavities, the laser interacts with the system (cavity+molecules) solely through the cavity mirrors. The cavity operator representing this interaction is $a + a^\dagger$. For open cavities, such as plasmonic cavities, the plasmonic dipoles are often much larger than molecular dipoles. Thus, in either situation, when interacting with laser pulses, only the cavity operators are taken into account.

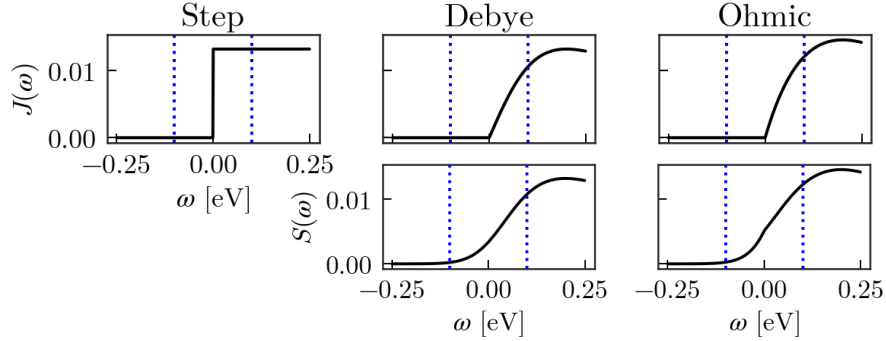


Fig. 4.5.: Different vibrational bath spectral densities $J(\omega)$ (upper panel) and their respective bath noise-power spectrum $S(\omega)$ defined in Eq. (2.87) (lower panel) to be used in the Bloch-Redfield formalism to simulate molecular relaxation. The functions employed here are (see (Eq. (4.10)-Eq. (4.12))) the step function $J_{\text{Step}}(\omega)$ with $\eta = \gamma = 0.0132$ eV (left panel), the Debye function $J_{\text{Debye}}(\omega)$ with $\eta = 2\gamma = 0.0264$, $\omega_d = 0.2$ eV and a temperature of 300 K in the noise-power spectrum function $S(\omega)$ (middle panel); and the Ohmic function $J_{\text{Ohmic}}(\omega)$ with $\eta/\omega_d = 15$ eV $^{-1}$, $\omega_d = 0.2$ eV and a temperature of 300 K in the noise-power spectrum $S(\omega)$ (right panel). Vertical dotted lines indicate the position of the Rabi frequency $\pm\Omega_R = \pm 0.1$ eV.

and observe what happens to the linear response spectra. In particular, we test a Debye function and an Ohmic function, which are defined as follows

$$J_{\text{Debye}}(\omega) = \frac{\eta\omega\omega_d}{\omega^2 + \omega_d^2}\Theta(\omega), \quad (4.11)$$

$$J_{\text{Ohmic}}(\omega) = \eta\frac{\omega}{\omega_d}e^{-\omega/\omega_d}\Theta(\omega). \quad (4.12)$$

In all the cases η is a dimensionless parameter that accounts for the system-bath coupling strength and ω_d is a cutoff frequency. The three spectral density functions are plotted¹⁰ in the upper panel of Fig. 4.5. At zero temperature, using the step function as considered in the previous calculations, the linear absorption and emission spectra are shown respectively in the panel labeled *Step* in Fig. 4.6. We can observe in the absorption spectrum two peaks corresponding to the polariton states $|L\rangle$ and $|U\rangle$, located at their respective frequencies $\omega_{LG} = 1.95$ eV and $\omega_{UG} = 2.05$ eV. It is expected for the upper polariton $|U\rangle$ to exhibit a lower absorption peak than the lower polariton $|L\rangle$, because $|U\rangle$ generally has higher decay rates. In particular, it has an additional decay channel, through molecular relaxation, towards $|L\rangle$ (see left panel of Fig. 4.1). However, this expected asymmetry between the two absorption peaks cannot be simulated by using a Lindblad term for the molecular dephasing-type operator $\sigma^\dagger\sigma$. In fact, if a Lindblad term is introduced for this operator, two completely symmetric peaks are obtained for both polaritons, as observed in the panel labeled as *Lindblad 1* in Fig. 4.6. The excitation-emission spectra of these two models are also completely different. While in the Bloch-Redfield step function model, a single predominant peak is observed at $(\omega_L = \omega_{UG}, \omega = \omega_{LG})$, in the

¹⁰Henceforth, in all spectral plots, we will use energy units for the frequencies.

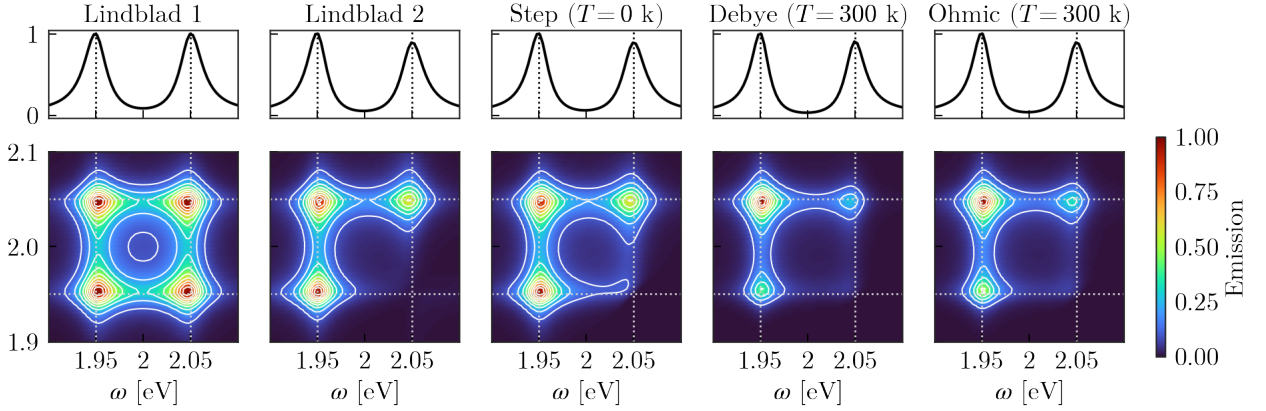


Fig. 4.6.: Normalized linear absorption spectra (upper panel) and linear emission spectra (lower panel) for different models of molecular relaxation. In the panel labeled as Lindblad 1, molecular relaxation is introduced as a Lindblad term for the operator $\sigma^\dagger\sigma$, with the decay rate $\gamma = 13$ meV/ \hbar . In the panel labeled as Lindblad 2, a Lindblad term has also been used, but for the upper triangle of the operator $\sigma^\dagger\sigma$ in the basis of JC Hamiltonian eigenstates, with the same rate $\gamma = 13$ meV/ \hbar . In the other three models, the Bloch-Redfield formalism is used with the respective labeled bath spectral density function with the same parameters as in the Fig. 4.5. The emission spectra have been plotted for different laser frequencies ω_L . Dotted lines indicate the lower and upper polariton frequencies, respectively. The parameters for the JC model are those of Fig. 4.1.

Lindblad 1 model, two symmetric diagonal peaks along with two symmetric cross-peaks are observed. The reason for this symmetry is that the Lindblad 1 model allows for transitions in both the $|U\rangle \rightarrow |L\rangle$ and the $|L\rangle \rightarrow |U\rangle$ directions, each occurring at the same rate. This additional pumping from L to U polariton, which is not permitted in the Bloch-Redfield step function model, leads to the emergence of the other symmetric cross-peak in the emission spectrum.

In general, each peak in this spectrum indicates that upon exciting the system with a laser frequency ω_L (as read in the y -axis), once the system reaches the steady state, it can be detected at the frequency ω (as read in the x -axis). In this regard, it is worth noting that in the Bloch-Redfield step function model, it is possible to excite U , then wait for its decay towards L , and finally detect L . However, in the Lindblad 1 model, it is also possible to excite through L and to detect in U , in addition to the trivial excitation-emission by the same states (diagonal peaks). One way to avoid the nonphysical $L \rightarrow U$ pumping even within the Lindblad formalism is to eliminate the matrix elements of the $\sigma^\dagger\sigma$ operator (expressed in the JC Hamiltonian eigenbasis ordered by energy) that produce transitions from lower to higher energy levels and to consider only the upper triangle in the Lindbladian matrix, which produce the physical transition from higher to lower energy levels. By introducing only the upper triangle of the $\sigma^\dagger\sigma$ operator as a Lindblad term, we obtain the results quoted as Lindblad 2 in the Fig. 4.6. With this modification, the $L - U$ asymmetry in the linear absorption peaks is restored.

Additionally, the L/U peak¹¹ in the emission spectrum also disappears in the Bloch-Redfield model with a step function for $J(\omega)$. When comparing the models Lindblad 1 (in which $\sigma^\dagger\sigma$ is introduced as a standard Lindblad term), Lindblad 2 (in which only the upper triangle of $\sigma^\dagger\sigma$ is introduced as a Lindblad term) and Step model (in which $\sigma^\dagger\sigma$ is introduced through the Bloch-Redfield formalism with $J(\omega)$ as step function) (see the first three panels of Fig. 4.6), we consider that the latter Bloch-Redfield model fits better the expected behavior at zero temperature. At this same zero temperature, if the step function is replaced with the Debye or the Ohmic function in the Bloch-Redfield formalism for molecular relaxation, the resulting spectra do not differ significantly from those obtained with the (zero temperature) step function. For this reason, these plots are not shown. However, the Debye and Ohmic spectral density functions are useful for studying temperature effects on the spectra. These effects can be incorporated by using the bath noise-power spectrum $S(\omega)$ [95], defined in Eq. (2.87).

The function $S(\omega)$ is plotted in the lower panel of Fig. 4.5 for the Debye and Ohmic bath spectral density functions. These functions, at a temperature $T > 0$, do not vanish for negative frequencies. For instance, there is a small contribution at the negative value of the Rabi frequency (as seen in the dotted lines of the Fig. 4.5), indicating that for temperatures other than zero, there is still a small rate of $L \rightarrow U$ pumping. However, this rate is much smaller than the $U \rightarrow L$ decay rate. Note that $S(0)$ is only well-defined if $\lim_{\omega \rightarrow 0} J(\omega)/\omega$ exists, which is not the case for the step function. The spectra obtained by using both $S(\omega)$ functions (for Debye and Ohmic) in the Bloch-Redfield formalism at a temperature of 300 K are shown in the two rightmost panels in Fig. 4.6, respectively. When comparing the spectra obtained by using the Debye and the Ohmic spectral density functions, no significant differences are observed. This leads us to conclude that the Bloch-Redfield formalism only weakly depends upon the choice for the spectral function as long as it is sufficiently smooth. Consequently, in the following, when investigating temperature effects, our choice will be the Debye function by default. The effect of temperature is only observed in the reduction of the cross-peaks intensity.

4.3. Two-dimensional non-linear spectra (2DS)

We again deal with the JC model relaxed by photon loss and molecular vibrational relaxation (described by the Bloch-Redfield formalism and using the step function for zero temperature). This polariton system is then subject to the interaction with the three delayed pulses of the 2D spectroscopy protocol. At different waiting times T , we compute the respective 2D nonlinear electronic spectra (2DS) $S_{(\text{NR}+\text{R})}^{(3)}(\omega_\tau, T, \omega_t)$, including the non-rephasing and the rephasing components. The Fig. 4.7 shows both the absolute value of the spectra (i.e., $|S_{(\text{NR}+\text{R})}^{(3)}(\omega_\tau, T, \omega_t)|$) along with the 2D absorptive spectrum (i.e., the real part $\mathcal{R}[S_{(\text{NR}+\text{R})}^{(3)}(\omega_\tau, T, \omega_t)]$). Nonlinear spectroscopy allows us to track the dynamic evolution of the system by collecting a series of snapshots of the 2DS at different waiting times T . Additionally, due to the presence of a third laser, we have access to states within the second excitation manifold.

¹¹ Henceforth, when we refer to the α/β peak in any 2D spectrum, it corresponds to an excitation with the α state frequency and a detection through the β state frequency.

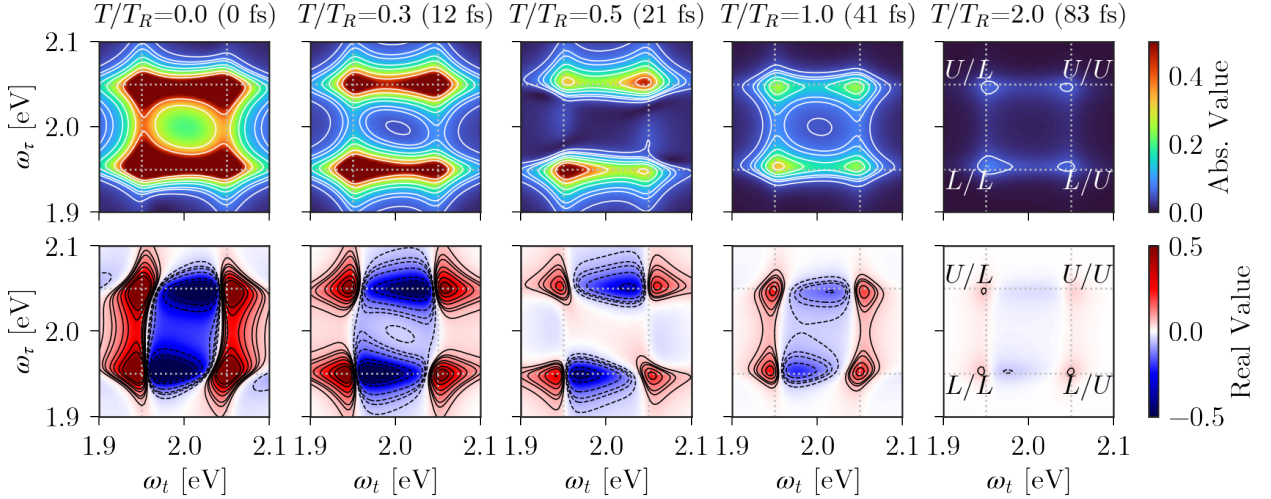


Fig. 4.7.: Two-dimensional non-linear electronic spectra (2DS) for the open JC model at different waiting times T . Both the absolute value $|S_{(\text{NR}+\text{R})}^{(3)}(\omega_\tau, T, \omega_t)|$ (upper panel) and the real value or 2D absorptive spectra $\mathcal{R}[S_{(\text{NR}+\text{R})}^{(3)}(\omega_\tau, T, \omega_t)]$ (lower panel) are plotted. The parameters of the model are chosen as in Fig. 4.1. Dotted right lines indicate the lower and upper polariton frequencies. All spectra are normalized to the maximum real value at time $T = 0$. The plots have been truncated to half of this maximum. The excitation frequency ω_τ lies along the y -axis, while the detection frequency ω_t lies along the x -axis. Solid contour lines at heights $[0.05, 0.08, 0.1, 0.15, 0.2, 0.3, 0.4]$ are included in the absolute spectrum and their negative counterparts also for the absorptive spectra.

In the 2D spectra, plotted as the absolute values, $|S_{(\text{NR}+\text{R})}^{(3)}(\omega_\tau, T, \omega_t)|$, shown in the upper panel of Fig. 4.7, four peaks can be observed located around the points quoted in the figure as L/L , L/U , U/L and U/U , where the frequencies of the L and U polaritons intersect. These peaks are separated by the Rabi frequency of the polariton system ($\Omega_R = \omega_{UL} = 0.1$ eV). We also appreciate that peaks slightly shift their positions with increasing waiting time T . However, the shape of the four peaks are quite similar, with the peak L/L always being the most intense. The cross peak L/U approximately displays a similar intensity as the U/L peak at any waiting time T . On the other hand, the absorptive spectra $\mathcal{R}[S_{(\text{NR}+\text{R})}^{(3)}(\omega_\tau, T, \omega_t)]$, shown in the lower panel of Fig. 4.7 exhibit both positive and negative peaks. At any waiting time T , there are four positive peaks representing transitions between Λ_0 and Λ_1 , and two negative peaks representing transitions between Λ_1 and Λ_2 . The separation between a negative peak and its paired positive peak in the L/L and U/U positions is a measure of the anharmonicity of the system. If the system were completely harmonic, both peaks would be located at the same position in the spectrum, and they tend to cancel to each other because of their opposite sign, resulting in a null 2DS. As the number of molecules inside the cavity increases, using a Tavis-Cummings model to represent the system, the whole polariton system becomes increasingly harmonic. Therefore, it is expected, as it will be confirmed later, that the most intense 2DS correspond to the JC case (with a

single molecule), and the 2DS intensity gradually decreases by augmenting the number of molecules, because harmonicity is being gained. The case with a higher number of molecules will be considered and studied with more detail in subsequent chapters.

4.4. Contributing pathways

During the 2D spectroscopy protocol, which involves the interaction of the system with three time-delayed pulses (see [Subsec. 3.6.1](#)), multiple processes of excitation and de-excitation occur simultaneously at each step of the protocol. In terms of the JC excitation manifolds, these processes can be summarized with the double-sided Feynman diagrams plotted in the [Fig. 4.8](#). All these interfering paths contribute to the signal used to construct the 2D maps shown in [Fig. 4.7](#). Please note that the rephasing and non-rephasing pathways only differ during the excitation process (Pulse 1 + Evolution τ + Pulse 2, shaded region in the [Fig. 4.8](#)). With the first pulse interaction, non-rephasing diagrams involve coherences of the form $|\Lambda_1\rangle\langle G|$, while rephasing diagrams involve coherences of the adjoint

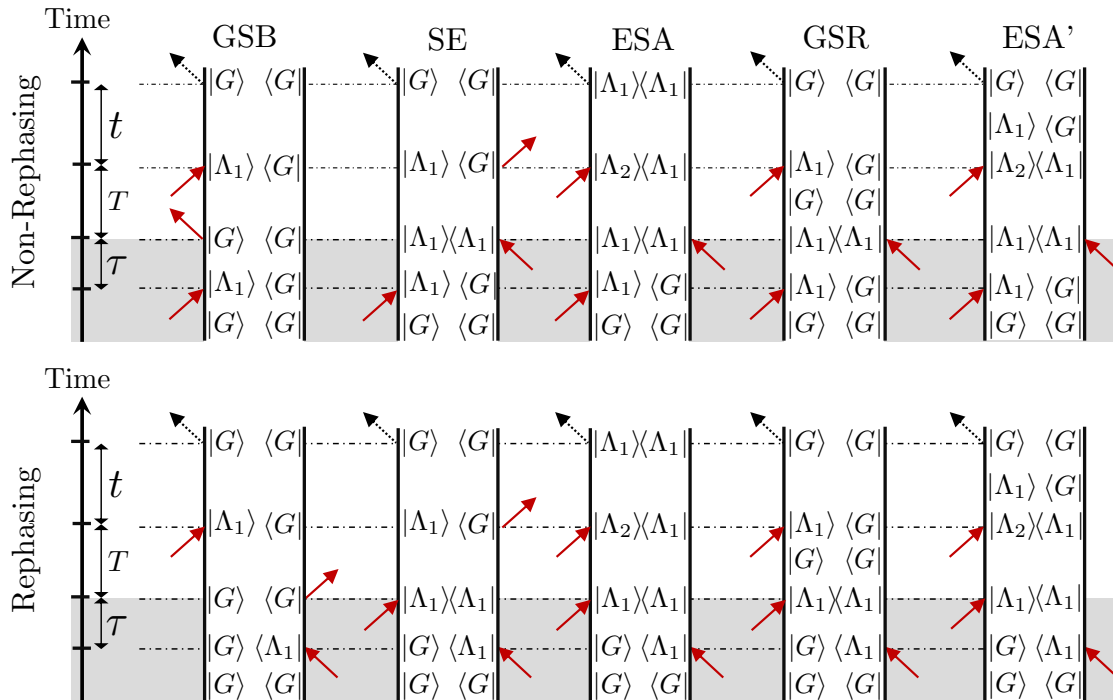


Fig. 4.8.: Total non rephasing (upper panel) and rephasing (lower panel) double-side Feynman diagrams illustrating the processes occurring during the 2D spectroscopy protocol. These diagrams are valid for both the JC and Tavis-Cummings models. Here, excitation manifolds Λ_i are considered instead of individual system states. The shaded region represents the whole excitation process, the only part where the rephasing and non-rephasing diagrams differ. Note that $|\Lambda_1\rangle\langle\Lambda_1|$ indicates both populations and coherences within the first excitation manifold.

form $|G\rangle\langle\Lambda_1|$. After the interaction with the second pulse, rephasing and non-rephasing signals involve the same type of intermediate and final states. The GSB (Ground State Bleaching), SE (Stimulated Emission), and ESA (Excited State Absorption) diagrams arise from the different terms obtained when applying the dipole superoperator to the density matrix of the system for each pulse interaction (see [Subsec. 3.5.3](#)). On the other hand, the GSR (Ground State Recovery) and ESA' (Excited State Absorption, prime) diagrams represent new processes resulting from the decay due to cavity photon loss during the waiting time T and during the detection time t , respectively. The GSR signals arise from decays of the type $|\Lambda_1\rangle\langle\Lambda_1| \rightarrow |G\rangle\langle G|$ during T , and the ESA' signals from decays of coherences in the form $|\Lambda_2\rangle\langle\Lambda_1| \rightarrow |\Lambda_1\rangle\langle G|$ during the detection time t . These photonic decays occur between different excitation manifolds $\Lambda_i \rightarrow \Lambda_j$, which allows us to explicitly identify them as new pathways in our excitation manifold notation. On the other hand, decays through vibrational relaxation occur between states of the same excitation manifold. This prevents us from explicitly identifying them in the diagrams shown in the [Fig. 4.8](#). However, we will analyze these decays in more detail later and introduce their respective pathways.

The Feynman diagrams, in terms of excitation manifolds, are valid for both the JC and the Tavis-Cummings models. The kets $|\Lambda_i\rangle$ and bras $\langle\Lambda_i|$ ($i = 1, 2$) appearing in the pathways represent any of the states (belonging to the respective excitation manifold Λ_i) involved at each step of the spectroscopic protocol. For example, for the interaction with the first pulse, $|\Lambda_1\rangle = \{|L\rangle, |U\rangle\}$ (for non-rephasing diagrams) and $\langle\Lambda_1| = \{\langle L|, \langle U|\}$ (for rephasing diagrams) since both polariton states can be excited

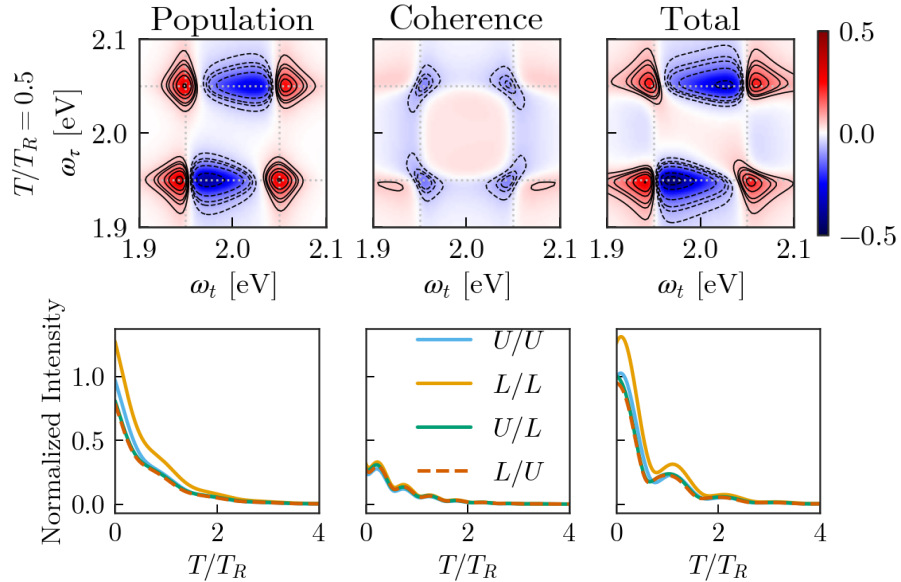


Fig. 4.9.: Upper panel: population (left), coherence (middle), and total (right) absorptive 2DS for open JC at $T = 0.5 T_R$. Same normalization and contour lines as in [Fig. 4.7](#). Lower panel: temporal T evolution of absolute value of the population (left), coherence (middle), and total (right) 2DS peaks.

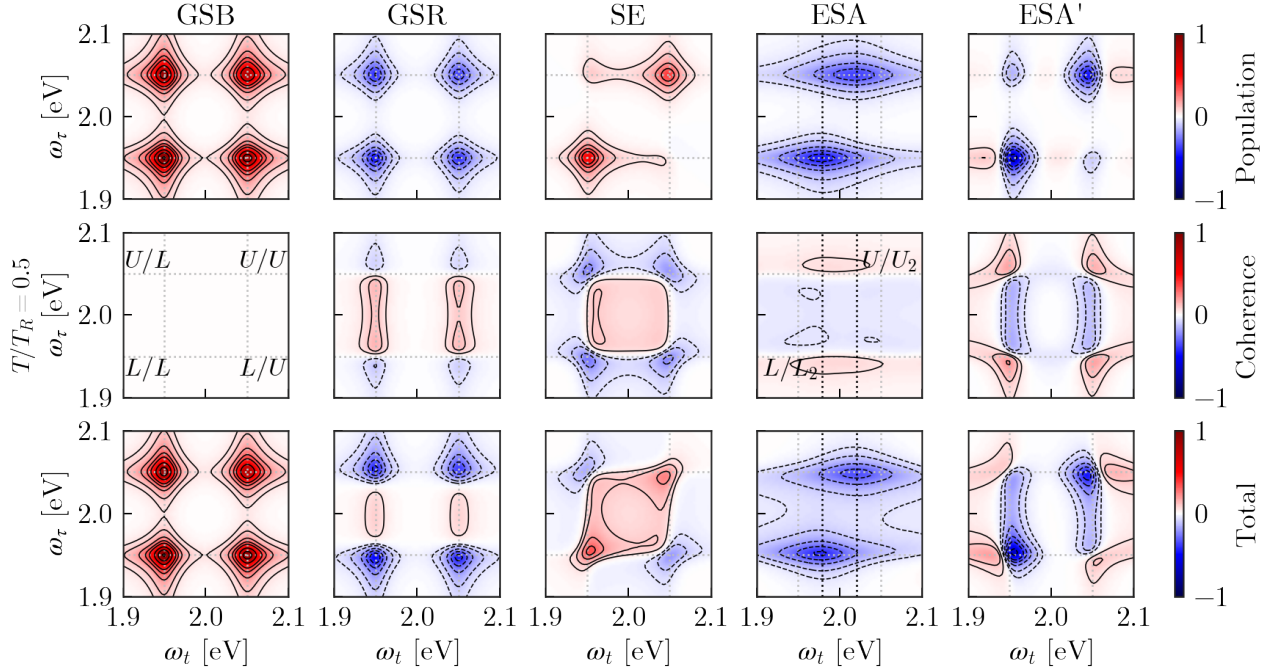


Fig. 4.10.: Contributions to the open JC absorptive 2DS $\mathcal{R}[S_{(\text{NR}+\text{R})}^{(3)}(\omega_\tau, T, \omega_t)]$, at the waiting time $T = 0.5 T_R \approx 20.73$ fs. The contributions (rephasing + non-rephasing) have been separated into population pathways (upper panel) and coherence pathways (middle panel). The combination of both are represented in the lower panel. Same normalization as in Fig. 4.7. The gray dotted lines represent the frequencies of the polariton states $\omega_{LG} = 1.95$ eV and $\omega_{UG} = 2.05$ eV. The black dotted straight lines in the ESA spectra represent the frequencies $\omega_{L_2L} = 1.98$ eV and $\omega_{U_2U} = 2.02$ eV. Contour lines at $\pm[0.05, 0.1, 0.2, 0.3, 0.4, 0.6, 0.8, 1]$.

from the ground state $|G\rangle$ with a dipole transition (see Fig. 4.1). In the interaction with the second pulse, for the diagrams that lead to $|\Lambda_1\rangle\langle\Lambda_1|$, we would then have 4 possibilities: the populations $\{|L\rangle\langle L|, |U\rangle\langle U|\}$ (they, along with the GSB pathways, give rise to what we will call **population pathways**) and the polariton coherences $\{|L\rangle\langle U|, |U\rangle\langle L|\}$ (that give rise to **coherence pathways**). The population, coherence, and total spectra obtained from these respective pathways are displayed in Fig. 4.9 at a specific waiting time of $0.5 T_R$. The population spectrum broadly encompasses the most relevant features of the total spectrum. In the lower panel of the Fig. 4.9, we observe the time evolution of each peak in 2DS (in absolute value) vs the waiting time T , for population, coherence and total spectra, respectively. The coherence spectrum has a lower intensity contribution but highlights the oscillations that are evident in the total spectrum, occurring with the Rabi frequency of the system.

The Fig. 4.10 displays the JC 2DS contributions (rephasing + non-rephasing) for population and coherence pathways, and the sum of both, at the waiting time $T = 0.5 T_R$. The summation of all contributions from this figure yields the respective absorptive 2DS in Fig. 4.9. Since during the excitation process, only the upper and lower polariton states (U and L) are involved, all the signals in the 2DS

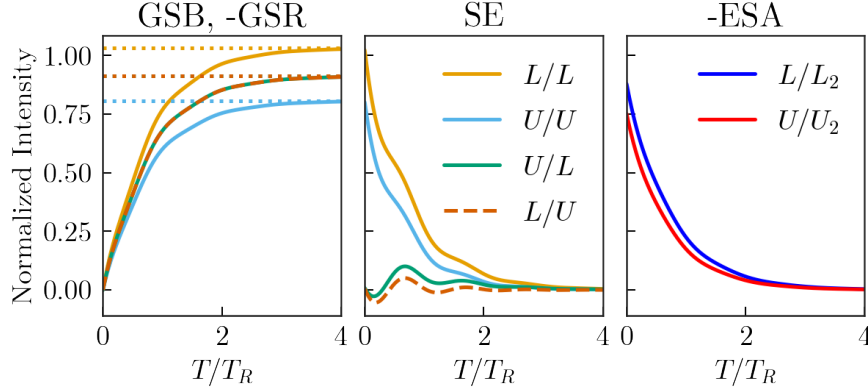


Fig. 4.11.: Temporal evolution during T (units of $T_R = 41.47$ fs) of the peak intensities appearing in each contribution to the absorptive population 2DS: GSB (dotted lines in the left panel), -GSR (solid lines in the left panel), SE (middle panel) and -ESA (right panel). The GSB L/U peak intensity coincides with the GSB U/L peak. For GSB, -GSR and SE, we consider peaks L/L ($\omega_\tau = \omega_t = \omega_{LG} = 0.95$ eV), U/U ($\omega_\tau = \omega_t = \omega_{UG} = 2.05$ eV), U/L ($\omega_\tau = \omega_{UG}, \omega_t = \omega_{LG}$), and L/U ($\omega_\tau = \omega_{LG}, \omega_t = \omega_{UG}$). In -ESA contribution, we consider the peaks L/L_2 ($\omega_\tau = \omega_{LG}, \omega_t = \omega_{L_2L} = 1.98$ eV), and U/U_2 ($\omega_\tau = \omega_{UG}, \omega_t = \omega_{U_2U} = 2.02$ eV). The same intensity normalization as in Fig. 4.7 has been used.

are located at their respective excitation frequencies, $\omega_\tau = \omega_{UG}$ (upper peaks) and $\omega_\tau = \omega_{LG}$ (lower peaks). In practical 2D spectroscopy experiments, during the excitation process, the pulses do not manage to produce polariton coherences with amplitudes as relevant as those obtained theoretically when considering laser pulses as temporal delta functions (sudden perturbation limit). For this reason, we will focus our attention on studying in more detail the 2DS formed only by population pathways. These spectra provide valuable insights into the dynamics of population transfer between polariton states.

The contributions to the population 2DS exhibit clearly localized (positive or negative) peaks, at the frequencies $\omega_\tau = \{\omega_{LG}, \omega_{UG}\}$ and $\omega_t = \{\omega_{LG}, \omega_{UG}\}$ for GSB, GSR, SE and $\omega_t = \{\omega_{L_2L}, \omega_{U_2U}\}$ for ESA. We can keep track of the evolution of the intensity of these peaks as a function of T (see Fig. 4.11), and therefore to extract information from the system dynamics. Let us study each contribution to the population spectrum separately.

4.4.1. GSB (Ground State Bleaching) and GSR (Ground State Recovery)

The intensity of the four peaks (diagonal and cross peaks) of the GSB contribution to population¹² 2DS in Fig. 4.10 can be plotted as a function of the waiting time T . These intensities remain constant along T (see dotted lines in left panel of Fig. 4.11). This is because in the GSB pathways the system returns to the ground state after the excitation process (see Fig. 4.8 and Fig. 4.12), and the ground

¹²There is no GSB contribution to the coherence 2DS since in GSB pathways no coherences are formed after the excitation process (only the population in $|GG\rangle$ contribute to GSB paths).

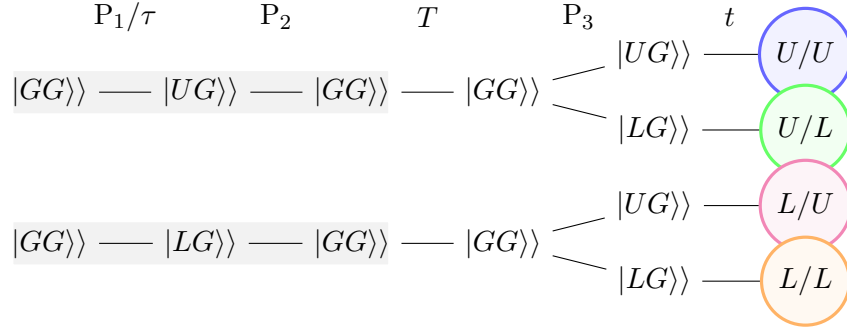


Fig. 4.12.: GSB non-rephasing relevant pathways for separated excitation of polaritons L (lower paths) and U (upper paths), respectively, and their contributions to each region around the diagonal peaks L/L and U/U and cross peaks L/U and U/L (colored circles) within the 2DS. The shaded gray region represents the excitation process. Each P_i ($i=1,2,3$) indicates the interaction with each pulse of the 2D spectroscopy protocol.

state does not evolve during T . In the Fig. 4.12 we make use of a notation that involves individual states instead of excitation manifolds and only for the non-rephasing¹³ contribution. This notation allows to separate the absorption of both polaritons L or U during the excitation process. The absorption of the upper polariton is represented in the upper paths of the Fig. 4.12 and the absorption of the lower polariton is represented in the lower paths. Additionally, this Fig. 4.12 shows which region within the 2DS is contributed by each pathway. For example, we can see that GSB diagonal peaks U/U and L/L represent respectively the absorption of U and L during both excitation and detection processes. It explains that the intensity of the GSB L/L peak (see again Fig. 4.11) be higher than that of the U/U peak. It is due to the higher absorption peak that L exhibits, compared to U , as indicated by the linear absorption spectrum (see Fig. 4.6). On the other hand, the cross peak U/L represents the absorption of U during excitation and of L during detection whereas the cross peak L/U represents the absorption of L during excitation and of U during detection. It explains that both cross peaks have the same intensity, as they involve the absorption of both L and U , although at different moments in the 2D spectroscopy protocol. In conclusion, except for a normalization factor, *any cut along the excitation or detection frequency in the GSB component of the 2DS yields the linear absorption spectrum.*

In the Fig. 4.12, the action of the first pulse (P_1) and the evolution during τ are combined into a single process. This is because, if the first pulse creates the coherence $|UG\rangle\rangle$ (upper pathway of the Fig. 4.12), for example, then this coherence can migrate to the coherence $|LG\rangle\rangle$ during the excitation time τ . This migration is due to both photon loss and molecular relaxation (see the third block in the Fig. 4.2), giving rise to a new pathway that is not illustrated in the Fig. 4.12. However, this migration is small compared to the amplitude that remains in $|UG\rangle\rangle$, and therefore, the most relevant pathway is the one shown at the top of the figure. The same analysis applies if the initial coherence is $|LG\rangle\rangle$ (lower pathway of the figure).

¹³The same conclusions in this section apply for the rephasing diagrams.

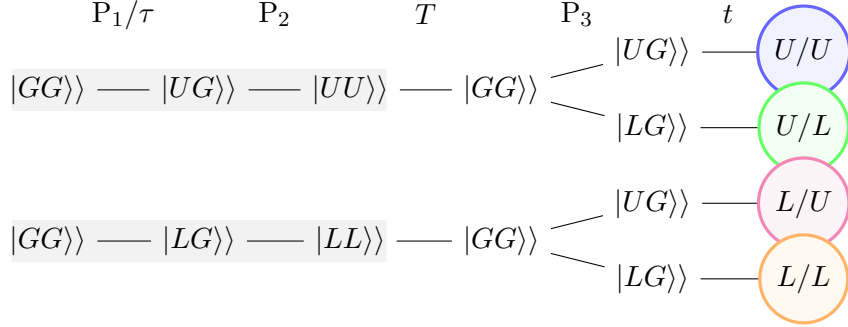


Fig. 4.13.: GSR non-rephasing relevant pathways for separated excitation of polaritons L (lower paths) and U (upper paths), respectively and their contributions to each region around the peaks L/L , U/U , L/U , and U/L within the 2DS. We use the same notation as in Fig. 4.12.

Fig. 4.13 displays the most relevant pathways for each peak in the GSR population spectrum. It is noteworthy that, unlike the GSB pathways where the system returns to the ground state during the excitation process, in this case, the polariton states L and U from the first excitation manifold are populated. However, a portion of the population in these states decays back to the ground during the evolution T . This recovered population in the ground state, originating from the polaritons in the first excitation manifold, produces the GSR pathways. It is therefore expected that the intensity of each GSR peak exhibits the same time evolution as the $\rho_{GG}(T)$ component of the density matrix when evolving from the initial condition of either $\rho(0) = |L\rangle\langle L|$ or $\rho(0) = |U\rangle\langle U|$. Indeed, if we recall the dynamic evolution of the polariton states (left and middle panel of Fig. 4.3), we observe that $\rho_{GG}(T)$ displays the same behavior as any of the GSR peaks (in Fig. 4.11), except for certain normalization factors. These normalization factors are again related to the absorption of each state and are precisely the values of the GSB intensities for each peak. In general, for the JC model, with $\alpha, \beta = \{L, U\}$, we have the following relationship for each α/β peak in the GSR component of the population spectrum

$$\alpha/\beta_{\{\text{GSR}\}}(T) = -\alpha/\beta_{\{\text{GSB}\}} \times \rho_{GG}(T; |\alpha\rangle), \quad (4.13)$$

where $\rho_{GG}(T; |\alpha\rangle)$ indicates the component $\rho_{GG}(T)$ of the system density matrix, when the initial condition is the state $|\alpha\rangle$. The minus sign indicates that the GSR contribution has an opposite sign to the GSB, and then the negative values of the GSR intensities are shown in the Fig. 4.11. The component GSR of the population spectrum thus allows us to extract the dynamics of the decays $L \rightarrow G$ and $U \rightarrow G$. With our JC model (see Fig. 4.3 and Eq. (4.4)), $\rho_{GG}(T; |L\rangle) = \rho_{GG}(T; |U\rangle) \approx 1 - \exp(-\kappa/2 T)$, i.e., the decay rate of the transitions $L \rightarrow G$ and $U \rightarrow G$ (mediated by photon losses) is $\kappa/2$ (remember that κ is the cavity decay rate), which also corresponds to the decay rate of the GSR peaks.

When each polariton state, either L or U , completely decays into the ground state G , $\rho_{GG} = 1$, and therefore the condition GSR=-GSB is fulfilled, meaning that GSB and GSR contributions cancel each other for long waiting times T . This represents the simple physical fact that for long enough times T ,

the dissipative system studied here will return to its ground state and lose all memory of the excitation pulse sequence. In the Fig. 4.11, it can be observed that this effect occurs at $T \sim 3 T_R$, both for the state L (L/L peak) and for the state U (U/U peak). Later, in our study of the Tavis-Cummings model with 2 emitters, we will observe that this behavior changes due to the presence of the dark state in the first excitation manifold. In that case, the cancellation of the GSB and GSR spectra occurs at different times for L and U , due to the new channel decay from U to the dark state.

4.4.2. SE (Stimulated Emission)

Fig. 4.14 displays the population SE pathways for each polariton L and U . Similar to the GSR spectrum, the SE spectrum reveals features of the populations of L and U attained during the excitation process. In this case, we focus not on the population that decays to the ground state but on the population that remains in L and U during the evolution T . This population, which is subsequently transferred to the ground state with the action of the third pulse, gives rise to the SE spectra.

By observing the first block of the Fig. 4.2, we notice that the Liouvillian dynamics during the waiting time T allows for the direct transfer $|UU\rangle\rangle \rightarrow |LL\rangle\rangle$ through vibrational relaxation and the transfer from $|UU\rangle\rangle$ to the coherences $|UL\rangle\rangle$ and $|LU\rangle\rangle$ via photon loss. Therefore, if the state U is populated during the excitation process (upper pathways in the Fig. 4.14), part of the population remains in U during T (contributing to the U/U peak) while another part migrates to L (contributing to the U/L peak). Additionally, the coherences $|UL\rangle\rangle$ (contributing to the U/U peak) and $|LU\rangle\rangle$ (contributing to the U/L peak) are formed during T . Consequently, the evolution during T of the SE U/U peak (middle panel of Fig. 4.11) should account for the components $\rho_{UU}(T;|U\rangle\rangle)$ and $\rho_{UL}(T;|U\rangle\rangle)$ of the system density matrix. On the other hand, the peak U/L should account for the components $\rho_{LL}(T;|U\rangle\rangle)$ and $\rho_{LU}(T;|U\rangle\rangle)$. We find the following relationships:

$$U/U_{\{\text{SE}\}}(T) \approx U/U_{\{\text{SE}\}}(0) [\rho_{UU}(T;|U\rangle\rangle) - \rho_{UL}(T;|U\rangle\rangle)] \quad (4.14)$$

$$U/L_{\{\text{SE}\}}(T) \approx \rho_{LL}(T;|U\rangle\rangle) - \rho_{LU}(T;|U\rangle\rangle) = \rho_{LL}(T;|U\rangle\rangle) - \rho_{UL}(T;|U\rangle\rangle). \quad (4.15)$$

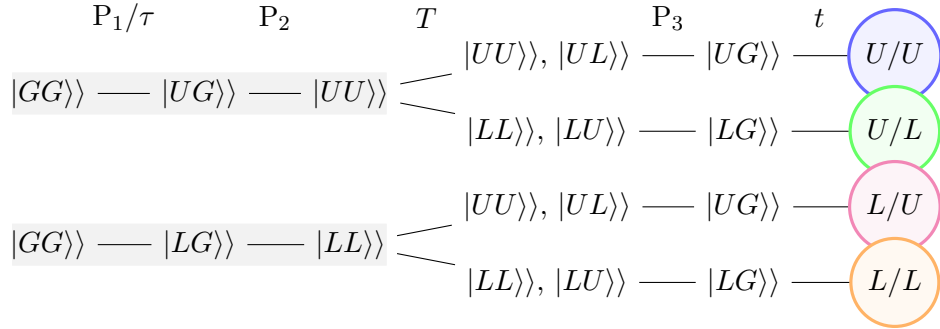


Fig. 4.14.: SE non-rephasing relevant pathways for separated excitation of polaritons L (lower paths) and U (upper paths), respectively and their contributions to each region around the peaks L/L , U/U , L/U , and U/L within the 2DS.

Now, let us focus on the excitation of L (lower pathways in the Fig. 4.14). From the first block of the Liouvillian (Fig. 4.2), we observe that during the waiting time T , the $|LL\rangle\rangle$ population produces coherences $|LU\rangle\rangle$ and $|UL\rangle\rangle$ formed by photon loss. However, the direct transfer $|LL\rangle\rangle \rightarrow |UU\rangle\rangle$ is not allowed. Therefore, one might think that the evolution of the SE peaks L/L and L/U accounts only for the components $\rho_{LL}(T;|L\rangle\rangle)$, $\rho_{LU}(T;|L\rangle\rangle)$, and $\rho_{UL}(T;|L\rangle\rangle)$ of the system density matrix. However, as can be seen in the left panel of Fig. 4.3, the component $\rho_{UU}(T;|L\rangle\rangle)$ also becomes slightly populated during the time evolution of $\rho(0) = |L\rangle\rangle\langle L|$, and this small contribution must be considered in the 2DS. In this sense, we have that the SE L/L peak must account for both $\rho_{LL}(T;|L\rangle\rangle)$ and $\rho_{LU}(T;|L\rangle\rangle)$, while the L/U peak must account for $\rho_{UU}(T;|L\rangle\rangle)$ and $\rho_{UL}(T;|L\rangle\rangle)$, and we find the approximated relationships

$$L/L_{\{SE\}}(T) \approx L/L_{\{SE\}}(0) [\rho_{LL}(T;|L\rangle\rangle) - \rho_{LU}(T;|L\rangle\rangle)] \quad (4.16)$$

$$L/U_{\{SE\}}(T) \approx \rho_{UU}(T;|L\rangle\rangle) - \rho_{UL}(T;|L\rangle\rangle) = \rho_{UU}(T;|L\rangle\rangle) - \rho_{LU}(T;|L\rangle\rangle). \quad (4.17)$$

At $T = 0$, no SE cross peaks are formed in the population 2DS (L and U , initially populated during the excitation process, do not decay yet). On the other hand, the SE diagonal peaks L/L and U/U show an initial non-zero value (see middle panel of Fig. 4.11), which, once again, accounts for the absorption intensities of both polaritons and it precisely corresponds to the respective values of the GSB contribution in each diagonal peak.

In our open JC model, the identity $\rho_{UL}(T;|U\rangle\rangle) = \rho_{UL}(T;|L\rangle\rangle)$ holds. Therefore, by subtracting the intensity of the $L/U_{\{SE\}}$ peak from the $U/L_{\{SE\}}$ peak, we obtain (see the Liouvillian matrix Eq. (4.4) for an insight) $\rho_{LL}(T;|U\rangle\rangle) - \rho_{UU}(T;|L\rangle\rangle) \approx \exp(-\kappa/2 T)(1 - \exp(-\gamma/4 T))$, meaning that we can extract the dynamics of the transfer $U \rightarrow L$, but in combination with the transfer $L \rightarrow U$. If the contribution $L \rightarrow U$ is small, the subtraction of these SE cross-peak intensities allows us to directly extract the dynamic information about the decay $U \rightarrow L$ mediated by vibrational scattering. The Fig. 4.15 allows us to compare $\rho_{LL}(T;|U\rangle\rangle)$, $\rho_{UU}(T;|L\rangle\rangle)$, $\rho_{LL}(T;|U\rangle\rangle) - \rho_{UU}(T;|L\rangle\rangle)$ and the subtraction

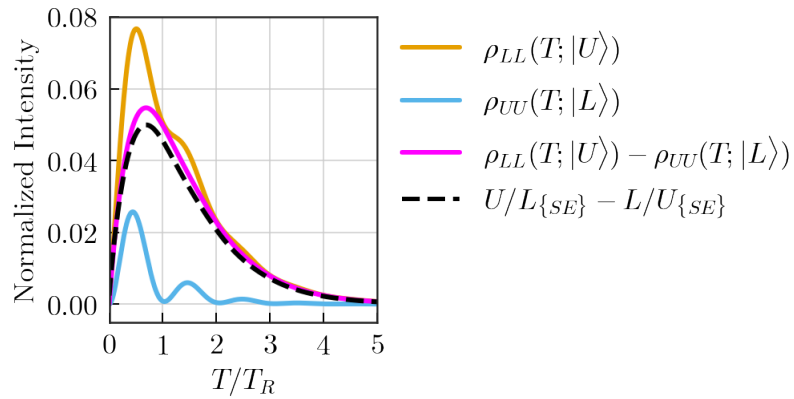


Fig. 4.15.: Comparison between the components of the system density matrix $\rho_{LL}(T;|U\rangle\rangle)$, $\rho_{UU}(T;|L\rangle\rangle)$, $\rho_{LL}(T;|U\rangle\rangle) - \rho_{UU}(T;|L\rangle\rangle)$ and the subtraction of the SE cross peaks $U/L_{SE} - L/U_{SE}$ from the population 2DS. The same parameters as in Fig. 4.1 have been used.

of the SE cross peaks $U/L_{\text{SE}} - L/U_{\text{SE}}$. We can observe that the subtraction (as a function of T) of these peaks is very close to $\rho_{LL}(T; |U\rangle) - \rho_{UU}(T; |L\rangle)$. Thus, once we identify the decay rate $L \rightarrow G$ (which in this case is approximately $\kappa/2$, as can be seen from the Liouvillian in Eq. (4.4)) from the GSR spectrum, it becomes possible to determine the rate $U \rightarrow L$. In our model, it is approximately $\gamma/4$ (see again the Liouvillian in Eq. (4.4)), by analyzing the curve $U/L_{\text{SE}} - L/U_{\text{SE}}$ as a function of T .

4.4.3. ESA (Excited State Absorption)

While in the SE population pathways, it is necessary to consider the coherences $|UL\rangle\rangle$ and $|LU\rangle\rangle$ and population exchanges $|UU\rangle\rangle \rightarrow |LL\rangle\rangle$ and $|LL\rangle\rangle \rightarrow |UU\rangle\rangle$ that occur during T , the population resulting from these transitions are hardly excited towards the second exciton manifold with the third pulse of the spectroscopic protocol. Consequently, these transitions are not relevant in the ESA pathways (see Fig. 4.16). The populations that persist in the states (L or U) during T , which were initially populated through the excitation process, are subsequently excited to L_2 and U_2 respectively. This leads to the negative peaks in the 2DS that we have denoted as L/L_2 and U/U_2 . Consequently, it is expected that both peaks (see right panel of Fig. 4.11) evolve according to the following relationships

$$U/U_{2\{\text{ESA}\}}(T) \approx U/U_{2\{\text{ESA}\}}(0) \rho_{UU}(T; |U\rangle) \approx U/U_{2\{\text{ESA}\}}(0) e^{(-\kappa/2+\gamma/4) T} \quad (4.18)$$

$$L/L_{2\{\text{ESA}\}}(T) \approx L/L_{2\{\text{ESA}\}}(0) \rho_{LL}(T; |L\rangle) \approx L/L_{2\{\text{ESA}\}}(0) e^{-\kappa/2 T}. \quad (4.19)$$

Clearly, the negative ESA peaks (see Fig. 4.10) are wider along the detection frequency axis compared to the other peaks. These ESA widths are related to the decays of the states L_2 and U_2 . Such decays are larger than the other previously analyzed peaks.

As a summary, the Fig. 4.17 indicates the set of dynamical processes that can be tracked using population 2DS, specifying the spectral region where they are visualized and to which contribution (GSR, SE, or ESA) they belong. In the SE contribution, it is important to highlight that, in addition to the processes indicated in the figure, the formation of coherences $|UL\rangle\rangle$ and $|LU\rangle\rangle$ during T must be taken into account, whose contributions are also present in the four peaks. On the other hand, although the two ESA peaks account for the processes $U \xrightarrow{T} U$ and $L \xrightarrow{T} L$, from which information

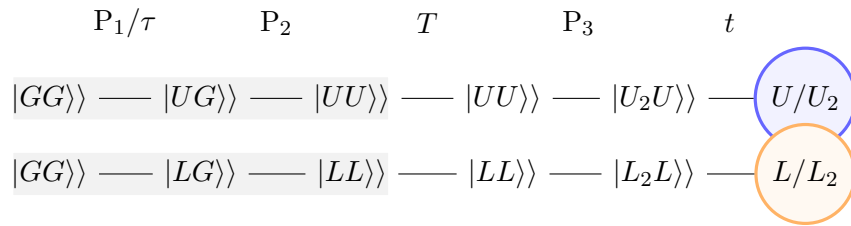


Fig. 4.16.: ESA non-rephasing relevant pathways for separated excitation of polaritons L (lower paths) and U (upper paths), respectively and their contributions to each region around the peaks L/L_2 , and U/U_2 within the 2DS.

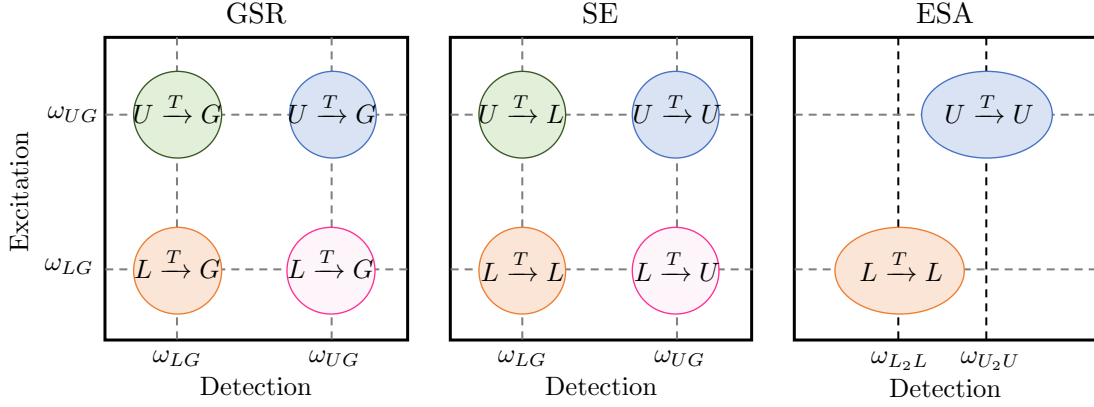


Fig. 4.17.: Most relevant physical transitions between states of the open JC system during the waiting time T that contribute to each region of the population 2DS, categorized by the distinct GSR, SE, and ESA population pathways.

can already be extracted through the SE diagonal peaks, it is noteworthy that their widths along the detection frequency provide insights into the decay rates of states U_2 and L_2 respectively. This will be further analyzed in the next section.

4.4.4. ESA' (Excited State Absorption Prime)

The contribution ESA' to population spectrum is somewhat more challenging to analyze as it exhibits interference between positive and negative peaks (see Fig. 4.10). This contribution, arising from the decays $|\Lambda_2\rangle \langle \Lambda_1| \xrightarrow{t} |\Lambda_1\rangle \langle G|$, is usually not included in the 2DS analyses done in the literature, as electronic excitations of free molecules decay on much slower timescales than the polaritons with very fast decay rates studied here. This pathway leads to a narrowing of the ESA line shape along the detection frequency ω_t , as observed in Fig. 4.18, which displays the sum of the ESA and ESA' contributions to 2DS population spectra. The widths along ω_τ and ω_t of ESA + ESA' peaks are similar to those of GSB and SE. This effect is typically accounted for by considering a spectral density function, which also influences the line shape (in ω_t) of the ESA contribution. In this sense, the ESA' pathway could be viewed as equivalent to modifying the spectral width function. However, within our formalism, there is no need to simulate this effect through a spectral width function. The ESA' contribution formally emerges as a new pathway generated by photon decays during the temporal evolution t , related to the detection.

4.5. Excitation and Detection Masks

In Sec. 3.7, we derived the expression Eq. (3.91) for the 2DS in terms of excitation and detection functions. We rewrite that expression as

$$S^{(3)}(\omega_\tau, T, \omega_t) = \sum_j E_j(\omega_\tau) e^{\lambda_j T} D_j(\omega_t), \quad (4.20)$$

where the excitation function $E_j(\omega_\tau) \equiv -(E_{j[\text{NR}]}(\omega_\tau) + E_{j[\text{R}]}(\omega_\tau))$ contains the rephasing and non rephasing PM contributions and the detection function $D_j(\omega_t) \equiv iD_{j[\text{NR}]}(\omega_t) = iD_{j[\text{R}]}(\omega_t)$ is any of the rephasing or non rephasing PM contributions (they both have the same detection function). This Eq. (4.20) exhibits also an exponential factor $e^{\lambda_j T}$ containing the Liouvillian eigenvalue λ_j that shapes the evolution during the waiting time T . We have already explained that the excitation process in the open JC model leads to a combination of the states $|GG\rangle$, $|LL\rangle$, and $|UU\rangle$ (which give rise to the population spectrum), as well as the coherences $|UL\rangle$ and $|LU\rangle$ (which contribute to the coherence spectrum). This combination represents the initial condition for the evolution during T in the 2D spectroscopic protocol. Since these five states¹⁴ belong to the same Liouvillian diagonal block (the first block in Fig. 4.2), and none of them can migrate to the second excitation manifold, the temporal evolution T remains confined within this 5x5 Liouvillian subspace. Therefore, it is expected that among all the 25 Liouvillian eigenvalues, only the excitation/detection functions associated to those five eigenvalues (λ_{GG} , λ_{LL} , λ_{UU} , λ_{UL} , and λ_{LU}) in this Liouvillian subspace contribute to the sum in Eq. (4.20).

The left panel of Fig. 4.19 shows how the absorptive 2DS quoted in Fig. 4.7 at waiting time $T = 0$ is built from the required excitation and detection functions. Note that the excitation/detection function associated to λ_{GG} is not necessary to be included. For any eigenvalue λ_j , both functions $E_j(\omega_\tau)$ and $D_j(\omega_t)$ do not depend on T , so that the factor $e^{\lambda_j T}$ carries the whole time T -evolution of the 2DS. There are other nonzero detection functions associated with the eigenvalues $\lambda_{L_2L_2}$, $\lambda_{U_2U_2}$, $\lambda_{U_2L_2}$, and $\lambda_{L_2U_2}$. However, since the corresponding excitation functions for those eigenvalues are zero, they do not contribute to the sum in Eq. (4.20). Then it is clear that the excitation and detection functions act as masks or filters, and only those eigenvalues for which both functions are nonzero contribute to the 2DS.

Out of the four nonzero excitation/detection functions, two correspond to Liouvillian population eigenvalues (λ_{LL} and λ_{UU}). For those eigenvalues, $E_j(\omega_\tau)$ are real, while $D_j(\omega_t)$ are complex. The other two correspond to coherence eigenvalues (λ_{UL} and λ_{LU}). For the coherence eigenvalues, both

¹⁴Here we use the term ‘states’ loosely, as the coherences $|UL\rangle = |U\rangle\langle L|$ and $|LU\rangle = |L\rangle\langle U|$ are not actual quantum states, since they are not Hermitian.

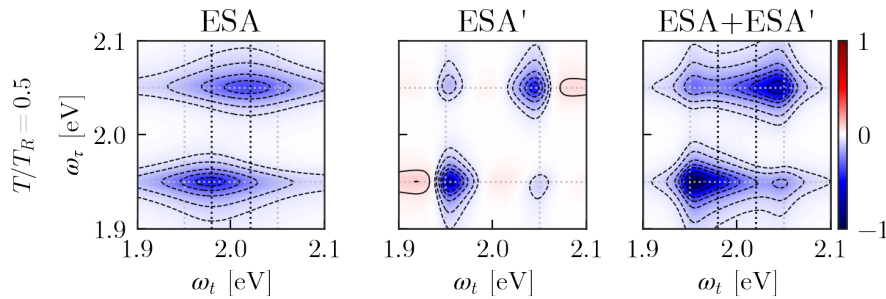


Fig. 4.18.: ESA, ESA' and ESA+ESA' population contributions to absorptive 2DS $\mathcal{R}[S_{(\text{NR}+\text{R})}^{(3)}(\omega_\tau, T, \omega_t)]$ for a waiting time $T = 0.5 T_R$. ESA and ESA' contributions are also plotted in Fig. 4.10. Parameters as used in that Fig. 4.10.

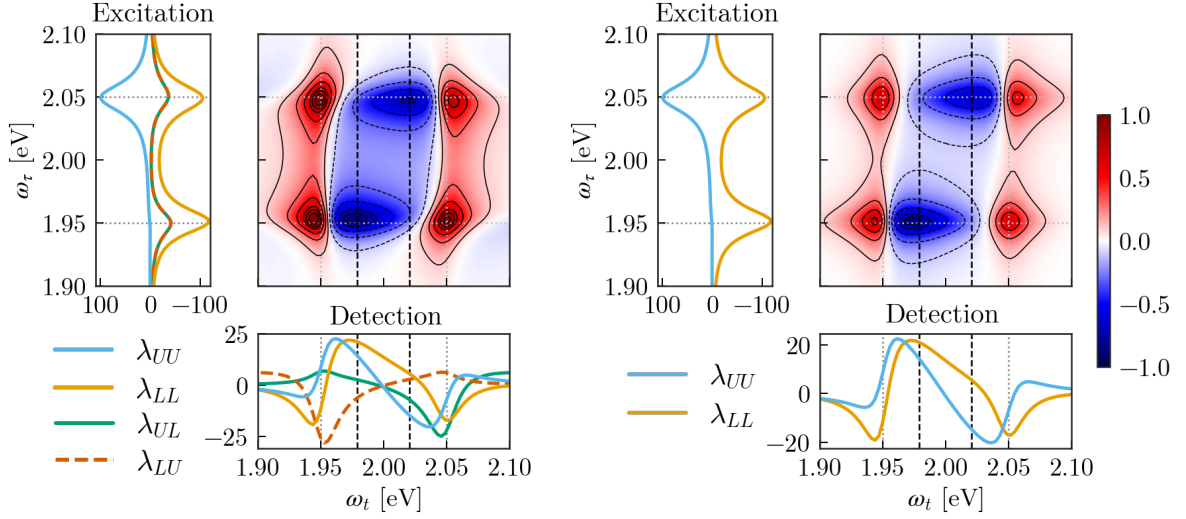


Fig. 4.19.: Left panel: Real part of 2DS $\mathcal{R}[S_{(\text{NR}+\text{R})}^{(3)}(\omega_\tau, T, \omega_t)]$ corresponding to the open JC model at the waiting time $T = 0$, formed by the contribution of all nonzero excitation functions (those associated to population eigenvalues λ_{LL} , λ_{UU} and to coherence eigenvalues λ_{UL} , λ_{LU}) and their corresponding detection functions (only real parts are plotted at left and bottom, respectively). Right panel: the same 2DS formed only by the excitation/detection functions associated with the population Liouvillian eigenvalues, namely λ_{LL} and λ_{UU} . The gray dotted lines indicate the frequencies $\omega_{LG} = 0.95$ eV and $\omega_{UG} = 2.05$ eV, while the black dashed lines indicate the frequencies $\omega_{U_2U} = 2.02$ eV and $\omega_{L_2L} = 1.98$ eV. Both 2DS are normalized as in Fig. 4.7. Contour lines are drawn at $\pm[0.1, 0.3, 0.5, 0.7, 0.8, 0.9]$.

$E_j(\omega_\tau)$ and $D_j(\omega_t)$ are complex. The most relevant features of the 2DS can be reproduced if only the terms associated with population eigenvalues are considered in the sum Eq. (4.20). In this case, the spectrum at $T = 0$ in the right panel of the Fig. 4.19 is obtained from the expression

$$\mathcal{R}[S_{(\text{NR}+\text{R})}^{(3)}(\omega_\tau, T = 0, \omega_t)] = \sum_{j=\{LL, UU\}} E_j(\omega_\tau) \mathcal{R}[D_j(\omega_t)], \quad (4.21)$$

where we have used that for population eigenvalues $E_j(\omega_\tau)$ are real. The contribution from population eigenvalues plays a leading role in shaping the 2DS while the coherence contributions provide slight modifications. It is important to clarify that this 2DS built from the Liouvillian population eigenvalues in Eq. (4.21) is similar but not completely equivalent to the population 2DS that we defined earlier in terms of Feynman pathways leading to population in Sec. 4.3. The coherence spectrum defined previously in terms of Feynman pathways leading to coherences is also not identical to the spectrum obtained by summing only those terms associated to the coherence eigenvalues. Remember that the coherence spectrum contributes to highlighting the Rabi oscillations (as a function of T) of the total spectrum, as shown in Fig. 4.9. Furthermore, the j -terms in the sum Eq. (4.20) associated with coherence eigenvalues contain phases $e^{\lambda_j T}$ that oscillate approximately with the system Rabi frequency. Indeed, whereas for the population eigenvalues, the phases in Eq. (4.20) take the form $e^{\lambda_{LL} T} = e^{-\Gamma_{LL} T}$ and $e^{\lambda_{UU} T} = e^{-\Gamma_{UU} T}$, which are entirely real, for the coherence terms the phases are of the complex

form $e^{\lambda_{UL}T} \approx e^{(-\Gamma_{UL}-i\Omega_R)T}$ and $e^{\lambda_{LU}T} \approx e^{(-\Gamma_{UL}+i\Omega_R)T}$, respectively.

We emphasize that excitation and detection functions are not observable quantities. The complex excitation mask $E_j(\omega_\tau)$ (real for population Liouvillian eigenvalues) is not the linear absorption spectrum, and the complex detection mask $D_j(\omega_t)$ is not the emission spectrum. However, these excitation and detection masks provide relevant information about the frequencies of the states involved in the spectroscopic protocol and the widths of the signals in the 2DS. Both the excitation and detection masks for the j -th eigenvalue read (see Eq. (3.92)) $E_j(\omega_\tau) = \sum_i f_i^j(\omega_\tau)$ and $D_j(\omega_t) = \sum_k g_k^j(\omega_t)$, where

$$f_i^j(\omega_\tau) \equiv - \sum_l \left[\frac{\mathcal{V}_{ji}^- \mathcal{V}_{il}^+}{\lambda_i \pm i\omega_\tau} + \frac{\mathcal{V}_{ji}^+ \mathcal{V}_{il}^-}{\lambda_i \pm i\omega_\tau} \right] c_l, \quad (4.22)$$

$$g_k^j(\omega_t) = i \frac{V_k^- \mathcal{V}_{kj}^+}{\lambda_k + i\omega_t}. \quad (4.23)$$

The first term in Eq. (4.22) is the non-rephasing contribution and the second is the rephasing one. $E_j(\omega_\tau)$ and $D_j(\omega_t)$ are thus contributed by the whole set of Liouvillian eigenvalues λ_i (associated to f_i functions) and λ_k (associated to g_k functions) respectively for a fixed frequency ω_τ and ω_t . However, only two of them contribute to the j -th excitation function and four to the j -th detection function. For instance, in Fig. 4.20 we show the relevant contributions to $E_{\lambda_{LL}}$ and $E_{\lambda_{UU}}$ together with $D_{\lambda_{LL}}$ and $D_{\lambda_{UU}}$.

The contribution λ_{LG} to $E_{\lambda_{LL}}$ has a width of $2\Gamma_{LG}$ and the contribution λ_{UG} to both $E_{\lambda_{LL}}$ and $E_{\lambda_{UU}}$ has a width¹⁵ of $2\Gamma_{UG}$. These are just the widths of the signals along the excitation frequency ω_τ in the 2DS. Analogously, the contributions to detection masks determine the widths along the detection frequency ω_t of the 2DS signals. Particularly, these contributions to detection functions are λ_{LG} , λ_{UG} , which provide the GSB, GSR, and SE spectra (since these eigenvalues belong to the first excitation manifold Λ_1), and λ_{L_2L} and λ_{U_2U} , which contribute to the ESA spectra (since these eigenvalues represent two excitations and belong to Λ_2). The signals associated with λ_{LG} and λ_{UG} have the same widths in ω_t and ω_τ , while the signals ESA, have widths in ω_t proportional to $2\Gamma_{L_2L}$ and $2\Gamma_{U_2U}$, which are larger than the widths along the excitation frequency ($2\Gamma_{LG}$ and $2\Gamma_{UG}$, respectively).

4.6. 2DS building history

For a quantitative insight into the state of the system during each step of the 2D spectroscopy protocol, the Fig. 4.21 depicts the real part of the Fourier transform of each component (in the Hamiltonian basis) of the system density matrix at each step. Both non-rephasing and rephasing contributions are taken into account.

¹⁵Remember that $\Gamma_{\alpha\beta}$ represents the negative value of the real part of the Liouvillian eigenvalue $\lambda_{\alpha\beta}$.

4.6.1. Excitation

As we have discussed previously, after the excitation process (interaction with the first pulse + evolution τ + interaction with the second pulse), the system is represented by a superposition of the states $|GG\rangle$, $|LL\rangle$, $|UU\rangle$, and the coherences $|UL\rangle$ and $|LU\rangle$. In the upper panel of the Fig. 4.21, we can quantitatively observe the contribution of each of these components to the excitation state. Remember that the states (density matrices) theoretically formed during the construction of the 2DS are not Hermitian. Hermiticity is lost because the interactions with the pulses are treated as commutators, either with the operator a or the operator a^\dagger (depending on the phase matching condition¹⁶), and neither of these operators is Hermitian. For this reason, it is not surprising to obtain, for example, negative values for the GG (population) component. We emphasize that the physical density matrix, of course, does stay Hermitian at all times.

When the excitation frequency is close to $\omega_{LG} = 1.95$ eV, the state $|LL\rangle$ is predominantly excited, while when it is close to $\omega_{UG} = 1.05$ eV, the state $|UU\rangle$ is more populated. The coherences $|UL\rangle$

¹⁶Although the total interactions with the pulses are actually commutators with $a + a^\dagger$ (which is Hermitian), the signals collected for the selected phase matching conditions (non-rephasing and rephasing in this case) are theoretically obtained by choosing either a or a^\dagger in each pulse interaction, making use of the rotating wave approximation.

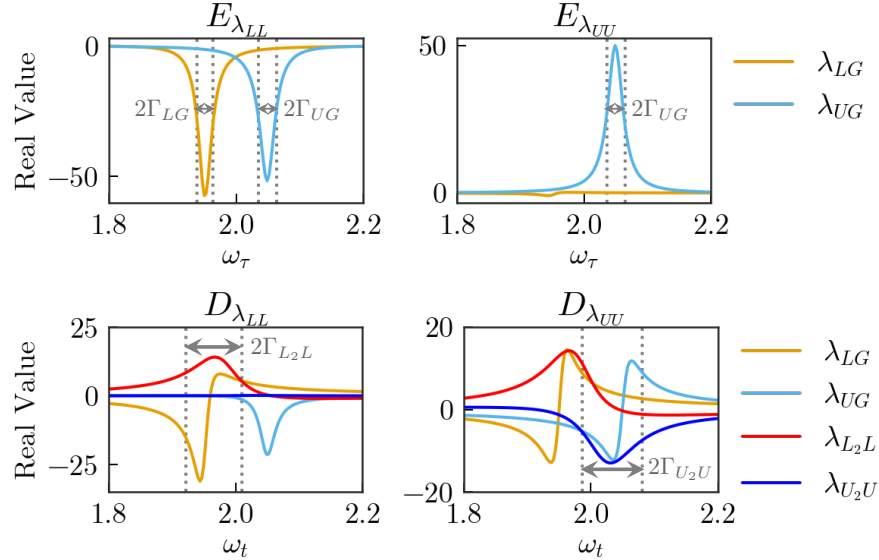


Fig. 4.20.: Upper panels: real part of relevant $f_i^j(\omega_\tau)$ functions defined in Eq. (4.22) whose sum is the excitation j -function $E_{\lambda_{LL}}(\omega_\tau)$ (left panel) and the excitation j -function $E_{\lambda_{UU}}(\omega_\tau)$ (right panel). Only the $f_i^j(\omega_\tau)$ functions associated to $\lambda_i = \{\lambda_{LG}, \lambda_{UG}\}$ are non-zero. Lower panels: real part of relevant $g_k^j(\omega_t)$ functions defined in Eq. (4.23) whose sum is the detection j -function $D_{\lambda_{LL}}(\omega_t)$ (left panel) and the detection j -function $D_{\lambda_{UU}}(\omega_t)$ (right panel). Only the $g_k^j(\omega_t)$ functions associated to $\lambda_k = \{\lambda_{LG}, \lambda_{UG}, \lambda_{L_2L}, \lambda_{U_2U}\}$ are non-zero. The widths of some f_i^j and g_k^j functions are labeled.

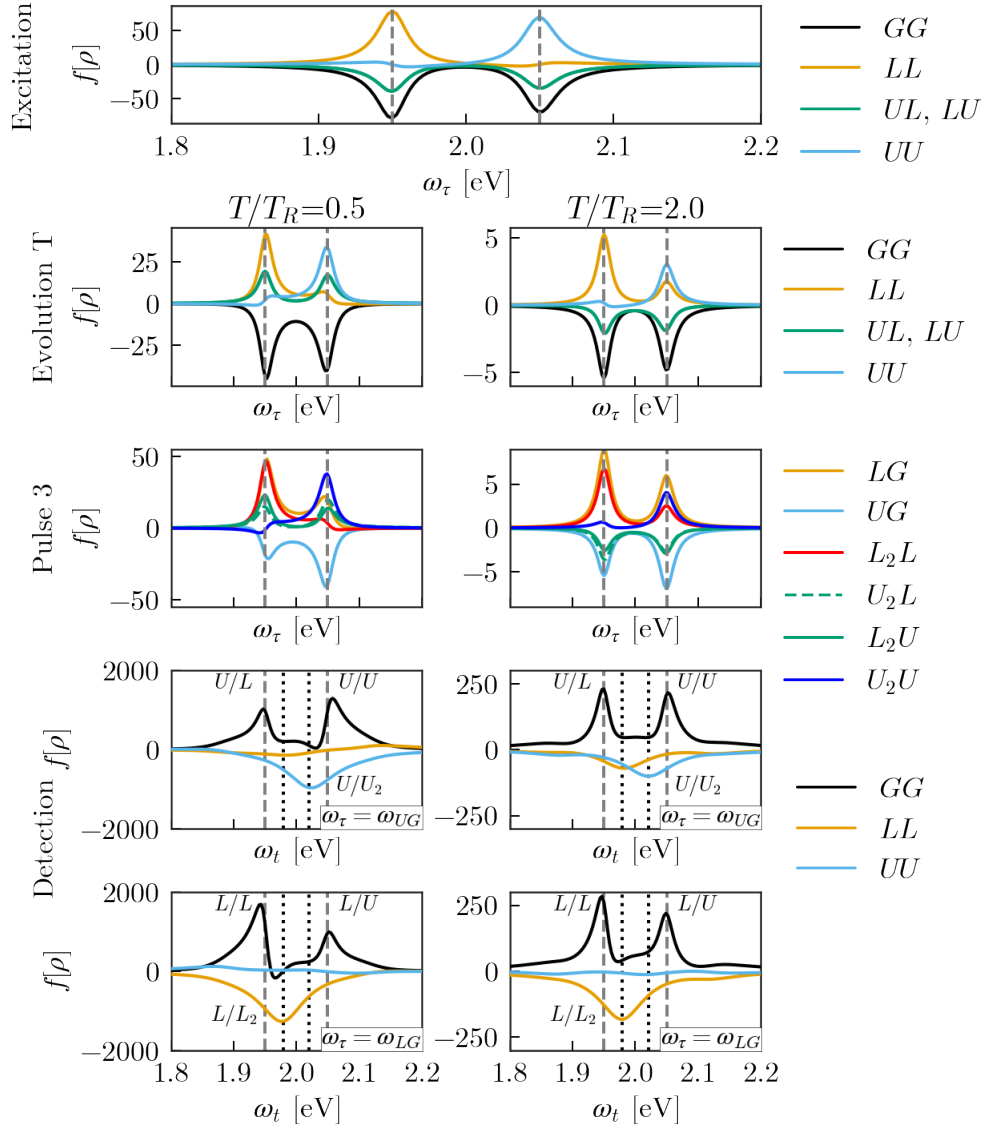


Fig. 4.21.: Plots, by Hamiltonian components of $f[\rho]$, defined as the real part of the Fourier transform of $\rho_{\text{NR}}^{(I)} + \rho_{\text{R}}^{(I)}$, being $\rho_{\text{NR/R}}^{(I)}$ the state of the system after the corresponding (I) step of the spectroscopic protocol (I = Excitation, Evolution T , Interaction with third pulse and detection). The detection state here refers to the state immediately before performing the trace of $a\rho(t)$, which is necessary to obtain the expectation value of the annihilation dipole operator. The subscripts NR and R refer to the states obtained through the non-rephasing and rephasing pathways, respectively. Except for the excitation process, the other processes have been plotted at two waiting times, $T = 0.5 T_R$ and $T = 2 T_R$ ($T_R = 41.47$ fs). Gray dashed lines are the frequencies ω_{LG} and ω_{UG} respectively. Black dotted lines are the frequencies ω_{L_2L} and ω_{U_2U} respectively. Each signal is labeled with the corresponding peak in the 2DS. The parameters are those of the Fig. 4.7.

and $|LU\rangle\rangle$ (which later will form the coherence spectrum) are present for both excitation frequencies. The component $|GG\rangle\rangle$ (which gives rise to the GSB spectrum) is also present for both excitation frequencies, showing a higher intensity for $\omega_\tau = \omega_{LG}$ than for $\omega_\tau = \omega_{UG}$. The excitation state is the initial condition for the evolution during T .

4.6.2. Evolution T

We have selected two waiting times to visualize the composition of the system state: a short time of $0.5 T_R$ and a longer one of $2 T_R$. The comparison between these two times will allow us to appreciate certain differences between the JC 2DS and the Tavis-Cummings 2DS in subsequent sections. In the JC model, the components of the state are not strongly modified at long values of T . What can be observed is a global decrease in their amplitudes during T and the oscillatory nature of the coherences UL and LU (positive, for example, at $0.5 T_R$ and negative at $2 T_R$).

4.6.3. Pulse 3

The third pulse forms the coherence LG from the populations that remained during the evolution T in $\{GG, LL, LU\}$, and the coherence UG from $\{GG, UU, UL\}$. The amplitude of LG is dominant at $\omega_\tau = \omega_{LG}$ and the amplitude of UG is dominant at $\omega_\tau = \omega_{UG}$. The contributions originated from GG are responsible of GSB and GSR spectra, while contributions originated from LL, UU, LU , and UL are responsible of SE spectrum. On the other hand, the coherence L_2L formed during the interaction with the third pulse primarily originates from the population that remained in LL during T , and the coherence U_2U originates from UU . These two coherences involving states from the second excitation manifold contribute to the ESA and ESA' spectra. L_2L is primarily populated at frequencies close to $\omega_\tau = \omega_{LG}$, while U_2U is mainly populated at frequencies near to $\omega_\tau = \omega_{UG}$.

4.6.4. Detection

The detection plots, unlike the previous ones, are presented in the [Fig. 4.21](#) as a function of the detection frequency ω_t . In this part, we only plot the population components of $a\rho(t)$, where $\rho(t)$ is the state of the system just after the interaction with the third pulse of the 2D spectroscopy and its subsequent evolution up to time t . We omit the coherences here because only populations contribute to the calculation of $\text{Tr}[a\rho(t)]$, which represents the final step to determine the 2DS value in the time domain. In other words, the sum of all components in the detection plots exactly corresponds to the value of the 2DS at each detection frequency and at the selected excitation frequencies, $\omega_\tau = \omega_{UG}$ and $\omega_\tau = \omega_{LG}$ for the respective waiting time T .

The component GG represents the sum of all GSB, GSR, SE, and ESA' contributions. Meanwhile, the components LL and UU represent the ESA contribution of the 2DS. The diagonal peaks U/U and L/L have higher amplitudes than the cross-peaks U/L and L/U at $0.5 T_R$. At $2 T_R$, all four peaks have similar amplitudes. Those four peaks are formed by the GG component. Incidentally ESA peak L/L_2 presents higher amplitude than U/U_2 for both short and long waiting times.

5. Multidimensional spectroscopy in the dissipative Tavis-Cummings model

5.1. Hamiltonian, Liouvillian and linear response

The generalization of the JC model to the case of two or more two-state emitters interacting strongly with the electromagnetic field in a cavity is the Tavis-Cummings (TC) model. The Hamiltonian associated to the TC model is

$$H_{TC} = \hbar\omega_c a^\dagger a + \hbar \sum_{i=1}^N \omega_i \sigma_i^\dagger \sigma_i + \hbar g \sum_{i=1}^N (a^\dagger \sigma_i + \sigma_i^\dagger a), \quad (5.1)$$

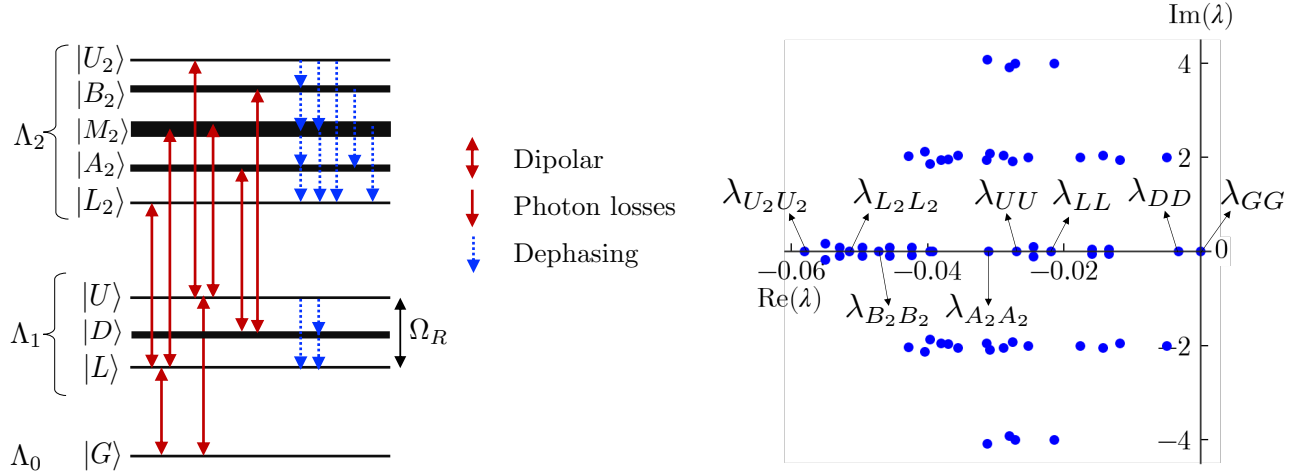


Fig. 5.1.: Left panel: energy scheme of the Tavis-Cummings (TC) model eigenstates for the excitation manifolds Λ_0 , Λ_1 and Λ_2 (not to scale). The splitting between polaritons of Λ_1 is the Rabi frequency Ω_R . Red arrows indicate the more relevant (matrix elements with absolute value larger than 10^{-4}) allowed radiative dipole transitions (both directions) and also transitions due to cavity photons losses (downward direction). Dotted arrows represent relevant transitions due to molecular relaxation. Right panel: Liouvillian eigenvalues for the open TC model with $N = 2$ up to the second excitation manifold. We have chosen $\hbar\omega_c = \hbar\omega_e = 2$ eV for all molecules and $\hbar\Omega_R = 0.1$ eV. Cavity lifetime is 15 fs ($\kappa = 44$ meV/ \hbar) and molecular relaxation time is 50 fs ($\gamma = 13$ meV/ \hbar).

where N is the number of emitters inside the cavity, and ω_i and σ_i (σ_i^\dagger is its adjoint) are the frequency and annihilation operator respectively of emitter i .

Unlike the energy distribution in the JC model (Fig. 4.1), the TC energy spectrum presents a collection of $N - 1$ degenerate dark states, denoted as $|D\rangle$, within the first excitation manifold Λ_1 (see Fig. 5.1). The second excitation manifold Λ_2 encompasses the lower energy polariton state $|L_2\rangle$, its higher energy counterpart $|U_2\rangle$, two sets of degenerate states, $|A_2\rangle$ and $|B_2\rangle$, and also a collection of degenerate intermediate states $|M_2\rangle$ (see Subsec. 1.3.2). Among the states $|M_2\rangle$, we group the middle polariton bright state, along with the set of degenerate dark states $|D_2\rangle$ in the second excitation manifold. This is because in the case of zero detuning ($\Delta = \omega_c - \omega_e = 0$), both types of states are degenerate. When there are $N = 2$ molecules inside the cavity, the second excitation manifold Λ_2 differs from the scheme presented in the left panel of Fig. 5.1. In this case, there are no states $|M_2\rangle$, $|A_2\rangle$ and $|B_2\rangle$, but there are two of a new kind of degenerate states $|C_2\rangle$, which have a dipolar transition with both dark and polariton states of Λ_1 .

Similar to the JC model studied in the previous chapter, we account for cavity photon losses through a Lindblad term for the operator a . Furthermore, we incorporate molecular relaxation by using the operator $\sigma_i^\dagger \sigma_i$ associated with each of the individual molecules, employing the Bloch-Redfield formalism with a vibrational bath spectral function $J(\omega) = \gamma \Theta(\omega)$ (a γ -normalized Heaviside step function). We obtain a master equation of the form

$$\mathfrak{L}[\rho] = -\frac{i}{\hbar}[H_{TC}, \rho] + \kappa \mathcal{L}(a)[\rho] + \sum_i \mathcal{B}(\sigma_i^\dagger \sigma_i)[\rho]. \quad (5.2)$$

When diagonalizing the Liouvillian matrix \mathfrak{L} in the TC Hamiltonian basis, we obtain a set of complex eigenvalues, as depicted in the right panel of Fig. 5.1 for $N = 2$ molecules. The eigenvalues of the Liouvillian for $N = 2$ emitters can be obtained analytically in the limit of no-pure dephasing as shown in [153]. The dimension of the Liouvillian space increases rapidly with the number of molecules N . For the case $N = 2$, the dimension of the Hilbert space is $\dim_H = 8$ (there are a total of 8 polariton states into Λ_0 (1), Λ_1 (3) and Λ_2 (4)), whereas the dimension of the Liouvillian space is $\dim_{\mathfrak{L}} = \dim_H^2 = 64$.

The Liouvillian superoperator Eq. (5.2) expressed in the Liouvillian space basis set is also a block diagonal matrix for the open TC model, just like the Liouvillian of the open JC model (see Fig. 4.2). For the TC model, the diagonal blocks are also of the form $\Lambda_i \Lambda_i$ ($i = 0, 1, 2$), $\Lambda_i \Lambda_{i-1}$ ($i = 1, 2$), and $\Lambda_2 \Lambda_0$ and their respective adjoint matrices. The $\Lambda_i \Lambda_i$ block of the TC model (analogous to the JC block in the left panel of Fig. 4.2), contains both populations (e.g., GG , LL , DD , UU) and coherences (e.g., LU , LD , UD). If we restrict ourselves to populations within this block $\Lambda_i \Lambda_i$, we obtain the matrix scheme represented in the left panel of Fig. 5.2. From all allowed transitions among population states (mediated by photon losses, molecular relaxation or both) we have also represented only the relevant ones as in Fig. 5.1. The dark states $|D\rangle$ in Λ_1 only have a decay channel through the lower polariton $|L\rangle$ of Λ_1 via molecular relaxation. The value of Γ_{DD} (mind that $\mathcal{R}[\lambda_{DD}] = -\Gamma_{DD}$) is small compared to the other values $\Gamma_{\alpha\alpha}$, as shown in the right panel of Fig. 5.1. It indicates that dark states decay very slowly and are quasi-stationary states. For example, if the upper polariton U is initially populated,

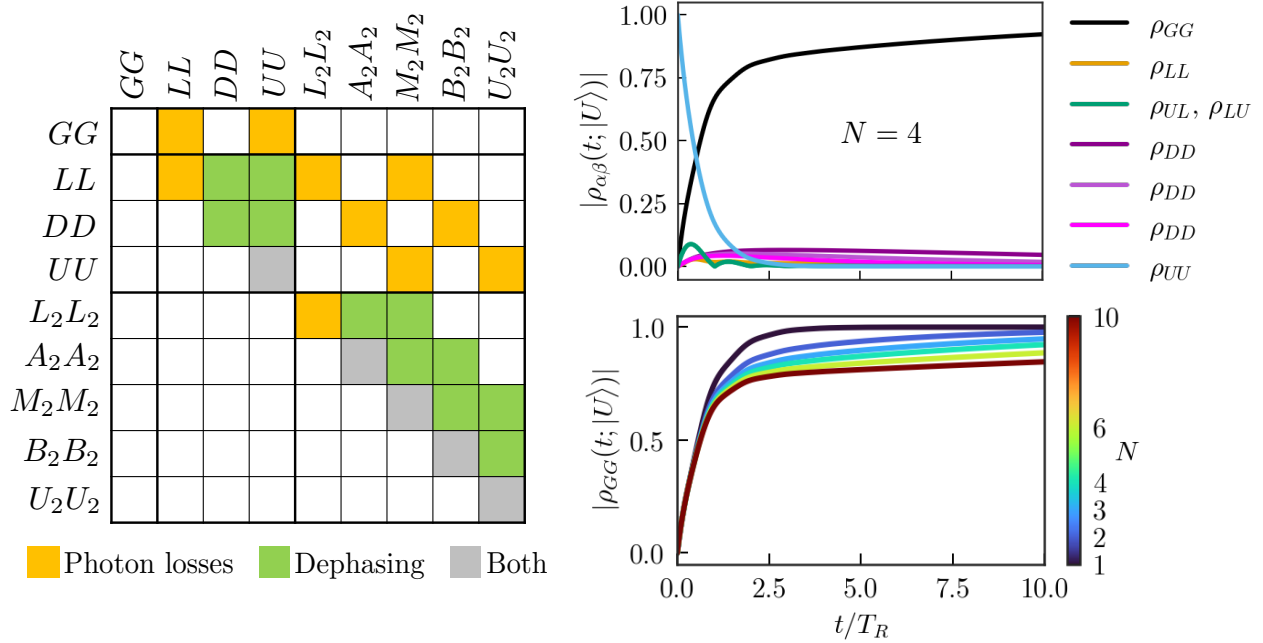


Fig. 5.2.: Left panel: Schematic representation of the Liouvillian matrix elements (in the TC Hamiltonian eigenbasis) only for the population states of the diagonal block $\Lambda_i\Lambda_i$ ($i = 0, 1, 2$). Orange color represents contributions due to cavity photon losses, green color are due to molecular relaxation, and gray color represents contributions of both molecular dephasing-type vibrational relaxation and cavity losses. Right panel: Absolute value of the respective elements of the time dependent density matrix $\rho(t) = e^{\mathcal{L}t}\rho(0)$ for the initial condition $\rho(0) = |U\rangle\langle U|$. We have used $N = 4$ molecules (upper panel) and different number of emitters $N = 1, 2, 3, 4, 5, 6$ and 10 (lower panel). We have used the same parameters as described in Fig. 5.1. Time t is in units of the Rabi period $T_R = 41.47$ fs of the system.

its dynamical evolution $\dot{\rho}(t) = \mathcal{L}[\rho(0)]$ with the Liouvillian in Eq. (5.2) is shown in the upper right panel of Fig. 5.2 for $N = 4$ molecules. At variance with the case of one single emitter (without dark states, where the U state ends up decaying into the ground state) for $N = 4$ and long evolution times a part of the population that would reach the ground state remains instead distributed among the three dark states as transients. As the number of molecules N increases, the populations take a longer time to decay to the ground state, as shown in the lower right panel of Fig. 5.2, due to the presence of a larger number of dark states.

In our open TC model, all states, except for the dark states $|D\rangle$, exhibit decay via photon losses (see left panel of Fig. 5.2). Additionally, with the exception of the lower polaritons in both Λ_1 and Λ_2 , all states decay via molecular relaxation. The Hamiltonian states used to represent the population matrix block in Fig. 5.2 are ordered with increasing energy. Consistent with the fact that the baths only induce relaxation, we find that the lower triangle of the matrix block is null, as these entries would describe pumping from a lower-energy state to a higher-energy one.

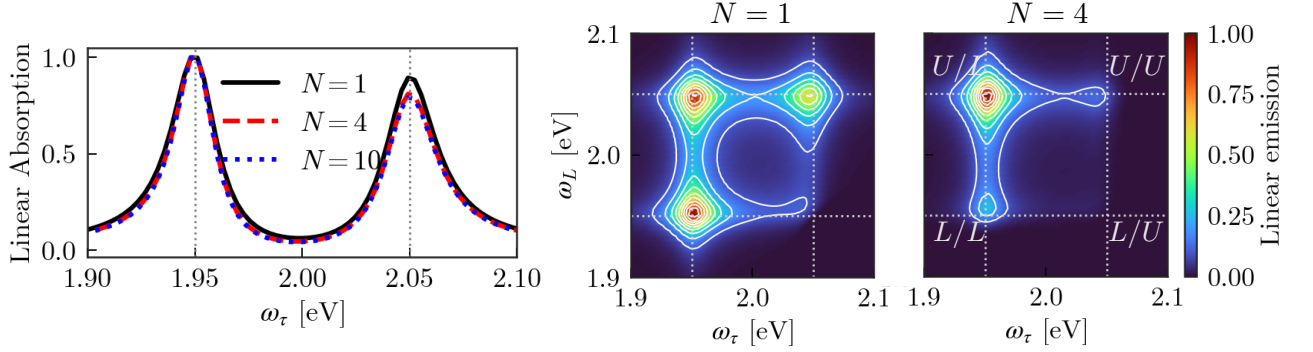


Fig. 5.3.: Left panel: Comparison of linear absorption spectrum for $N = 1$ (open JC model) and open TC model with $N = 4$, and $N = 10$ molecules. All spectra are normalized to unity at their maximum, that is, the lower peak L , with $\omega_{LG} = 1.95$ eV. Right panel: Comparison of linear emission spectrum for $N = 1$ (open JC model) and open TC model with $N = 4$. Except for N all parameters here used are the same as quoted in Fig. 5.1. Vertical dotted lines represent the frequencies $\omega_{LG} = 1.95$ eV and $\omega_{UG} = 2.05$ eV respectively.

If only the population states (not coherences) are considered up to the first excitation manifold, the analogue to the JC Liouvillian in Eq. (4.4) now reads for $N = 2$ molecules as

$$\mathfrak{L}_{\Lambda_1 \Lambda_1} = \begin{matrix} & \begin{matrix} GG & LL & UL & DD & LU & UU \end{matrix} \\ \begin{matrix} GG \\ LL \\ UL \\ DD \\ LU \\ UU \end{matrix} & \left(\begin{array}{cccccc} 0 & \kappa/2 & \kappa/2 & 0 & \kappa/2 & \kappa/2 \\ 0 & -\kappa/2 & -\kappa/4 + \gamma/8 & \gamma/4 & -\kappa/4 + \gamma/8 & \gamma/8 \\ 0 & -\kappa/4 & -\kappa/2 - 3\gamma/16 - i\Omega_R & -\gamma/8 & \gamma/16 & -\kappa/4 + \gamma/8 \\ 0 & 0 & -\gamma/8 & -\gamma/4 & -\gamma/8 & \gamma/4 \\ 0 & -\kappa/4 & \gamma/16 & -\gamma/8 & -\kappa/2 - \gamma/8 + i\Omega_R & -\kappa/4 + \gamma/8 \\ 0 & 0 & -\kappa/4 & 0 & -\kappa/4 & -\kappa/2 - 3\gamma/8 \end{array} \right), \end{matrix} \quad (5.3)$$

The dark states in Λ_1 , which represent molecular (but not cavity) excitations cannot be reached from the ground state $|G\rangle$ via a dipolar interaction. The dipole transition $|G\rangle \rightarrow |D\rangle$ is not allowed, as shown in Fig. 5.1. Consequently, a peak around the dark states energy ($\omega_{DG} = 2.0$ eV for the parameters described in Fig. 5.3) is absent in the linear spectra of the open TC model (see Fig. 5.3). However, dark states play an important role in the dynamics of the polaritons L and U of the Λ_1 excitation manifold, since transitions $|U\rangle \rightarrow |D\rangle \rightarrow |L\rangle$ are possible through molecular relaxation (see Fig. 5.2). In the linear absorption spectrum (left panel of Fig. 5.3), after normalizing the signals, it is difficult to discern noticeable differences between the case with $N = 1$ (JC model) and the cases with $N = 4$ or $N = 10$ molecules (TC model). For $N > 1$, a slight variation in the relative intensity of the peaks centered around the frequencies of the polaritons L and U can be observed compared to the $N = 1$ case. On the other hand, the linear emission spectrum, depicted in the right panel of the Fig. 5.3, exhibits noticeable differences between the TC and JC models. The diagonal peaks L/L and U/U

are less intense for $N > 1$ (TC), in comparison to the case of $N = 1$ (JC). The emission from the polariton states is reduced precisely due to the population that remains trapped in the dark states, whose number scales as $N - 1$.

5.2. Two-dimensional non-linear spectra (2DS)

The absorptive 2DS for the open TC with a different number N of molecules and at different waiting times T are shown in Fig. 5.4. These spectra are normalized to the maximum of their respective initial values (at $T = 0$). We can observe that as the number of molecules increases, the upper signals along the ω_{UG} excitation frequency of the 2DS (corresponding to the excitation of the upper polariton and

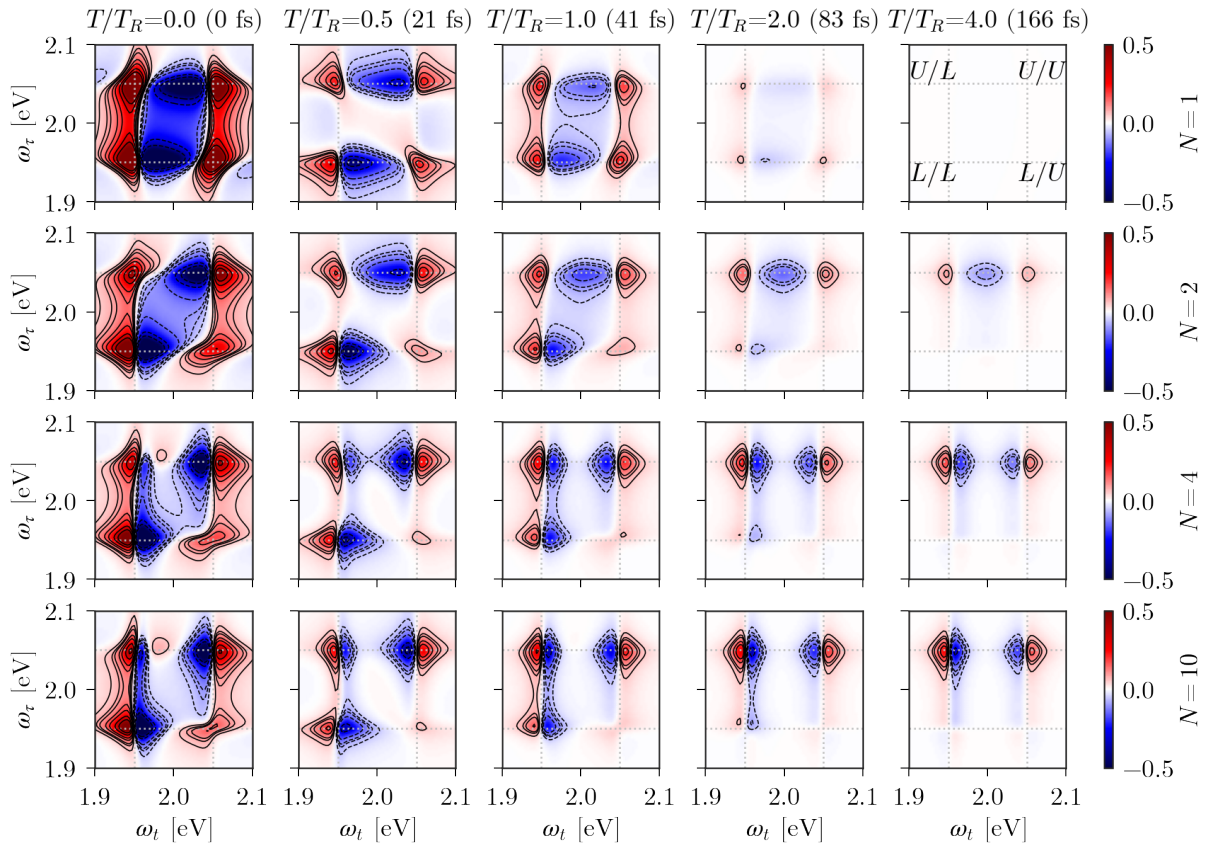


Fig. 5.4.: Electronic 2DS for the open TC model at different waiting times T for different number of molecules $N = 1, 2, 4$ and 10 . Here the real value or 2D absorptive spectra $\mathcal{R}[S_{(NR+R)}^{(3)}(\omega_\tau, T, \omega_t)]$ (lower panel) is plotted. The parameters of the model are chosen as in Fig. 5.1, for the number of molecules N . Dotted right lines indicate the lower $\omega_{LG} = 1.95$ eV and upper $\omega_{UG} = 2.05$ eV polariton frequencies. All spectra are normalized to their maximum real value at time $T = 0$. The plots have been truncated to half of this maximum. The excitation frequency ω_τ lies along the y -axis, while the detection frequency ω_t lies along the x -axis. Solid contour lines represent heights $\pm[0.05, 0.08, 0.1, 0.15, 0.2, 0.3, 0.4]$.

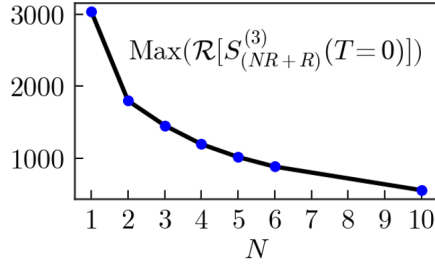


Fig. 5.5.: Maximum value of the absorptive 2DS $\mathcal{R}[S_{(NR+R)}^{(3)}]$ at the waiting time $T = 0$, as a function of the number of molecules N . This maximum value decreases with a factor $\sim 1/N^{2/3}$. The parameters quoted in Fig. 5.1 are used.

including the U/L and U/U peaks) take longer times to decay compared to its initial value. This is consequence of the behavior shown in the right panel of Fig. 5.2, where populations take longer to decay to the ground state as N increases, due to the presence of dark states. However, it should be noted that the maximum initial value of the absorptive 2DS decreases with a factor close to $1/N^{2/3}$ (see Fig. 5.5). This is because as N increases, the system becomes more harmonic [103], and its nonlinear response (measured by the 2DS) is fading away. The cause of the scaling law $N^{-2/3}$ is yet unknown.

For $N = 4$ and $N = 10$, the 2DS display similar features at all waiting times. This is a common characteristic for any $N > 2$ case, since all these systems have a similar energy scheme (that shown in Fig. 5.1). The only anomalous 2DS are those corresponding to the cases $N = 1$ (JC) and $N = 2$, as the energy schemes of these two systems are also exceptional cases. Note, for example, that for $N = 2$, at $T = 4 T_R$ a negative peak centered at the frequency of the dark state $\omega_{DG} = 2.0$ eV is observed. However, this peak splits into two for $N > 2$, as explained later in detail in Subsec. 5.3.2. These peaks represent transitions to the non-degenerate states $|A_2\rangle$ and $|B_2\rangle$ (for $N > 2$) or to the states $|C_2\rangle$ (for $N = 2$), which are degenerate, thus producing a single signal in their respective 2DS.

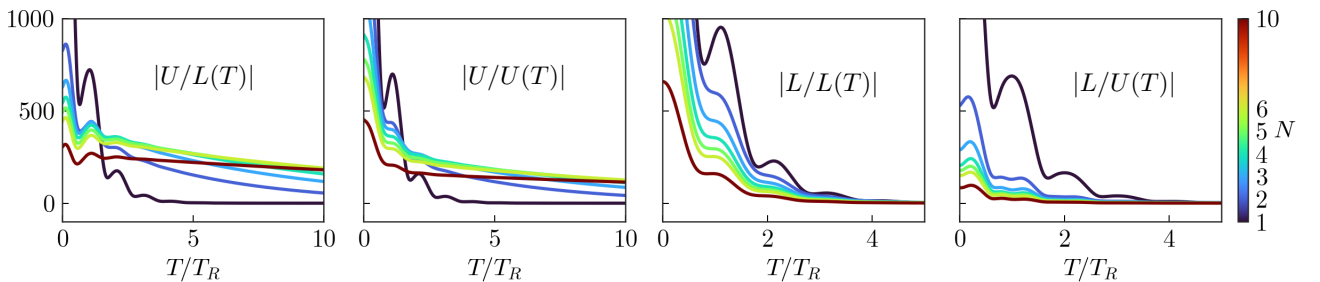


Fig. 5.6.: Evolution of the intensity for the peaks U/L , U/U , L/L , and L/U obtained from the absolute value of the 2DS $|S_{(NR+R)}^{(3)}|$ as a function of the waiting time T . This time is given in units of the Rabi period $T_R = 41.47$ fs. The plot includes the results for a different number of molecules $N = 1, 2, 3, 4, 5, 6$ and 10 of the TC model with the parameters used in Fig. 5.1.

To provide a more detailed visualization of the behavior of the 2DS signals as a function of the waiting time T and the number of molecules N in the TC model, we plot in Fig. 5.6 the intensity of the peaks U/L , U/U , L/L , and L/U as a function of both parameters. For this, we use the signals from the absolute value of the 2DS $|S_{(\text{NR}+\text{R})}^{(3)}|$ instead of the absorptive spectrum $\mathcal{R}[S_{(\text{NR}+\text{R})}^{(3)}]$. Once again, we observe that the peaks U/L and U/U are the most robust at long times T and especially for a high number of molecules N . These U/L and U/U peaks correspond to the excitation (with the first two pulses of the 2D spectroscopic protocol) of the upper polariton U . The transition $U \xrightarrow{T} D$ via molecular relaxation allows the dark states to be populated during T evolution. The slowly-varying signal at long waiting times T mostly represents the track of excitations of the residual population in dark states D though the third pulse, since these states take a considerable time to finally decay (see Fig. 5.2) through the lower polariton L . On the other hand, the peaks L/L and L/U represent an excitation through the lower polariton L (with the first two pulses of the 2D spectroscopy). Since the decaying transition $L \xrightarrow{T} D$ is not allowed by the Liouvillian of the TC model (see Fig. 5.2), the dark states are not populated during the build-up of the 2DS. At long waiting times T , the population in L decay to the ground state G via photon losses and no population remains to be excited by the third pulse in the 2D spectroscopy protocol. Consequently, at long waiting times, the magnitude of the 2DS signal through the L excitation (lower peaks) tend to vanish. In contrast, the non-zero magnitude in the U excitation pathways (upper peaks) reveal the population that remains in the dark states. In fact, while upper peaks still do not vanish at $T = 10 T_R$ for $N > 1$ (see again Fig. 5.6), the lower peaks already vanish at $T \approx 4 T_R$ for any number of emitters N . Finally we note that for short T , all peaks show a lower intensity as the number of molecules increases. This is a consequence of the loss of anharmonicity of the TC model as N increases (see Fig. 5.5).

5.3. Population pathways

We have already defined in Sec. 4.4 the population and coherence spectra, whose sum constitutes the absorptive 2DS $\mathcal{R}[S_{(\text{NR}+\text{R})}^{(3)}]$ shown in Fig. 5.4. We explained that for practical experimental purposes, the population 2DS is of greater interest. In this section, we will focus on the contributions to the absorptive population 2DS for the open TC model. The GSB, GSR, SE, and ESA' contributions are similar for any number of molecules, whether $N = 1$ (JC) or $N > 1$ (TC). The ESA contribution will be discussed separately in Subsec. 5.3.2. For example, Fig. 5.7 displays each of these four contributions for $N = 4$ at a waiting time $T = 0.5 T_R$. In fact, no noticeable differences are observed in the shape of the signals compared to the contributions shown in Fig. 4.10 for the open JC model with $N = 1$. The T evolution of the peaks appearing in the signals GSB, GSR and SE can be interpreted similarly as already done for the JC model (see Fig. 4.17).

5.3.1. GSR (Ground State Recovery) and dark states

First of all, as explained previously, GSB implies that the system returns to the ground state after the excitation process (pulse 1 + pulse 2), and the ground state does not evolve during T . Then the GSB intensity remains constant during T as shown in Fig. 5.8. The GSR peaks in the TC model, just like

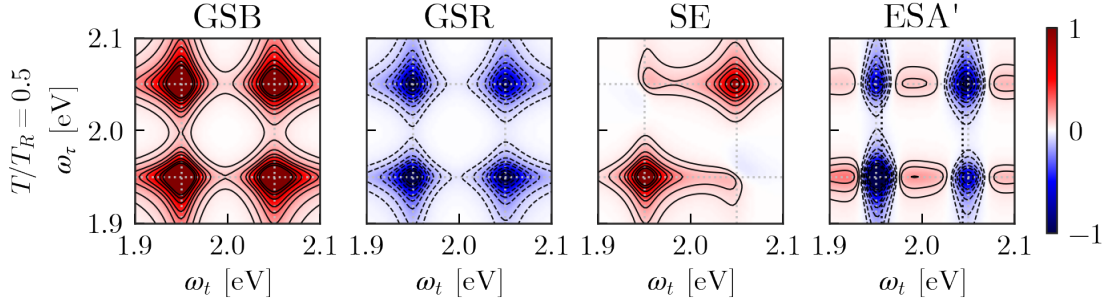


Fig. 5.7.: Population pathways GSB, GSR, SE, and ESA' contributing to the open TC absorptive 2DS ($\mathcal{R}[S_{(\text{NR}+\text{R})}^{(3)}(\omega_\tau, T, \omega_t)]$) at the waiting time $T = 0.5 T_R$ ($T_R = 41.47$ fs) for $N = 4$ molecules. Same normalization as in Fig. 5.4. The gray dotted lines represent the frequencies of the polariton states L ($\omega_{LG} = 1.95$ eV) and U ($\omega_{UG} = 2.05$ eV). The black dotted straight lines in the ESA' contribution represent the frequencies $\omega_{L_2L} = 1.956$ eV and $\omega_{U_2U} = 2.044$ eV. Contour lines are plotted at $\pm[0.05, 0.1, 0.2, 0.3, 0.4, 0.6, 0.8, 1]$.

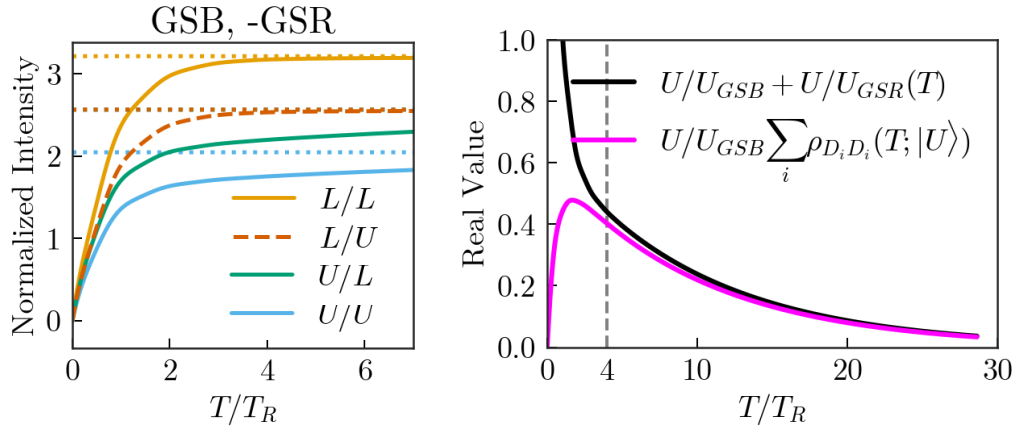


Fig. 5.8.: Left panel: Temporal evolution during T (units of $T_R = 41.47$ fs) of the peak intensities appearing in the contributions to the absorptive population 2DS: GSB (constant dotted lines) and -GSR (solid lines) for the open TC model with $N = 4$ molecules. The GSB L/U peak intensity coincides with the GSB U/L peak. We consider the peaks L/L ($\omega_\tau = \omega_t = \omega_{LG} = 0.95$ eV), U/U ($\omega_\tau = \omega_t = \omega_{UG} = 2.05$ eV), U/L ($\omega_\tau = \omega_{UG}$, $\omega_t = \omega_{LG}$), and L/U ($\omega_\tau = \omega_{LG}$, $\omega_t = \omega_{UG}$). Right panel: comparison between the sum of the population 2DS peaks $U/U_{\{\text{GSB}\}} + U/U_{\{\text{GSR}\}}(T)$ (a mutual cancellation along T) and the population of dark states (normalized with the U/U GSB peak intensity) $U/U_{\{\text{GSB}\}} \sum_{i=1}^{N-1} \rho_{D_i D_i}(T; |U\rangle)$.

The same intensity normalization as in Fig. 5.4 has been used.

in the JC, correspond to the population of the state $|G\rangle$ when the initial condition is $|U\rangle$ ($\rho_{GG}(T;|U\rangle)$ – upper peaks) or when the initial condition is $|L\rangle$ ($\rho_{GG}(T;|L\rangle)$ – lower peaks). However, in the TC model we can observe a difference in the behavior of -GSR peaks, as shown in the left panel of Fig. 5.8. In the TC case, unlike JC, the GSR upper peaks do not cancel with their respective GSB peaks at times where the JC model already does (see Fig. 5.8 for $T/T_R = 7$). This is parallel to the behavior shown in Fig. 5.2 (right panel), where the ground state G accumulates population more slowly due to the leaking of intermediate metastable dark states D , populated from the U states. From the waiting time $T \approx 4 T_R$ onward, the mutual cancellation of GSB and GSR peaks follows the trend of the total population of dark states (see right panel of Fig. 5.8 for the case $\beta = U$)

$$U/\beta_{\{\text{GSB}\}} + U/\beta_{\{\text{GSR}\}}(\text{long } T) \approx U/\beta_{\{\text{GSB}\}} \sum_{i=1}^{N-1} \rho_{D_i D_i}(\text{long } T; |U\rangle), \quad (5.4)$$

where $\rho_{D_i D_i}(T; |U\rangle)$ is the population in the i -th dark state $|D_i\rangle$ originating from the initial condition $|U\rangle$ and $\beta \in \{U, L\}$. We would need a much longer waiting time T (approximately $30 T_R$) for both GSB and GSR signals to fully cancel each other out and the 2DS to completely vanish.

5.3.2. ESA (Excited State Absorption)

The ESA contribution to the population 2DS is the one that differs the most between the JC and TC models. In fact, this contribution also shows differences between the cases $N = 2$ and $N = 4$ (as a representative of $N > 2$). This is due to the difference in the scheme of energy levels in the second excitation manifold. Fig. 5.9 shows a comparison of the ESA contribution for $N = 2$ and $N > 2$, at short and long waiting times T . The leftmost and rightmost panels show the simulation results, while the middle panels provide an explanatory scheme of what each signal represents. For any number of molecules at short waiting times, for example $T = 0.5 T_R$, the polariton states L and U , populated during the excitation process (pulse 1 + evolution T + pulse 2), keep most of their population. These states are subsequently excited towards states in the second excitation manifold Λ_2 by the action of the third pulse P_3 of the 2D spectroscopy. If the state initially populated is L , we then observe the transitions $L \xrightarrow{P_3} L_2$ and $L \xrightarrow{P_3} C_2$ (for $N = 2$) or $L \xrightarrow{P_3} M_2$ (for $N > 2$) (lower orange signals in second column of Fig. 5.9). These are excitations of the population that remains in the lower polariton during the evolution T : $L \xrightarrow{T} L$.

On the other hand, the population that remains in the upper polariton during T : $U \xrightarrow{T} U$, can be excited by P_3 towards the states $U \xrightarrow{P_3} U_2$ and $U \xrightarrow{P_3} C_2$ (for $N = 2$) or $U \xrightarrow{P_3} M_2$ (for $N > 2$), producing the respective upper signals in blue color (see the first middle column in Fig. 5.9). Additionally, when the state populated during the excitation process is U (upper signals of the 2DS –with excitation frequency $\omega_\tau = \omega_{UG^-}$), this state can decay towards the dark states during the evolution T : $U \xrightarrow{T} D$. The population that reaches the dark states can be excited by P_3 according to the transitions $D \xrightarrow{P_3} C_2$ (for $N = 2$) or $D \xrightarrow{P_3} A_2$ and $D \xrightarrow{P_3} B_2$ (for $N > 2$), producing the respective upper signals in green (see the first middle column in Fig. 5.9). Of course, this type of signals is not present in the JC model, due to the absence of dark states.

Given that the frequencies ω_{M_2U} and ω_{A_2D} for the case $N > 2$ are close to each other, these two signals (blue and green in the middle panels in Fig. 5.9) overlap in the 2DS and appear as a single signal centered at an intermediate frequency (leftmost upper peak in the left lower panel of the Fig. 5.9). It is possible that in this peak there is also a contribution from the transition $L \xrightarrow{P_3} L_2$, originating from the decays $D \xrightarrow{T} L$ and $U \xrightarrow{T} L$. However, to isolate this contribution is challenging, even at longer waiting times T . The overlap of the signals also occurs in the upper right peak of the ESA contribution for $N > 2$ at $T = 0.5 T_R$. This is because the frequencies ω_{U_2U} and ω_{B_2D} are also close to each other, producing a global single signal. There may be also a contribution in this peak from the transition $L \xrightarrow{P_3} M_2$, originating from $D \xrightarrow{T} L$ and $U \xrightarrow{T} L$. For the case of $N = 2$, the upper signal located at

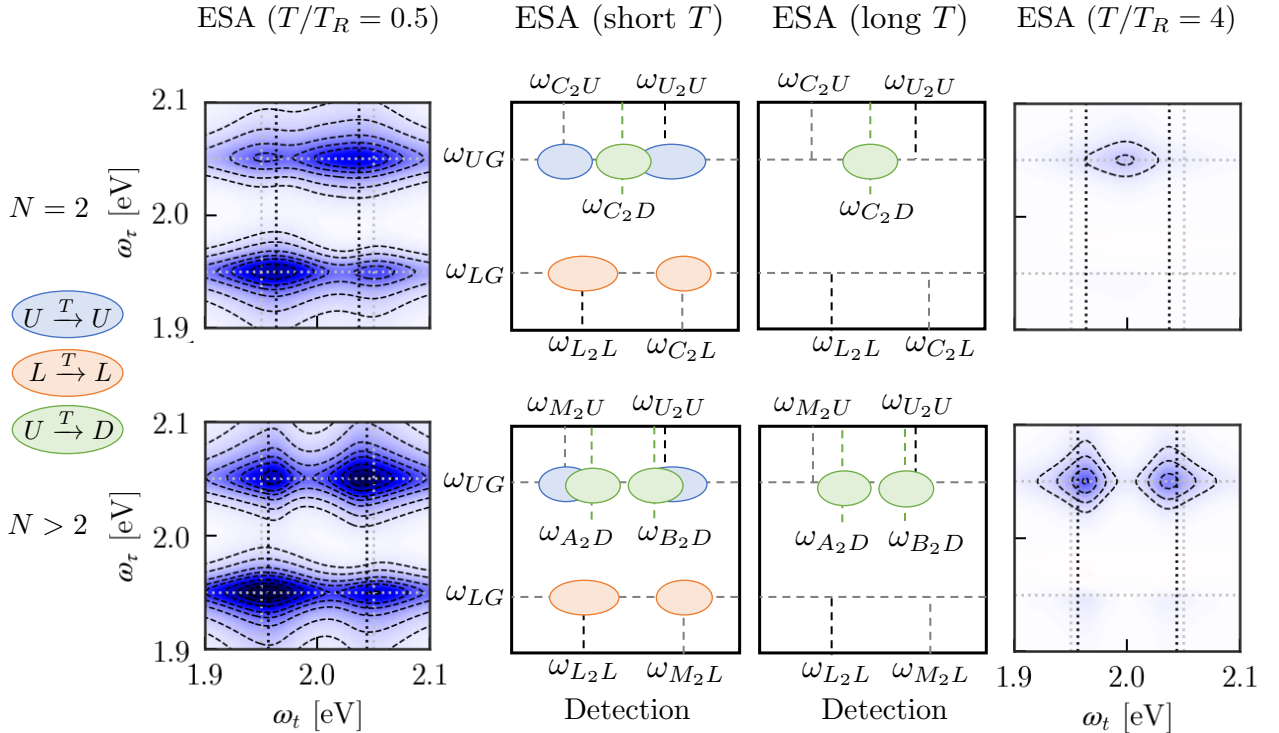


Fig. 5.9.: Population ESA pathways contributing to the open TC absorptive 2DS at the waiting times $T = 0.5 T_R$ (left panels) and $T = 4 T_R$ (right panels) for $N = 2$ molecules (upper panels) and for $N = 4$ molecules (lower panels). Middle panels represent a schematic representation of the signals at both short and long waiting times. Same normalization as in Fig. 5.4. The gray dashed lines represent the frequencies of the polariton states ω_{LG} (equivalent to ω_{C_2U} for $N = 2$ and to ω_{M_2U} for $N > 2$) and ω_{UG} (equivalent to ω_{C_2L} for $N = 2$ and to ω_{M_2L} for $N > 2$). The black dashed straight lines are the frequencies ω_{L_2L} and ω_{U_2U} . Green dashed lines in the middle panels represent the frequencies ω_{C_2D} for $N = 2$ and ω_{A_2D} , ω_{B_2D} for $N > 2$. The colors of the signals in the middle panels represent the states (populated during the temporal evolution T) that are excited towards Λ_2 with the third pulse of the 2D spectroscopic protocol.

the frequency ω_{C_2D} causes a shift towards the center of the 2DS for those signals corresponding to the frequencies ω_{C_2U} and ω_{U_2U} . As a result, only two upper peaks are observed in the 2DS (see upper leftmost panel in Fig. 5.9).

At longer waiting times, for example $T = 4 T_R$, the population in the state L has decayed to the ground state G via photon losses. Consequently, no signals are observed in the lower regions of the ESA 2DS (with excitation frequency $\omega_\tau = \omega_{LG}$ –see the rightmost column in Fig. 5.9–). On the other hand, a portion of the population achieved in U during the excitation process, has decayed to G via photon losses, or to L via molecular relaxation. The population that reached the dark states via molecular relaxation: $U \xrightarrow{T} D$ still remains, as these dark states take more time to decay. Therefore, the signals produced by excitation with P_3 from the dark states are still observed at their respective detection frequencies ω_{C_2D} for $N = 2$ and ω_{A_2D} and ω_{B_2D} for $N > 2$.

5.4. Temperature effects on polariton states

In Sec. 4.2, we investigated temperature effects on the linear emission spectrum of the JC model by using different vibrational bath spectral densities. In this section, we explore the temperature effects

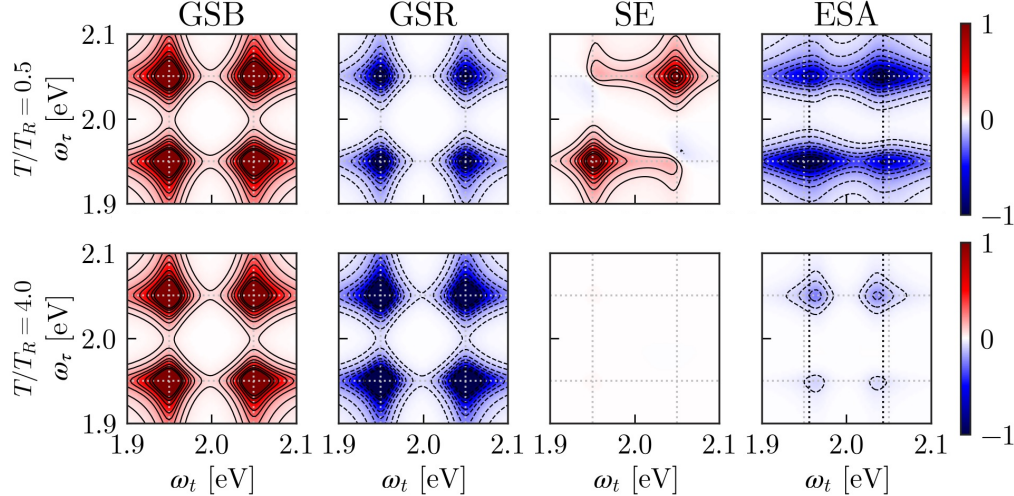


Fig. 5.10.: Population pathways GSB, GSR, SE, and ESA contributing to the open TC absorptive 2DS ($\mathcal{R}[S_{(\text{NR}+\text{R})}^{(3)}(\omega_\tau, T, \omega_t)]$) at the waiting times $T = 0.5 T_R$ (upper panel) and $T = 4 T_R$ (lower panel) for $N = 4$ molecules at a temperature of 300 K. A vibrational bath power spectrum function $S(\omega)$ has been used within the Bloch-Redfield formalism with a Debye spectral density function $J_{\text{Debye}}(\omega)$ with $\eta = 2\gamma = 0.0264$ and $\omega_d = 0.2$ eV. Same normalization as in Fig. 5.4. The gray dotted lines represent the frequencies of the polariton states L ($\omega_{LG} = 1.95$ eV) and U ($\omega_{UG} = 2.05$ eV). The black dotted straight lines in the ESA contribution represent the frequencies $\omega_{L_2L} = 1.956$ eV and $\omega_{U_2U} = 2.044$ eV. Contour lines are plotted at $\pm[0.05, 0.1, 0.2, 0.3, 0.4, 0.6, 0.8, 1]$.

on the 2DS for the TC model. We employ a Debye-type function to model the vibrational bath spectral density within the Bloch-Redfield formalism. Our focus is to study the contributions to the population 2DS since they provide a simpler understanding of the dynamics of the polariton states. The Fig. 5.10 shows the GSB, GSR, SE and ESA contributions to the population 2DS at a temperature of 300 K. The effect of temperature is hardly noticeable in the shape of the spectra. The most significant difference is observed in the ESA contribution at a waiting time $T = 4 T_R$, where lower signals appear (at the excitation frequency $\omega_\tau = \omega_{LG} = 1.95$ eV) that were not present at zero temperature (see right lower panel in Fig. 5.9). To extract detailed information about the dynamics of polariton states, let us analyze each contribution separately.

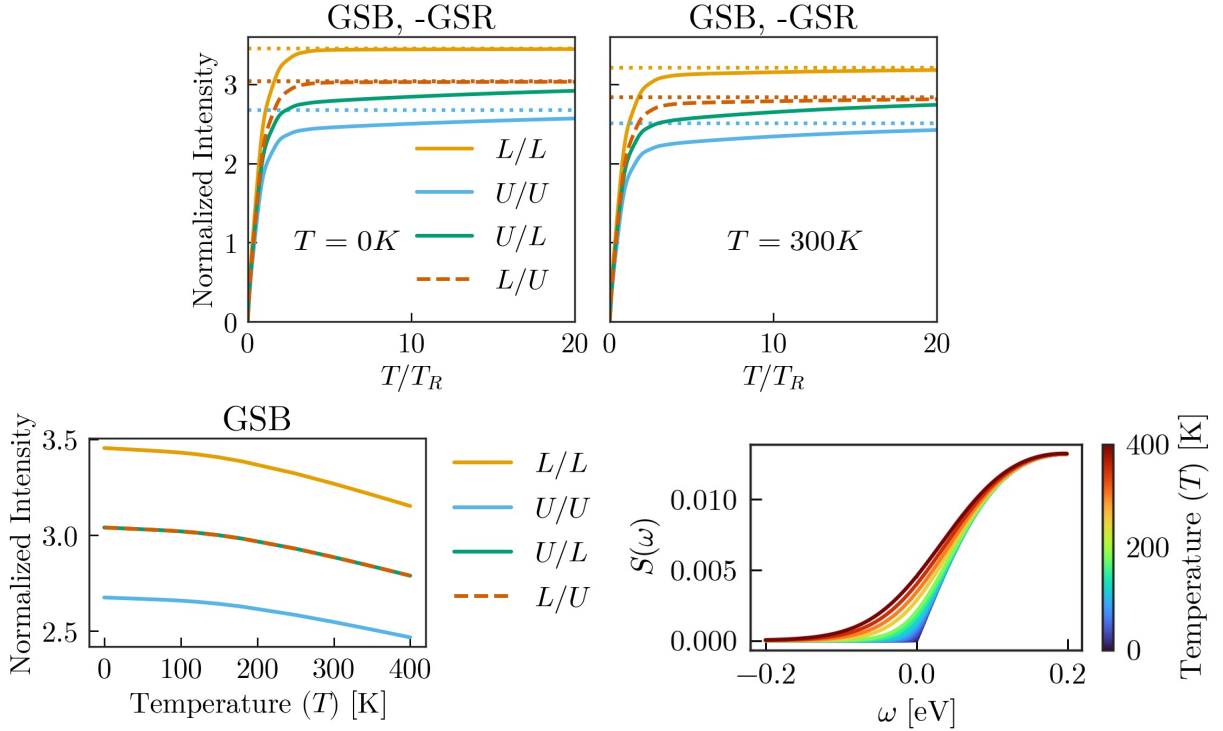


Fig. 5.11.: Upper panel: Temporal evolution during T (units of $T_R = 41.47$ fs) of the peak intensities appearing in the contributions to the absorptive population 2DS: GSB (dotted lines) and -GSR (solid lines) for the open TC model with $N = 4$ molecules at zero temperature (left panel) and at a temperature of 300 K (right panel). A Debye spectral density function has been used with the same parameters as in Fig. 5.10. Lower left panel: Peak intensities appearing in the contribution GSB of the 2DS against temperature. Lower right panel: Vibrational bath power spectrum function used to include temperature effects within the Bloch-Redfield formalism with a Debye density function (same parameters as in Fig. 5.10) at different temperatures.

5.4.1. GSB and GSR: Population pumping L to D

The GSB contribution, which physically represents a double linear absorption process of polariton states, decreases as the temperature increases. This is observed in the lower left panel of the Fig. 5.11, where the intensity of the peaks L/L , U/U , L/U , and L/U of the GSB spectrum are plotted against temperature. The increase in temperature leads to incoherent pumping of the TC Hamiltonian states. In Fig. 5.11 the vibrational bath power spectrum function $S(\omega)$ is shown at different temperatures. At higher temperatures, $S(\omega)$ exhibits non-zero values over an increasingly wider range of negative transition frequencies. This implies the possibility of transitions from lower energy Hamiltonian states to higher energy states (pumping) during the temporal evolution of the system. Incoherent pumping results in population losses of polariton states, causing a reduction in their linear absorption and consequently in the GSB and the total 2D absorptive spectrum. For a fixed frequency, e.g., $\omega = -0.05$ eV, $S(\omega)$ exhibits a quasi-parabolic behavior with respect to the temperature T , given by $S(\omega) \sim (k_B T)^2$. This behavior is inherited by the GSB spectrum. The intensities of the GSB peaks follow laws of the form (in this set of equations T represents temperature)

$$L/L_{\{\text{GSB}\}}(T) \sim L/L_{\{\text{GSB}\}}(T=0) - 3.2 \times 10^{-5}(k_B T)^2 \quad (5.5)$$

$$U/U_{\{\text{GSB}\}}(T) \sim U/U_{\{\text{GSB}\}}(T=0) - 2.2 \times 10^{-5}(k_B T)^2 \quad (5.6)$$

$$U/L_{\{\text{GSB}\}}(T) \sim U/L_{\{\text{GSB}\}}(T=0) - 2.7 \times 10^{-5}(k_B T)^2. \quad (5.7)$$

Note that the $L/L_{\{\text{GSB}\}}$ peak has a higher reduction constant (3.2×10^{-5}) compared to the $U/U_{\{\text{GSB}\}}$ peak (2.2×10^{-5}). This is because the lower polariton L , being a lower energy state, undergoes more incoherent pumping channels than the upper polariton U under the influence of temperature. On the other hand, the $U/L_{\{\text{GSB}\}}$ and $L/U_{\{\text{GSB}\}}$ peaks (which follow the same law) exhibit an intermediate constant (2.7×10^{-5}) since these peaks represent both the linear absorption of L and U .

The possibility of the pumping $L \xrightarrow{T} D$ during the temporal evolution at the waiting time T implies that, at a nonzero temperature, upon exciting the state L , a portion of the population reaches the dark states, and it takes more time to eventually decay to the ground state. The pumping $L \xrightarrow{T} D$ may be experimentally a significant process (see, for instance, [10]) Consequently, the cancellation between the GSB and GSR signals of the 2DS corresponding to the excitation of L (peaks L/L and L/U) will take longer compared to the case of zero temperature. This behavior is observed in the upper panel of Fig. 5.11. The intensity of the peaks $-L/L_{\{\text{GSR}\}}$ and $-L/U_{\{\text{GSR}\}}$ approaches the respective peaks $L/L_{\{\text{GSB}\}}$ and $L/U_{\{\text{GSB}\}}$ more rapidly when the temperature is zero (upper left panel of Fig. 5.11), in comparison, for instance, with the case of a room temperature of 300 K (upper right panel of Fig. 5.11).

In Sec. 5.3, we discussed that the sum of the contributions GSB and GSR of the 2DS is directly related to the population of dark states. When including the effects of temperature, this premise remains valid, as shown in Fig. 5.12. From a waiting time of approximately $6 T_R$, the sum of the intensities of the diagonal peaks $U/U_{\{\text{GSB}\}} + U/U_{\{\text{GSR}\}}$ and $L/L_{\{\text{GSB}\}} + L/L_{\{\text{GSR}\}}$ compares well with the respective populations of the dark states $U/U_{\{\text{GSB}\}} \sum_i \rho_{D_i D_i}(T; |U\rangle)$ and $L/L_{\{\text{GSB}\}} \sum_i \rho_{D_i D_i}(T; |L\rangle)$. It is observed that when the state initially excited is U (left panels of Fig. 5.12), at waiting times $T > 6 T_R$,

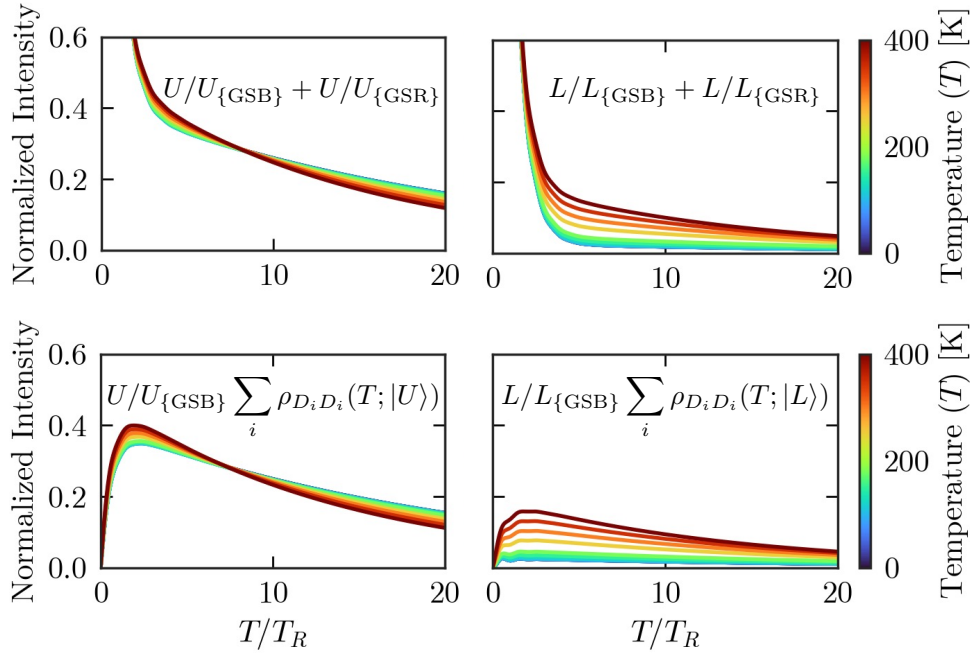


Fig. 5.12.: Comparison between the sum of the diagonal peaks GSB and GSR of the population 2DS (upper panels) and the population of dark states (lower panels) achieved through the evolution of the state U (left) and the state L (right). An open TC with $N = 4$ molecules at different temperatures has been used, with a noise-spectral power spectrum function with the same parameters as in Fig. 5.10. All graphs are plotted as a function of the waiting time T .

the population of dark states is slightly decreased as the temperature increases. On the other hand, when the state initially populated is L (right panels of Fig. 5.12), there is a noticeable increase in the population of the dark states with the rise in temperature. We have already explained that this is due to the incoherent pumping induced by the temperature. In this Fig. 5.12, at higher temperatures, the retarded cancellation between the GSB and GSR lower signals (corresponding to the excitation of L) becomes more evident and clearly represents an increase in the population of the dark states originating from the pumping from L during the temporal evolution T .

5.4.2. SE: Slight population pumping L to U

In Subsec. 4.4.2, we discussed that the SE contribution to the 2DS contains information about the transfers $L \xrightarrow{T} L, U$ (lower peaks) and $U \xrightarrow{T} L, U$ (upper peaks) during the temporal evolution at the waiting time T . One would expect the intensity of the peak $L/U_{\{SE\}}$ to increase as the temperature is higher, as the pumping $L \xrightarrow{T} U$ would intensify. However, this pumping channel $L \xrightarrow{T} U$ (occurring at transition frequency $\omega_{LU} = -0.1$ eV) is not as intense as the $L \xrightarrow{T} D$ channel (with transition frequency $\omega_{LD} = -0.05$ eV this process must have a greater rate due to the large number of final dark states). Note in Fig. 5.11 that $S(\omega_{LD}) > S(\omega_{LU})$, and thus the transition $L \xrightarrow{T} U$ (and consequently

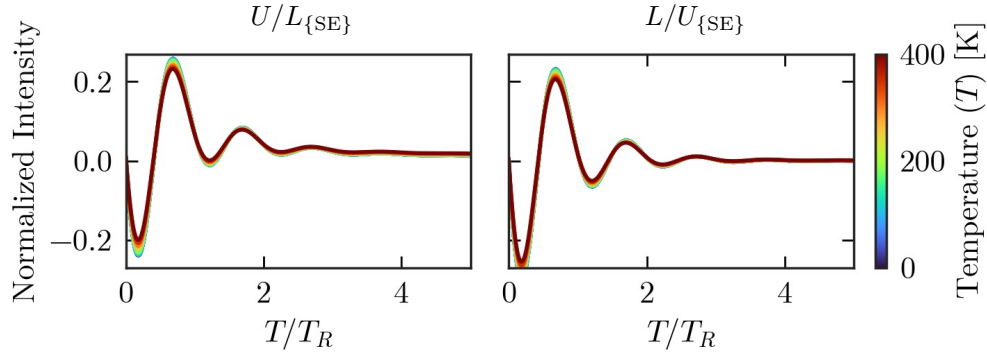


Fig. 5.13.: Temporal evolution during T (units of $T_R = 41.47$ fs) of the peak intensities $U/L_{\{SE\}}$ (left panel) and $L/U_{\{SE\}}$ (right panel) of the SE contribution to the population 2DS at different temperatures. Same parameters as in Fig. 5.10.

the peak $L/U_{\{SE\}}$ is not notably altered by the temperature variation (see right panel in Fig. 5.13). In fact, at early waiting times, both peaks $L/U_{\{SE\}}$ and $U/L_{\{SE\}}$ show a slight decrease in intensity with increasing temperature. This is probably due to an effect of the coherences $\rho_{UL}(T)$, which are also present in both signals (see Eq. (4.15) and Eq. (4.17)).

The transitions $L \rightarrow U$ and $U \rightarrow L$ are also challenging to track in the SE spectrum because the population reaching the respective U and L states decays (or gets pumped) rapidly, for example, to the dark states. The SE signals do not contain direct information about the population in the dark states, and therefore, it is not possible to trace such transitions. The ESA contribution, on the other hand, offers the possibility of extracting more information in this regard since it involves the dark states, which have a longer lifetime, thus facilitating their study.

5.4.3. ESA: Population transfer L-U-D and U-L-D

We have already mentioned in Subsec. 5.3.2 that the ESA population contribution for $N > 2$ displays four upper signals (see Fig. 5.9) located around the excitation frequency $\omega_\tau = \omega_{UG}$ with detection frequencies $\omega_t = \omega_{M_2U}$ -peak U/M_2^- , ω_{U_2U} -peak U/U_2^- , ω_{A_2D} -peak U/DA_2^- , and ω_{B_2D} -peak U/DB_2^- ; and also two lower signals located around the excitation frequency $\omega_\tau = \omega_{LG}$ with detection frequencies $\omega_t = \omega_{M_2L}$ -peak L/M_2^- and ω_{L_2L} -peak L/L_2^- . Now, with the increase in temperature, two new lower signals emerge with detection frequencies: ω_{A_2D} -peak L/DA_2^- and ω_{B_2D} -peak L/DB_2^- , which account for the pumping $L \rightarrow D$.

As an example of the variation of these signals with temperature, Fig. 5.14 shows the temporal evolution of four of them at different temperatures. Let us analyze the dynamic processes contributing to each of these signals:

- U/U_2 : The intensity of this peak shows a similar behavior to the peaks U/DA_2 and U/DB_2 (not shown) and also to the sum $U/U_{\{GSB\}} + U/U_{\{GSR\}}$ (see Fig. 5.11). We have already seen that at long waiting times T , this behavior represents the population of dark states, originating

from the decay $U \xrightarrow{T} D$. This indicates that at long waiting times, the dominant process in these three ESA peaks is $U \xrightarrow{T} D \xrightarrow{P_3} B_2$ (for peaks U/U_2 and U/DB_2) and $U \xrightarrow{T} D \xrightarrow{P_3} A_2$ (for peak U/DA_2). At short waiting times, we also observe the process $U \xrightarrow{T} U \xrightarrow{P_3} U_2$.

- **L/L_2 :** Analogously, the processes contributing to this peak and the peaks L/DA_2 and L/DB_2 are $L \xrightarrow{T} L \xrightarrow{P_3} L_2$ and $L \xrightarrow{T} D \xrightarrow{P_3} A_2$ (for peaks L/L_2 and L/DA_2), and $L \xrightarrow{T} D \xrightarrow{P_3} B_2$ (for peak L/DB_2). This is inferred as the behavior of these three peaks is similar to the population of dark states originating from the decay $L \xrightarrow{T} D$ (see Fig. 5.11).
- **U/M_2 :** What is interesting in studying the variations of the 2DS signals with respect to temperature is that we can determine if the population of the dark states we are observing in the 2DS originates from L or from U , as both exhibit different behaviors with temperature changes (see Fig. 5.11). The peak U/M_2 represents an excitation from U , but its behavior in Fig. 5.14 resembles the population of the dark states originating from the decay $L \xrightarrow{T} D$ in Fig. 5.11. This indicates that in the peak U/M_2 , in addition to the process $U \xrightarrow{T} U \xrightarrow{P_3} M_2$, contributes the process (remember that the frequency ω_{A_2D} is close to ω_{M_2D}).

$$U \xrightarrow{T} L \xrightarrow{T} D \xrightarrow{P_3} A_2. \quad (5.8)$$

In this sense, the ESA peak U/M_2 allows us to track the transition $U \rightarrow L$ through the population that subsequently decays towards the dark states, originating from L .

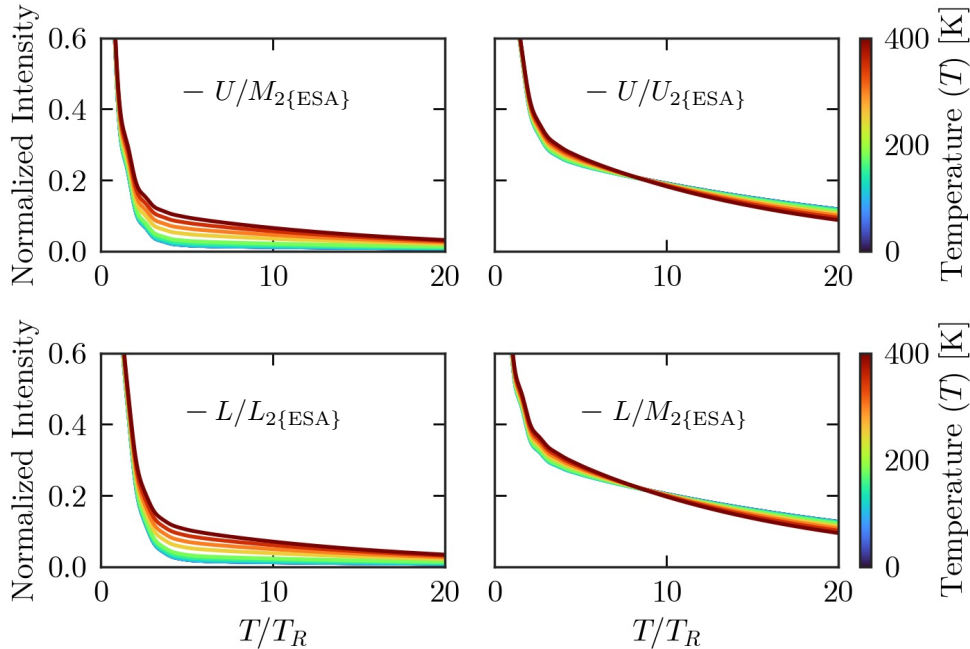


Fig. 5.14.: Temporal evolution during T (units of $T_R = 41.47$ fs) of the peak intensities $-U/M_2\{\text{ESA}\}$, $-U/U_2\{\text{ESA}\}$, $-L/L_2\{\text{ESA}\}$, and $-L/M_2\{\text{ESA}\}$ of the ESA contribution to the population 2DS at different temperatures. Same parameters as in Fig. 5.10.

- L/M_2 : Similarly, the peak L/M_2 allows us to track, in addition to the transition $L \xrightarrow{T} L \xrightarrow{P_3} L_2$, the processes of the form

$$L \xrightarrow{T} U \xrightarrow{T} D \xrightarrow{P_3} B_2. \quad (5.9)$$

5.5. Comparison with experiments

Recent studies on polariton systems incorporating molecular J-aggregates within a microcavity have revealed three primary characteristics in their 2DS as the waiting time T increases (see Fig. 5.15). These features include:

- a swift emergence of asymmetry in the 2DS, characterized by the prevalence of the cross peak U/L against the cross peak L/U .

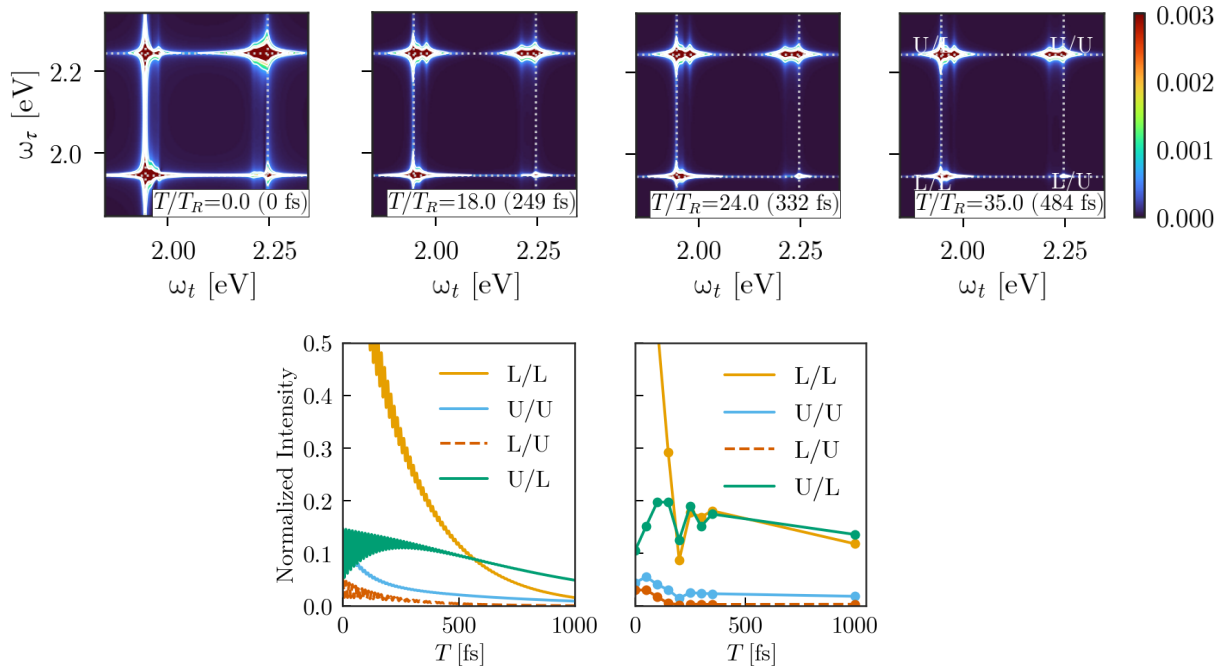


Fig. 5.15.: Upper panel: 2DS $|S_{(NR+R)}^{(3)}(\omega_\tau, T, \omega_t)|$ for a TC model with $N = 5$ emitters, at different waiting times T (in units of the Rabi period $T_R = 13.8$ fs). All spectra are normalized to the maximum value at $T/T_R = 0$. The parameters $\omega_e = 2.09$ eV and $\omega_c = 2.1$ eV have been used, with a Rabi splitting $\Omega_R = 0.3$ eV. Dotted lines indicate the transition frequencies $\omega_{LG} = 1.945$ eV and $\omega_{UG} = 2.245$ eV. Cavity lifetime is 120 fs and exciton lifetime (decay by vibrational relaxation) is chosen as 60 fs. We have considered a Debye spectral function (with cut-off $\omega_d = 0.2$ eV) at room temperature ($T = 300$ K). Lower panel: Time evolution of the diagonal and cross peaks intensities during the waiting time T for the theoretical model (left panel) and for experimental data [38] corresponding to a system of J-aggregates within an optical cavity. The peak heights are normalized such that the value of the highest peak L/L at $T/T_R = 0$ is unity.

- the diagonal peak L/L , initially the strongest, shows the most rapid reduction in intensity during the waiting time T , eventually tending to parallel the U/L cross peak intensity.
- the dominance of the L/L and U/L peaks in comparison to the U/U and L/U peaks at long waiting times T .

In our study to replicate these observations, we employed a dissipative TC model with $N > 2$, in this case we use an ensemble of $N = 5$ molecules. It is noteworthy that larger groups of molecules do not exhibit significant differences in the 2DS as previously mentioned in [Sec. 5.2](#). In the model we use a molecular natural frequency $\omega_e = 2.09$ eV and a cavity mode that is slightly blue-shifted at $\omega_c = 2.1$ eV. We found that for a good comparison between theory and experiment a small detuning $\Delta > 0$ is necessary. Consistent with the experimental setup, the Rabi frequency was set at $\Omega_R = 0.3$ eV. To more accurately match the experimental conditions, we also incorporate temperature effects in our model. This is achieved by integrating the exciton-phonon coupling with a bath noise power spectrum $S(\omega)$, using a thermal population $n(\omega)$ at room temperature $T = 300K$ and a Debye spectral function $J(\omega)$ with a cut-off parameter $\omega_d = 0.2$ eV. Our findings indicate that to accurately replicate the three experimental characteristics identified earlier, the cavity lifetime (120 fs) should be slightly longer than the molecular exciton lifetime (60 fs). These phenomena originate from the relaxation mechanisms within the Λ_1 and Λ_2 state manifolds. It is important to acknowledge that while our simplified model does not perfectly align with the experimental scenario, it is still meaningful qualitatively. In the experiments, J-aggregates interact with their surroundings and among themselves, and they have a complex phonon structure that could lead to a slower decay of the peak intensities compared to that caused solely by electronic motion. The oscillations observed in the L/L and U/L peaks versus waiting time T in the experiment (as it is displayed for waiting times T below 500 fs in the lower right panel of [Fig. 5.15](#)) are not the result of electronic Rabi oscillations. The latter are considerably quicker and they are evident in the evolution of the theoretical L/U and U/L peak intensities under 400 fs in the lower left panel of [Fig. 5.15](#) (note that the figure shows shadowed areas between the upper and lower amplitudes of the oscillations). Despite the limitations of our model, its ability to replicate the trends of these three key experimental features is quite relevant.

To extract parameters of physical relevance from the experimental 2DS, such as partial decay rates due to incoherences in the dynamics, helps in the understanding of processes involved in polariton photodynamics. The time evolution of both diagonal and cross peaks as a function of the waiting time T provides insights into the inherent decay processes. From [Eq. \(4.20\)](#), we can determine the spectral values at any point (ω_τ, ω_t) in the 2DS. Specifically, for the L/L diagonal peak, we have derived an analytical expression for its intensity:

$$|S(\omega_L, T, \omega_L)|^2 = C_1 e^{-2\Gamma_{LL}T} + e^{-(\Gamma_{LL} + \Gamma_{UL})T} [C_2 \cos(\Omega_R T) + C_3 \sin(\Omega_R T)] + e^{-2\Gamma_{UL}T} [C_4 \cos^2(\Omega_R T) + C_5 \sin^2(\Omega_R T) + C_6 \sin(2\Omega_R T)], \quad (5.10)$$

where Γ_{LL} (negative real value of the λ_{LL} Liouvillian eigenvalue) is approximately $\kappa/2$ and Γ_{UL} is near to $\kappa/2 + \gamma/8$. From the latter expression, we have further developed a simplified equation to fit the 2DS L/L peak:

$$|S(\omega_L, T, \omega_L)|^2 \sim |A e^{-2\Gamma_{LL}T} + e^{-2\Gamma_{UL}T} [B \cos(\Omega_R T) + C \sin(\Omega_R T)]|. \quad (5.11)$$

As an example, in the case of the JC model (see Fig. 4.9), we have used the theoretical values $\kappa = 0.044$ eV (corresponding to a lifetime of 15 fs) for cavity photon loss and $\gamma = 0.0132$ (equivalent to a lifetime of 50 fs) for the exciton. By fitting the L/L peak intensity against the waiting time T using this 5-parameter function $(A, B, C, \kappa, \gamma)$ in Eq. (5.11), and extracting the Rabi frequency Ω_R directly from the oscillations observed in the plot, we found decay times of approximately 15 and 43 fs, respectively. This approach demonstrates the effectiveness of our method in closely approximating the decay rates from the experimental 2DS data, providing valuable insights into the underlying mechanisms of polariton photodynamics.

As $N \rightarrow \infty$ the TC model becomes linear, analogous to two coupled harmonic oscillators [103]. This thermodynamic limit results in the loss of anharmonicity, which is crucial for producing a nonzero 2DS. However, a realistic treatment of 2DS for large systems would require going beyond the third-order perturbative limit, as the number of absorbed photons would also increase with N for a given driving strength, reaching much higher excitation manifolds Λ_n , with the nonlinearity scaling as n/N . In practical terms, when dealing with large systems, the behavior is anticipated to be similar to that of a TC model with a smaller number of molecules. This expectation is supported by the reasonable congruence observed between theoretical predictions and experimental data, as exemplified in Fig. 5.15. Thus, despite the challenges posed by larger systems, the TC model performance remains robust and relevant in approximating the behavior of more complex systems.

6. Interacting Molecules and Energy Transport

In this chapter, we explore new effects on the structure and dynamics of polariton states, caused by introducing explicitly in the TC Hamiltonian the dipole-dipole interaction between molecules. These effects are indeed visualized in the 2DS. Furthermore, we provide an analysis from the 2D spectra to check out the presence of transport mechanisms in a polariton molecular system composed by two types of molecules.

6.1. Adding molecule-molecule interaction to the TC model

So far, with the TC model, we have considered that the only way molecules interact is through radiation, without accounting for a direct interaction between them. In situations where the dipole moments of the molecules are substantially large compared with the strength of the radiation-matter interaction, or when the concentration of molecules within optical cavities is high enough to facilitate the intermolecular interaction, it becomes necessary to add a term for molecule-molecule interaction to the TC Hamiltonian. It could be the case of organic molecules like TDBC that form J-aggregates [38] and have large dipole moments. This new Hamiltonian, that we denote as the Interacting Molecules (IM) model, can be expressed as follows

$$H_{IM} = \hbar\omega_c a^\dagger a + \hbar \sum_{i=1}^N \omega_i \sigma_i^\dagger \sigma_i + \hbar \sum_{i=1}^N g_i (a^\dagger \sigma_i + \sigma_i^\dagger a) + \hbar \sum_{i \neq j} \frac{G_{ij}}{|i-j|^3} (\sigma_i^\dagger \sigma_j + \sigma_j^\dagger \sigma_i), \quad (6.1)$$

where the constant G_{ij} accounts for the interaction strength between the i -th and j -th molecules, and the term $1/|i-j|^3$ is an approximation that represents the dependence of the dipole-dipole interaction upon the distance between both molecules (located in sites i and j). This proposed model is actually a reasonable model for a (single) aggregate made up of N molecular monomers, interacting through the dipole-dipole interaction and coupled to a cavity mode. Upon the choice of the interaction parameter G one may address molecular J- or H-aggregates. Here we only study the $G > 0$ case for simplicity, since it induces more dramatic changes in the dynamics and spectra.

6.1.1. Energy structure, linear response and dynamics

The new molecule-molecule interaction included in the Hamiltonian notably modifies the eigenvalue spectrum of the polaritons and dark states, as shown in Fig. 6.1. Recall that for any number of molecules N , the TC Hamiltonian presents $N - 1$ degenerate dark states in the first excitation manifold Λ_1 . The TC Hamiltonian corresponds to the case $G_{ij} = 0 \forall i, j$ in the plots of Fig. 6.1. For simplicity we will assume that $G_{ij} = G$ for all i, j , thus without considering orientational effects among molecules. When $G > 0$, this degeneracy between dark states breaks down, and some of the dark states

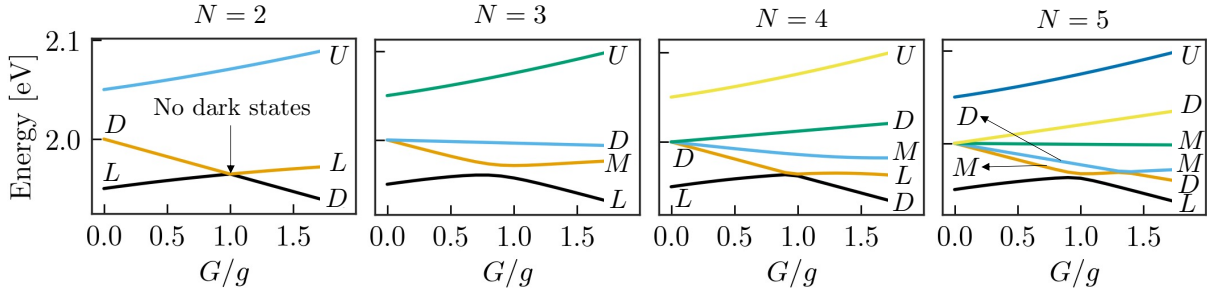


Fig. 6.1.: Energy of the eigenstates in the first excitation manifold Λ_1 of the Interacting Molecules (IM) Hamiltonian, as a function of the ratio G/g between the molecule-molecule interaction strength G and the radiation-molecule interaction strength g for a different number of molecules $N = 2, 3, 4$ and 5 . The lowest energy bright state has been identified as the lower polariton L , the highest energy bright state has been identified as the upper polariton U , the intermediate bright states have been labeled as middle polaritons M , and the dark states have been identified with the label D . The parameters used are $\hbar\omega_c = \hbar\omega_i = 2.0$ eV (for all molecules), $g_i = g = \Omega_R/2\sqrt{N}$ (for all molecules), with a Rabi frequency $\hbar\Omega_R = 0.1$ eV associated with the radiation-matter interaction g , and $G_{ij} = G$ (for all pairs of molecules), is the parameter varied in the plot. The ordering of labels before and after the anticrossings indicates the identification of states upon a linear absorption spectrum.

become bright states coupled to the cavity (labeled here as middle polaritons M). We can observe the appearance of avoided crossings for certain values of the interaction strength G . For $G \approx g$, the first anticrossing occurs between the two lowest energy states for any number of molecules. Any anticrossing indicate an exchange of character between the states involved. For example, for $N = 2$ and $G < g$, the lowest energy state in Λ_1 comes from a bright state and it represents the lower polariton L . The second state (ordered by energy) is a dark state. After the avoided crossing located when $G = g$, the lowest energy state becomes dark, and the following one becomes bright (in the following, for simplicity, we will name bright state to any polariton state that results from a bright state of matter coupled to the cavity photons and it displays an absorption peak). This indicates an exchange of character $L \leftrightarrow D$. In another case, for $N = 5$, in addition to the anticrossing between the two lowest states in Λ_1 when $G = g$, a second anticrossing is observed between the second (M) and third (D) states at $G/g \sim 1.3$. When the number of molecules increases, more anticrossings appear within the first excitation manifold Λ_1 , with fully degenerated dark states for $G = 0$. Of course, a similar behavior is found in the second excitation manifold Λ_2 (not included here). Our ordering of labels before and after the anticrossings comes from the expected identification of states as corresponding to visible peaks in a linear absorption spectrum for different values of G/g .

Similar to the TC Hamiltonian, the first excitation manifold of IM Hamiltonian is composed of $N + 1$ states. If the number of molecules inside the cavity is odd, the two lowest states of Λ_1 remain bright states even after the first avoided crossing (and before other possible anticrossings), the next one is a dark state, and the remaining polaritons alternate between bright and dark (see the bottom left panel

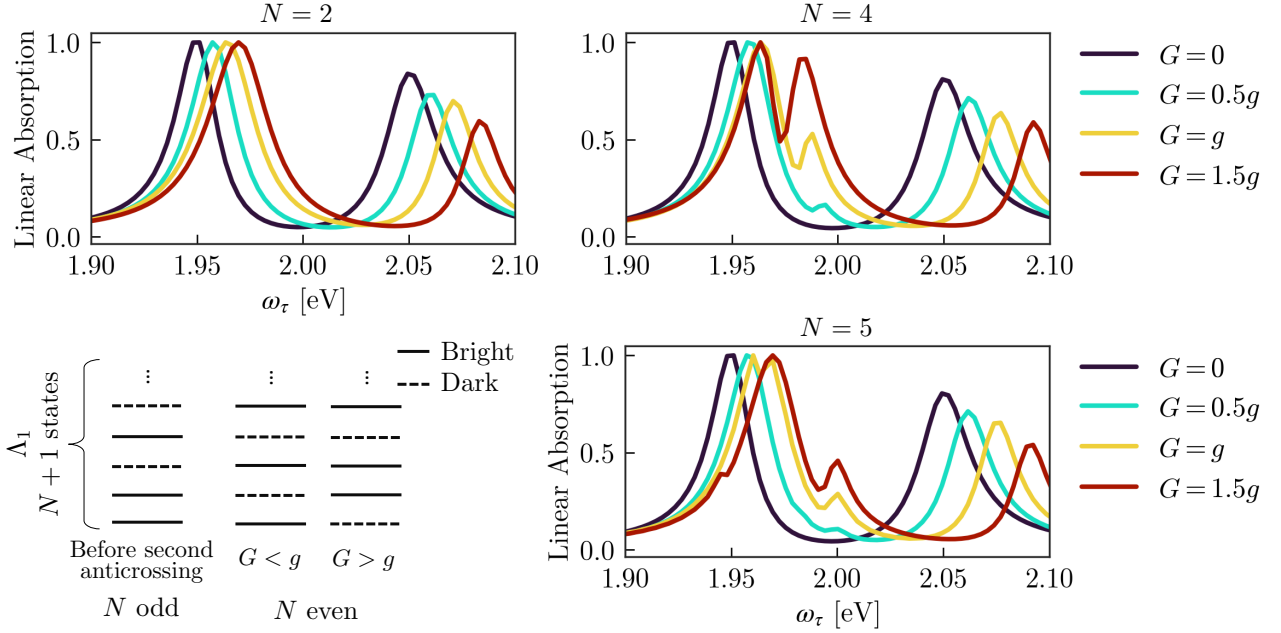


Fig. 6.2.: Upper and lower right panels: Linear absorption spectrum of the IM model with the parameters of Fig. 6.1 for different values of G . The spectra are normalized to their maxima. Lower left panel: Energy scheme of the IM model eigenstates in Λ_1 for N odd and N even. In the first anticrossing (for $G \approx g$) the two lowest energy states exchange their character. Photon lifetime is 15 fs and molecular relaxation time is 50 fs. Note for example that the four peaks in the absorption spectrum for $N = 5$ and $G/g > 1$ correspond to the sequence of states (L, M, M, U) according to Fig. 6.1.

of Fig. 6.2). This results in $(N-1)/2+2$ bright states and $(N-1)/2$ dark states when N is odd. On the other hand, if the number of molecules is even, the lowest Hamiltonian eigenstate is bright (if $G < g$) or dark (if $G > g$), the next one is dark (if $G < g$) or bright (if $G > g$), and the higher states alternate between bright and dark, resulting in $N/2+1$ bright states and $N/2$ dark states (as shown the bottom left panel of Fig. 6.2 for even N). For instance, if $N = 2$ and $G \neq g$, there are three states in Λ_1 : two are bright (L and U in Fig. 6.1) and one is dark (D in Fig. 6.1). Consequently, it is expected that the linear absorption spectrum of this system may exhibit two peaks located at frequencies ω_{LG} and ω_{UG} respectively (see the upper panel of Fig. 6.2 for $N = 2$). The particular case of $N = 2$ and $G = g$ results in three bright states in Λ_1 (the dark state disappears merging into a degenerate brightness, as shown in Fig. 6.1 for $N = 2$ at $G/g = 1$). Hence in the linear absorption spectrum, two peaks are also observed, the lowest corresponding to the absorption of the two degenerated L and L' bright states. For $N = 4$, there are two dark states and three bright states, represented by the three peaks in the linear absorption spectrum in Fig. 6.2, and for $N = 5$, there are two dark states and four bright states, as observed in the four peaks of the respective linear absorption spectrum in Fig. 6.2. The shifting of peaks in all linear absorption spectra when varying the value of G in Fig. 6.2 corresponds to the shifting of energies of the respective bright states in Fig. 6.1. We emphasize that when $G \approx g$, an

exchange of character between the two lowest states of Λ_1 occurs. For **even** N , this has two strong implications:

- Considering the respective energy scheme in the lower-left panel of Fig. 6.2, it is observed that when $G > g$, the lowest energy state is dark, and the second lowest one is bright (the lower polariton L). This lowest energy dark state cannot decay due to photon losses towards the ground state nor through molecular vibrational relaxation, as there are no lower energy states in Λ_1 . As a result, it becomes a stationary state, which is not present in the TC Hamiltonian.
- The lower polariton L can now decay through vibrational relaxation towards the stationary dark state. This represents a new decay channel that is not present in the TC Hamiltonian without molecule-molecule interactions.

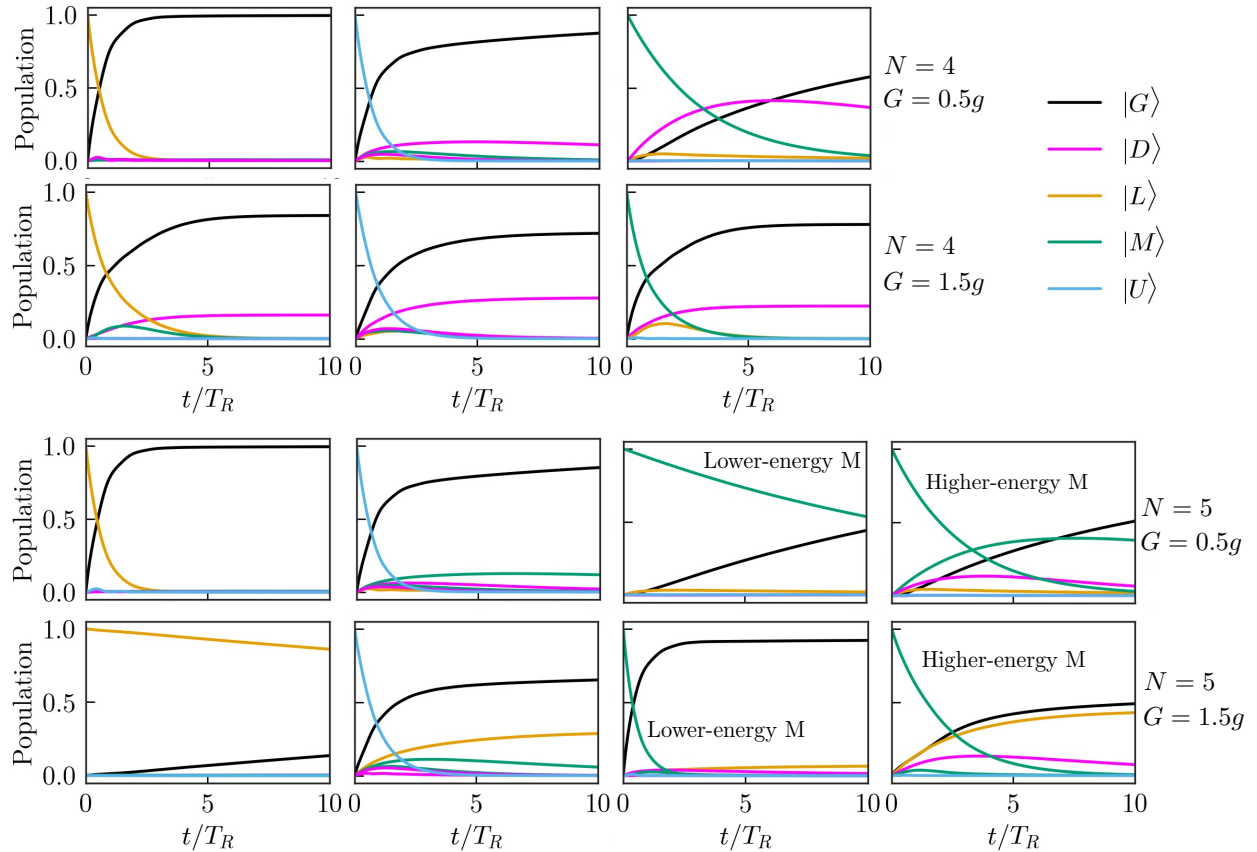


Fig. 6.3.: Dynamics of polariton states under the IM Hamiltonian with dissipation, for $N = 4$ (two upper panels) and $N = 5$ (two lower panels) molecules. The same parameters as in Fig. 6.2 have been used, with two values of G ($0.5g$ and $1.5g$, with $\hbar g = 0.1/2\sqrt{N}$ eV). In the first column the initial condition is L , in the second column is U and in the third (and fourth for $N = 5$) column(s) the initial condition is a middle polariton M . Note that for $N = 5$ molecules there are two middle polaritons, here denoted as higher and lower energy M .

For **odd** N , at $G \approx g$ the character exchange occurs between two states that are both bright i.e., the L and the lowest middle M polariton states (see the respective energy plots in Fig. 6.1 for $N = 3$ and $N = 5$). Therefore, the lowest energy state remains bright even when $G > g$ and can decay through photon losses towards the ground state (it does not become a stationary state). And the second lowest state remains as a middle bright polariton (until a possible next anticrossing with a dark state). Because of this exchange of character, the lowest energy middle polariton M for odd N displays an absorption peak with higher intensity than the lower polariton when $G > g$ as shown in Fig. 6.2 for $N = 5$.

To get an idea of the dynamic behavior of the polariton states of the IM model, Fig. 6.3 shows the temporal evolution of their respective populations for $N = 4$ and $N = 5$ molecules. Tab. 6.1 summarizes a description of the main dissipative transitions of the polariton dynamics shown in Fig. 6.3.

Lower (L)		
	$G < g$	$G > g$
Even N	$L \rightarrow G$	$L \rightarrow D$ (new - no present in TC) No considerable modification of the lifetime compared with $G < g$
Odd N	$L \rightarrow G$	$L \rightarrow G$ (lower yield compared with $G < g$ due to the character exchange $L \leftrightarrow M$) The lifetime is enhanced.

Upper (U)		
	$G < g$	$G > g$
Even N	$U \rightarrow G$ $U \rightarrow D$	$U \rightarrow G$ (lower yield compared with $G < g$) $U \rightarrow D$ (higher yield compared with $G < g$) No considerable modification of the lifetime compared with $G < g$
Odd N	$U \rightarrow G$ $U \rightarrow M$ (no present in TC)	$U \rightarrow G$ $U \rightarrow M$ $U \rightarrow L$ (lower yield compared with TC) No considerable modification of the lifetime compared with $G < g$

Lower-middle M		
	$G < g$	$G > g$
Even N	$M \rightarrow G$ $M \rightarrow D$	$M \rightarrow G$ (higher yield compared with $G < g$) $M \rightarrow D$ (lower yield compared with $G < g$) The lifetime is slightly reduced.
Odd N	$M \rightarrow G$	$M \rightarrow G$ (higher yield compared with $G < g$ due to the character exchange $L \leftrightarrow M$) The lifetime is reduced.

Tab. 6.1.: Description of the main transitions during dynamics of polariton states according to Fig. 6.3.

6.1.2. Effects of molecule-molecule interaction on 2DS

The total absorptive 2D spectrum of the IM Hamiltonian (Fig. 6.4) exhibits a rather complex structure when increasing the number N of interacting molecules, compared to the TC Hamiltonian (Fig. 5.4). Unlike the 2DS for the TC model, which only presents signals at the excitation frequencies ω_{LG} and ω_{UG} associated to L and U polaritons respectively, our IM model exhibits signals at more excitation frequencies: ω_{MG} , corresponding to the middle polaritons from Λ_1 (except for $N = 2$, with no middle polaritons). The number of middle polaritons, and consequently, the number of signals in the 2D maps, increases with the number N of interacting molecules (see, for instance, the $N = 5$ column in Fig. 6.4). For odd N , these new signals are more robust during the waiting time T for $G > g$ than for $G < g$. For even N , when $G \geq g$, the 2DS exhibits a non-zero asymptotic value for $T \rightarrow \infty$, as a result of the existence of a stationary dark state. For example, in Fig. 6.4 for $N = 2$ and $N = 4$, the spectra observed at $T = 5 T_R$ with $G = 1.5 g$ remain almost unchanged for longer waiting times. Indeed, under these conditions, at $T = 5 T_R$, the dynamics of the states has already stabilized to a steady value, as shown in Fig. 6.3 for $N = 4$.

The new diagonal peaks appearing in the spectra account for the absorption processes of the middle polaritons M , while the new cross peaks represent the dynamic interaction of these states with the other states of the first excitation manifold Λ_1 . We have already mentioned that a straightforward understanding of the total 2DS is a challenging task as they are the result of the interference between different physical processes described by Feynman pathways. It is advisable to analyze separately the various paths that contribute to the 2DS, and again, we focus only on the population 2DS, as they are of greater experimental interest.

GSB (Ground State Bleaching) and GSR (Ground State Recovery)

The GSB spectrum accounts for the linear absorption of the polariton states. Any cut along the excitation or detection frequency of the GSB spectra shown in lower panel of Fig. 6.5 for different number of molecules coincides with the respective linear absorption spectrum of Fig. 6.2 for the case $G = 1.5 g$. For example, for $N = 2$, a cut along the excitation frequency $\omega_\tau = \omega_{LG}$ of the GSB spectrum in Fig. 6.5 would result in two peaks centered at the detection frequencies $\omega_t = \omega_{LG}$ and $\omega_t = \omega_{UG}$, which are the same peaks as in Fig. 6.2 for $N = 2$ with $G = 1.5 g$, except for a normalization factor.

Note that in this case, the peak associated with L is broader and more intense than that associated with U , although for other values of G (see Fig. 6.2) it is observed that the L peak is narrower than the U . This has to do with the lifetime of both polaritons in each situation. The intensities of the GSB peaks are asymmetric (each polariton L , M , U presents a different linear absorption peak than the others). These GSB intensities are factors that accompany the intensities of the respective peaks GSR and SE peaks during their evolution in the waiting time T (see, for example, Eq. (4.13)).

In the upper panel of Fig. 6.5, the intensity of the diagonal GSB peaks (representing the intensity of the linear absorption peak of each polariton) is shown as a function of the ratio G/g , between the

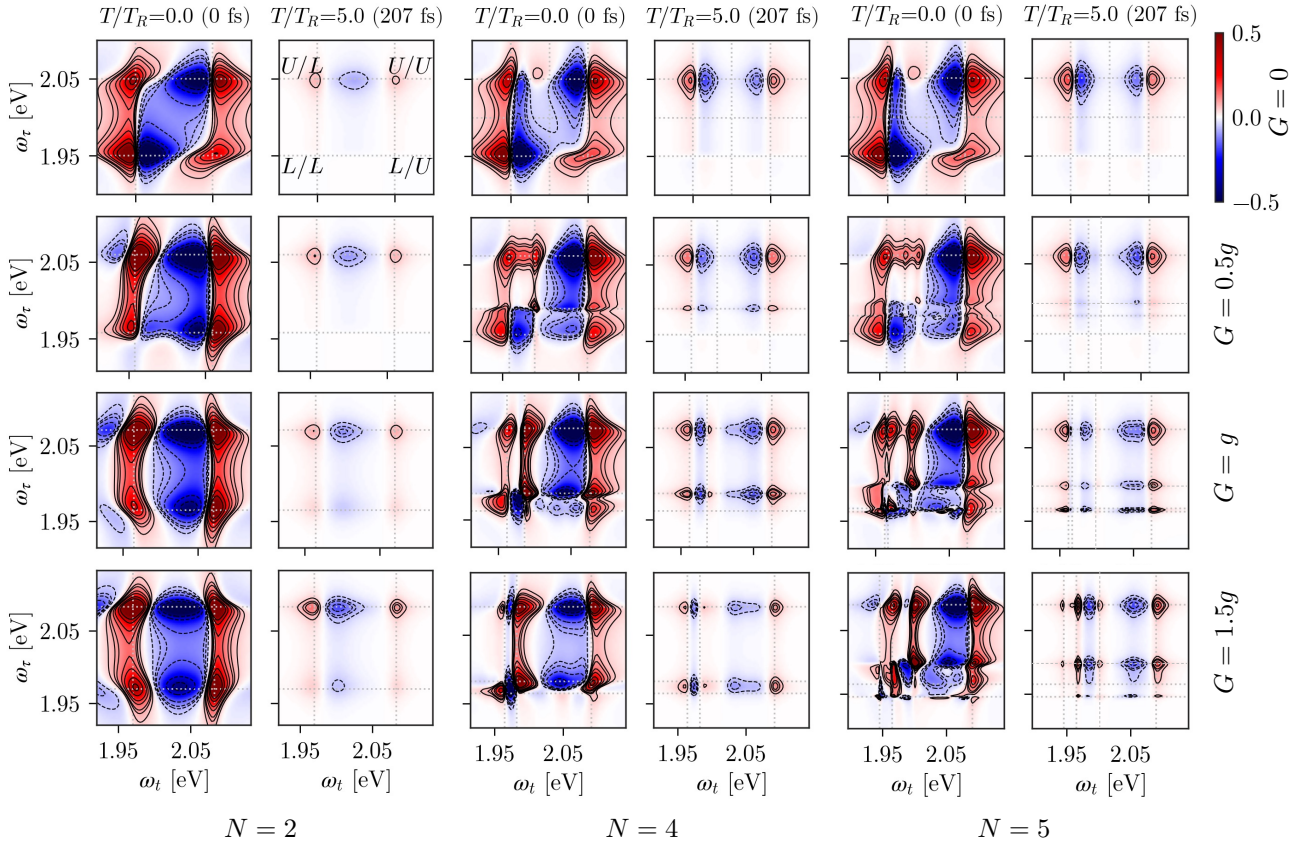


Fig. 6.4.: Electronic 2DS for the open IM model at waiting times $T = 0$ and $T = 5 T_R$ ($T_R = 41.47$ fs) for $N = 2, 4$ and 5 molecules with different molecule-molecule interaction strengths $G = 0, 0.5g, 1.0g$, and $1.5g$ ($\hbar g = 0.1/2\sqrt{N}$ eV). Here the 2D absorptive spectra $\mathcal{R}[S_{(\text{NR}+\text{R})}^{(3)}(\omega_\tau, T, \omega_t)]$ is plotted. The parameters of the model are chosen as in Fig. 6.2. Dotted straight lines indicate the lower ω_{LG} , upper ω_{UG} and middle ω_{MG} (for $N = 4$ and $N = 5$) polariton frequencies. All spectra are normalized to their maximum real value at time $T = 0$. The plots have been truncated to half of this maximum. The excitation frequency ω_τ lies along the y -axis, while the detection frequency ω_t lies along the x -axis. Solid/dashed contour lines represent heights $\pm[0.05, 0.08, 0.1, 0.15, 0.2, 0.3, 0.4]$.

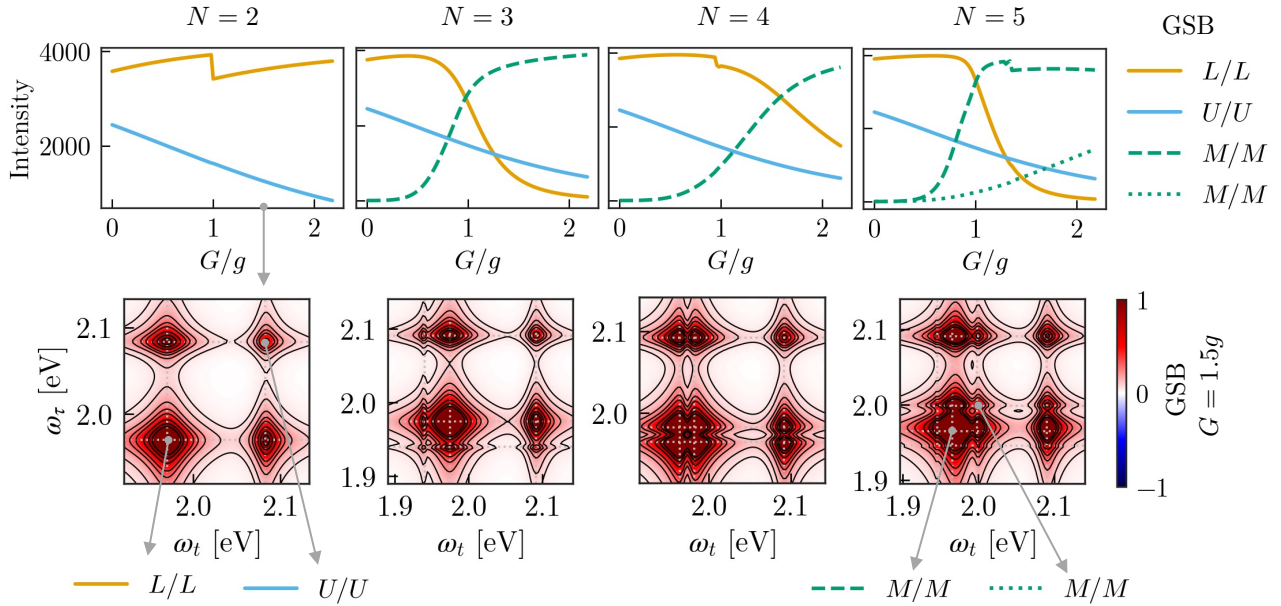


Fig. 6.5.: Upper panel: Diagonal peak intensities appearing in the GSB contribution to the 2DS (lower panel shows a specific case with $G = 1.5g$) against the molecule-molecule interaction strength G (in units of g , with $\hbar g = 0.1/2\sqrt{N}$ eV). The plots are for different number of molecules $N = 2, 3, 4$, and 5 with the IM Hamiltonian. The same parameters as in Fig. 6.2 have been used. The GSB spectra in lower panel are normalized to the maximum real value of the respective population 2DS at $T = 0$ with $G = 0$. Solid contour lines represent heights [0.05, 0.1, 0.2, 0.3, 0.4, 0.6, 0.8, 1]. Dotted gray lines indicate the lower ω_{LG} , upper ω_{UG} and middle ω_{MG} (for $N > 2$) polariton frequencies.

molecule-molecule interaction strength G and the cavity-molecule interaction strength g . For even N , the L/L peak presents a discontinuity at $G \approx g$. This is indicative of the character exchange that L undergoes from this value of G with the next dark state. At that value of G , there is also a character exchange of L with the next bright state (M) for odd N . We observe that for $G > g$, the L/L peak decreases if $N > 2$ with the increase of G . However, this decrease occurs at a slower rate if N is even (character exchange with dark state) than if N is odd (character exchange with bright state). In fact, for $G \approx 2g$ and N odd, L presents a very low linear absorption intensity compared to its value at $G = 0$ (TC model). The U/U peak always shows a decreasing behavior with the increase of G , for any number of molecules. The M/M peak, represented by the dashed green lines in Fig. 6.5, shows a similar behavior for any number of molecules, with the exception that for $N = 5$ it presents a discontinuity at $G \approx 1.3g$, which again is indicative of the character exchange of this state. Because of that, for certain values of G , this middle polariton can have the highest absorption peak, even surpassing those of the L and U states. For $N = 5$, we observe that the M/M peak associated with the higher energy middle state (green dotted line) shows an increasing absorption behavior with the increase of G .

The GSR contribution to the population 2DS, which accounts for the decay of polariton states of

Λ_1 to the ground state during the waiting time, is shown in the left column of Fig. 6.6 for different number of molecules of the open IM model at a time $T = 0.5 T_R$. The shape of the signals from this contribution is similar to the shapes of the GSB contribution since both must cancel each other out when all the population has migrated to the ground state (if no other stationary states are formed).

$G = 0$ and $G < g$: The behavior of the intensity $L/L_{\{-\text{GSR}\}}$ in relation to the respective intensity $L/L_{\{\text{GSB}\}}$ does not vary significantly between the TC model ($G = 0$) and the case $G < g$ for any number of molecules (see second column of Fig. 6.6). This indicates that the decay $L \xrightarrow{T} G$ is not

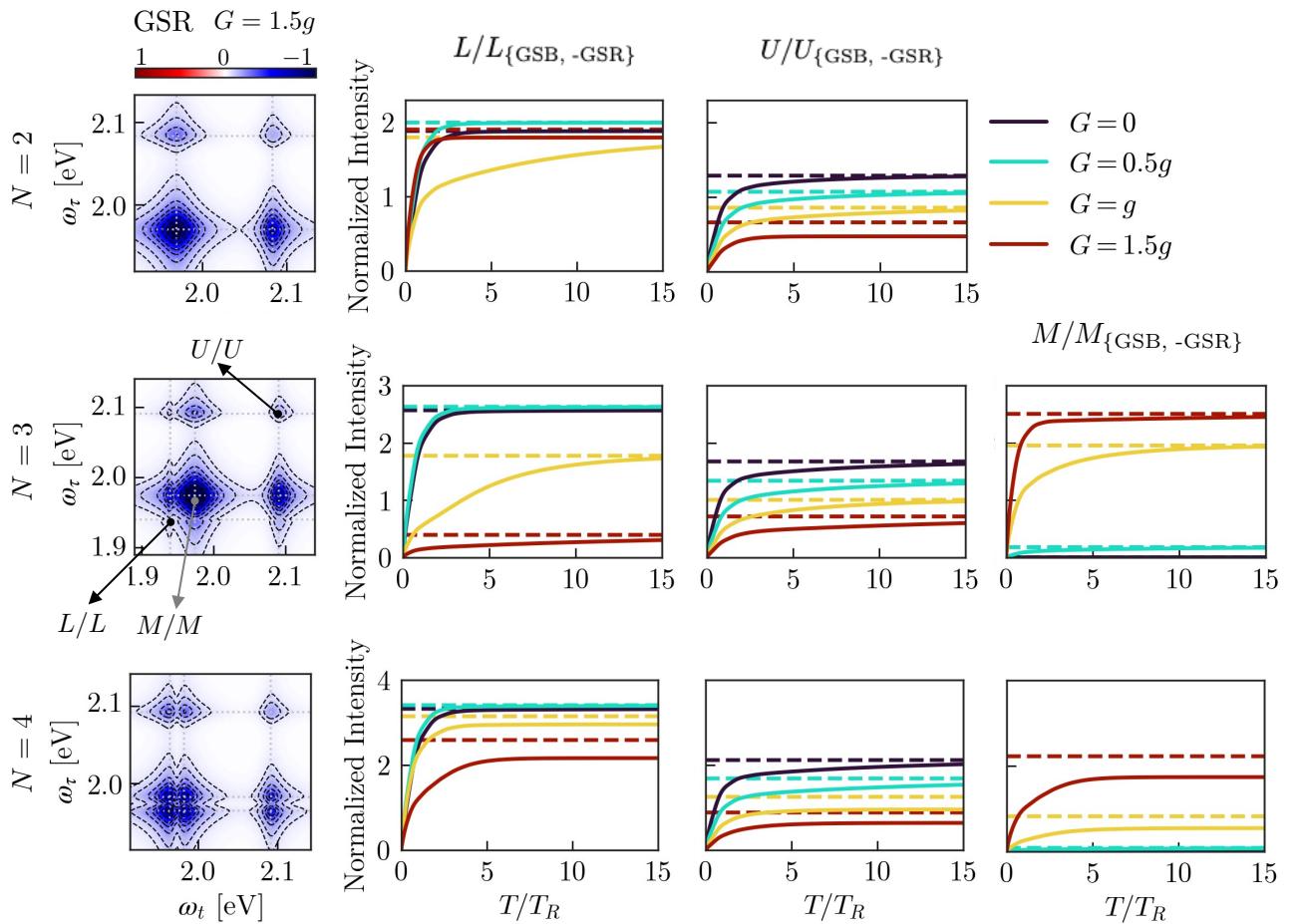


Fig. 6.6.: Left column: GSR contribution to the population 2DS for different number of molecules of the open IM Hamiltonian at a waiting time $T = 0.5 T_R$ with $G = 1.5 g$. Contour lines, normalization and dotted gray lines as in the lower panel of Fig. 6.5. Other columns: Temporal evolution during T (units of $T_R = 41.47$ fs) of the peak intensities L/L (second column), U/U (third column) and M/M (fourth column) appearing in the contributions to the population 2DS: GSB (dashed lines) and -GSR (solid lines) for the open IM model with different number of molecules $N = 2, 3$, and 4 , and $G = 0, 0.5g, g, 1.5g$. The same parameters as in Fig. 6.2 have been used.

notably altered by the molecule-molecule interaction when it is small compared to the cavity-molecule interaction; and also that no new decay channels for L appear that compete with the channel towards the ground state. On the other hand, the intensities associated with the U/U peak (third column of Fig. 6.6) exhibit a more noticeable difference between the cases $G = 0$ and $G = 0.5g$. It is concluded that the population of the U state takes a longer time to reach the ground state when $G > 0$, even when $G < g$. In the case of even N , it is due to the fact that the transition $U \xrightarrow{T} D$ becomes stronger with the increase in the value of G (see Fig. 6.3), and in the case of odd N , it is due to the emergence of a new significant decay channel $U \xrightarrow{T} M$. Neither the GSB nor the GSR contribution show high intensities in the M/M zone (fourth column of Fig. 6.6 for $N > 2$) when $G = 0.5g$. Under this condition, regardless of the number of molecules, the linear absorption peak of the middle polaritons M is very small compared to the L and U peaks (see Fig. 6.2 for $N = 4$ or $N = 5$ with $G = 0.5g$). Consequently, the respective GSB and GSR peaks should also be of low intensity.

$G = g$ and $G > g$: When N is even and $G \geq g$ ($G > g$ for $N = 2$), we have identified that a dark stationary state is formed, which prevents the total population to decay to the ground state. Consequently, the GSB and GSR contributions fail to cancel each other out for long times T , and a non-zero asymptotic spectrum is expected to be found for even N and $G \geq g$, as shown in Fig. 6.4. Under these conditions, the difference between the GSB and -GSR intensities shown in Fig. 6.6 at long times T indicates the population that remains in the dark stationary state. For the special case $N = 2$ and $G = g$, we notice that $L/L_{\{-\text{GSR}\}}$ takes longer to cancel out $L/L_{\{\text{GSB}\}}$ compared to other values of G . This is because in this situation, dark states are not formed, but rather two lower bright polaritons L and L' with the same energy. The population migrating from them to the ground state ($L, L' \xrightarrow{T} G$) is attenuated by the population exchange between them ($L, L' \xrightarrow{T} L, L'$), which causes a delay in the total population reaching the ground state.

For odd values of N , like $N = 3$ in the second row in Fig. 6.6, we observe that the $L/L_{\{-\text{GSR}\}}$ peak takes longer to cancel out the $L/L_{\{\text{GSB}\}}$ peak when $G \geq g$, compared to the case $G < g$, and the intensity of the $L/L_{\{\text{GSB}\}}$ peak is smaller when $G \geq g$. This is due to the exchange of character (thus exchange of lifetimes) between the L and the lower-energy M polariton already discussed for the results in Fig. 6.3. In this odd N case no stationary states are formed and thus all the GSB and -GSR peaks L/L , U/U , and M/M show a cancellation at long times T . The U/U peaks take longer to cancel out as the value of G increases. This is because when $G \geq g$, the channel $U \xrightarrow{T} L$ becomes relevant in the dynamics, attenuating the channel $U \xrightarrow{T} G$. Additionally, the channel $U \xrightarrow{T} M$ is also present. The opposite effect is observed in the M/M peak (the cancellation takes less time as G increases) since M decreases its lifetime when $G \geq g$ by the character exchange with L .

SE (Stimulated Emission)

The cross peaks of the SE (stimulated emission) contribution to the population 2DS (Fig. 6.7 shows the temporal evolution of these peaks for the IM Hamiltonian) provide information about the population transfer between the different polariton states of Λ_1 . These cross peaks (for example $U/L_{\{\text{SE}\}}$ as in Eq. (4.15)) are mostly a contribution of the density matrix coherences (for example $\rho_{UL}(T)$).

For even N , the transition $U \xrightarrow{T} L$ (see panels in second column for $N = 2$ and $N = 4$ in Fig. 6.7) loses intensity with the increase of G as the transition $U \xrightarrow{T} D$ gains importance in the dynamic evolution (see Fig. 6.3 for $N = 4$). For odd N , the transition $U \xrightarrow{T} L$ gains importance when $G \geq g$ at long waiting times, as a result of the character exchange between L and M , and in compensation, the transition $U \xrightarrow{T} M$ decreases in intensity also for long T (see third column in Fig. 6.7). The pumping transitions ($L \xrightarrow{T} U$, $L \xrightarrow{T} M$, $M \xrightarrow{T} U$) are weak for any number of molecules in the IM model, even for $G \geq g$.

The transition lower-energy $M \xrightarrow{T} L$ is not very strong for any number of molecules as shown in Fig. 6.3. However, the $M/L_{\{SE\}}$ peaks in Fig. 6.7 dominate against the other peaks at long T . It

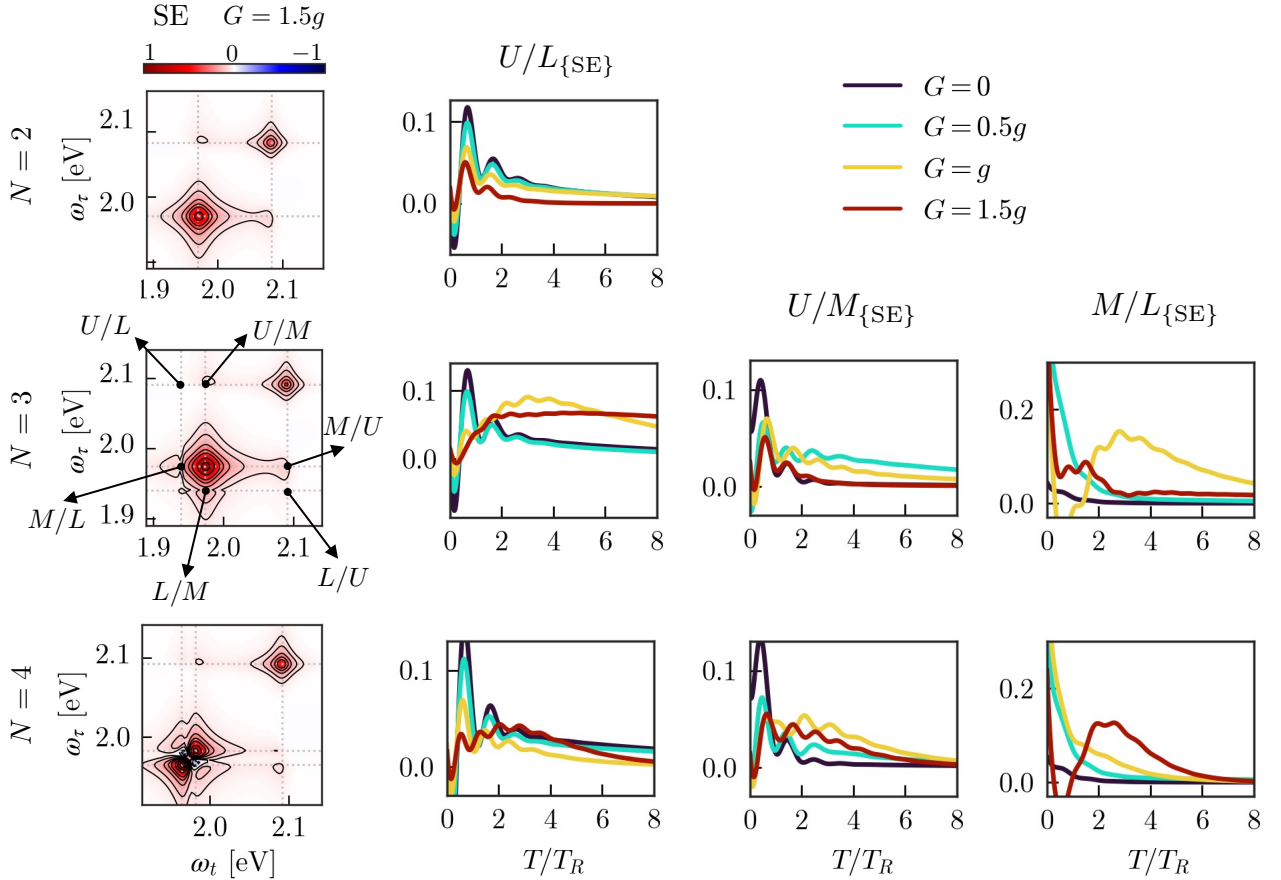


Fig. 6.7.: Left column: SE contribution to the population 2DS for different number of molecules of the open IM Hamiltonian at a waiting time $T = 0.5 T_R$ with $G = 1.5 g$. Contour lines, normalization and dotted gray lines as in the lower panel of Fig. 6.5. Other columns: Temporal evolution during T of the cross peak intensities appearing in the contribution SE for different number of molecules in the open IM model and $G = 0, 0.5g, 1.0g,$ and $1.5g$. The same parameters as in Fig. 6.2 have been used.

is important to be careful when extracting information from the 2D maps, as the peaks associated with some physical process may overlap with other peaks. In this case, for example, by observing the left column of Fig. 6.7, we notice that the $M/L_{\{SE\}}$ and $L/M_{\{SE\}}$ peaks overlap with the diagonal much more intense peaks $L/L_{\{SE\}}$ and $M/M_{\{SE\}}$ and, it happens for any waiting time T , so that the information retrieved from the time evolution of the intensity of a less intense cross peaks like $M/L_{\{SE\}}$ may be of difficult interpretation. To extract more precise information, it would be necessary to eliminate the contribution of the diagonal peaks.

ESA (Excited State Absorption)

The ESA contribution, which was studied for example in Subsec. 5.3.2, is the best tool within the 2D maps for tracking dark states over long waiting times, as these states tend to have the longest lifetimes and, therefore, are still susceptible to being excited to Λ_2 (with the third pulse of the spectroscopic protocol). For instance, if we analyze the simplest case in the IM model ($N = 2$), Fig. 6.8 shows the ESA signals of the spectra, indicating the frequency of contributing transitions. In this $N = 2$ case, with $G > 0$ ($G \neq g$), the second excitation manifold Λ_2 is composed of 3 polariton states: lower L_2 (mainly connected through dipolar transition with L), middle M_2 (connected with both L and U), and upper U_2 (mainly connected with U), as well as a state connected with the dark state D of Λ_1 , which we name D_2 .

For $G < g$ (first column of Fig. 6.8), at early waiting times (for example, $T = 0.5 T_R$), we observe two upper ESA signals centered at the excitation frequency $\omega_\tau = \omega_{UG}$. These signals allow us to follow the temporal evolution of the population that, after being excited to the state U , remains in that state during T and is then excited with the third pulse to M_2 (process $U \xrightarrow{T} U \xrightarrow{P_3} M_2$, located at the detection frequency $\omega_t = \omega_{M_2U}$) or to U_2 (process $U \xrightarrow{T} U \xrightarrow{P_3} U_2$, located at the detection frequency $\omega_t = \omega_{U_2U}$). With less intensity, the third process contributing to the upper ESA signals at short times represents the migration of the population in U to the dark state D and the subsequent excitation of this population to D_2 (process $U \xrightarrow{T} D \xrightarrow{P_3} D_2$, located at the detection frequency $\omega_t = \omega_{D_2D}$). However, this last process is not as strong at short times as it is at long times (for example, $T = 5 T_R$), where all the initial population in U has relaxed and part of it still remains in the dark state, producing the only signal we observe in the 2D map ESA at long times.

These three processes at short times, representing the upper signals, are also present for $G = g$ (second column of Fig. 6.8) and $G > g$ (third column of Fig. 6.8). The two lower signals located at the excitation frequencies $\omega_\tau = \omega_{LG}$ at short times (when $G < g$), respectively represent the processes $L \xrightarrow{T} L \xrightarrow{P_3} L_2$, located at the detection frequency $\omega_t = \omega_{L_2L}$ and $L \xrightarrow{T} L \xrightarrow{P_3} M_2$, located at the detection frequency $\omega_t = \omega_{M_2L}$. Since for $G < g$, the transition $L \xrightarrow{T} D$ is not relevant in the dynamics, we do not observe a lower signal at long times T that accounts for such transition. However, for $G > g$, where the character exchange $L \leftrightarrow D$ has occurred, the process $L \xrightarrow{T} D$ becomes relevant in the dynamics, and therefore, in such a case, the lower signal at long times T , located at $\omega_t = \omega_{D_2D}$ (process $L \xrightarrow{T} D \xrightarrow{P_3} D_2$), is indeed observed, as shown in the bottom right map of Fig. 6.8.

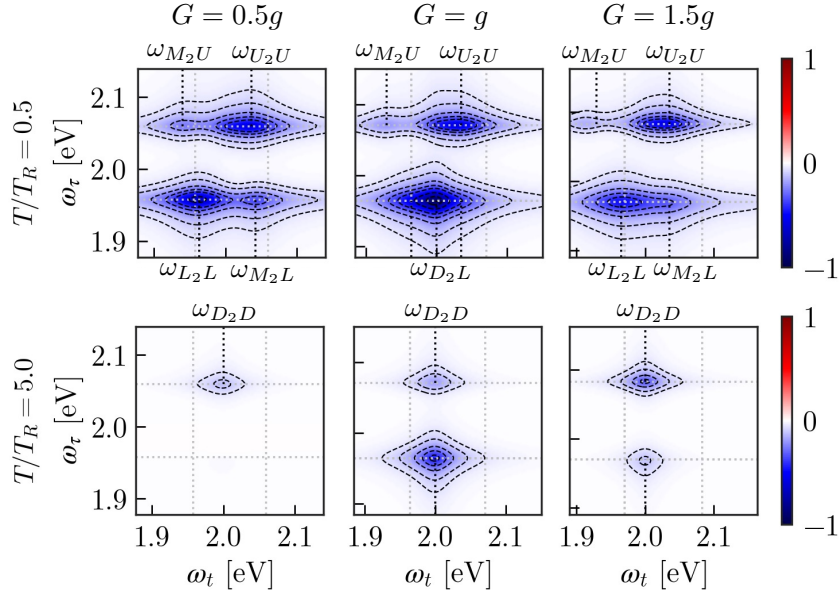


Fig. 6.8.: ESA contribution to the population 2DS for $N = 2$ molecules of the open IM Hamiltonian at the waiting times $T = 0.5 T_R$ and $T = 5 T_R$ with $G = 0.5g, g, 1.5g$. Normalization and dotted gray lines as in the lower panel of Fig. 6.5. The same parameters as in Fig. 6.2 have been used. Black dotted lines represent the respective labeled transition frequencies between states of Λ_1 and states of Λ_2 .

In the particular case of $G = g$ at short waiting times, the lower signals represent the processes $L, L' \xrightarrow{T} L, L' \xrightarrow{P_3} L_2$ (located at $\omega_t = \omega_{L_2L}$), $L, L' \xrightarrow{T} L, L' \xrightarrow{P_3} M_2$ (located at $\omega_t = \omega_{M_2L}$) and also a new signal appears, even more intense than the previous two, representing the process $L, L' \xrightarrow{T} L, L' \xrightarrow{P_3} D_2$ (located at $\omega_t = \omega_{D_2L}$) since in this specific case the degenerate states L and L' are connected through dipolar transition with the state D_2 of Λ_2 . Given that the state L formed when $G = g$ ($N = 2$), have long lifetime, at advanced times ($T = 5 T_R$) we observe a lower signal representing the process $L, L' \xrightarrow{T} L \xrightarrow{P_3} D_2$ and an upper signal representing the transition $U \xrightarrow{T} L \xrightarrow{P_3} D_2$, both of them located at the detection frequency ω_{D_2L} .

The same type of ESA signals described for $N = 2$ would be obtained for other values of N , considering that new signals at more excitation frequencies ω_τ appear, due to the presence of new polariton states in Λ_1 . The location in ω_t of these new signals will depend on how the states of Λ_1 are connected by dipole transitions with those of Λ_2 . This varies depending on the number of interacting molecules and the value of G . For example, for $N = 3$, when $G > 0$, the states L, M , and U in Λ_1 are dipole connected with five states of Λ_2 , while the D states in Λ_1 are connected with two states of Λ_2 . In any case, the ESA signals for large T reveal the excitations that results from long living states in Λ_1 to Λ_2 .

6.2. Energy transport between two groups of molecules and cavity

The energy transport in polariton systems has been an area of active research in the last years (see for instance [154, 12, 10] and references therein). In this section, we consider two groups of molecules, one of them is called the donor group, whose characteristic frequency is denoted by ω_D , and the other is the acceptor group, with frequency ω_A . Each of these groups may be composed by one or several molecules, in such a way that the Donor-Acceptor Hamiltonian (DA) describing the system in strong coupling with a cavity of frequency ω_c is

$$H_{DA} = \hbar\omega_c a^\dagger a + \hbar \sum_{I=\{D,A\}} \left[\omega_I \sum_{i=1}^{N_I} \sigma_i^{\dagger I} \sigma_i^I + g_I \sum_{i=1}^{N_I} (a^\dagger \sigma_i^I + \sigma_i^{\dagger I} a) \right], \quad (6.2)$$

where σ_i^D and σ_i^A are the de-excitation operators for the i th molecule of donor and acceptor groups respectively, N_D and N_A represent the respective numbers of molecules in each group, and g_D and g_A are the cavity-molecule interaction strengths for each group. Once again, we introduce photonic losses in the cavity using a Lindblad term for the operator a , with a decay rate of $\kappa = 1/T_\kappa$ (where T_κ represents the cavity lifetime). We also consider molecular vibrational relaxation through the Bloch-Redfield formalism, employing individual operators $\sigma_i^\dagger \sigma_i$ for all molecules in both the acceptor and donor groups. We use a step-type vibrational bath spectral function $J(\omega) = \gamma = 1/T_\gamma$ for $\omega \geq 0$ and $J(\omega) = 0$ for $\omega < 0$, where T_γ denotes the lifetime of the molecular excitons, which we assume to be the same for both groups of molecules.

6.2.1. Properties of the model and energy distribution of the states

When there are N_A acceptor molecules and N_D donor molecules inside the cavity, three polariton states are formed in the first excitation manifold Λ_1 (lower L , middle M , and upper U), and also $N_A - 1$ degenerate dark states D_A associated with excitations of the acceptor group, and $N_D - 1$ dark states D_D associated with the donor group. In the top left panel of Fig. 6.9, the energies of these states are shown as a function of the cavity frequency ω_c for $N_A = N_D = 2$, $\omega_A = 1.9$ eV, and $\omega_D = 2.1$ eV. Acceptor dark states D_A are quasi-degenerate with the middle polariton M for $\omega_c < \omega_A$, and with the lower polariton L for $\omega_c > \omega_A$; whereas donor dark states D_D are quasi-degenerate with U for $\omega_c < \omega_D$, and with M for $\omega_c > \omega_D$. In the interval $\omega_A < \omega_c < \omega_D$, middle polaritons M break their quasi-degeneracy. We can observe two points of character exchange between states: when $\omega_c = \omega_A$, the exchange $L \leftrightarrow M$ occurs, and when $\omega_c = \omega_D$, the exchange $M \leftrightarrow U$ takes place.

The middle polariton M only appears when $\omega_A \neq \omega_D$. If $\omega_A = \omega_D = \omega_e$, even when $\omega_c \neq \omega_e$, the TC model discussed in Chap. 5 is recovered, in which only two polariton states L and U are formed in Λ_1 . The dipolar transition $G \rightarrow M$ (which would be achieved by excitation with the first two pulses of the 2D spectroscopy protocol) is maximized when $\omega_c = (\omega_A + \omega_D)/2$. For that value of ω_c , the transitions $G \rightarrow L$ and $G \rightarrow U$ are minimized, as indicated by the plot in the upper middle panel of Fig. 6.9. The exchange of character between states are reflected in the linear absorption spectrum for different cavity frequencies, as shown in the upper right panel of Fig. 6.9. When $\omega_c < \omega_A$, L is the polariton that shows the highest peak of linear absorption, but in the zone $\omega_A < \omega_c < \omega_D$, the

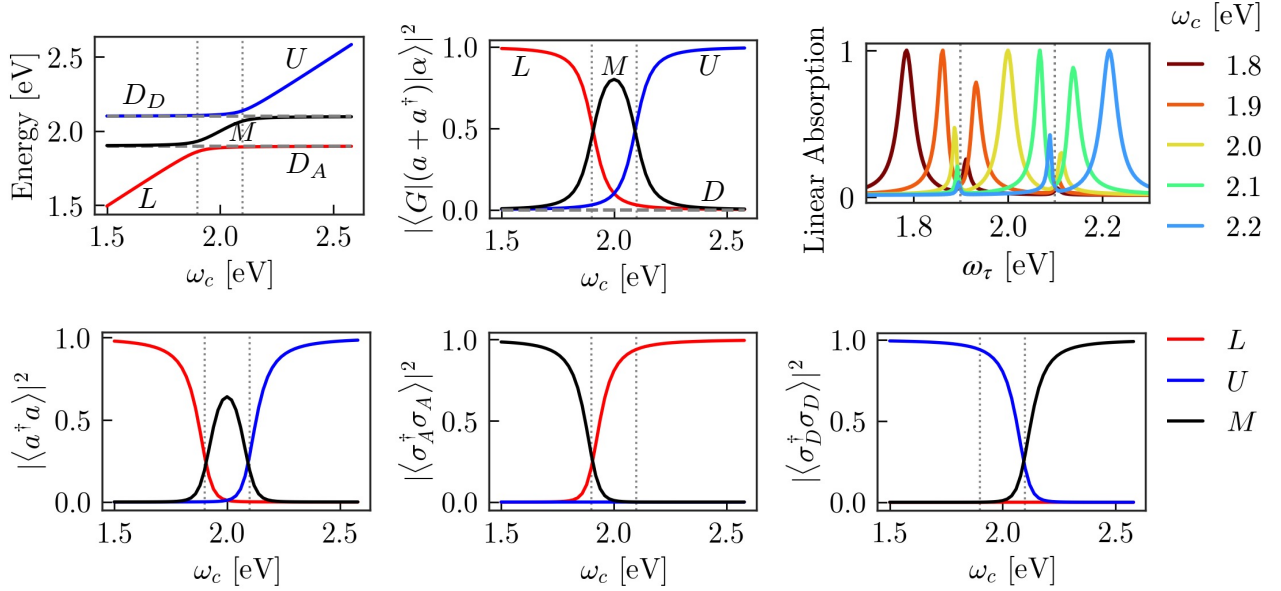


Fig. 6.9.: Upper panel: energy of the lower polariton L (red), upper polariton U (blue) middle polariton M (black) and dark states D (dashed gray) in the first excitation manifold Λ_1 of the Donor-Acceptor (DA) Hamiltonian, as a function of the cavity frequency ω_c (left panel). Probability of the dipolar transition $|G\rangle \rightarrow |\alpha\rangle$ ($|\langle G|(a+a^\dagger)|\alpha\rangle|^2$), where $\alpha = L, U, M, D$ (DA model eigenstates), as a function of the cavity frequency ω_c (middle panel). Linear absorption spectra (normalized to their maxima) of the DA model for different values of ω_c (right panel). Lower panel: Square modulus of the expectation value of the operators of cavity excitations $a^\dagger a$ (left panel), acceptor molecules excitations $\sigma_A^\dagger \sigma_A$ (middle panel), and donor molecule excitations $\sigma_D^\dagger \sigma_D$ (right panel) for the polariton states L, U , and M of the DA model. In all cases, the parameters used are $N_A = N_D = 2$, $\omega_A = 1.9$ eV, $\omega_D = 2.1$ eV (dotted vertical lines in the plots), $\hbar g_A = \hbar g_D = 0.025$ eV, cavity lifetime is 15 fs, and exciton lifetime (vibrational relaxation) is 50 fs for both groups of molecules.

highest peak corresponds to a transition from G to M , and for $\omega_c > \omega_D$, a transition to U displays the highest peak. The choice of the cavity frequency ω_c determines how the energy of the photonic and molecular excitations is distributed among the polariton states. In the lower panel of Fig. 6.9 the contribution of each state to the photonic excitations is shown (left panel, identified by the square modulus of the expectation value of the number operator $a^\dagger a$), to the excitations of the acceptor group (middle panel, identified with the operator $\sigma_A^\dagger \sigma_A$), and to the excitations of the donor group (right panel, identified with the operator $\sigma_D^\dagger \sigma_D$). The photonic energy is mainly represented by the polariton L when $\omega_c < \omega_A$, by M when ω_c is near to $(\omega_A + \omega_D)/2$, and by U when $\omega_c > \omega_D$. On the other hand, the excitonic energy of the acceptor group is primarily concentrated in the middle polariton M when $\omega_c < \omega_A$ and in L when $\omega_c > \omega_A$, while the energy of the donor group is stored in U when $\omega_c < \omega_D$ and in M when $\omega_c > \omega_D$. In this way, by applying the 2D spectroscopy protocol to the DA system for a given cavity frequency ω_c , it is possible to trace the dynamic evolution of the polariton states and consequently determine how photonic and excitonic energy is transported.

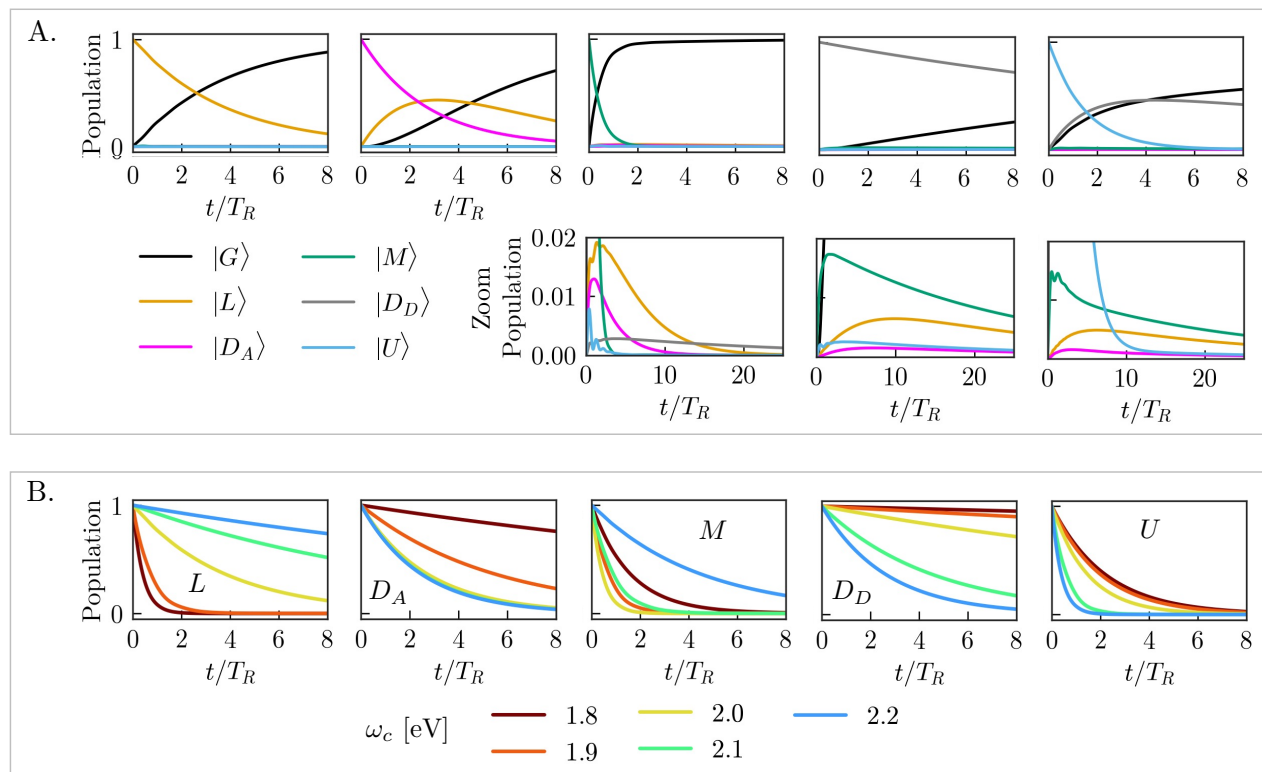


Fig. 6.10.: A. Upper panel: Populations for the dissipative dynamics of eigenstates of the DA Hamiltonian with $\omega_c = 2.0$ eV and for different initial conditions. Lower panel: Zoom of the dynamics of the respective column, over a more extended period of time. B. Time dependent evolution of the state initially populated for different cavity frequencies ω_c . In each column the label of the state for the initial condition is inserted within the plot. Time is measured in units of $T_R = 41.47$ fs and the same parameters as in Fig. 6.9 have been used.

To get an idea of the dynamic evolution of the eigenstates of DA model, Fig. 6.10 shows the evolution of the respective populations when the initial condition is chosen to be one of the eigenstates of Λ_1 (L , D_A , M , D_D , U) for $N_A = N_D = 2$. In this case, the cavity frequency is $\omega_c = (\omega_A + \omega_D)/2 = 2.0$ eV, indicating that L represents the excitations of the acceptor group, U those of the donor group, and M those of the cavity (see lower panel in Fig. 6.9). Similar to the TC model, the lower polariton L decays only to the ground state through cavity photon losses (see the middle left panel of Fig. 6.10). The decay rate $L \rightarrow G$ (by photon loss) decreases as the cavity frequency increases, as observed in the lower left panel of Fig. 6.10, where the population $\rho_{LL}(t; |L\rangle)$ is shown for different values of ω_c . This is explained by the fact that L loses its photonic character with the increase of ω_c (see bottom panel in Fig. 6.9), becoming less affected by the photon losses of the cavity. For the specific case of $\omega_c = 2.0$ eV, the decay of L translates into the de-excitation of the acceptor molecules (see bottom panel in Fig. 6.9). On the other hand, the D_A states (second column in Fig. 6.10) can decay to L only through vibrational relaxation of acceptor molecules. For this case with $\omega_c = 2$ eV, the decay

yields from D_A to L along with that from U to D_D are the most relevant out of all transitions due to vibrational relaxation. However, these relevant transitions do not imply an energy transport, since for $\omega_c = 2$ eV the states L and D_A carry the energy of the acceptor molecules; and the states U and D_D carry that of the donor molecules (see bottom panel in Fig. 6.9). Contrary to the behavior of the L state, the state D_A decays faster when the cavity frequency ω_c increases. This is because as omega increases, the state L , which is the only decay channel of D_A , carries the energy from acceptor group, enhancing the transition $D_A \rightarrow L$. Photonic excitations, represented by the middle polariton M when $\omega_c = 2.0$ eV, primarily decay to the ground state (third column in Fig. 6.10). However, the zoom in Fig. 6.10 indeed shows those transitions $M \rightarrow L$ and $M \rightarrow D_A$, which are relevant for energy transport from cavity to acceptor molecules. In general, M has the shortest lifetime when ω_c is close to $(\omega_A + \omega_D)/2$, due to its photonic character, and its lifetime increases when ω_c departs from this middle point frequency. Both D_D and U (last two columns of Fig. 6.10) have longer lifetimes as ω_c decreases (where U reduces its photonic character). For the case $\omega_c = 2.0$ eV, the main decay channel of U is through D_D , although direct transitions $U \rightarrow M$ (energy transfer from the donor group to the cavity), $U \rightarrow L$, and $U \rightarrow D_A$ (transfer from the donor to the acceptor group) can also occur (see zoom plots in Fig. 6.10).

6.2.2. Energy transfer pathways

In our dissipative DA model, we consider two primary decay mechanisms: photonic losses from the cavity and molecular vibrational relaxation. Consequently, the Liouvillian can be divided into three parts:

$$\mathfrak{L} = \mathfrak{L}^{\text{Ham}} + \mathfrak{L}^{\text{Cav}} + \mathfrak{L}^{\text{Vib}}, \quad (6.3)$$

where $\mathfrak{L}^{\text{Ham}}[\rho] = [H_{DA}, \rho]/i\hbar$ is the part associated with the coherent Hamiltonian dynamics, $\mathfrak{L}^{\text{Cav}}[\rho] = \kappa \mathcal{L}(a)[\rho]$ corresponds to the photonic decay of the cavity, and $\mathfrak{L}^{\text{Vib}}[\rho] = \sum_i \mathcal{B}(\sigma_i^\dagger \sigma_i)[\rho]$ represents the vibrational relaxation of both groups of molecules. In general, the matrix elements of the Liouvillian that connect population states, namely those of the form $\mathfrak{L}_{\alpha\alpha,\beta\beta}$, account for the transition rates $\beta \rightarrow \alpha$. In the Chap. 4, we discussed that the nonzero matrix elements of $\mathfrak{L}^{\text{Cav}}$ are proportional to κ and those of $\mathfrak{L}^{\text{Vib}}$ are proportional to γ . Thus, we can study the strength of the transitions associated with both decay mechanisms as a function of the cavity frequency ω_c . This is done by plotting $\mathfrak{L}_{\alpha\alpha,\beta\beta}^{\text{Cav}}/\kappa$ versus ω_c (for the photonic decay mechanism) and $\mathfrak{L}_{\alpha\alpha,\beta\beta}^{\text{Vib}}/\gamma$ versus ω_c (for the vibrational relaxation mechanism). To study the energy transport between polariton states, the mechanism of vibrational relaxation is of particular interest, as photon decay only allows transitions from the polariton states to the ground state G , whereas vibrational relaxation accounts for transitions among all states of Λ_1 . Fig. 6.11 displays the respective Liouvillian matrix elements $\mathfrak{L}_{\alpha\alpha,\beta\beta}^{\text{Vib}}/\gamma$, which account for transitions between the different states of Λ_1 .

The upper panel of Fig. 6.11 shows the strength of the main dissipative transitions from the state U to other states of Λ_1 for the case $N_A = N_D = 2$. The transition $U \rightarrow D_D$ is the most intense and it is particularly strong when $\omega_c < \omega_D$, that is, when the state U carries the energy of the donor molecules (see lower panel in Fig. 6.9). Therefore, this transition, in this frequency range, does not represent an

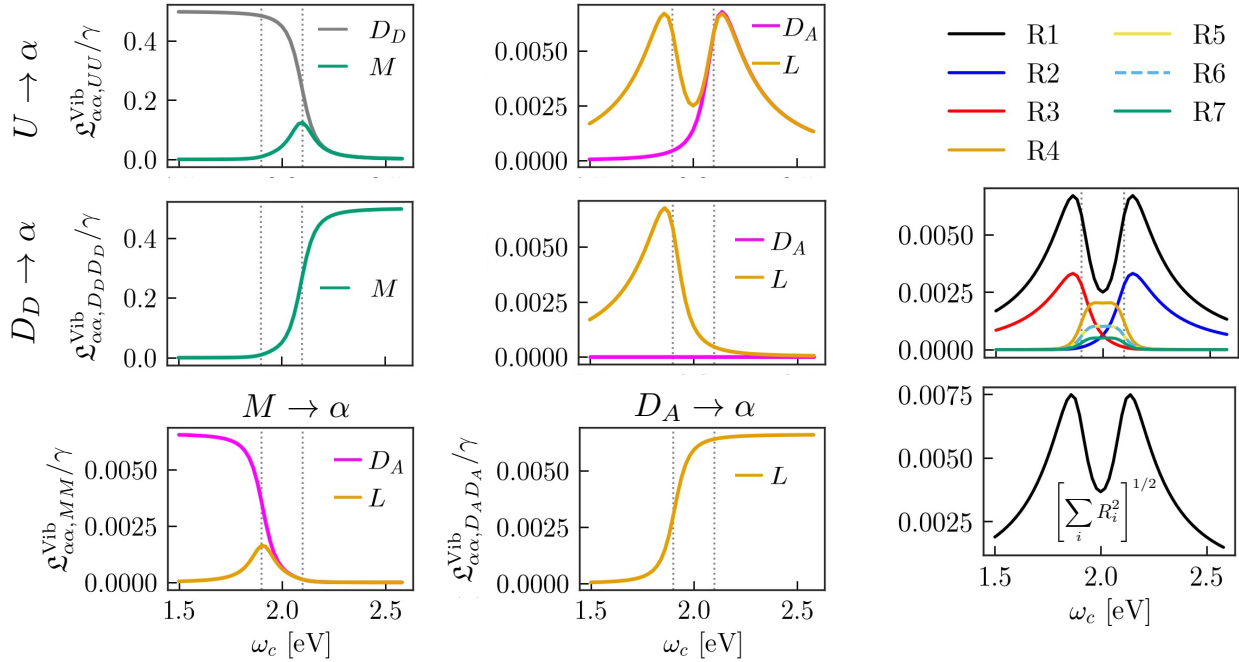


Fig. 6.11.: First and second columns: Non-zero matrix elements that connect population states of the Liouvillian associated with vibrational relaxation $\mathfrak{L}_{\alpha\alpha, \beta\beta}^{\text{Vib}}/\gamma$, accounting for the transition intensities $\beta \rightarrow \alpha$, as a function of the cavity frequency ω_c . In the top row, transitions from U ($\beta = U$) to the states $\alpha = D_D, M, D_A, L$ are plotted. In the middle row, transitions from D_D to the states $\alpha = M, D_A, L$ are shown. In the bottom row, transitions from M to the states $\alpha = D_A, L$ (first column) and from D_A to the state $\alpha = L$ (second column) are displayed. Third column: Upper panel: Intensity of the transitions associated with the seven possible pathways defined in Eq. (6.4) representing the energy transport from U to L as a function of ω_c . Lower panel: Square root of the sum of the square of the intensities of the seven routes starting from U and ending at L , as a function of ω_c . The same parameters as in Fig. 6.9 have been used.

energy transport. The transition $U \rightarrow M$ gains intensity in the area where ω_c is close to ω_D , where both U and M represent excitations of both the acceptor molecules and the cavity (as shown in the bottom panel of Fig. 6.9) and thus there is also no energy transport during this transition in such frequency range. On the other hand, the transition $U \rightarrow L$ is maximized at frequencies $\omega_c = 1.86$ eV and $\omega_c = 2.14$ eV (frequencies close, but not equal to $\omega_A = 1.9$ eV and $\omega_D = 2.1$ eV respectively). Near the $\omega_c = 1.86$ eV zone, U carries the excitations of the donor group and L carries the photon energy of the cavity. Thus, at this frequency ($\omega_c = 1.86$ eV), the transition $U \rightarrow L$ indicates an energy transport from the donor molecules to the cavity. Whereas near the $\omega_c = 2.14$ eV zone, both transitions $U \rightarrow L$ and $U \rightarrow D_A$ (also maximized in this zone), indicate an energy transport from the cavity to the acceptor molecules (as shown by the energy distribution in the lower panel of Fig. 6.9). The middle row in Fig. 6.11 indicates the transitions from the state D_D . $D_D \rightarrow M$ exhibits the same behavior of the donor molecules excitations (see Fig. 6.9) carried by the state M , thus indicating that this transition

does not represent an energy transport. However, the transition $D_D \rightarrow L$, maximized when $\omega_c = 1.86$ eV represents an energy transport from the donor molecules to the cavity. The transition $D_D \rightarrow D_A$ is not possible in this case for any value of the cavity frequency ω_c . The transitions $M \rightarrow D_A$ and $D_A \rightarrow L$ do not indicate energy transport since their intensities in Fig. 6.11 show the same behavior of the molecular acceptor excitations carried by the middle polariton M and the lower polariton L in Fig. 6.9, respectively. Finally, the transition $M \rightarrow L$, which is maximized in the zone where ω_c is close to ω_A , also does not indicate energy transport, since in this zone L and M both represent the excitations of both the cavity and the acceptor molecules.

To study an energy transport process that starts by exciting the state U and ends in the state L , we must consider all possible paths that would occur during the dynamic evolution. These paths are indicated below with their respective energy transport processes (among cavity (C), donor molecules (D), and acceptor molecules (A)), depending on the chosen cavity frequency ω_c :

$$\begin{aligned}
\text{R1: } U \rightarrow L : D \rightarrow C (\omega_c = 1.86 \text{ eV}), D \rightarrow A (\omega_c = 2.0 \text{ eV}), C \rightarrow A (\omega_c = 2.14 \text{ eV}) \\
\text{R2: } U \rightarrow D_A \rightarrow L : C \rightarrow A \rightarrow A (\omega_c = 2.14 \text{ eV}) \\
\text{R3: } U \rightarrow D_D \rightarrow L : D \rightarrow D \rightarrow C (\omega_c = 1.86 \text{ eV}) \\
\text{R4: } U \rightarrow M \rightarrow L : D \rightarrow C \rightarrow A (\omega_c = 2.0 \text{ eV}) \\
\text{R5: } U \rightarrow D_D \rightarrow M \rightarrow L : D \rightarrow D \rightarrow C \rightarrow A (\omega_c = 2.0 \text{ eV}) \\
\text{R6: } U \rightarrow M \rightarrow D_A \rightarrow L : D \rightarrow C \rightarrow A \rightarrow A (\omega_c = 2.0 \text{ eV}) \\
\text{R7: } U \rightarrow D_D \rightarrow M \rightarrow D_A \rightarrow L : D \rightarrow D \rightarrow C \rightarrow A \rightarrow A (\omega_c = 2.0 \text{ eV})
\end{aligned} \tag{6.4}$$

We can define the intensities or probabilities of these paths by multiplying the respective matrix elements of the Liouvillian involved. For instance, for the path R2, we define its intensity as $\mathfrak{L}_{D_A D_A, U U}^{\text{Vib}} \times \mathfrak{L}_{L L, D_A D_A}^{\text{Vib}} / \gamma^2$. Defined in this way, each of the intensities associated with the seven paths starting from U and ending at L are plotted in the upper panel of the third column in Fig. 6.11. For all cavity frequencies ω_c , the most probable path turns out to be R1 ($U \rightarrow L$). This route represents energy transport for all values of ω_c . Particularly, for cavity frequencies 1.86, 2.0, and 2.14 eV, Eq. (6.4) details how the respective energy transport processes occur. Other routes are also relevant in certain frequency ranges. For example, near to $\omega_c = 2.14$ eV, the R2 route (energy transport from the cavity to the acceptor molecules) is significant, and near to $\omega_c = 1.86$ eV, the R3 route (energy transport from the donor molecules to the cavity) is relevant. The routes R4 to R7 are important around the central frequency $(\omega_A + \omega_D)/2 = 2.0$ eV and represent energy transport from the donor molecules to the cavity and subsequently to the acceptor molecules.

Note that the matrix elements of $\mathfrak{L}^{\text{Vib}}$ associated with vibrational decay plotted in Fig. 6.11 are divided by γ , which corresponds to the constant value (at positive frequencies with zero temperature) of the vibrational bath noise power spectrum function $S(\omega)$. If another function $S(\omega)$ is used, the intensity of each transition $\alpha \rightarrow \beta$ shown in the figure should be multiplied by the corresponding value $S(\omega_{\alpha\beta})$.

6.2.3. 2D Spectroscopy applied to the energy transport process

In the 2D spectroscopy protocol, the interaction of the first and second pulses with the system successfully excites the polariton states according to the intensity of their dipole couplings shown in the upper middle panel of Fig. 6.9. In this section, we choose $\omega_c = 2.0$ eV. At this frequency we expect the initial state predominantly populated is M (which carries the cavity energy), although the states U (with donor energy) and L (with acceptor energy) can also be excited, as shown in the upper middle panel of Fig. 6.9. 2DS allows us to track the dynamics of the total transfer $U \rightarrow L$, to which all possible paths R1 to R7 contribute simultaneously. However, it is also possible to isolate some processes. For example, one can track the transition $U \rightarrow M$ (contributed by the paths $U \rightarrow M$ and $U \rightarrow D_D \rightarrow M$), which is present in routes R4 to R7, and also the transfer $M \rightarrow L$ (contributed by the paths $M \rightarrow L$ and $M \rightarrow D_A \rightarrow L$) can be studied separately.

Fig. 6.12 shows the total 2DS at a waiting time $T = 0.5 T_R$ and its respective decomposition into different Feynman pathways. The high intensity of the peaks $M/M_{\{SE\}}$ and $M/M_{\{GSB\}}$ is indicative that the most populated state during the excitation process is the middle polariton M , as expected. In this Fig. 6.12, an scheme with the locations of the different transition frequencies is shown to an approximate scale in the top right panel. The red color represents transitions $\Lambda_0 \rightarrow \Lambda_1$ between the ground state and the bright polariton states of the first excitation manifold; blue color denotes transitions $\Lambda_1 \rightarrow \Lambda_2$ between bright polariton states of different excitation manifolds, while magenta and gray colors represent transitions $\Lambda_1 \rightarrow \Lambda_2$ from the dark states of the acceptor group and the donor group, respectively. This graph helps us to understand that the different peaks appearing in all the plotted spectra may be due to the interference of various processes occurring at very close frequencies. For example, the top left peak in the ESA spectrum ($U/D_{D\{ESA\}}$) represents the excitation of the U state (population reached during the excitation process) and then, considering the evolution during the waiting and detection times, we have two possible paths

- $U \xrightarrow{T} U \xrightarrow{t} P_2$: the population is excited to any accessible polariton state P_2 of Λ_2 . This process is observed at the lower detection frequency $\omega_t = \omega_{P_2U}$ of the diagram in Fig. 6.12.
- $U \xrightarrow{T} D_D \xrightarrow{t} D_2$: the population decays to the dark state of donor molecules D_D during T , and subsequently, this state is excited to an accessible state D_2 of Λ_2 from D_D . This process is detected at the lower frequency $\omega_t = \omega_{D_2D_D}$ in Fig. 6.12.

According to the frequency diagram shown in Fig. 6.12, these two processes are detected at the same frequency in the top left peak (which by the way also coincides with ω_{LG}), thus interfering in the left $U/D_{D\{ESA\}}$ peak.

Now, we are interested in analyzing those peaks in the 2DS contributed from energy transport processes. Fig. 6.13 allows us to study the processes that start with the excitation of state U (donor group excitations) and whose energy migrates towards the acceptor group (L) or towards the cavity (M). In this Fig. 6.13, we show a function $f_{2DS}(T)$ extracted from the 2DS and compare it with a function $f_\rho(T)$ obtained from the temporal evolution during T of the system density operator, assuming the initial state U . We identify correlations between the 2DS and the density operator of the system that help us to understand the following energy transport mechanisms:

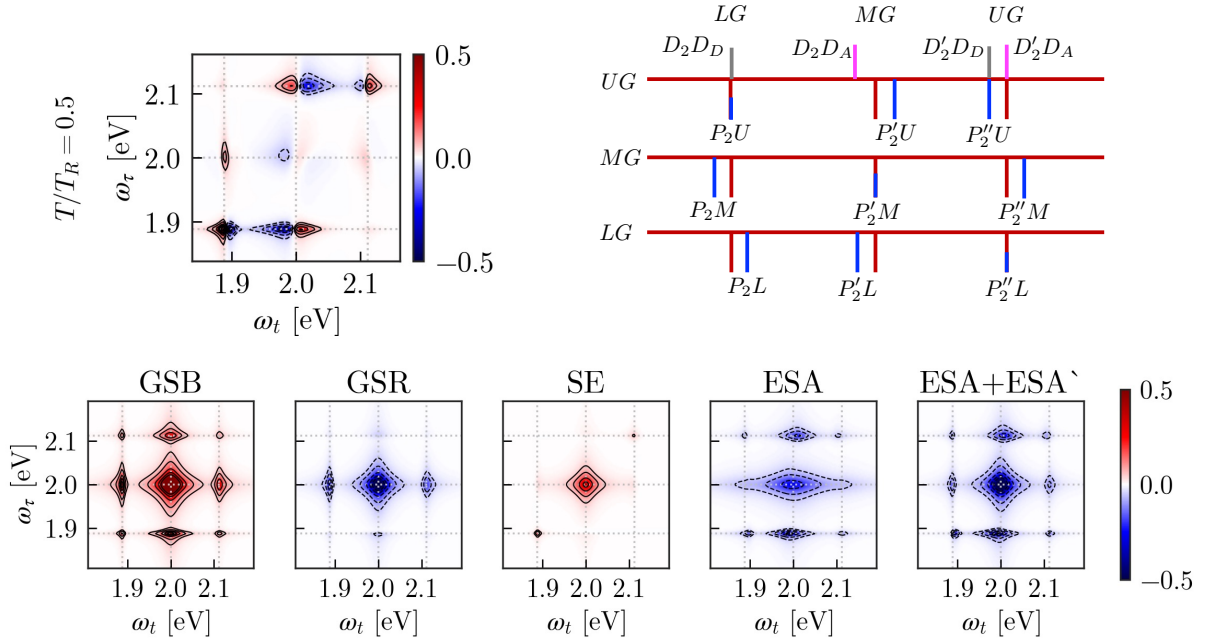


Fig. 6.12.: Upper left panel: electronic population 2DS for the dissipative DA model at the waiting time $T = 0.5 T_R$ ($T_R = 41.47$ fs) for $N_D = N_A = 2$ molecules, and cavity frequency $\hbar\omega_c = 2.0$ eV. The real value or 2D absorptive spectra $\mathcal{R}[S_{(\text{NR}+\text{R})}^{(3)}(\omega_\tau, T, \omega_t)]$ is plotted. The parameters of the model are chosen as in Fig. 6.9. The spectrum is normalized to its maximum value. Upper right panel: schematic diagram, on an approximate scale, of the frequencies associated with the transitions $\Lambda_0 \rightarrow \Lambda_1$ (ω_{LG} , ω_{MG} , and ω_{UG} in red) and the transitions $\Lambda_1 \rightarrow \Lambda_2$ from the dark states of acceptor molecules ($\omega_{D_2D_A}$ in magenta), from the dark states of donor molecules ($\omega_{D_2D_D}$ in gray), and from the bright polariton states (ω_{P_2L} , ω_{P_2M} , and ω_{P_2U} in blue). We have denoted by D_2 and P_2 the dark and bright states, respectively, of Λ_2 that have a dipole connection with the dark and bright states, respectively, of Λ_1 . Lower panel: Decomposition of the population 2DS in the upper panel into their contributing Feynman pathways GSB, GSR, SE, and ESA. The sum $\text{ESA}+\text{ESA}'$ is also shown. These maps are normalized to the maximum value of the GSB component at time $T = 0.5 T_R$. All 2D plots have been truncated to half of their respective normalization value. Dotted right lines indicate the polariton frequencies ω_{LG} , ω_{MG} and ω_{UG} respectively. Solid/dashed contour lines represent heights $\pm[0.05, 0.08, 0.1, 0.15, 0.2, 0.3, 0.4]$.

- Donor \rightarrow Cavity \rightarrow Acceptor and direct transfer Donor \rightarrow Acceptor: The interference between these two mechanisms is recorded in the temporal evolution during T of the density matrix element $f_\rho(T) = \rho_{LL}(T)$ (we emphasize that we take the state U as the initial state), which represents the transition $U \rightarrow L$. This function $\rho_{LL}(T)$ is plotted with dashed line in the left panel of Fig. 6.13. The dynamics of both transport mechanisms leave their mark on the 2DS. They contribute to the peak $U/L_{\{\text{SE}\}}$. We propose the function $f_{2DS}(T) = 0.625 \times U/L_{\{\text{SE}\}}(T)$ (solid line in the left panel of Fig. 6.13), whose average value exhibits a behavior similar to the

respective $\rho_{LL}(T)$ function.

- Donor \rightarrow Cavity: This mechanism is recorded in the matrix element $f_\rho(T) = \rho_{MM}(T)$ (dashed line in middle panel of Fig. 6.13), representing the transition $U \rightarrow M$. This transference leaves its fingerprint on the peak $U/M_{\{SE\}}$. We propose the function $f_{2DS}(T) = U/L_{\{SE\}}(T)/3$ (solid line in middle panel of Fig. 6.13), which, except for very short waiting times, fairly fits $\rho_{MM}(T)$ well.

We also plot the transition $U \rightarrow D_D$ in the right panel of Fig. 6.13. It is represented with $f_\rho(T) = \rho_{D_D D_D}(T)$ (dashed line) and $f_{2DS}(T) = 0.769(c_0 \times U/U_{\{SE\}}(T) - U/D_{D\{ESA\}}(T))$ (solid line), with $c_0 = [U/D_{D\{ESA\}}](0)/[U/U_{\{SE\}}](0)$. This transition does not represent an energy transport process. It is an energy exchange between polariton states mainly carrying excitations from the donor group. The function extracted from the 2DS that we propose in this case takes into account that the population migrating towards the dark states D_D from U is the one that mainly contributes to one of the $-U/D_{D\{ESA\}}$ peaks for the detection frequency $\omega_t = \omega_{D_2 D_D}$ (in particular, we use the right higher frequency shown in Fig. 6.12). However, from the frequency diagram shown in Fig. 6.12, we see that the higher frequency $\omega_{D_2 D_D}$ is close to ω_{UP_2} , implying that in that ESA peak, there is also a contribution from the population remaining in U during the waiting time T , which is extracted from the $U/U_{\{SE\}}$ peak.

Finally, Fig. 6.14 illustrates the energy transfer process from the cavity to the acceptor molecular group, identified by transitions starting from the state M and ending in the states L (left panel of

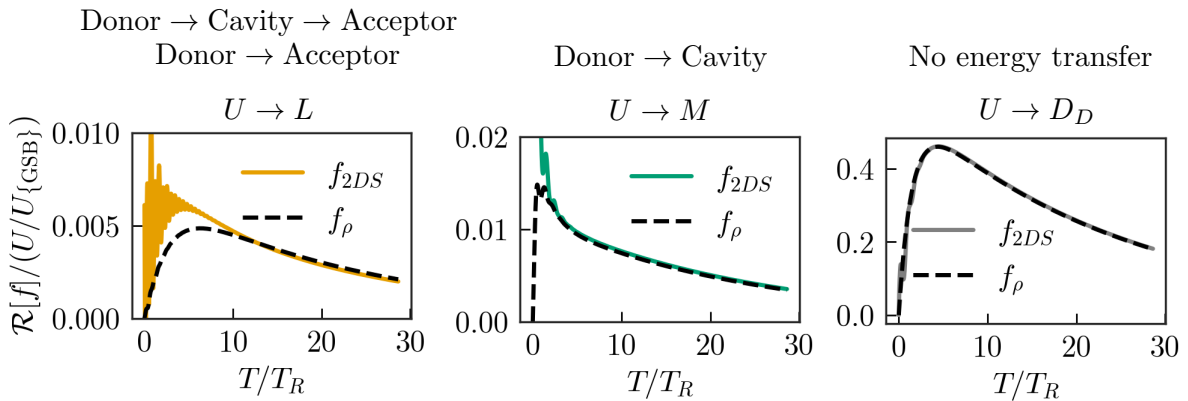


Fig. 6.13.: Plots of the real part of a function f_ρ extracted from the evolution during T of the density operator of the system with the initial condition $|\rho(0)\rangle\rangle = |UU\rangle\rangle$ (dashed lines) and of a “fitted” function f_{2DS} (solid lines) extracted from the T evolution of the 2DS. In each panel we track a particular transition $U \rightarrow L$ (left panel), $U \rightarrow M$ (middle panel) and $U \rightarrow D_D$ (right panel). They represent the respective labeled energy transport mechanisms, except by $U \rightarrow D_D$ in which there is no energy transport. The explicit forms of $f_\rho(T)$ and $f_{2DS}(T)$ are described in the text. All the $f_{2DS}(T)$ functions are divided by the constant real value of $U/U_{\{GSB\}}$.

Fig. 6.14) or the state D_A (right panel of Fig. 6.14). In these cases we use the following functions, taking as initial condition for the density operator the state M , i.e., $|\rho(0)\rangle\rangle = |MM\rangle\rangle$

- Cavity \rightarrow Acceptor transport: It is represented by the transfer $M \rightarrow L$. This transition is recorded in the matrix element $f_\rho(T) = \rho_{LL}(T)$ (dashed line in left panel of Fig. 6.14). We propose the function $f_{2DS}(T) = 2 \times M/L_{\{SE\}}(T)$ (solid line in the left panel of Fig. 6.14), whose average value exhibits a behavior similar to the respective $\rho_{LL}(T)$ function.
- Cavity \rightarrow Acceptor transport: It is represented by the transfer $M \rightarrow D_A$. This transition is recorded in the matrix element $f_\rho(T) = \rho_{D_A D_A}(T)$ (dashed line in right panel of Fig. 6.14). On the other hand, the function $f_{2DS}(T) = 0.4(c_0 \times M/M_{\{SE\}}(T) - M/D_{A\{ESA\}}(T))$ (solid line in right panel of Fig. 6.14), with $c_0 = [M/D_{A\{ESA\}}](0)/[M/M_{\{SE\}}](0)$. Here we use the same argument as we did to explain the choice of $f_{2DS}(T)$ in the case of the transition $U \rightarrow D_D$.

In conclusion we find valuable the analysis of 2DS and the time evolution of some specific peaks to check out the presence of transport mechanisms in a polariton molecular system and to discriminate its nature, namely, Donor-Acceptor, Donor-Cavity-Acceptor or Cavity-Acceptor. Further sophistication of the model in order to optimize the control over transport is left for future works.

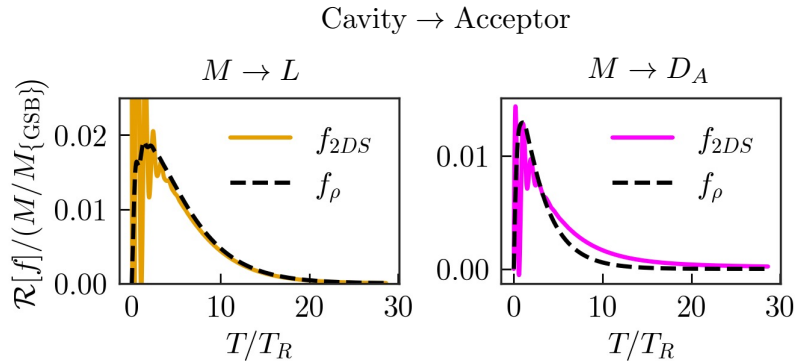


Fig. 6.14.: Plots of the real part of a function f_ρ extracted from the evolution during T of the density operator of the system with the initial condition $|\rho(0)\rangle\rangle = |MM\rangle\rangle$ (dashed lines) and of a “fitted” function f_{2DS} (solid lines) extracted from the T evolution of the 2DS. In each panel we track a particular transition $M \rightarrow L$ (left panel) and $M \rightarrow D_A$ (right). They represent an energy transport from cavity to acceptor molecules. The explicit forms of $f_\rho(T)$ and $f_{2DS}(T)$ are described in the text. All the $f_{2DS}(T)$ functions are divided by the constant real value of $M/M_{\{GSB\}}$.

Part IV.

Conclusions

Conclusions

In this thesis we have developed a comprehensive theoretical approach to unveil the fast internal dynamics of molecular polariton states subject to external weak classical fields. This perturbative approach turns out to be useful for both linear and nonlinear spectroscopies. Our system consists of an ensemble of molecules strongly coupled to an electromagnetic field within a cavity. Regarding the matter part, each molecule is approximated as an electronic two-level system, and with respect to radiation, a single quantized mode is considered. In addition, to match the experimental realm, dissipative effects due to molecular nonradiative decay processes and photon losses from the cavity are included, thus leading to a formalism in terms of master equations for the density operator.

In the matter-field strong coupling regime within the cavity, two kind of states, named bright (lower and upper) and dark molecular polaritons, are formed in the first excitation manifold. Similarly these sort of states are also found in upper excitation manifolds. Bright states can be reached directly by absorption from the ground state while dark states cannot. This opens the question about the contribution of dark states to the polariton photodynamics. In this work, we shed light on how these dark states indeed play a crucial role and partially shape the line profiles in the absorption and emission linear spectroscopies as well as in the surface profiles in two-dimensional spectroscopy.

1. We have developed mathematical expressions for the linear $S^{(1)}(t)$ and third-order nonlinear $S^{(3)}(\tau, T, t)$ response functions in the time domain, both in Hilbert space and Liouville space, assuming the weak field approximation for external laser pulses, which allows for a perturbative approach. These expressions can be interpreted as expectation values in Liouville space, but they are also directly related to one-time and three-time correlation functions, respectively, in Hilbert space. These obtained general expressions are valid for a master equation derived from any Liouvillian. Incidentally, they are valid for any dipolar interaction operator between the quantum system under study and the classical fields of a given spectroscopic protocol.
2. Within the semi-impulsive limit (sudden ultrashort pulses) and the rotating wave approximation, we have derived expressions to calculate the linear absorption and emission spectra from the previous linear response function. In this work, we have introduced new formulas, not yet reported in the literature, for the calculation of 2D absorptive spectra, obtained from the third-order nonlinear response function under rephasing and non-rephasing phase matching conditions. These new expressions are written in terms of a sum (which runs over the Liouvillian eigenstates) of products of excitation $E_j(\omega_\tau)$ and detection $D_j(\omega_t)$ functions, and an exponential factor

which contains the waiting time, i.e., $\exp(\lambda_j T)$, responsible for the decay. In fact, this expression reflects the consecutive experimental steps of the 2D spectroscopy protocol (excitation, waiting and detection).

3. Since in the Liouville space representation, the temporal evolution operator of the full dissipative system is expanded in the Liouvillian eigenstates, the calculation of the dynamics and, consequently, of both linear and nonlinear spectra are analytical. This makes of our method of solution a very efficient computational tool for the calculation of 2D spectra.
4. For the dissipative Jaynes- and Tavis-Cummings models employed in this work, we have considered a molecular vibrational bath within the Bloch-Redfield formalism and cavity photon losses through the Lindblad formalism. Despite the simplicity of these models, they have proven to be highly valuable for studying dynamic effects of polariton states. For instance, we demonstrate that these models capture the expected asymmetries of lower L and upper U polariton peaks present in the linear absorption spectra. Similarly, these models also reproduce the experimental asymmetries in both the diagonal and cross peaks in 2D spectra.

We find that these effects arise from the difference between the relaxation channels of both states, being the dark states those involved in the U decay channel. We stress that employing the molecular pure dephasing operator $\sigma^\dagger\sigma$ as a Lindblad term to simulate the vibrational bath turns out to be incorrect, since this Lindblad model fails to reproduce the asymmetry between L and U peaks in linear and non-linear spectroscopies.

5. Analyzing the Feynman path contributions to the 2D population spectra, we conclude that each of these contributions provide specific information about the dynamics of the polariton states as follows
 - Ground state bleach (GSB): except for a normalization factor, any cut along the excitation or detection frequency in the GSB component of the 2DS yields the linear absorption spectrum.
 - Ground state recovery (GSR): it allows us to track the population migrating from the polariton states L and U towards the ground state G during the waiting time T . The asymmetry in the GSR signals is of the same nature as that presented in the linear absorption peaks and it is due to the different relaxation mechanisms present in both polariton states. Asymptotically, the magnitude of the GSR peaks is greater when the initially populated state is L than when the state U is populated. This is because part of the population from U gets trapped in the dark states, which take much longer time to decay to the ground state.
 - Stimulated emission (SE): it allows tracking the population remaining in the polariton states L and U during the waiting time T , after these states have been populated during the excitation process.
 - Excited state absorption (ESA): At long waiting times, when the bright polaritonic states have relaxed, dark states leave their distinctive imprint on the ESA contribution. In the 2D spectra, the dynamics of dark states can be directly visualized, unlike in linear spectra.

-
6. By incorporating dissipative processes into the model, we unveil the existence of two new Feynman path diagrams named ground state recovery (GSR) and excited state absorption prime (ESA'). The former has received scant attention in the literature, while the ESA' contribution has not been reported until now to our knowledge. This contribution arises from the decay of coherences between different excitation manifolds due to cavity photon losses.
 7. The open Tavis-Cummings model used in [Chap. 5](#) allows us to study other physical effects on polaritonic dynamics. We have studied temperature effects, which lead to incoherent pumping of polariton states, leaving a fingerprint on the different contributions to the 2D spectra. Each contribution allows us to track different pumping and/or relaxation pathways. Furthermore, our model enabled a reasonable comparison with 2D spectra obtained in experiments with J-aggregates (see [Sec. 5.5](#)). The temporal evolution during the waiting time T of the spectral signals obtained from our simulations reflects some of the behaviors also present in the experiments.
 8. We have briefly analyzed the case of interacting molecules, by adding a dipole-dipole interaction term to the Hamiltonian. In the case of a high concentration in solution of these J-aggregates, one cannot disregard this interaction among emitters. Within our model we conclude that 2D spectra may display drastic changes in the linear and 2D spectra, by shifting the peaks and by modifying the intensities, which is due to an exchange of character of polariton states in energy anticrossings as the ratio between the emitter-emitter interaction strength and the emitter-cavity coupling G/g varies.
 9. Finally, the last chapter deals with energy transport in molecular ensembles of Donors and Acceptors, with different natural frequencies ω_D and ω_A , respectively. This kind of Donor-Acceptor systems are characterized by the presence of new middle polaritons M and also because there are two different sets of degenerate dark states.

The choice of the cavity frequency ω_c determines how the energy of the photonic and molecular excitations is distributed among the polariton states. Excitation to the lower polariton state L dominates for $\omega_c < \omega_A$, to the middle polariton for $\omega_A < \omega_c < \omega_D$ and to upper polariton U for $\omega_c > \omega_D$. The modification of the polariton energy spectrum and the eigenstate composition with ω_c determines the frequency peaks and intensities in the absorption spectra. We have analyzed a series of energy transport paths from U to L polaritons for different relevant cavity frequencies. In 2D spectra (using $\omega_c = (\omega_A + \omega_D)/2$) a new series of X/M peaks appear due to the prevalence of the middle polariton M in absorption. In fact, in this case, M represents the cavity, L mainly corresponds to the Acceptor and U state represents the Donor. We analyzed mechanisms for processes initiated with the excitation of the Donor (U polaritons) with a subsequent energy migration to the Acceptor (L polaritons) or to the cavity itself (M polaritons), being able to discriminate the nature of the transport mechanism as Donor-Acceptor, Donor-Cavity-Acceptor or Cavity-Acceptor.

Conclusiones

En esta tesis hemos desarrollado un enfoque teórico para abordar la dinámica interna rápida de los estados de polaritones moleculares sujetos a campos pulsados débiles externos. Este enfoque perturbativo resulta útil tanto para espectroscopías lineales como no lineales. Nuestro sistema consta de un conjunto de moléculas fuertemente acopladas a un campo electromagnético dentro de una cavidad. Respecto a la parte de materia, cada molécula se aproxima como un sistema electrónico de dos niveles, y respecto a la radiación, se considera un único modo de cavidad cuantizado. Además, para simular el entorno experimental, se incluyen los efectos disipativos debidos a procesos de relajación molecular no radiativa y pérdidas de fotones de la cavidad, lo que conduce a un formalismo en términos de ecuaciones maestras para el operador de densidad.

En el régimen de acoplamiento fuerte entre materia y cavidad, en la primera variedad de excitación se forman dos tipos de estados, los denominados polaritones moleculares (inferior L y superior U) y los estados oscuros materiales no acoplados con el modo de radiación. De manera similar, estos estados también se encuentran en las variedades de excitación superior. Los estados de polaritones se pueden excitar directamente mediante la absorción desde el estado fundamental, mientras que los estados oscuros no. Esto abre la pregunta sobre la contribución de los estados oscuros a la fotodinámica de polaritones. En este trabajo, arrojamos luces sobre cómo estos estados oscuros juegan un papel crucial y, ocasionalmente, dan forma a los perfiles de picos en las espectroscopías lineales de absorción y emisión, así como a las señales de la espectroscopia bidimensional.

1. Hemos desarrollado expresiones matemáticas para las funciones de respuesta lineal de primer orden $S^{(1)}(t)$ y no lineal de tercer orden $S^{(3)}(\tau, T, t)$ en el dominio del tiempo, tanto en el espacio de Hilbert como en el espacio de Liouville, asumiendo la aproximación de campo débil para pulsos láser externos, lo que permite un enfoque perturbativo. Estas expresiones pueden interpretarse como valores esperados en el espacio de Liouville, pero también están directamente relacionadas con funciones de correlación de primer y tercer orden, respectivamente, en el espacio de Hilbert. Estas expresiones generales obtenidas son válidas para una ecuación maestra derivada de cualquier Liouvilliano. De hecho, son válidas para cualquier operador de interacción dipolar entre el sistema cuántico estudiado y los campos clásicos dado un protocolo espectroscópico.
2. Dentro del límite semi-impulsivo (pulsos láser ultracortos súbitos) y la aproximación de la onda rotante, hemos derivado expresiones para calcular los espectros lineales de absorción y emisión a partir de la función de respuesta lineal. En este trabajo hemos introducido nuevas fórmulas, aún no reportadas en la literatura, para el cálculo de espectros de absorción 2D, obtenidas a partir de la función de respuesta no lineal de tercer orden en condiciones de *phase-matching* llamadas *rephasing* y *non-rephasing*. Estas nuevas expresiones están escritas en términos de una suma (que recorre los estados propios del Liouvilliano) de los productos de las funciones de excitación $E_j(\omega_\tau)$ y de detección $D_j(\omega_t)$, y de un factor exponencial que contiene el denominado tiempo de espera T , es decir, $\exp(\lambda_j T)$, responsable del comportamiento de decaimiento polaritónico. De hecho,

esta expresión refleja los pasos experimentales consecutivos de un protocolo de espectroscopia 2D (excitación, espera y detección).

3. Dado que en la representación del espacio de Liouville, el operador de evolución temporal del sistema disipativo completo se expande en los estados propios del Liouvilliano, el cálculo de la dinámica y, en consecuencia, de los espectros lineales y no lineales es analítico. Esto hace de nuestro método de solución una herramienta computacional muy eficiente para el cálculo de espectros 2D.
4. Para los modelos disipativos de Jaynes- y Tavis-Cummings empleados en este trabajo, hemos considerado un baño molecular de osciladores dentro del formalismo de Bloch-Redfield y las pérdidas de fotones de la cavidad a través del formalismo de Lindblad. A pesar de la simplicidad de estos modelos, han demostrado ser muy valiosos para estudiar los efectos dinámicos de los estados de polaritones. Por ejemplo, demostramos que estos modelos capturan las asimetrías esperadas de los picos de abrosción de polaritones presentes en los espectros lineales. De manera similar, estos modelos también reproducen las asimetrías experimentales tanto en los picos diagonales como en los picos cruzados de los espectros 2D.

Encontramos que estos efectos surgen de la diferencia entre los canales de relajación de ambos estados polaritónicos L y U , siendo los estados oscuros un canal adicional para U , que no interviene en el decaimiento de L . Destacamos que emplear el operador de dephasing molecular puro $\sigma^\dagger\sigma$ como término de Lindblad para simular el baño vibracional resulta incorrecto, ya que este modelo de Lindblad no logra reproducir la asimetría entre los picos L y U , tanto en espectroscopias lineales como no lineales.

5. Al analizar las contribuciones de los caminos de Feynman a los espectros de población 2D, concluimos que cada una de estas contribuciones proporciona información específica sobre la dinámica de los estados polaritónicos de la siguiente manera
 - “Blanqueamiento” del estado fundamental (GSB): excepto por un factor de normalización, cualquier corte a lo largo de la frecuencia de excitación o detección en el componente GSB del 2DS reproduce el espectro de absorción lineal.
 - Recuperación del estado fundamental (GSR): nos permite rastrear la población que migra desde los estados de polaritón L y U hacia el estado fundamental G durante el tiempo de espera T . La asimetría en las señales GSR es de la misma naturaleza que la que se presenta en los picos de absorción lineal y se debe a los diferentes mecanismos de relajación presentes en ambos estados polaritónicos. Asintóticamente, la magnitud de los picos de GSR es mayor cuando el estado inicialmente excitado es L que cuando se excita U . Esto se debe a que parte de la población de U queda atrapada en los estados oscuros, que tardan mucho más tiempo en decaer al estado fundamental.
 - Emisión estimulada (SE): permite rastrear la población que permanece en los estados de polaritón L y U durante el tiempo de espera T , luego de que estos estados hayan sido poblados durante el proceso de excitación.

- Absorción desde el estado excitado (ESA): en tiempos de espera largos, cuando los estados polaritónicos se han relajado, los estados oscuros dejan su huella distintiva en las contribuciones ESA. En los espectros 2D, la dinámica de los estados oscuros se puede visualizar directamente por las contribuciones ESA, a diferencia de los espectros lineales.
- 6. Al incorporar procesos disipativos en el modelo, revelamos la existencia de dos nuevos diagramas o caminos de Feynman denominados recuperación del estado fundamental (GSR) y absorción desde el estado excitado primado (ESA'). El primero ha recibido escasa atención en la literatura, mientras que hasta ahora, según sabemos, la contribución del camino ESA' no ha sido reportada. Esta contribución surge del decaimiento de las coherencias entre diferentes variedades de excitación debido a las pérdidas de fotones en la cavidad.
- 7. El modelo abierto de Tavis-Cumming utilizado en [Chap. 5](#) nos permite estudiar otros efectos físicos sobre la dinámica polaritónica. Hemos estudiado los efectos de la temperatura, que conducen a un bombeo incoherente de estados polaritónicos, dejando una huella en las diferentes contribuciones a los espectros 2D. Cada contribución nos permite rastrear diferentes vías de bombeo y/o de relajación. Además, nuestro modelo permitió una comparación razonable con espectros 2D obtenidos en experimentos con J-agregados moleculares (ver [Sec. 5.5](#)). La evolución temporal durante el tiempo de espera T de las señales espectrales obtenidas en nuestras simulaciones refleja algunos de los comportamientos también presentes en los experimentos.
- 8. Hemos analizado brevemente el caso de moléculas que interactúan, añadiendo un término de interacción dipolo-dipolo al hamiltoniano. En el caso de altas concentraciones en solución de estos agregados moleculares J, no se puede ignorar la interacción entre emisores. Dentro de nuestro modelo concluimos que nuestros resultados pueden mostrar cambios drásticos en los espectros lineales y 2D, al desplazarse los picos y modificarse sus intensidades relativas, lo cual se debe a un intercambio de carácter entre estados polaritónicos en los anticruces de energía presentes cuando la relación entre el interacción emisor-emisor y el acoplamiento emisor-cavidad varía.
- 9. Finalmente, el último capítulo trata del transporte de energía entre grupos moleculares de Donantes y Aceptadores, con diferentes frecuencias naturales ω_D y ω_A , respectivamente. Este tipo de sistemas Donante-Aceptor se caracterizan por la presencia de nuevos polaritones intermedios M y también porque existen dos conjuntos diferentes de estados oscuros degenerados. La elección de la frecuencia de la cavidad ω_c determina cómo la energía del fotón y de las excitaciones moleculares se distribuyen entre los estados polaritónicos. La excitación al estado polaritónico inferior L domina para $\omega_c < \omega_A$, al polaritón medio para $\omega_A < \omega_c < \omega_D$ y al polaritón superior U para $\omega_c > \omega_D$. La modificación del espectro de autoenergías del Hamiltoniano polaritónico y la composición de los autoestados al variar ω_c determinan las nuevas frecuencias de los picos y sus intensidades en los espectros de absorción. Hemos analizado una serie de rutas relevantes de transporte de energía de polaritones U a L para diferentes frecuencias de la cavidad. En espectros 2D (usando $\omega_c = (\omega_A + \omega_D)/2$) aparecen picos en nuevas frecuencias de excitación y detección: los picos X/M y M/X con $X = L, U$ debido al dominio del polaritón medio M en la absorción. En este caso, el estado M porta la energía de la cavidad, L la del grupo Aceptor

y U la del grupo Donante. Analizamos los mecanismos de procesos iniciados con la excitación del Donante (polaritones U) con una posterior migración de energía al Aceptor (polaritones L) o a la propia cavidad (polaritones M), pudiendo discriminar así la naturaleza del mecanismo de transporte como Donante-Aceptor, Donante-Cavidad-Aceptor o Cavidad-Aceptor.

References

- [1] Jacopo Fregoni, Francisco J Garcia-Vidal, and Johannes Feist. Theoretical challenges in polaritonic chemistry. *ACS photonics*, 9(4):1096–1107, 2022. Referred to on page [2](#), [11](#), [21](#), [40](#), [71](#).
- [2] Francesca Fassioli, Kyu Hyung Park, Sarah E. Bard, and Gregory D. Scholes. Femtosecond photophysics of molecular polaritons. *The Journal of Physical Chemistry Letters*, 12(46):11444–11459, 2021. Referred to on page [2](#).
- [3] Jorge A Campos-Gonzalez-Angulo, Raphael F Ribeiro, and Joel Yuen-Zhou. Resonant catalysis of thermally activated chemical reactions with vibrational polaritons. *Nature communications*, 10(1):1–8, 2019. Referred to on page [2](#).
- [4] Javier Galego, Clàudia Climent, Francisco J Garcia-Vidal, and Johannes Feist. Cavity casimir-polder forces and their effects in ground-state chemical reactivity. *Physical Review X*, 9(2):021057, 2019. Referred to on page [2](#), [11](#), [16](#).
- [5] Arkajit Mandal and Pengfei Huo. Investigating new reactivities enabled by polariton photochemistry. *The Journal of Physical Chemistry Letters*, 10(18):5519–5529, 2019. Referred to on page [2](#).
- [6] Javier Galego, Francisco J Garcia-Vidal, and Johannes Feist. Many-molecule reaction triggered by a single photon in polaritonic chemistry. *Physical Review Letters*, 119(13):136001, 2017. Referred to on page [2](#).
- [7] Felipe Herrera and Frank C Spano. Cavity-controlled chemistry in molecular ensembles. *Physical Review Letters*, 116(23):238301, 2016. Referred to on page [2](#), [20](#).
- [8] Javier Galego, Francisco J Garcia-Vidal, and Johannes Feist. Cavity-induced modifications of molecular structure in the strong-coupling regime. *Physical Review X*, 5(4):041022, 2015. Referred to on page [2](#), [11](#).
- [9] Javier Galego, Francisco J Garcia-Vidal, and Johannes Feist. Suppressing photochemical reactions with quantized light fields. *Nature Communications*, 7(1):13841, 2016. Referred to on page [2](#), [11](#).
- [10] Alessio Cargioli, Maksim Lednev, Lorenzo Lavista, Andrea Camposeo, Adele Sassella, Dario Pisignano, Alessandro Tredicucci, Francisco J. Garcia-Vidal, Johannes Feist, and Luana Persano. Active control of polariton-enabled long-range energy transfer. *Nanophotonics*, 2024. Referred to on page [2](#), [110](#), [130](#).

- [11] Ilia Sokolovskii, Ruth H Tichauer, Dmitry Morozov, Johannes Feist, and Gerrit Groenhof. Multi-scale molecular dynamics simulations of enhanced energy transfer in organic molecules under strong coupling. *Nature Communications*, 14(1):6613, 2023. Referred to on page 2.
- [12] Rocío Sáez-Blázquez, Johannes Feist, Francisco J García-Vidal, and Antonio I Fernández-Domínguez. Theory of energy transfer in organic nanocrystals. *Advanced Optical Materials*, 8(23):2001447, 2020. Referred to on page 2, 130.
- [13] Jingyu Liu, Qing Zhao, and Ning Wu. Vibration-assisted exciton transfer in molecular aggregates strongly coupled to confined light fields. *The Journal of Chemical Physics*, 150(10):105102, 2019. Referred to on page 2.
- [14] R Sáez-Blázquez, Johannes Feist, Antonio Isaac Fernández-Domínguez, and FJ García-Vidal. Organic polaritons enable local vibrations to drive long-range energy transfer. *Physical Review B*, 97(24):241407, 2018. Referred to on page 2.
- [15] Johannes Feist and Francisco J Garcia-Vidal. Extraordinary exciton conductance induced by strong coupling. *Physical review letters*, 114(19):196402, 2015. Referred to on page 2.
- [16] Javier Del Pino, Francisco J Garcia-Vidal, and Johannes Feist. Exploiting vibrational strong coupling to make an optical parametric oscillator out of a raman laser. *Physical review letters*, 117(27):277401, 2016. Referred to on page 2.
- [17] Daniel Polak, Rahul Jayaprakash, Thomas P Lyons, Luis Á Martínez-Martínez, Anastasia Leventis, Kealan J Fallon, Harriet Coulthard, David G Bossanyi, Kyriacos Georgiou, Anthony J Petty, et al. Manipulating molecules with strong coupling: harvesting triplet excitons in organic exciton microcavities. *Chemical science*, 11(2):343–354, 2020. Referred to on page 2.
- [18] Felipe Herrera and Jeffrey Owrutsky. Molecular polaritons for controlling chemistry with quantum optics. *The Journal of chemical physics*, 152(10):100902, 2020. Referred to on page 2.
- [19] Matthew Du, Raphael F Ribeiro, and Joel Yuen-Zhou. Remote control of chemistry in optical cavities. *Chem*, 5(5):1167–1181, 2019. Referred to on page 2.
- [20] Manuel Hertzog, Mao Wang, Jürgen Tony, and Karl Börjesson. Strong light–matter interactions: a new direction within chemistry. *Chemical Society Reviews*, 48(3):937–961, 2019. Referred to on page 2, 11.
- [21] Johannes Feist, Javier Galego, and Francisco J Garcia-Vidal. Polaritonic chemistry with organic molecules. *ACS Photonics*, 5(1):205–216, 2018. Referred to on page 2, 11.
- [22] Raphael F Ribeiro, Luis A Martínez-Martínez, Matthew Du, Jorge Campos-Gonzalez-Angulo, and Joel Yuen-Zhou. Polariton chemistry: controlling molecular dynamics with optical cavities. *Chemical science*, 9(30):6325–6339, 2018. Referred to on page 2, 11.
- [23] Thomas W Ebbesen. Hybrid light–matter states in a molecular and material science perspective. *Accounts of chemical research*, 49(11):2403–2412, 2016. Referred to on page 2.

- [24] Johannes Flick, Nicholas Rivera, and Prineha Narang. Strong light-matter coupling in quantum chemistry and quantum photonics. *Nanophotonics*, 7(9):1479–1501, 2018. Referred to on page 2.
- [25] Adriana Canales, Denis G Baranov, Tomasz J Antosiewicz, and Timur Shegai. Abundance of cavity-free polaritonic states in resonant materials and nanostructures. *The Journal of Chemical Physics*, 154(2), 2021. Referred to on page 2.
- [26] Rahul Bhuyan, Maksim Lednev, Johannes Feist, and Karl Börjesson. The effect of the relative size of the exciton reservoir on polariton photophysics. *Advanced Optical Materials*, 12(2):2301383, 2024. Referred to on page 2, 25, 39.
- [27] Arpita Mukherjee, Johannes Feist, and Karl Borjesson. Quantitative investigation of the rate of intersystem crossing in the strong exciton–photon coupling regime. *Journal of the American Chemical Society*, 145(9):5155–5162, 2023. Referred to on page 2, 25.
- [28] Gerrit Groenhof, Claudia Climent, Johannes Feist, Dmitry Morozov, and J Jussi Toppari. Tracking polariton relaxation with multiscale molecular dynamics simulations. *The journal of physical chemistry letters*, 10(18):5476–5483, 2019. Referred to on page 2, 25.
- [29] T Takagahara. Theory of dephasing relaxation of excitonic polaritons. *Physical Review B*, 31(12):8171, 1985. Referred to on page 2, 25.
- [30] Heinz-Peter Breuer, Francesco Petruccione, et al. *The theory of open quantum systems*. Oxford University Press on Demand, 2002. Referred to on page 2, 11, 25, 28, 32, 34, 35, 38.
- [31] Patrick Wen, Gabriel Christmann, JJ Baumberg, and Keith A Nelson. Influence of multi-exciton correlations on nonlinear polariton dynamics in semiconductor microcavities. *New Journal of Physics*, 15(2):025005, 2013. Referred to on page 3.
- [32] N. Takemura, S. Trebaol, M. D. Anderson, V. Kohnle, Y. Léger, D. Y. Oberli, M. T. Portella-Oberli, and B. Deveaud. Two-dimensional fourier transform spectroscopy of exciton-polaritons and their interactions. *Phys. Rev. B*, 92:125415, 2015. Referred to on page 3, 42.
- [33] Bo Xiang, Raphael F Ribeiro, Yingmin Li, Adam D Dunkelberger, Blake B Simpkins, Joel Yuen-Zhou, and Wei Xiong. Manipulating optical nonlinearities of molecular polaritons by delocalization. *Science advances*, 5(9):eaax5196, 2019. Referred to on page 3, 42.
- [34] Shmuel Sufrin, Bar Cohn, and Lev Chuntonov. Probing the anharmonicity of vibrational polaritons with double-quantum two-dimensional infrared spectroscopy. *Nanophotonics*, 13(14):2523–2530, 2024. Referred to on page 3.
- [35] Wei Wang, Parinda Vasa, Ephraim Sommer, Antonietta De Sio, Petra Gross, Ralf Vogelgesang, and Christoph Lienau. Observation of lorentzian lineshapes in the room temperature optical spectra of strongly coupled jagggregate/metal hybrid nanostructures by linear two-dimensional optical spectroscopy. *Journal of Optics*, 16(11):114021, 2014. Referred to on page 3.

- [36] Hai Wang, Hai-Yu Wang, Hong-Bo Sun, Andrea Cerea, Andrea Toma, Francesco De Angelis, Xin Jin, Luca Razzari, Dan Cojoc, Daniele Catone, et al. Dynamics of strongly coupled hybrid states by transient absorption spectroscopy. *Advanced Functional Materials*, 28(48):1801761, 2018. Referred to on page 3.
- [37] Shota Takahashi and Kazuya Watanabe. Decoupling from a thermal bath via molecular polariton formation. *The Journal of Physical Chemistry Letters*, 11(4):1349–1356, 2020. Referred to on page 3, 6.
- [38] Lars Mewes, Mao Wang, Rebecca A Ingle, Karl Börjesson, and Majed Chergui. Energy relaxation pathways between light-matter states revealed by coherent two-dimensional spectroscopy. *Communications Physics*, 3(1):1–10, 2020. Referred to on page 3, 6, 9, 17, 42, 114, 117.
- [39] Francesca Fassioli, Kyu Hyung Park, Sarah E Bard, and Gregory D Scholes. Femtosecond photophysics of molecular polaritons. *The Journal of Physical Chemistry Letters*, 12(46):11444–11459, 2021. Referred to on page 3.
- [40] Zhedong Zhang, Kai Wang, Zhenhuan Yi, M. Suhail Zubairy, Marlan O. Scully, and Shaul Mukamel. Polariton-Assisted Cooperativity of Molecules in Microcavities Monitored by Two-Dimensional Infrared Spectroscopy. *J. Phys. Chem. Lett.*, 10(15):4448–4454, 2019. Referred to on page 3, 6.
- [41] M. Elious Mondal, Eric R. Koessler, Justin Provazza, A. Nickolas Vamivakas, Steven T. Cundiff, Todd D. Krauss, and Pengfei Huo. Quantum dynamics simulations of the 2D spectroscopy for exciton polaritons. *The Journal of Chemical Physics*, 159(9):094102, 09 2023. Referred to on page 3, 6, 42.
- [42] Zhedong Zhang, Xiaoyu Nie, Dangyuan Lei, and Shaul Mukamel. Multidimensional coherent spectroscopy of molecular polaritons: Langevin approach. *Phys. Rev. Lett.*, 130:103001, Mar 2023. Referred to on page 3, 6, 57, 64.
- [43] Minjung Son, Zachary T Armstrong, Ryan T Allen, Abitha Dhavamani, Michael S Arnold, and Martin T Zanni. Energy cascades in donor-acceptor exciton-polaritons observed by ultrafast two-dimensional white-light spectroscopy. *Nature Communications*, 13(1):7305, 2022. Referred to on page 4.
- [44] R. J. Thompson, G. Rempe, and H. J. Kimble. Observation of normal-mode splitting for an atom in an optical cavity. *Phys. Rev. Lett.*, 68:1132–1135, Feb 1992. Referred to on page 5.
- [45] Darius Abramavicius, Benoit Palmieri, Dmitri V Voronine, Frantisek Sanda, and Shaul Mukamel. Coherent multidimensional optical spectroscopy of excitons in molecular aggregates; quasiparticle versus supermolecule perspectives. *Chemical reviews*, 109(6):2350–2408, 2009. Referred to on page 6, 11.
- [46] Thomas A. A. Oliver. Recent advances in multidimensional ultrafast spectroscopy. *Royal Society Open Science*, 5(1):171425, 2018. Referred to on page 6, 42.

- [47] Andrius Gelzinis, Ramūnas Augulis, Vytautas Butkus, Bruno Robert, and Leonas Valkunas. Two-dimensional spectroscopy for non-specialists. *Biochimica et Biophysica Acta (BBA)-Bioenergetics*, 1860(4):271–285, 2019. Referred to on page [6](#), [42](#), [48](#).
- [48] Shaul Mukamel. Multidimensional femtosecond correlation spectroscopies of electronic and vibrational excitations. *Annual review of physical chemistry*, 51(1):691–729, 2000. Referred to on page [6](#), [42](#), [49](#).
- [49] David M Jonas. Two-dimensional femtosecond spectroscopy. *Annual review of physical chemistry*, 54:425, 2003. Referred to on page [6](#), [42](#), [48](#).
- [50] Antonietta De Sio, Xuan Trung Nguyen, and Christoph Lienau. Signatures of strong vibronic coupling mediating coherent charge transfer in two-dimensional electronic spectroscopy. *Zeitschrift für Naturforschung A*, 74(8):721–737, 2019. Referred to on page [6](#), [42](#), [44](#).
- [51] Francesco Segatta, Lorenzo Cupellini, Sandro Jurinovich, Shaul Mukamel, Maurizio Dapor, Simone Taioli, Marco Garavelli, and Benedetta Mennucci. A quantum chemical interpretation of two-dimensional electronic spectroscopy of light-harvesting complexes. *Journal of the American Chemical Society*, 139(22):7558–7567, 2017. Referred to on page [6](#), [42](#).
- [52] Raphael F. Ribeiro, Adam D Dunkelberger, Bo Xiang, Wei Xiong, Blake S Simpkins, Jeffrey C Owrutsky, and Joel Yuen-Zhou. Theory for nonlinear spectroscopy of vibrational polaritons. *The journal of physical chemistry letters*, 9(13):3766–3771, 2018. Referred to on page [6](#), [57](#).
- [53] Travis M Autry, Gaël Nardin, Christopher L Smallwood, Kevin Silverman, Daniele Bajoni, Aristide Lemaître, Sophie Bouchoule, Jacqueline Bloch, and Steven Cundiff. Excitation ladder of cavity polaritons. *Physical Review Letters*, 125(6):067403, 2020. Referred to on page [6](#).
- [54] Prasoon Saurabh and Shaul Mukamel. Two-dimensional infrared spectroscopy of vibrational polaritons of molecules in an optical cavity. *The Journal of chemical physics*, 144(12):124115, 2016. Referred to on page [6](#), [42](#).
- [55] Zimo Yang, Bo Xiang, and Wei Xiong. Controlling quantum pathways in molecular vibrational polaritons. *ACS Photonics*, 7(4):919–924, 2020. Referred to on page [6](#), [56](#).
- [56] Andrea B Grafton, Adam D Dunkelberger, Blake S Simpkins, Johan F Triana, Federico J Hernández, Felipe Herrera, and Jeffrey C Owrutsky. Excited-state vibration-polariton transitions and dynamics in nitroprusside. *Nature communications*, 12(1):1–9, 2021. Referred to on page [6](#), [42](#).
- [57] Bo Xiang, Raphael F Ribeiro, Liying Chen, Jiayi Wang, Matthew Du, Joel Yuen-Zhou, and Wei Xiong. State-selective polariton to dark state relaxation dynamics. *The Journal of Physical Chemistry A*, 123(28):5918–5927, 2019. Referred to on page [6](#).
- [58] Lars Mewes, Mao Wang, Rebecca A Ingle, Karl Börjesson, and Majed Chergui. Energy relaxation pathways between light-matter states revealed by coherent two-dimensional spectroscopy. *Communications Physics*, 3(1):1–10, 2020. Referred to on page [6](#).

-
- [59] D. S. Dovzhenko, S. V. Ryabchuk, Yu. P. Rakovich, and I. R. Nabiev. Light–matter interaction in the strong coupling regime: configurations, conditions, and applications. *Nanoscale*, 10:3589–3605, 2018. Referred to on page [11](#).
- [60] Tao E. Li, Bingyu Cui, Joseph E. Subotnik, and Abraham Nitzan. Molecular polaritonics: Chemical dynamics under strong light–matter coupling. *Annual Review of Physical Chemistry*, 73(Volume 73, 2022):43–71, 2022. Referred to on page [11](#).
- [61] Rocio Sáez-Blázquez, Johannes Feist, Antonio Isaac Fernández-Domínguez, and FJ García-Vidal. Enhancing photon correlations through plasmonic strong coupling. *Optica*, 4(11):1363–1367, 2017. Referred to on page [11](#), [17](#).
- [62] Claude Cohen-Tannoudji, Jacques Dupont-Roc, and Gilbert Grynberg. *Photons and atoms—introduction to quantum electrodynamics*. J. Wiley, New York, 1997. Referred to on page [11](#), [13](#), [14](#).
- [63] Christopher Gerry and Peter L. Knight. *Introductory quantum optics*. Cambridge University Press, 2005. Referred to on page [11](#), [20](#), [21](#).
- [64] Johannes Feist, Antonio I Fernández-Domínguez, and Francisco J García-Vidal. Macroscopic qed for quantum nanophotonics: emitter-centered modes as a minimal basis for multiemitter problems. *Nanophotonics*, 10(1):477–489, 2020. Referred to on page [11](#).
- [65] Petros-Andreas Pantazopoulos, Johannes Feist, Akashdeep Kamra, and Francisco J García-Vidal. Electrostatic nature of cavity-mediated interactions between low-energy matter excitations. *arXiv preprint arXiv:2311.00183*, 2023. Referred to on page [11](#).
- [66] Mónica Sánchez-Barquilla, Francisco J García-Vidal, Antonio I Fernández-Domínguez, and Johannes Feist. Few-mode field quantization for multiple emitters. *Nanophotonics*, 11(19):4363–4374, 2022. Referred to on page [11](#).
- [67] Ivan Medina, Francisco J García-Vidal, Antonio I Fernández-Domínguez, and Johannes Feist. Few-mode field quantization of arbitrary electromagnetic spectral densities. *Physical Review Letters*, 126(9):093601, 2021. Referred to on page [11](#).
- [68] Rocio Sáez Blázquez. *Dressing the vacuum: Strong light-matter coupling for enhancing photon correlations and exciton transport*. PhD thesis, Universidad Autónoma de Madrid, 2020. Referred to on page [11](#), [34](#), [36](#), [39](#), [40](#), [55](#).
- [69] Javier Galego Pascual. *Polaritonic Chemistry. Manipulating molecular structure through strong light-matter coupling*. PhD thesis, Universidad Autónoma de Madrid, 2019. Referred to on page [11](#), [15](#).
- [70] Daniele Sanvitto and Stéphane Kéna-Cohen. The road towards polaritonic devices. *Nature materials*, 15(10):1061–1073, 2016. Referred to on page [11](#).

- [71] Alexey V Kavokin, Jeremy J Baumberg, Guillaume Malpuech, and Fabrice P Laussy. *Microcavities*, volume 21. Oxford university press, 2017. Referred to on page [11](#), [16](#).
- [72] M.S. Tame, K.R. McEnery, Ş.K. Özdemir, J. Lee, S.A. Maier, and M.S. Kim. Quantum plasmonics. *Nature Physics*, 9:329–340, 2013. Referred to on page [11](#).
- [73] David J Griffiths. *Introduction to electrodynamics*. Cambridge University Press, 2023. Referred to on page [12](#), [13](#).
- [74] Edwin Albert Power and Sigurd Zienau. Coulomb gauge in non-relativistic quantum electrodynamics and the shape of spectral lines. *Philosophical Transactions of the Royal Society of London. Series A, Mathematical and Physical Sciences*, 251(999):427–454, 1959. Referred to on page [14](#).
- [75] R. Gr. Woolley. Molecular quantum electrodynamics. *Proceedings of the Royal Society of London. A. Mathematical and Physical Sciences*, 321(547):557–572, 1971. Referred to on page [14](#).
- [76] Daniel A Steck. *Quantum and atom optics*. University of Oregon, 2007. Referred to on page [14](#).
- [77] Shaul Mukamel. *Principles of nonlinear optical spectroscopy*. Oxford University Press, 1995. Referred to on page [15](#), [28](#), [32](#), [42](#), [45](#), [49](#), [52](#), [56](#).
- [78] Edwin Albert Power and T Thirunamachandran. The multipolar hamiltonian in radiation theory. *Proceedings of the Royal Society of London. A. Mathematical and Physical Sciences*, 372:265–273, 1980. Referred to on page [15](#).
- [79] Tal Schwartz, James A Hutchison, Cyriaque Genet, and Thomas W Ebbesen. Reversible switching of ultrastrong light-molecule coupling. *Physical review letters*, 106(19):196405, 2011. Referred to on page [15](#).
- [80] D. G. Lidzey, D. D. C. Bradley, M. S. Skolnick, T. Virgili, S. Walker, and D. M. Whittaker. Exciton-photon coupling in an organic semiconductor microcavity. *Nature*, 395:53–55, 1998. Referred to on page [15](#), [20](#).
- [81] M. G. Raizen, R. J. Thompson, R. J. Brecha, H. J. Kimble, and H. J. Carmichael. Normal-mode splitting and linewidth averaging for two-state atoms in an optical cavity. *Phys. Rev. Lett.*, 63:240, 1989. Referred to on page [15](#), [20](#).
- [82] Jeanne Heintz, Nemanja Markesevic, Elise Y Gayet, Nicolas Bonod, and Sébastien Bidault. Few-molecule strong coupling with dimers of plasmonic nanoparticles assembled on dna. *ACS nano*, 15(9):14732–14743, 2021. Referred to on page [15](#), [20](#).
- [83] Rohit Chikkaraddy, Bart De Nijs, Felix Benz, Steven J Barrow, Oren A Scherman, Edina Rosta, Angela Demetriadou, Peter Fox, Ortwin Hess, and Jeremy J Baumberg. Single-molecule strong coupling at room temperature in plasmonic nanocavities. *Nature*, 535(7610):127–130, 2016. Referred to on page [15](#), [20](#).

- [84] Kotni Santhosh, Ora Bitton, Lev Chuntonov, and Gilad Haran. Vacuum rabi splitting in a plasmonic cavity at the single quantum emitter limit. *Nature communications*, 7(1):ncomms11823, 2016. Referred to on page 15, 20.
- [85] Ruth H Tichauer, Johannes Feist, and Gerrit Groenhof. Multi-scale dynamics simulations of molecular polaritons: The effect of multiple cavity modes on polariton relaxation. *The Journal of Chemical Physics*, 154(10), 2021. Referred to on page 16.
- [86] A Delga, J Feist, J Bravo-Abad, and FJ Garcia-Vidal. Theory of strong coupling between quantum emitters and localized surface plasmons. *Journal of Optics*, 16(11):114018, 2014. Referred to on page 16.
- [87] Stefan Scheel and Stefan Yoshi Buhmann. Macroscopic qed-concepts and applications. *arXiv preprint arXiv:0902.3586*, 2009. Referred to on page 16.
- [88] Filippo Alpeggiani and Lucio Claudio Andreani. Quantum theory of surface plasmon polaritons: planar and spherical geometries. *Plasmonics*, 9:965–978, 2014. Referred to on page 16, 17.
- [89] Clàudia Climent, Javier Galego, Francisco J Garcia-Vidal, and Johannes Feist. Plasmonic nanocavities enable self-induced electrostatic catalysis. *Angewandte Chemie International Edition*, 58(26):8698–8702, 2019. Referred to on page 17.
- [90] Mohammad Ramezani, Alexei Halpin, Johannes Feist, Niels Van Hoof, Antonio I Fernáandez-Domínguez, Francisco J Garcia-Vidal, and Jaime Gómez Rivas. Dispersion anisotropy of plasmon–exciton–polaritons in lattices of metallic nanoparticles. *Acs Photonics*, 5(1):233–239, 2018. Referred to on page 17.
- [91] SRK Rodriguez, J Feist, MA Verschuuren, FJ Garcia Vidal, and J Gómez Rivas. Thermalization and cooling of plasmon-exciton polaritons: towards quantum condensation. *Physical review letters*, 111(16):166802, 2013. Referred to on page 17.
- [92] Bransden B.H. and Joachain C.J. *Physics of Atoms and Molecules*. Pearson Education Limited, 2005. Referred to on page 17, 18, 19.
- [93] Attila Szabo and Neil S. Ostlund. *Modern Quantum Chemistry*. McGraw-Hill, Inc, 1989. Referred to on page 18, 19.
- [94] Ian Fleming. *Frontier orbitals and organic chemical reactions*. Wiley, 1978. Referred to on page 19.
- [95] Javier del Pino, Johannes Feist, and Francisco J Garcia-Vidal. Quantum theory of collective strong coupling of molecular vibrations with a microcavity mode. *New Journal of Physics*, 17(5):053040, 2015. Referred to on page 20, 40, 80.
- [96] J. M. Fink, R. Bianchetti, M. Baur, M. Göppl, L. Steffen, S. Filipp, P. J. Leek, A. Blais, and A. Wallraff. Dressed collective qubit states and the tavis-cummings model in circuit qed. *Phys. Rev. Lett.*, 103:083601, 2009. Referred to on page 20.

-
- [97] Johannes Feist. Hybrid light–matter states formed in self-assembling cavities, 2021. Referred to on page [20](#).
- [98] Diego R Abujetas, Johannes Feist, Francisco J García-Vidal, Jaime Gómez Rivas, and José A Sánchez-Gil. Strong coupling between weakly guided semiconductor nanowire modes and an organic dye. *Physical Review B*, 99(20):205409, 2019. Referred to on page [20](#).
- [99] H. Walther. Experiments on cavity quantum electrodynamics. *Phys. Rep.*, 219:263, 1992. Referred to on page [20](#).
- [100] K. Härkönen, F. Plastina, and S. Maniscalco. Dicke model and environment-induced entanglement in ion-cavity qed. *Phys. Rev. A*, 80:033841, 2009. Referred to on page [20](#).
- [101] M. Tavis and F. W. Cummings. Exact solution for an n -molecule—radiation-field hamiltonian. *Phys. Rev.*, 170:379, 1968. Referred to on page [21](#).
- [102] K. Fudji and *et al.* Explicit form of solution of two atoms tavis-cummings model. *arXiv:quant-ph/0403008*, 2004. Referred to on page [21](#).
- [103] Barry M Garraway. The dicke model in quantum optics: Dicke model revisited. *Philosophical Transactions of the Royal Society A: Mathematical, Physical and Engineering Sciences*, 369(1939):1137–1155, 2011. Referred to on page [21](#), [103](#), [116](#).
- [104] R. H. Dicke. Coherence in spontaneous radiation processes. *Phys. Rev.*, 93:99, 1954. Referred to on page [22](#).
- [105] K. Hepp and E. H. Lieb. On the superradiant phase transition for molecules in a quantized radiation field: the dicke maser model. *Ann. Phys., NY*, 76:360, 1973. Referred to on page [22](#).
- [106] Qiongtao Xie, Honghua Zhong, Murray T Batchelor, and Chaohong Lee. The quantum rabi model: solution and dynamics. *Journal of Physics A: Mathematical and Theoretical*, 50(11):113001, 2017. Referred to on page [22](#).
- [107] Anton Frisk Kockum, Adam Miranowicz, Simone De Liberato, Salvatore Savasta, and Franco Nori. Ultrastrong coupling between light and matter. *Nature Reviews Physics*, 1(1):19–40, 2019. Referred to on page [22](#).
- [108] E. T. Jaynes and F. W. Cummings. Comparison of quantum and semiclassical radiation theories with application to the beam maser. *Proc. IEEE*, 51:89, 1963. Referred to on page [22](#).
- [109] Carlos Gonzalez-Ballester, Johannes Feist, Eduardo Gonzalo Badía, Esteban Moreno, and Francisco J Garcia-Vidal. Uncoupled dark states can inherit polaritonic properties. *Physical review letters*, 117(15):156402, 2016. Referred to on page [22](#).
- [110] Stéphane Kéna-Cohen and Joel Yuen-Zhou. Polariton chemistry: Action in the dark, 2019. Referred to on page [22](#).

-
- [111] Felipe Herrera and Frank C Spano. Dark vibronic polaritons and the spectroscopy of organic microcavities. *Physical Review Letters*, 118(22):223601, 2017. Referred to on page [22](#).
- [112] Hebin Li and Steven T. Cundiff. Chapter One - 2D Coherent Spectroscopy of Electronic Transitions. In Ennio Arimondo, Chun C. Lin, and Susanne F. Yelin, editors, *Advances In Atomic, Molecular, and Optical Physics*, volume 66, page 1. Academic Press, January 2017. Referred to on page [25](#).
- [113] JJ Sakurai and Jim Napolitano. Modern quantum mechanics 3rd edition, 2020. Referred to on page [27](#).
- [114] Howard J Carmichael. *Statistical methods in quantum optics 1: master equations and Fokker-Planck equations*, volume 1. Springer Science & Business Media, 1999. Referred to on page [32](#), [39](#).
- [115] Felix Bloch. Generalized theory of relaxation. *Physical Review*, 105(4):1206, 1957. Referred to on page [35](#).
- [116] Alfred G Redfield. On the theory of relaxation processes. *IBM Journal of Research and Development*, 1(1):19–31, 1957. Referred to on page [35](#).
- [117] Goran Lindblad. On the generators of quantum dynamical semigroups. *Communications in Mathematical Physics*, 48:119–130, 1976. Referred to on page [37](#).
- [118] Vittorio Gorini, Andrzej Kossakowski, and Ennackal Chandy George Sudarshan. Completely positive dynamical semigroups of n-level systems. *Journal of Mathematical Physics*, 17(5):821–825, 1976. Referred to on page [37](#).
- [119] Jan Jeske and Jared H Cole. Derivation of markovian master equations for spatially correlated decoherence. *Physical Review A*, 87(5):052138, 2013. Referred to on page [38](#).
- [120] Daniel Manzano. A short introduction to the lindblad master equation. *AIP Advances*, 10(2):025106, 2020. Referred to on page [39](#).
- [121] Diego Fernández de la Pradilla, Esteban Moreno, and Johannes Feist. Taming the bloch-redfield equation: Recovering an accurate lindblad equation for general open quantum systems. *arXiv preprint arXiv:2402.06354*, 2024. Referred to on page [39](#).
- [122] Rocío Sáez-Blázquez, Johannes Feist, Elisabet Romero, Antonio I Fernández-Domínguez, and Francisco J García-Vidal. Cavity-modified exciton dynamics in photosynthetic units. *The Journal of Physical Chemistry Letters*, 10(15):4252–4258, 2019. Referred to on page [39](#).
- [123] Jan Jeske, J David, Martin B Plenio, Susana F Huelga, and Jared H Cole. Bloch-redfield equations for modeling light-harvesting complexes. *The Journal of chemical physics*, 142(6), 2015. Referred to on page [39](#).

- [124] Alessandro Sergi and Konstantin G Zloshchastiev. Non-hermitian quantum dynamics of a two-level system and models of dissipative environments. *International Journal of Modern Physics B*, 27(27):1350163, 2013. Referred to on page 39.
- [125] Javier Del Pino, Florian AYN Schröder, Alex W Chin, Johannes Feist, and Francisco J Garcia-Vidal. Tensor network simulation of non-markovian dynamics in organic polaritons. *Physical review letters*, 121(22):227401, 2018. Referred to on page 39.
- [126] JMea Gerard, D Barrier, JY Marzin, R Kuszelewicz, L Manin, E Costard, V Thierry-Mieg, and T Rivera. Quantum boxes as active probes for photonic microstructures: The pillar microcavity case. *Applied Physics Letters*, 69(4):449–451, 1996. Referred to on page 40.
- [127] AJ Bennett, DC Unitt, P See, AJ Shields, P Atkinson, K Cooper, and DA Ritchie. Microcavity single-photon-emitting diode. *Applied Physics Letters*, 86(18), 2005. Referred to on page 40.
- [128] Korenobu Matsuzaki, Hsuan-Wei Liu, Stephan Götzinger, and Vahid Sandoghdar. On quantum efficiency measurements and plasmonic antennas. *ACS Photonics*, 8(6):1508–1521, 2021. Referred to on page 40.
- [129] Pallavi Bhattacharyya and Graham R Fleming. Two-dimensional electronic–vibrational spectroscopy of coupled molecular complexes: A near-analytical approach. *The journal of physical chemistry letters*, 10(9):2081–2089, 2019. Referred to on page 42.
- [130] Vivek Tiwari. Multidimensional electronic spectroscopy in high-definition—Combining spectral, temporal, and spatial resolutions. *The Journal of Chemical Physics*, 154(23):230901, 2021. Referred to on page 42.
- [131] Akihito Ishizaki and Yoshitaka Tanimura. Modeling vibrational dephasing and energy relaxation of intramolecular anharmonic modes for multidimensional infrared spectroscopies. *The Journal of chemical physics*, 125(8):084501, 2006. Referred to on page 42.
- [132] Franklin D. Fuller and Jennifer P. Ogilvie. Experimental implementations of two-dimensional fourier transform electronic spectroscopy. *Annual Review of Physical Chemistry*, 66(1):667–690, 2015. Referred to on page 42.
- [133] Nguyen Thanh Phuc and Pham Quang Trung. Direct and ultrafast probing of quantum many-body interactions through coherent two-dimensional spectroscopy: From weak-to strong-interaction regimes. *Physical Review B*, 104(11):115105, 2021. Referred to on page 42.
- [134] Daniel Finkelstein-Shapiro, Pierre-Adrien Mante, Sema Sarisozen, Lukas Wittenbecher, Iulia Minda, Sinan Balci, Tõnu Pullerits, and Donatas Zigmantas. Understanding radiative transitions and relaxation pathways in plexcitons. *Chem*, 7(4):1092–1107, 2021. Referred to on page 42.
- [135] C Heshmatpour, J Hauer, and F Šanda. Interplay of exciton annihilation and transport in fifth order electronic spectroscopy. *Chemical Physics*, 528:110433, 2020. Referred to on page 42, 49.

- [136] Bo Xiang, Raphael F Ribeiro, Adam D Dunkelberger, Jiayi Wang, Yingmin Li, Blake S Simpkins, Jeffrey C Owrutsky, Joel Yuen-Zhou, and Wei Xiong. Two-dimensional infrared spectroscopy of vibrational polaritons. *Proceedings of the National Academy of Sciences*, 115(19):4845–4850, 2018. Referred to on page 42.
- [137] Konstantin E Dorfman and Shaul Mukamel. Multidimensional photon correlation spectroscopy of cavity polaritons. *Proceedings of the National Academy of Sciences*, 115(7):1451–1456, 2018. Referred to on page 42.
- [138] Leonas Valkunas, Darius Abramavicious, and Tomáš Mančal. *Molecular Excitation Dynamics*. Wiley, 2013. Referred to on page 42, 45, 56.
- [139] Minhaeng Cho. *Coherent multidimensional spectroscopy*, volume 226. Springer, 2019. Referred to on page 42.
- [140] Peter Hamm and Martin Zanni. *Concepts and methods of 2D infrared spectroscopy*. Cambridge University Press, 2011. Referred to on page 42, 45, 52, 56, 57.
- [141] Dominik Lentrodt and Jörg Evers. Ab initio few-mode theory for quantum potential scattering problems. *Physical Review X*, 10(1):011008, 2020. Referred to on page 43.
- [142] Maxim F Gelin, Dassia Egorova, and Wolfgang Domcke. Efficient calculation of time-and frequency-resolved four-wave-mixing signals. *Accounts of chemical research*, 42(9):1290–1298, 2009. Referred to on page 44, 45, 64.
- [143] Anton Frisk Kockum, Adam Miranowicz, Vincenzo Macrì, Salvatore Savasta, and Franco Nori. Deterministic quantum nonlinear optics with single atoms and virtual photons. *Physical Review A*, 95(6):063849, 2017. Referred to on page 45.
- [144] Daniele Brida, Cristian Manzoni, and Giulio Cerullo. Phase-locked pulses for two-dimensional spectroscopy by a birefringent delay line. *Optics letters*, 37(15):3027–3029, 2012. Referred to on page 45.
- [145] M Abdullah, Farah T Mohammed Noori, and Amin H Al-Khursan. Second-order nonlinear susceptibility in quantum dot structure under applied electric field. *Superlattices and Microstructures*, 82:219–233, 2015. Referred to on page 48.
- [146] Mansoor Sheik-Bahae and Michael P Hasselbeck. Third-order optical nonlinearities. *Handbook of Optics*, 4:16–1, 2000. Referred to on page 51.
- [147] Amin H. Al-Khursan, M.K. Al-Khakani, and K.H. Al-Mossawi. Third-order non-linear susceptibility in a three-level qd system. *Photonics and Nanostructures - Fundamentals and Applications*, 7(3):153–160, 2009. Referred to on page 51.
- [148] Peter Hamm. Principles of nonlinear optical spectroscopy: A practical approach or: Mukamel for dummies. *University of Zurich*, 41(5):77, 2005. Referred to on page 51, 63.

-
- [149] Robert W Boyd. *Nonlinear optics*. Academic press, 2020. Referred to on page [51](#).
- [150] Tomáš Neuman and Javier Aizpurua. Origin of the asymmetric light emission from molecular exciton–polaritons. *Optica*, 5(10):1247–1255, 2018. Referred to on page [54](#).
- [151] Peter A Rose and Jacob J Krich. Efficient numerical method for predicting nonlinear optical spectroscopies of open systems. *The Journal of Chemical Physics*, 154(3):034108, 2021. Referred to on page [64](#).
- [152] Tomáš Mančal, Andrei V Pisiakov, and Graham R Fleming. Two-dimensional optical three-pulse photon echo spectroscopy. i. nonperturbative approach to the calculation of spectra. *The Journal of chemical physics*, 124(23):234504, 2006. Referred to on page [64](#).
- [153] Nicolás Quesada. Strong coupling of two quantum emitters to a single light mode: The dissipative tavis-cummings ladder. *Physical Review A—Atomic, Molecular, and Optical Physics*, 86(1):013836, 2012. Referred to on page [99](#).
- [154] David M. Coles, Niccolo Somaschi, Paolo Michetti, Caspar Clark, Pavlos G. Lagoudakis, Pavlos G. Savvidis, and David G. Lidzey. Polariton-mediated energy transfer between organic dyes in a strongly coupled optical microcavity. *Nature Materials*, 13:712–719, 2014. Referred to on page [130](#).